Spatio-Temporal and Polarisation Dynamics of Semiconductor Microcavity Lasers

Von der Fakultät Mathematik und Physik der Universität Stuttgart
zur Erlangung der Würde eines
Doktors der Naturwissenschaften (Dr. rer. nat.)
genehmigte Abhandlung

vorgelegt von

Joachim Hamm

aus Leonberg

Tag der mündlichen Prüfung: Oktober 15, 2004

Hauptberichter	Mitberichter
Prof. Dr. O. Hess	Prof. Dr. G. Mahler

2004

Theoretische Quantenelektronik
Institut für Technische Physik, DLR
Pfaffenwaldring 38-40
D-70569 Stuttgart

Acknowledgements

This page is dedicated to all the people who did inspire and support me during the time of my PhD. I thank Ahu, my friends, my family, my colleagues and all the other people who influenced my way of thinking, one way or another. In the most explicit manner I would like to thank the persons who directly contributed to this work:

Prof. Dr. O. Hess for his supervision, expertise and advice. His ability to recognise and support my skills has opened opportunities and changed the direction I am heading to.

Prof. Dr. G. Mahler for his suggestions and the *Übernahme des Mitberichts. Which is apparently hard to translate.*

Klaus Böhringer for discussions concerning microscopic processes in semiconductor structures. *Expert for all the "things with the hats on" and a master of the coffee brewing art.*

Andreas Klaedtke for cheerful discussions about microcavity dynamics and time-domain laser models. *Sitting in one room: he, me, the rabbit, and a dead plant.*

Christian Herrmann for more discussions about cavity modes and the DFB boundary conditions. *The always reliable source for online-news and their interpretation.*

Dr. Christian-Simmendinger for the administration of the nasty SR-8000K, and his support on code development and optimisation. *Berserker-style base rush.*

Dr. Dietmar Preisser for discussions about broad-area laser structures. *Successfully penetrating the security system of the German Aerospace Center.*

Dr. Edeltraud Gehrig for discussions about temperature dynamics and low-dimensional system modelling. *There is quite some space on* `/var`. *Why not use it?*

Dr. Stefan Scholz for discussions about structured photonic systems. *Some truely philosophical questions: Windows or Linux? Python or Perl?*

Andreas Barchanski from TU-Darmstadt for providing experimental data.

(Joachim Hamm)

Zusammenfassung

Mikroresonator Halbleiterlaser sind durch eine starke interne Kopplung von aktivem Material und Lichtfeld charakterisiert. Die dynamische Wechselwirkung zwischen dem Ladungsträger- und dem Photonensystem wird dabei sowohl durch die dynamischen Eigenschaften der Ladungsträger im Quanten-Well als auch durch die Lichtfelddynamik innerhalb des Mikroresonators beeinflußt. Die im Rahmen dieser Arbeit entwickelten Methoden und Modelle erlauben es uns die nichtlinearen raumzeitlichen Eigenschaften von zwei ausgewählten Mikroresonator-Lasern zu untersuchen: dem vertikal-Resonator oberflächenemittierenden Halbleiter Laser (VCSEL) und dem optisch gepumpten oberflächenemittierenden Halbleiter Laser mit externem Resonator (VECSEL).

Die longitudinale Lichtfeld Mode eines VCSELs ist fest zwischen den Bragg-Spiegeln (DBRs) eingespannt. Obwohl der Laser longitudinal monomodig ist, sind mit einem typischen Apertur-Durchmesser von $5 - 15\,\mu$m transversale Freiheitsgrade verbunden, die sich im Anschwingen von transversalen Seitenmoden äußern. Zudem erlaubt die Rotationssymmetrie der Resonatorstruktur die Ausbildung von zwei linearen Polarisationsfeldern. Zirkular oder diagonal polarisiertes Licht ergibt sich aus einer entsprechenden phasenverschobenen Überlagerung dieser linearen Moden. Unsere Hauptinteresse konzentriert sich auf ein Verständnis der Mechanismen, die sich hinter dem komplexen Wechselspiel zwischen der transversalen Modendynamik und der Polarisation-Dynamik verbergen, welche durch das spin-polarisierte aktive Medium vermittelt werden. In ähnlicher Weise wie das räumliche Lochbrennen die Inversion in bestimmten räumlichen Teilbereichen entvölkert und damit eine nichtlinear Kopplung zwischen den transversalen Moden bewirkt, bricht die Spin-Polarisation der Quanten-Wells die Rotationssymmetrie und koppelt damit die ursprünglich gleichberechtigten Polarisationsmoden. Neben diesem Effekt, der einer nichtlinearen induzierten Doppelbrechung entspricht, unterliegt der Mikroresonator eines VCSELs, in Folge des elektro-optischen Effekts, linearer Doppelbrechung. Experimente unterstreichen die Bedeutung dieser Kopplungsmechanismen und zeigen in Abhängigkeit von Lasertyp und Betriebsbedingungen eine Frequenzaufspaltung von typischerweise 5-40 GHz. VCSEL mit einem kleinen Apertur-Durchmesser strahlen transversal monomodiges Licht ab. Für solche Systeme tritt ein Selektionsmechanismus ein, der zur Folge hat, dass eine der beiden linearen Polarisationsmoden unterdrückt wird. In breiteren Strukturen mit einem Apertur-Durchmesser von mehr als $10\,\mu$m dagegen, kann die schwächere zusammen mit der bevorzugten linearen Polarisationsmode schwingen, indem sie einen anderen Satz von transversale Moden einnimmt und damit unterschiedliche räumliche Gewinngebiete besetzt.

Aufbauend auf einem zeitaufgelösten Modell untersuchen wir die Mechanismen, die den transversalen Modenübergängen und dem Polarisationsverhalten zugrunde liegen. In den ersten Kapiteln der vorliegenden Arbeit wird dazu ein Gerüst aus Gleichungen abgeleitet, welches die wichtigsten Aspekte der Lichtfelddynamik, der bandaufgelösten Ladungsträgerdynamik und von Temperatureffekten erfaßt und auf eine einheitliche Beschreibungsebene zusammenführt. Die Allgemeingültigkeit der abgeleiteten Gleichungen und eine effiziente numerische Implementation erlauben es uns, verschiedene Aspekte der Dynamik zu extrahieren und getrennt zu untersuchen; Ladungsträger Dynamik (spektrales Lochbrennen, Spin-Polarisation), räumliche Effekte (räumliches Lochbrennen und Selbstfokusierung), temperaturbezogene Effekte (thermischer Linseneffekt) und nichtlineare Eigenschaften (Amplituden-Phasen Kopplung) repräsentieren sind Beispiele interner Prozesse, welche die experimentell beobachteten Ausgangsgrößen, wie Leistung, Schwellstrom, Slope-Efficiency und Strahlqualität, von VCSELn prägen.

Inspiriert von sowohl dem Erfolg als auch dem Konzept der VCSEL werden ständig neue Typen von oberflächenemittierende Halbleiter Laser entwickelt. Eine dieser Bauarten, der VECSEL, kann als optisch gepumpte Hochleistungsvariante des VCSELs aufgefaßt werden. Trotz vieler Gemeinsamkeiten, wie Quanten-Wells, die in den Modenmaximas platziert werden, dem Mikroresonator und dem frequenzselektiven Bragg-Spiegel, unterscheidet sich der VECSEL von dem kleineren VCSEL in mancher Hinsicht: da der VECSEL keinen oberen Bragg-Spiegel besitzt, ist die Kavität nicht länger longitudinal monomodig. Darüber hinaus wird der externe Resonatorspiegel üblicherweise in einigen Zentimetern Entfernung von dem VECSEL Chip angebracht. Mit ca. 100 ps ist die Umlaufzeit im externen Resonator ein Vielfaches der internen Umlaufzeit im Mikroresonator. Der damit einhergehende Modenabstand von ungefähr 100 GHz ist klein genug, um mehreren 100 longitudinalen Moden Platz im positiven Gain-Bereich des aktiven Quanten-Well Materials zu bieten. In radialer Richtung dagegen, wird das Lichtfeld mittels des gekrümmten externen Resonators auf einer breiten TEM_{00} Mode festgehalten. Im Gegensatz zu VCSELn werden VECSEL üblicherweise optisch gepumpt und stellen aussichtsreiche Kandidaten für Ultrakurzpulsanwendungen und Anwendungen um im Hochleistungsbereich dar. Mehrfach Quanten-Well Strukturen (MQW) und ein Pumpfleck von typischerweise 100 μm transversaler Ausdehnung ermöglichen Ausgangsleistungen von mehr als 500 mW. Eine Integration sättigbarer Absorber in den optischen Weg oder den Chip als solchen, erlaubt eine passive Kopplung der longitudinalen Moden. Die nichtlineare Kopplung zwischen Lichtfeld und Ladungstägern ist nicht zuletzt aufgrund der hohen Intensitäten stark ausgeprägt und wird durch Effekte, wie die Konkurrenz der longitudinalen Moden, die Wechselwirkung der Polarisationsmoden, die bandaufgelöste Ladungsträger und den nicht-ambipolaren Transport der Ladungsträger, beeinflußt. Darüber hinaus prägt der externe Spiegel, der als eine zeitlich verzögerte Rückkopplungsschleife interpretiert werden kann, dem System eine weitere charakteristische Zeitskala auf. Die Vielzahl neuer Aspekte kombiniert mit dem flexiblen optischen und elektronischen VECSEL Design, eröffnet neue Felder für Theorie, Experiment und Anwendung.

Von einem theoretischen Standpunkt der aus, sollte erwähnt werden, dass nicht alle der für VCSEL abgeleiteten Bewegungsgleichungen ohne Einschränkung auf VECSEL Systeme angewendet werden können. Die Vielzahl der koexistierenden longitudinalen Moden erfordert eine vollständige Beschreibung der Felder im Zeitraum. Dies wiederum bedeutet, dass die Materialgleichungen, die die Ladungsträgerdynamik in den Quanten-Wells beschreiben, in den Zeitraum übertragen werden müssen. Für diesen Zweck, entwickeln wir raumzeitliche Gleichungen welche wir auf die Ladungsträger in den Quanten-Wells und die optische Kavität abbilden. Diese Gleichungen beinhalten sowohl den Elektron / Loch Ladungsträgertransport als auch die Frequenzabhängigkeit der Gewinnantwort (Gain). Weiterhin zeigen wir auf, in welcher Weise die Bandstruktur einbezogen werden kann, wodurch ein Übergang von der vereinfachten zwei-Niveau Beschreibung zu einem realistischen Materialmodell für die Quanten-Wells vollzogen wäre. Basierend auf der *total-field scattered-field* Methode entwickeln wir eine neue Art von Randbedingungen, die den Umlauf im externen Resonator auf eine zeitlich verzögerte Rückkopplung abbildet. Das Diskretisierungsschema und dessen numerische Implementation erlaubt eine effiziente Simulation ausgedehnter Kavitätsstrukturen. Zusammenfassend kann gesagt werden, dass das vorgestellte Modell ein neuartiges Werkzeug zur Untersuchung von ultrakurzzeit- und sub-Pikosekunden Phänomenen in Mikroresonatoren darstellt. Weitere Schritte in Richtung eines realistischeren Materialmodells müssen in Betracht gezogen werden, um die Besonderheiten der betrachteten Laserstrukturen grundlegend zu erfassen.

Die Zielsetzung schnellere und leistungsstärkere Halbleiterlaser zu entwickeln, geht Hand in Hand mit einer Miniaturisierung der Laserstrukturen bis in den Nanometerbereich. Eine entkoppelte theoretische Beschreibung, welche selbst für einfachste Halbleiterlaser nur beschränkte Gültigkeit besitzt, wird durch die immer engere Verzahnung der lokalisierten Ladungsträger und der Resonatormoden, sowohl in räumlicher als auch in zeitlicher Hinsicht, erschwert. Dagegen bieten die hier vorgestellten Methoden eine flexible Basis, um die verschiedenen physikalischen Prozesse und ihr Wechselspiel auf natürliche Weise in einem Bottom-Up Ansatz zu integrieren. Durch eine wachsende Verfügbarkeit leistungsstarker und kostengünstiger Rechenplatformen wird eine direkte Lösung der Bewegungsgleichungen im Zeitraum zukünftig an Attraktivität gewinnen und die technologischen Entwicklung immer neuer Mikroresonator Halbleiterlaser als ein verläßliches Werkzeug zur Untersuchung derer optischen und elektronischen Eigenschaften begleiten.

Abstract

Microcavity semiconductor lasers are known for their inherent tight coupling between active material and light-field. The dynamic interaction between the carrier and the photon subsystems is influenced equally strong by both, the dynamics of carriers within the quantum-well and the intra-cavity light-field dynamics. In this work, we develop theoretical models and investigate the nonlinear spatio-temporal behaviour of two prominent types of microcavity lasers, the vertical-cavity surface-emitting laser (VCSEL) and the vertical extended cavity surface-emitting laser (VECSEL).

Within a VCSEL the light-field is clamped between the distributed Bragg reflectors (DBRs) such that the laser becomes longitudinal single-mode. However, with an aperture diameter of typically $5 - 15\,\mu$m, the VCSEL experiences transverse degrees of freedom. Moreover, the rotational symmetry of the cavity structure allows for two linear polarisation modes. Circular polarised light can be emitted if these polarisation modes (PM) are shifted against each other by a $\pm\pi/2$ phase difference. It is of particular interest to understand the complex interplay of the spectrum of transverse modes with the polarisation as mediated by the spin-polarised semiconductor material. While spatial-hole burning, the depletion of carriers in certain spatial regions, causes a nonlinear coupling of modes (mode-beating), it is the spin-polarisation of the medium which breaks the rotational symmetry of the active quantum-wells and thereby induces birefringence. Experiments show that cavity-birefringence and the induced nonlinear birefringence are two mechanisms which destroy the equality of polarised modes. Dependent on device and operating conditions a frequency split of the linear polarisation modes of typically $5 - 40$ GHz is observed. Systems with a small aperture diameter are transversely single-mode (TEM_{00}) and experience – depending on the carrier pump – a decay of one of the polarisation states. In broader structures, with an aperture diameter larger than $10\,\mu$m the weaker linear polarisation mode can dynamically coexist with the favoured polarisation mode by occupying a different set of transverse modes.

Based on a dynamical model and spatially resolved time-domain simulations, we analyse the intriguing mechanisms behind these mode-transitions. In the first chapters of this work we develop the framework of equations that describe the microcavity light-field dynamics, aspects of band-resolved carrier dynamics, and the temperature transfer between the hot carrier system and the lattice. The flexibility of the model and the efficiency of its numerical implementation allows us to extract various aspects of the dynamics and target them separately; quantum-well carrier dynamics (spectral hole-

burning, spin-polarisation), spatial effects (spatial hole-burning, self-focusing) temperature related effects (thermal lensing) and nonlinear properties are just few examples of internal processes which shape the experimentally observed output characteristics of the laser.

Inspired by both, the success and the concept of the VCSEL, new varieties of surface emitting microcavity lasers have recently been developed. One of them, the VECSEL, may be regarded as a optically pumped high-power version of the VCSEL. In spite of many similarities, like the quantum-wells positioned in the cavity-mode maxima, the micro-resonator, and the frequency selective DBR mirror, there are aspects which render the VECSEL to be a much different system: Due to the fact, that there is no top-DBR but an external mirror the VECSEL is no longer single-mode in the longitudinal direction (along the optical z-axis). As the external mirror can be some centimeters away from the chip the round-trip within the external resonator is much larger ($\sim 100\,\mathrm{ps}$) than that of the internal micro-resonator. The longitudinal mode-spacing is of order 0.1 THz which allows typically 100 longitudinal-modes to fit into the broad positive gain maximum. In radial direction, however, the curvature of the external mirror stabilises the mode on a broad TEM_{00} Gaussian-type mode. In difference to VCSELs, VECSELs are usually optically pumped and are promising candidates for high-power applications and ultra-fast pulse generation. Multiple quantum-well structures (MQW) and a pump spot of $\sim 100\,\mu\mathrm{m}$ allow output intensities of $> 100\,\mathrm{mW}$ while saturable absorbers integrated into the beam-path or the chip itself can be used for passive mode-locking. The nonlinear coupling between light-field and active-material is inherently strong and is influenced by longitudinal mode-competition, polarisation mode dynamics, carrier sub-band dynamics, and non-ambipolar carrier transport. Furthermore, the external resonator can be interpreted as a delayed feedback loop which imposes an additional characteristic timescale on the system. These new aspects in combination with a high degree of electronic and optical configurability, open new fields for theory, experiment, and application.

From a theoretical point of view it is important to note, that not all of the equations developed for the VCSEL apply to VECSEL structures. The multi-mode characteristics, in particular, demand a full-time domain description of the optical field. This, however, requires a full-time domain implementation of the active quantum-well material. Within this work we therefore derive and implement a spatio-temporal full-time domain model of the longitudinal cavity and the quantum-well material which includes non-ambipolar carrier transport as well as a frequency dependent gain response. Furthermore, we show how the band-structure can be taken into account which would extend the description from a simple two-level system to the more complex material response of active quantum-well structures. Based on the total-field scattered-field approach a novel kind of delayed feedback boundary conditions are developed and enable us to simulate long cavity structures with a minimalistic numerical effort. The model presented constitutes a new tool for the dynamical investigation of ultra-fast phenomena and processes in these structures. Further steps, in particular, in the direction of more realistic material models, have to be made in order to understand and explore the characteristics of these

novel structures.

Today's aim to build faster and more powerful semiconductor laser devices goes hand in hand with a miniaturisation of the semiconductor laser structures down to the nanometer-scale. Difficult even for simple bulk semiconductor devices, the even tighter coupling of the carrier and light-field sub-systems with respect to time- and length-scales disallow a separate dynamical treatment of the physical processes which take place within such novel microcavity semiconductor lasers. Due to their flexibility and their physical nature, time-domain simulations constitute an appropriate tool for targeting the entangled dynamics within the cavity, the structure and the active quantum-wells. We predict that along with the technological progress of microcavity semiconductor lasers and the availability of inexpensive computing power time-domain methods will gain more importance and constitute a valuable tool to analyse the optical and electronic properties of these devices.

Table of Symbols

Symbol	*Meaning*
$\langle \dots \rangle$	quantum-mechanical expectation value
$\langle \dots \rangle_z$	longitudinal mean-field average
$\lvert c\, i\, \mathbf{k} \rangle$	eigenket of Bloch-function
$\lvert j\, m_j \rangle$	angular momentum eigenstate
α	line-width enhancement factor
α	scaling parameter
β	spontaneous emission coupling efficiency
Γ_{aug}	Auger recombination rate
Γ_{rel}	relaxation damping
Γ_{sp}	carrier loss due to spontaneous emission
Γ_z	$= \langle \eta \rangle_z$, longitudinal confinement factor
γ	generic loss rate, line-width
γ_1, γ_2, γ_3	Luttinger parameters
γ_{amb}	temperature relaxation, lattice to ambient
γ_{aug}	carrier loss due to intraband Auger recombination
γ_{nr}	non-radiative recombination rate
γ_{p}	phenomenological polarisation dephasing rate
γ_k^{p}	microscopic polarisation dephasing rate
$\gamma_k^{\mathrm{e/h}}$	microscopic carrier-carrier scattering rate
γ_{res}	resonator loss rate
Δ_{so}	energy offset of split-off band
ϵ	dielectric constant
ϵ_0	dielectric vacuum constant
$\epsilon_{\mathbf{k}}^{\mathrm{e/h}}$	electron / hole energies
$\eta(z)$	longitudinal confinement function
η	internal pump efficiency
Θ_z	$= \langle \zeta \rangle_z$, longitudinal confinement factor for oxide aperture
κ	polarisation coupling constant
Λ	carrier pump rate
Λ_{thr}	threshold pump
$\mu^{\mathrm{e/h}}$	chemical potential
ξ	oscillator coupling constant

continued on next page ...

... continued from previous page

Symbol	*Meaning*
ξ	spin-orbit coupling constant
τ	characteristic time scale
$\tau^{\mathrm{e/h}}$	effective carrier scattering time
τ^{p}	effective polarisation scattering time
ϕ	phase
$\phi_{n,i}(z)$	z-confinement part of the wave-function
$\chi(\Omega, N)$	dielectric susceptibility
$\psi(\mathbf{r}, z, t)$	quantum-mechanical wave-function
$\delta\omega$	line-width
Ω	optical field centre frequency
Ω_{rel}	relaxation frequency
ω	transition frequency
$\Delta\omega$	$= \omega - \Omega$, frequency detuning
$\omega_{\mathbf{k}}$	band-resolved transition frequency
$\Delta\omega_{\mathbf{k}}$	$= \omega_{\mathbf{k}} - \Omega$, band-resolved frequency detuning
ω_{g}	band-gap frequency (at Γ-point)
$\mathcal{E}_\Omega$	electric field strength per photon
A	area covered by active zone
$\hat{a}, \hat{a}^\dagger$	photon annihilation and creation operators (vector potential)
$\hat{b}, \hat{b}^\dagger$	photon annihilation and creation operators (electric field)
B^0	Weisskopf-Wigner constant of spontaneous emission
B_Ω	spontaneous emission rate per mode
b_Ω	spontaneous emission factor per mode
c	speed of light
$\hat{c}$, $\hat{c}^\dagger$	electron annihilation and creation operators
$c_{\mathrm{q,V}}$	specific heat per volume and
D_f	ambipolar carrier diffusion constant
$D_f^{\mathrm{e/h}}$	electron/hole carrier diffusion constant
$D_{\mathbf{k}}$	density of states
D_p	$= 1/(2K_0)$, diffraction constant
$\hat{d}$, $\hat{d}^\dagger$	hole annihilation and creation operators
d	thickness of active (quantum-well) zone
$\mathbf{E}$	electric field vector
$\mathbf{E}^\pm$	left- / right-rotating parts of the electric field amplitude
$\mathcal{E}_{\mathrm{g}}$	band-gap at Γ-point
$\mathcal{E}_{\mathbf{k}}^{\mathrm{e/h}}$	renormalised electron / hole energies
E_x	electric field component
$F_N(t)$, $F_E(t)$, ...	stochastic forces
f	smallness parameter for paraxial expansion
$f_{\mathbf{k}}^{\mathrm{e/h}}$	electron/hole Fermi-function

continued on next page ...

... continued from previous page

Symbol	*Meaning*
$G(\Omega, N)$	$= -\mathrm{Im}\,[\,\chi\,]$, gain function
G	carrier generation rate
$G_{\mathrm{sat}}(\Omega, I)$	saturated gain
$g(\Omega, N)$	$= \partial G/\partial N\vert_{N_{\mathrm{thr}}}$, differential gain
g, g^*	quantum-optical mode coupling factor
$g(z)$	longitudinal mode function
g_Ω	mode coupling constant
$\hat{\mathcal{H}}$	system Hamiltonian
$\hat{\mathcal{H}}_{\mathrm{kin}}$	kinetic part of the Hamiltonian
$\hat{\mathcal{H}}_{\text{c-L}}$	carrier-light interaction part of the Hamiltonian
$\hat{\mathcal{H}}_{\mathrm{I}}$	particle interaction part of the Hamiltonian
$\hat{\mathcal{H}}_{\text{c-c}}$	carrier-carrier interaction part of the Hamiltonian
$\hat{\mathcal{H}}_{\text{c-LO}}$	carrier-phonon interaction part of the Hamiltonian
I	field intensity
I_{sat}	saturated intensity
I_{st}	stationary intensity
K_0	$= \Omega/c$, vacuum k-vector
K_{eff}	$= \Omega/n_{\mathrm{eff}}$, effective k-vector
$\mathbf{k} = (k_x, k_y)$	microscopic transverse k-vector
k_{op}	optical transition wave-vector
L	length parameters (e.g. length of structure)
ℓ	characteristic length
$\mathbf{M}$	$= \langle 1\vert\mathbf{r}\vert 2\rangle$, generic dipole- transition vector associated with an optical transition $1 \leftrightarrow 2$
$\mathbf{M}_{0,\mathbf{k}}$	k-resolved bulk dipole matrix element
$\mathbf{M}_{ij,\mathbf{k}}$	k-resolved quantum-well dipole matrix element for sub-band transition $i \leftrightarrow j$
$(1/m^*)$	effective electron mass tensor Γ-point
m_0	intrinsic electron mass
m_{e}	effective conduction band electron mass at Γ-point
m_{h}	effective valence band hole mass at Γ-point
m_{lh}	effective valence band heavy hole mass at Γ- point
m_{hh}	effective valence band light hole mass at Γ- point
m_{r}	effective reduced mass at Γ-point
N	total carrier density
N_0	dipole density
N_{thr}	threshold density
N_{tr}	transparency density
$\delta\mathbf{n}^{\mathrm{c}}$	refractive index tensor of crystal
n_{eff}	effective refractive index

continued on next page ...

. . . continued from previous page	
Symbol	*Meaning*
δn^{g}	transverse refractive index change of oxide layer
$n_{\mathbf{k}}^{\mathrm{e/h}}$	Wigner functions for the electron/hole densities
$u_{\mathbf{k}}^{\mathrm{e/h}}$	microscopic electron/hole energy densities
n_{QW}	number of quantum-wells embedded in structure
$\mathbf{P}$	dielectric polarisation vector
P_x	polarisation vector component
$\hat{\mathbf{p}} = (\hat{p}_x, \hat{p}_y)$	transverse momentum operator
$p_{\mathbf{k}}$	microscopic intraband-polarisation
$\hat{p}_z$	z-momentum operator
Q	mode related Q-factor
$\mathbf{r} = (x, y)$	transverse space coordinate
R_{abs}	absorption rate
R_{em}	emission rate
S_0, S_1, S_2, S_3	Stokes parameters
T_{l}	lattice temperature
T_0	ambient temperature
$T_{\mathrm{p}}^{\mathrm{e/h}}$	electron/hole plasma temperature
$\Delta U_{\text{c-ph}}^{\mathrm{e/h}}$	total energy transfer plasma to lattice due to carrier-phonon scattering
$U_{\mathrm{eq}}^{\mathrm{e/h}}$	total plasma equilibrium energy
$\mathcal{U}_{\mathbf{k}}^{\pm}$	renormalised electric field amplitude
$u_{n,i,\mathbf{k}}(\mathbf{r})$	lattice periodic Bloch-function
$\hat{\mathcal{V}}(\mathbf{r})$	lattice potential
V_{t}	thermal volume
$\hat{\mathcal{V}}_z(z)$	well potential
v_{eff}	$= c/n_{\mathrm{eff}}$, effective phase velocity
$W_{i_1 i_2 i_3 i_4}$	matrix elements of the Coulomb-potential
w	characteristic width

Contents

1 Overview

Modern semiconductor diode lasers are complex nanostructured devices which are integrated into components for science, telecommunication, optical storage, and medical application [1]. They are a mass product omnipresent in many person's daily life[1]. They come in a variety of different designs to meet the demands concerning speed, wavelength and output power.

Since 1962, when for the first time continuous wave (cw) operation of a simple homojunction semiconductor laser diode at nitrogenic temperatures has been demonstrated [2], the development of semiconductor diode lasers was steadily driven by a increasing growing and etching precision which made it possible to design, build, and control more sophisticated structures and optical cavities on a nanometer scale. Today, a combination of optical microcavity design, new semiconductor material systems[2], and an enhanced control over electronic properties by integration of quantum-well or quantum-dot structures, makes it possible to cover wavelengths from the blue (< 400 nm, based on Gallium-Nitride) [5], to the mid- and far-infrared (quantum cascade lasers) [6]. Cheap production costs, high emission powers of more than one Watt, long life-times, and a high power conversion efficiency of 30%-50% [7] make diode lasers more attractive than traditional gas-, solid-state or dye-lasers for a growing number of applications.

Keeping pace with the technological evolution the theory of laser dynamics is continuously extended and revised: even simple semiconductor lasers are complex systems in the sense that the numerous internal subsystems, the optical field, the lattice, and carriers are closely coupled in a complex nonlinear fashion [8–10]. Aspects of the quantum-mechanical interaction of light, microcavity and semiconductor material have to be taken into consideration in order to explain and understand the behaviour of new sophisticated types of semiconductor laser devices: normal-mode coupling in microcavities [11], quantum noise and squeezed light states [12, 13], the carrier capture and confinement in quantum-wells or quantum-dots [14,15] or spin-polarisation effects [16]. These few exam-

[1] The sale numbers of laser diodes for the years 2001 and 2002 (see FIGURE 1.1) categorised according to field of application might give a good impression of the importance of laser diodes in our modern, technologically oriented world.

[2] many of the II-VI and III-V semiconductor alloys that feature a direct but small band-gap may be used for optical active semiconductors. Limitations arise if one tries to grow layers of different material on each other as this requires the lattice constants to sufficiently match. These materials can be considered designed or synthetic materials as these alloys cannot be found in nature. They are classified into binary (GaAs), ternary ($Ga_xIn_{1-x}As$) or even quaternary alloys ($Ga_xIn_{1-x}As_ySb_{1-y}$) [3, 4]. In addition there is a broad range of materials available used to dope the semiconductor crystal.

ples create the allusion of semiconductor lasers being miniature quantum opto-electronic laboratories.

Our work covers some fundamental aspects of the theory and the simulation of the nonlinear dynamics of a particular interesting type of a microcavity semiconductor laser, the vertical cavity surface-emitting semiconductor laser. Based on first principles, comprehensive physical models are developed which enable us to analyse and understand the complex interplay between the different subsystems and their impact on characteristic laser properties. Superior to simple rate equation models, phase sensitive equations describing the dynamics of the optical field are derived. We take into account multi-mode behaviour, and implement a dynamic material model reflecting the characteristics of the semiconductor band-structure as realistic as possible. The efficient numerical implementations of these models – in combination with a number of diagnostic methods – allow us to carry out extensive numerical studies and to compare them with and understand the nature of the dynamical effects observed in experiment.

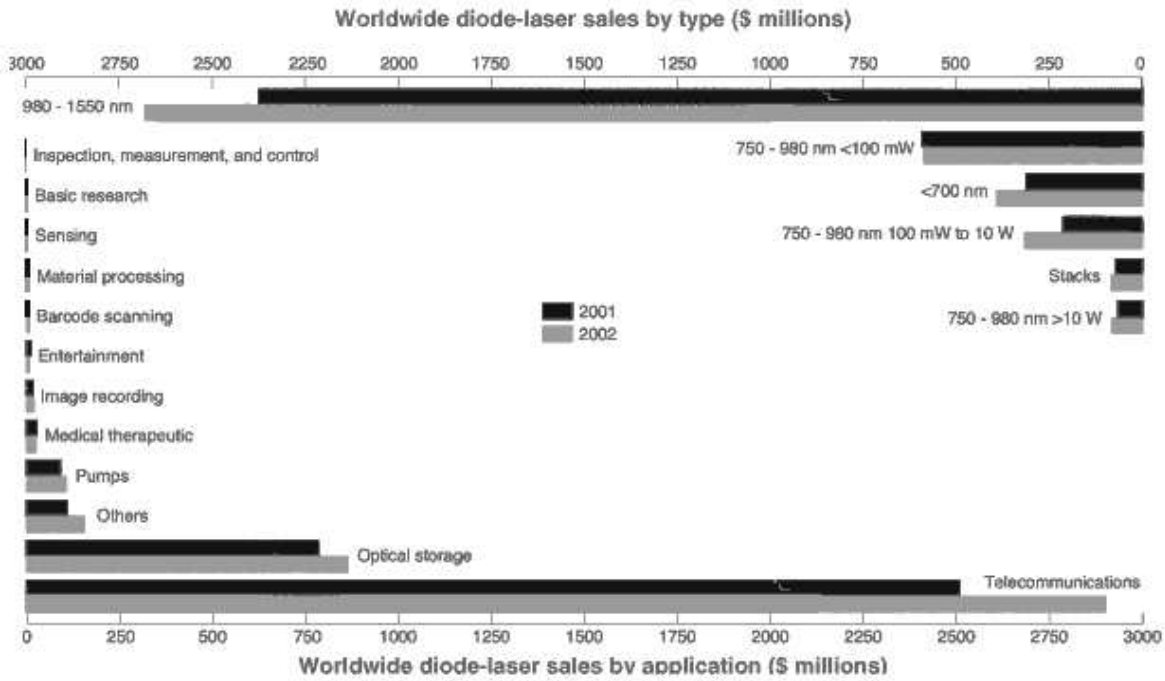

Figure 1.1: Sales of semiconductor laser diodes for the years 2001 and 2002 in millions US Dollars. While data-com and optical storage applications take by far the biggest part, there are growing markets for diode lasers in the area of medicine and entertainment industry. Although high power applications, e.g. material processing, are still dominated by solid state and gas lasers, semiconductor lasers are already commonly used as efficient optical pump sources for other high power laser devices.

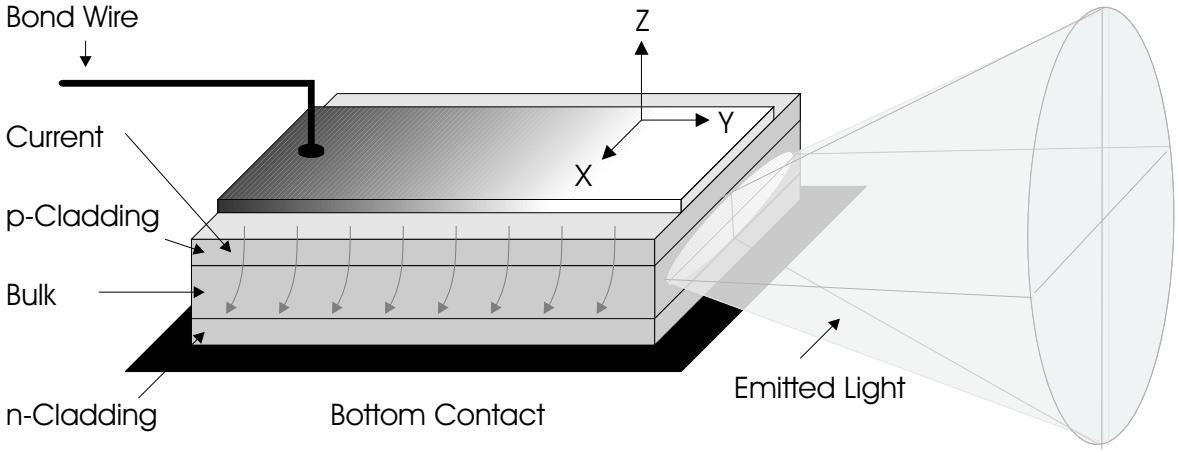

Figure 1.2: Broad area edge emitting diode laser. The structure shown is a gain guided heterostructure. In case of the Al-GaAs material system, the active zone consists of a p-doped GaAs layer which is embedded between cladding layers of p-doped Al-GaAs and n-doped Al-GaAs. Edge emitters feature a high power output due to a high round-trip gain but the light emitted from the facet is highly divergent and astigmatic. Nowadays, the conventional heterostructure bulk design is replaced by more sophisticated designs. Index structuring improves the optical confinement and beam quality and the output power can be increased by active multi quantum-well (MQW) layers.

In order to understand some of the key concepts we take a look at the traditional edge-emitting design as depicted in FIGURE 1.2. An edge-emitter is a slab of a direct semiconductor (e.g. Gallium Arsenide) with typical extensions of 200 μm in longitudinal and 20 μm in transverse direction. The material is doped to form a p-n diode in the lateral z-direction. Carriers are injected in forward-bias, implying a current flow from the top-metallisation layer to the substrate at the bottom of the diode laser. The active laser zone, where the coherent amplification of light takes place is located in between the junction. Early generations of edge-emitting diode-lasers, the *homo-junction* diodes, could not be operated in *continuous wave* (cw) at room temperatures. The *double hetero-junction* design is providing a much better carrier guiding and confinement and thus led to a significantly lower threshold in particular in combination with a transverse index profile; the *buried double hetero-structure* features both, a lateral and transverse index structure and improves the confinement of the optical field to the active region. Such diode lasers, bearing a transverse index structure, are classified *index guided*, while lasers without index guiding are merely *gain guided*. FIGURE 1.3 is showing the energetic diagram of a double hetero-junction laser along the lateral axis and visualises how the carriers of the conduction and the valence band – driven by the electric field potential – are drifting toward the active Gallium Arsenide zone where the processes of stimulated emission and absorption take place.

The advances in epitaxial technology – molecular beam epitaxy (MBE) and metal-

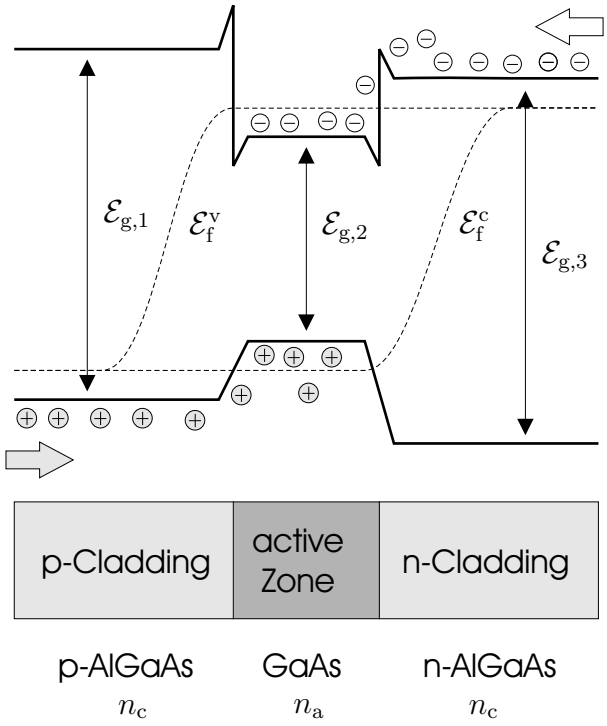

Figure 1.3: Valence and conduction band diagram of a heterostructure diode laser slab. The electrons and holes which are injected into the n- and p-doped cladding layers are driven by the external and the internal electrostatic fields and move towards the active layer, where radiative recombination and coherent light-amplification can take place. The Fermi-levels accord the carrier fill states of the bands under equilibrium conditions.

organic vapour deposition (MO-CVD) – made it possible to grow and etch structures composed of layers of a few nanometers in thickness. For low-power applications, the concept of the vertical-cavity surface-emitting semiconductor laser (VCSEL, see FIGURE 1.4) became an attractive substitute for edge-emitters. A vertical-cavity surface-emitting laser consists of two highly reflecting Bragg mirrors which encompass a $n \cdot \lambda$ or $(n + 1/2) \cdot \lambda$ *defect zone*[3]. This microcavity is characterised by a concentration of the electrical field intensity to the defect region which is typically some micrometer in length. In order to retrieve a strong light-matter coupling the active material layers are positioned to match the maxima of the defect-mode (or cavity-mode). The original design is based on research carried out at the Tokyo Institute of Technology [17, 18] but suffered from a number of problems, e.g. how to handle current injection along the optical axis, how to reduce carrier leakage, and how to increase the continous wave (cw) operating temperature. Nevertheless, the VCSEL design was an extremely promising candidate for industry: fully parallelisable, arrays of hundreds or thousands of VCSELs can be grown

[3] A stack of Bragg-layers can be considered a finite one-dimensional photonic crystal. In that sense the insertion of an additional layer in between the Bragg layers can be interpreted as the introduction of a defect into the otherwise perfect crystal.

on a single chip, ready to use after etching and metallisation. It took a couple of technological advances to tackle the problems: the improvement of quantum-well structures by the introduction of strained layers, the replacement of proton-implanted carrier guiding with oxide-apertures, and improved doping-profiles of the Bragg mirrors to reduce the series resistances are just some examples. At the end of the 90s the VCSELs were mature devices and available for application in telecommunications as packaged components.

While first generations of proton-implanted VCSELs were based on (GaIn)(AsP)/InP with a wavelength range limited around 850 nm [18], it has been the the exponentially growing telecommunication market in the late 90s which was focusing attention on other material systems in order to gain access to the near-infrared wavelengths windows at 1550 nm and 1310 nm[4] [19–22]. Apart from the designs there are various material systems available. New semiconductor compound materials such as (GaIn)(NAs)/GaAs [20, 21, 23], ZnSe (demonstrated 1991), or the blue GaN (first diode lasers around 1995) are now covering big parts of the visible and infrared spectrum (FIGURE 1.5). While the efforts continue to explore more exotic material systems and build laser devices which fill the gaps between the blue end of the spectrum down to the FIR (up to 26 μm), many of the parameters associated with these materials are not well known. For the theoretical work presented here, we concentrate on the Al-GaAs/GaAs material system. Although, not the most interesting diode laser material system it is still considered the most common, and – even more important for us – the best known in terms of its material properties. Within this work we focus on the analysis of dynamical processes and their interplay rather than on the differences between specific materials.

The ongoing effort to build high-power versions of vertical emitters (VCSELs have an emission power in the range of some milli-Watt) and, at the same time, to overcome the disadvantages of traditional broad-area lasers (such as filamentation or the highly astigmatic beam profile) inspired a new type of a vertical surface-emitting semiconductor diode laser, namely the vertical extended cavity surface-emitting laser (VECSEL). Its design features aspects of a solid-state laser type known as the *optically pumped solid-state disk-laser*. The basic idea is, to mount a thin disk of active-material onto a metallic bottom mirror which is attached to a heat-sink. An external mirror is used to create a stable resonator-cavity. One of the biggest advantages of this configuration is that it is possible to optically pump the disk using a rather large pump-spot of several hundred micrometer in diameter and to efficiently remove the produced heat from the thin disk at the same time. In difference to a solid-state disk laser, the chip of a VECSEL integrates a DBR which serves as bottom mirror. This mirror is frequency selective and thus guarantees the electric-field maxima to match the positions of the quantum-well layers. For some devices an anti-reflective (AR-) coating is affixed to the top of the chip in order to avoid a double-resonator situation. The external mirror is arranged in some centimeters distance and supports a stable transverse Gaussian mode operation.

[4] these are the wavelengths of minimal attenuation (1550 nm) and minimal deispersion (1310 nm) in premium optical silica fibres.

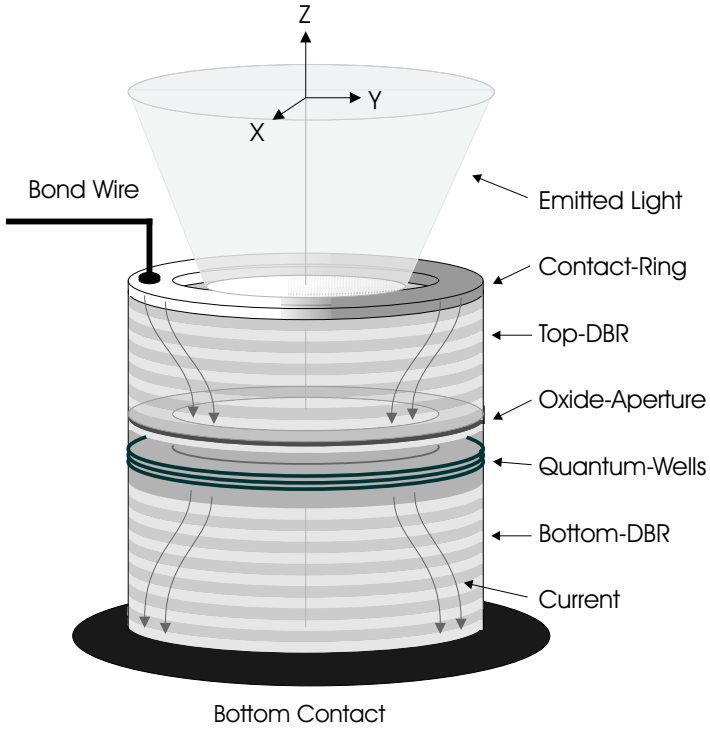

Figure 1.4: Schematic picture of a VCSEL. Between the top- and bottom-DBR there is a defect of length λ enclosed. This defect contains one or more active quantum-well layers. Typically Al-GaAs-VCSELs feature several (10 to 30) Al-GaAs/GaAs mirror pairs with $n_1 \approx 3.5$ and $n_2 \approx 3.1$. The oxide-aperture serves both, to confine the carriers injected by the ring-contact to the centre of the structure and to confine the optical field via a radial refractive index change (index guiding).

Between the AR-coating and the bottom-DBR multiple quantum-well layers which are embedded into the structure capture the electrons and holes generated within the barrier states. Once trapped in the quantum-wells the electrons relaxate to the lowest sub-band levels where they take part in the process of coherent light amplification. In difference to solid-state disk-lasers the possibilities of nanostructuring a semiconductor chip are manifold and include modifications of the dielectric structure, and the electronic levels of the quantum-wells and the barriers (e.g. *GRINSCH*-structures) [24]. However, as the chip has to be mounted with its DBR on the heat-sink, the cooling of the chip is one of the most critical design issues to be improved: with increasing mode-selectivity and reflectivity, that is with each additional Bragg-layer at the end of the structure, the heat transport becomes worse.

Along with the development and improvements of microcavity semiconductor laser devices the theory has been successively adapted and improved to explain new aspects and details originating from cavity and material properties. Several levels of description exist: active material calculations, transport phenomena, line-width calculations [25],

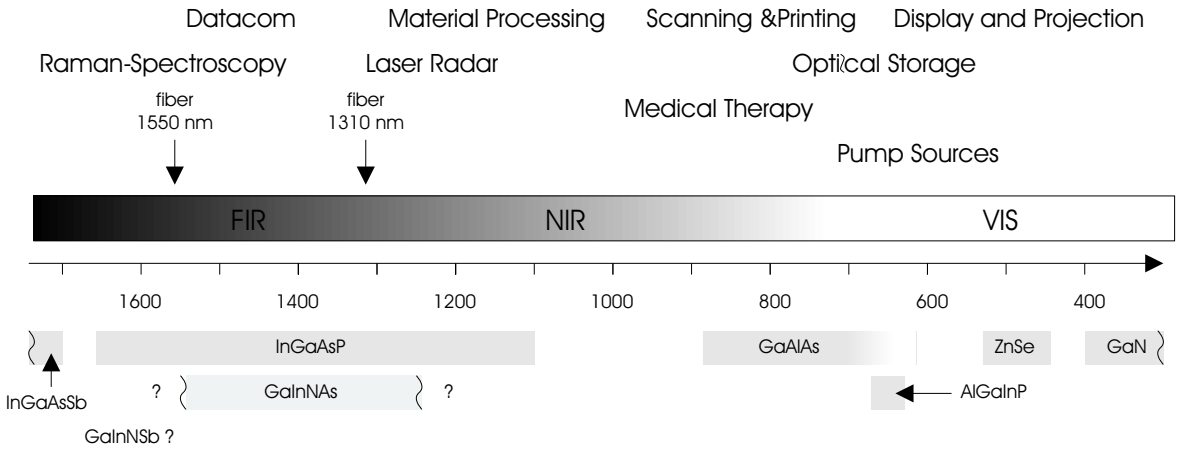

Figure 1.5: Coverage of the optical spectrum by semiconductor diodes and their application. The Al-GaAs material is by far the best known material system. It can be used to build diode lasers with wavelengths ranging from 620 nm to 895 nm. Below 720 nm however, the lifetime of Al-GaAs based diode lasers is very short. Note, that beyond 1600 nm materials such as InGaAsSb ($1.7 - 4.4\,\mu$m) or cryogenic PbSSe, PbSnTe, PbSnSe down to to $26\,\mu$m cover the FIR. Another very promising new material system, covering the fibre-communication wavelengths, are the dilute nitrides InGaAsN.

energy balance equations, calculation of the (cold) optical cavity-modes [26–29], heat transport, and nonlinear dynamics [30] are just a handful of examples which illustrate the variety of aspects involved. In this work, we aim to analyse and understand the dynamical interplay of the dielectric microcavity and the electronic quantum-well properties in combination with thermal properties. The challenge is to derive a model, which incorporates the nonlinear interaction between the various physical subsystems, namely the light-field, the carriers, and the phonons on a theoretical basis. In difference to other types osf lasers, semiconductor lasers bear some unique features that have to be taken into account: 1) Phase-sensitive effects are dominant due to a strong amplitude-phase coupling (high alpha-factor). Simple rate models fail. 2) The density of the active carriers is far higher than in gas lasers. 3) Carriers are not bound to the active atoms, but are dislocated over the crystal lattice. 4) Many-body interactions between carriers are dominant. 5) The optical transition occurs between bands rather than between discrete levels. The gain-spectrum is very broad compared to other types of lasers and depends on temperature and the carrier fill-level. In addition, the band-structure of the semiconductor material changes if low-dimensional systems like quantum-wells are used or if the material is under stress. 6) A variety of time-scales and rates ranging from fs-scale (~ 100 fs for carrier-carrier scattering) to ns-scale (dark Shockley-Read-Hall recombination) are involved.

Clearly, there are limitations in trying to setup and run a realistic computer model on base of an actual device. Although the dynamical semiconductor laser models presented

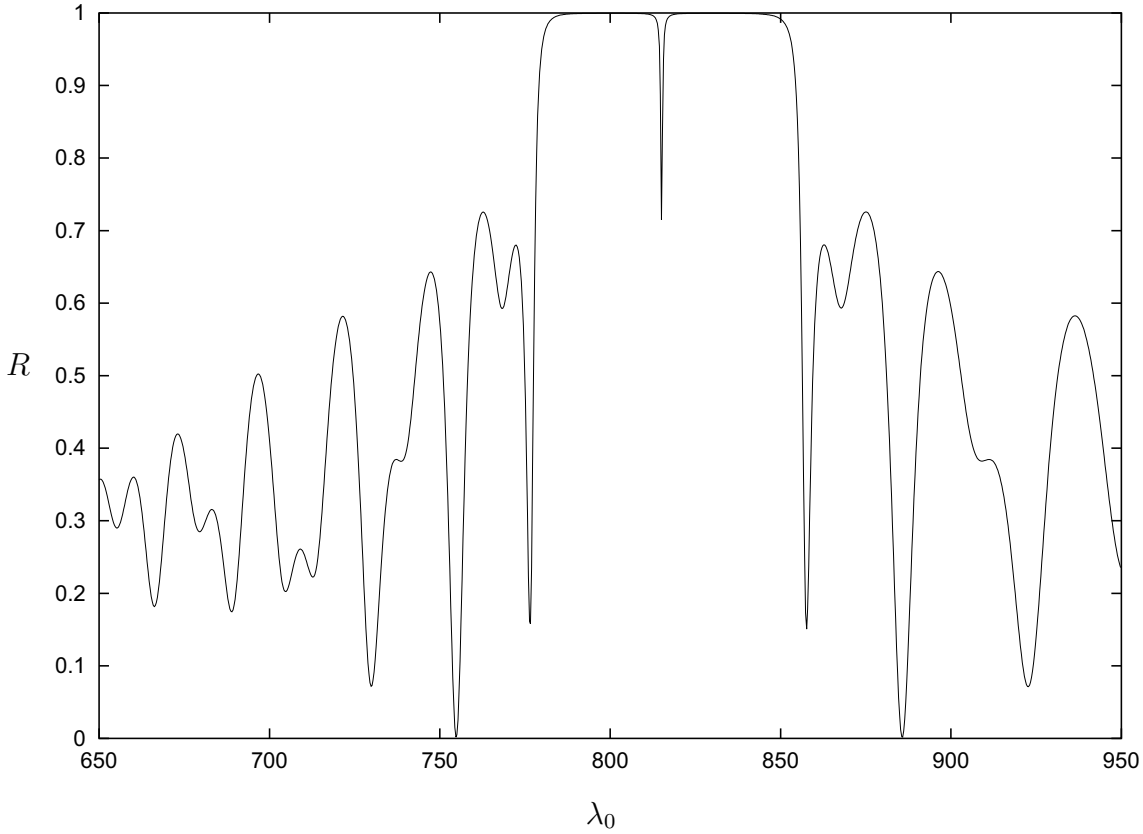

Figure 1.6: Reflective spectra of a VCSEL structure with 25 Bragg-Layers at the top and 20 at the bottom. In the middle of the stop-band at 815 nm vacuum wavelength there's the cavity-dip where reflectance drops to 0.715. As the stop-band does not allow any other propagating modes the VCSEL can be considered a single-mode microcavity. This is why a VCSEL is considered the most simple microcavity laser that can be realised. The spectra was calculated with $n_1 = 3.590$ and $n_2 = 3.2$. The irregular side-bands are a result of the broken symmetry as the bottom mirror has less periods and is sitting on n_1 substrate.

in this work are offering a complex description they still had to be tailored to essential parts: higher order correlations between photon and elctron states are not explictly contained and the influcence of the crystal lattice e.g. is implemented on phenomenological level only, which means that we do not include a quantum-mechanical treatmeant of the phonons. The current generation of supercomputers which we use to run our simulations are far more powerful than 10 years ago. Apart from this it is not practicable, to perform realistic three-dimensional simulations of a diode-laser which are covering a nanosecond time window. Thus, approximations remain a key issue. A well-adapted approximation may rely on an effective describtion or treat processes which act on different time scales separatly. In some situations it is focuse on time-domain simulations of the light-field and the carrier dynamics within the active material zone. The aim is to explain short-time (picosecond) phenomena in combination with the spatial near-field

patterns. Two classes of models have been developed, a *transverse model*, dedicated to the analysis of transverse multi-mode dynamics, and a *longitudinal model*. For the transverse model we develop a formalism, which allows us to decouple the parts of the optical field variables which are dependent on longitudinal coordinates from those dependent on the transverse coordinates. This is done in an approximative way in CHAPTER 3. This implicit single-mode approach assumes that the laser features only one, longitudinal confined mode. Although the longitudinal mode itself features a stationary profile, it must be calculated in order to quantify the effective parameters for the transverse field equations. We demonstrate that this can be done within the framework of the *paraxial approximation*. However, it has to be extended in some essential part before it can be applied to VCSEL cavities. The second model which covers longitudinal dynamics does not incorporate transvere dynamics. It can be applied to various types of longitudinal multi-mode systems which are transversly single-mode lasers. This is of special interest for systems where we want to study pulse generation, or pulse propagation. In this work, we apply it to vertical external cavity surface-emitting lasers which are featuring multiple longitudinal modes but are stabilised to a transverse mode of Gaussian shape.

The light-field dynamic is one main ingredient of our VCSEL model, the other is the calculation of the dynamical response of the active semiconductor material. In accordance with real devices, we assume that the active zone of a VCSEL consists of a couple of GaAs quantum-wells positioned into the mode maxima of the confined longitudinal field mode. The material gain of a quantum-well semiconductor laser is not merely homogeneously broadened. Dependent on the internal field intensities spectral hole burning is more or less distinct. We derive and integrate spectral equations, the *4-band semiconductor-Bloch equations*, which describe the k-resolved intraband dynamics of the carriers trapped in the lowest quantum-wells states. This microscopic theory is presented in CHAPTER 4. It features an angular momentum dependent coupling of the light-field to the two-dimensional electron gases of the the lowest valence and conduction sub-band. In CHAPTER 5 the light-field and the active quantum-well part are combined to a transverse resolved dynamical VCSEL model. Extensive numerical simulations are carried out and aim to analyse the carrier light-field interaction and to develop a deeper understanding of the origin of their nonlinear dynamical interplay. Spatial and polarisation resolved time-series of relevant variables and fields are recorded and compared with experimental data. From these time-series we can extract spectral information, like the shape, the polarisation and the intensity of transverse modes, which successively level above threshold with an increasing pump strength. Furthermore, the impact of temperature, known to be of critical influence, is integrated into the model equations and numerically investigated. The developed model and the numerical simulations demonstrate, that it is possible to reproduce the experimental observations on a substantial level. The framework we develop constitutes a valuable tool for analysing the impact of structural details and changes, and serves as a fundament for further theoretical investigations.

As previously mentioned, the transverse model discussed in CHAPTER 5 can be used for

the analysis of the longitudinal single-mode VCSELs but is not suitable for studying the dynamics of VECSELs. Here, the situation is different in many respects: while VCSEL structures bear an aperture diameter of typically $6-20\,\mu$m, the pump spot of a VECSEL has a diameter of some $100\,\mu$m. The external mirror is designed to stabilise a transverse Gaussian mode. For this reason, one can generally assume that in quasi-equilibrium all internal fields show a static dependence on transverse coordinates (e.g. rotational symmetry). The longitudinal model we apply does treat the transverse direction in an effective way by incorporating additional loss terms for the carriers and the light-field consistent with transverse transport and diffraction processes. As a VECSEL cavity can be regarded as a combination of an conventional cavity and a dielectric Bragg structure the mode spacing is much smaller than for a VCSEL. Several longitudinal optical modes are supported. In this sense, the situation is diametrical to that of a broader VCSEL structure, where transverse mode dynamics is important, but the longitudinal direction can be eliminated. The model discussed in CHAPTER 6 involves carrier and heat transport and resolves the fields in the longitudinal direction. Heat transport and the drift and diffusion processes of carriers within the internal electrical field potential occur perpendicular to the quantum-wells. The VECSEL model presented in CHAPTER 6 utilises a number of interacting solvers which are acting on different time-scales. It incorporates the motion and capturing of carriers as well as temperature issues and, of course, the interplay of field modes inside the cavity structure. We also present a new kind of boundary conditions which are a crucial part of the optical subsystem, the delayed-feedback boundary-conditions (DFBC). The DFBC are a FDTD implementation and reflect the external mirror structure. VECSELs are relatively young devices, and the problems are manifold as they often touch the interplay between the thermal, the carrier related, and the optical subsystem. CHAPTER 6 presents first numerical results of time-domain longitudinal simulations, emphasising the importance of a coprehensive multi-scale model. It can be applied to specific problems and applications which require a longitudinal mode analysis, that is pulse-generation (by including saturable absorbers), and possible modifications of the dielectric chip design. Together with the technological progress and new experimental studies, it will become necessary to extend the presented model and to carry out more extensive numerical simulations.

2 Basic Concepts of Microcavity Laser Dynamics

2.1 Introduction

Microcavity lasers are known for their inherently strong coupling between the cavity-mode and the induced dipoles of the active laser-material [11, 31–33]. Therefore, we propose a full time-domain description of a laser which, due to its nature, is able to fully conceive the phase-sensitive interplay of several longitudinal optical modes coupled with the active material. In close analogy to the quantum-mechanical optical Bloch-equations we derive a time-domain model describing the material response in combination with all possible optical frequencies and modes supported by the microcavity. This mesoscopic model, subsequently referred to as the *full time-domain Maxwell-Bloch equations* (FTD-MBE), constitutes an extension of the commonly used *Maxwell-Bloch equations* [34, 35] to full time-domain. Because of the accurate description of longitudinal multi-mode dynamics it is most suitable to explain ultra-fast phenomena and pulse-propagation experiments.

In this chapter the fundamental dynamical equations and properties of a microcavity laser system will be derived. Hence, we do not focus on structural or material specific details but rather on the light-matter interaction and the various levels of approximation that can be applied to the FTD-MBE equations. Although not adapted to a specific active material, it gives the important terms and quantities needed for a characterisation of microcavity laser systems and serves as a fundamental model for the longitudinal simulations carried out in Chapter 6.

The simplest gain media one can choose is a Lorentzian two-level model whose representation in time-domain is a damped harmonic oscillator equation. One of the strengths of this model is an extremely efficient numerical implementation. The numerical algorithm for solving Maxwell's equation in combination with a discretised differential equation for the material polarisation is known as *auxiliary differential equation finite-difference time-domain* method (ADE-FDTD)[1] [36–39].

[1] in full time-domain there are two principal methods incorporating a non-instantaneous material response into the FDTD algorithm [36]. The ADE-FDTD method combines the FDTD method for Maxwell's equations with a set of discretised differential equations which describe the active material response in time-domain. Although this method is known to be very efficient the problem is to find a suitable set of auxiliary differential equations driven by the electric field which give the right mate-

A more strict derivation of the FTD-MBE based on quantum-mechanical first principles has been addressed in [40]. A numerical efficient implementation matching the theoretical result and demonstrating lasing can be found in [41]. The most prominent features of this model are the numerical robustness and the possibility to implement highly efficient solvers – see APPENDIX C.

The dynamical variables of our system are the electric field, the polarisation of the active media, and the carrier density. For now we restrict the description to one spatial dimension which is aligned along the direction of propagation (z-axis) and neglect all transverse dynamics. The resulting model gives an introduction on the fundamental laser quantities and the spectral dynamics of a laser. It also constitutes the basis for the theory and numerical analysis presented later-on in CHAPTER 6.

In an additional section we discuss the extension of the full time-domain Maxwell-Bloch model to Langevin equations which are based on quantum-statistical considerations. The resulting *full time-domain Laser-Langevin equations* contain the impact of spontaneous emission and system-bath fluctuations.

In the last section of this chapter a method is presented, which makes it possible to adapt the FTD-MB equations to any given material gain by superposing a small set of Lorentzians. This method is applicable to efficiently implement the complex gain function of a semiconductor laser material in combination with our time-domain model in the limits of a reasonable numerical effort.

2.2 The Full Time-Domain Maxwell-Bloch Equations

Our starting point are Maxwell's equation for the $\mathbf{H}$ and $\mathbf{E}$ fields. Using *SI units* and dropping the *macroscopic* carrier density ρ,

$$\begin{aligned} \nabla \times \mathbf{H} &= \epsilon_0 \epsilon \partial_t \mathbf{E} + \partial_t \mathbf{P} + \mathbf{J} \,, \\ \nabla \times \mathbf{E} &= -\mu_0 \partial_t \mathbf{H} \,, \end{aligned} \tag{2.1}$$

where as the vector-fields are defined as usual, e.g.

$$\mathbf{H} = H_x \mathbf{e}_x + H_y \mathbf{e}_y + H_z \mathbf{e}_z \,. \tag{2.2}$$

rial response in frequency domain. Two prominent examples where this is possible are the Lorentz- and Debye-media. There exists another method known as the *piecewise-linear recursive convolution method* (PLRC-FDTD) which is of more systematic nature and evaluates the convolution integral of the functional response $P[E]$. Inserting the Fourier transform of the susceptibility $\chi(\omega)$ a so-called *recursive accumulator* Ψ^n is derived. The recursive accumulator is closely related to P and has to be updated at each time-step by adding most recent contributions. The computational effort for the PLRC-method for Debye- or Lorentz-media is higher than the one for a corresponding ADE-FDTD algorithm. Another drawback is that, depending on the material model, Ψ^n and E might become complex (as it happens for the Lorentz-media) and the computational effort doubles.

Neglecting all transverse dynamics, and setting $\mathbf{J} = 0$ one can assume that the optical field is approximately described by a plane wave travelling in z-direction. In that case, the one-dimensional Maxwell Equations provide an accurate description. They read,

$$\begin{aligned} &\partial_t \mathbf{H}^* = \epsilon_0\, c\, \partial_z \mathbf{E}\,, \\ &\epsilon_0\, \epsilon \cdot \partial_t \mathbf{E} = c\, \partial_z \mathbf{H}^* - \partial_t \mathbf{P} + \mathbf{J} \end{aligned} \tag{2.3}$$

using two-dimensional component notation,

$$\mathbf{H}^* = (-H_y, H_x)\,, \quad \mathbf{E} = (E_x, E_y), \quad \mathbf{P} = (P_x, P_y), \quad \mathbf{J} = (J_x, J_y)\,. \tag{2.4}$$

Note, that we have inserted

$$\mathbf{D} = \epsilon_0\, \epsilon \cdot \mathbf{E} + \mathbf{P} \tag{2.5}$$

for $\mathbf{D}$. This reflects the fact that $\mathbf{P}$ is considered being the dynamic part of the polarisation only. $\partial_t \mathbf{P}$ and $\mathbf{J}$ are the microscopic and macroscopic current densities respectively, ϵ denotes the static dielectric tensor emerging from an interaction with electrons of the inner atomic shells.

For a full-time domain description we have to choose an appropriate response function for the laser-material polarisation $\mathbf{P}$. In contrast to the correspondent complexified equations that would result from a rotating wave approach it is impossible to use an instantaneous response-function as it fails to describe the phase shifted response which would be necessary to effectuate material gain. A practicable solution is to implement $\mathbf{P}$ as a nonlinear functional of the electric field is to find a corresponding differential equation which offers the right response in frequency domain [38, 39]. In general, this is not a trivial task. However, it is well known (e.g. [8, 42–45]) that the coherent response of a quantum-mechanical two-level to an dipole excitation maps to that of a driven, damped harmonic oscillator,

$$\partial_t^2 \mathbf{P} + 2\gamma\, \partial_t \mathbf{P} + \omega_0^2 \mathbf{P} = -\xi \cdot \mathbf{E}(N_2 - N_1) = -2\, \xi \cdot \mathbf{E}\,(N - N_{\mathrm{tr}})\,. \tag{2.6}$$

N_1, N_2 are the carrier densities associated with the lower and upper level and N_{tr} is the so-called *transparency density*. For an excitation frequency $\omega = (\omega_0^2 - \gamma^2)^{1/2}$ the electric field $\mathbf{E}$ and the polarisation $\mathbf{P}$ are in resonance.

While the oscillator strength $\xi = (m_0/e^2)\, \xi$ equals $\mathbf{1}$ within the classical picture, one can deduce from quantum-mechanical perturbation theory

$$\xi = \frac{2\omega}{\hbar} \mathbf{M}\mathbf{M}^T \tag{2.7}$$

for a selected optical transition frequency ω and the corresponding dipole matrix-element vector $\mathbf{M}$. In this context the harmonic oscillator maps to a two-level system with $N = N_2$ carriers in the upper level and $N_1 = 2N_{\mathrm{tr}} - N$ carriers occupying the lower level.

For the upper levels carrier density N we use the dynamical equation

$$\partial_t N = -\gamma_{\rm nr} N + \Lambda + \frac{1}{\hbar\omega}(\partial_t \mathbf{P}) \cdot \mathbf{E} \,. \tag{2.8}$$

Besides the coherent carrier generation term which is proportional to $(\partial_t \mathbf{P}) \cdot \mathbf{E}$ and emerges from Pointing's theorem we supplemented the energy balance with a non-radiative recombination term proportional to $\gamma_{\rm nr}$ and a carrier injection term Λ. The set of equations (2.3), (2.6), and (2.8) are the one-dimensional FTD-MBE equations. It will be shown in the subsequent calculation that they are equivalent to the Maxwell-Bloch equations of a two-level laser-transition coupled to an optical field.

2.3 Spectral Dynamics and the Maxwell-Bloch Equations

It can be shown that the above equations map to the well known Maxwell-Bloch equations, which are known to describe a two-level system coupled to a light-field on a quantum-mechanical level. We will briefly sketch the approximations that have to be carried out but refer to [41] for a more rigorous derivation.

First of all, we neglect the effect of the pumping current on the electro-magnetic field and set $J = 0$. From (2.3) the electromagnetic wave equation can be deduced

$$\frac{\epsilon}{c^2}\partial_t^2 \mathbf{E} = \partial_z^2 \mathbf{E} - \frac{1}{\epsilon_0\, c^2}\partial_t^2 \mathbf{P} \,. \tag{2.9}$$

In the case of an isotropic dielectric tensor we separate the phase and the amplitude of a plane wave by applying the ansatz

$$\mathbf{E} = \hat{\mathbf{E}} \exp(-i\Omega t - ikz) + c.c. \,, \quad \text{with} \quad k = \sqrt{\epsilon}\,\Omega/c \,. \tag{2.10}$$

This renders the wave equation complex. At this level we implicitly restricted our description to a single longitudinal mode and dropped all effects related to *spatial hole-burning* as typical for multi-mode devices. Note, that this assumption is in general well justified for VCSEL devices but might be bad for other cavity geometries like edge-emitters. Applying the *slowly varying amplitude approximation* (SVAA), we end up with the following simplified equation of motion,

$$\frac{\sqrt{\epsilon}}{c}\partial_t \hat{\mathbf{E}} - \partial_z \hat{\mathbf{E}} = i\frac{\Omega}{2\sqrt{\epsilon}\,\epsilon_0\, c}\hat{\mathbf{P}} \,, \tag{2.11}$$

for the complex field amplitude $\hat{E}$. A more detailed calculation, deducing a complex, first order equation of motion for E from the wave-equation for the longitudinal dielectric structure of a VCSEL resonator is presented in Chapter 3. The remaining z-dependency can be eliminated by averaging over a resonator round-trip. Both, the

losses per round-trip, $\gamma_{\rm res}$, and the spatial overlap between field mode and active media, Γ_z, are effective parameters obtained from this *mean-field* averaging procedure. The partial differential equation (2.11) is then reduced to a rate-equation of the kind

$$\frac{\sqrt{\epsilon}}{c}\partial_t\hat{\mathbf{E}} = -\gamma_{\rm res}\hat{\mathbf{E}} + i\kappa\hat{\mathbf{P}}\,, \quad \kappa = \Gamma_z\frac{\Omega}{2\sqrt{\epsilon}\,\epsilon_0\,c}\,. \tag{2.12}$$

$\gamma_{\rm res}$ is connected to the mode's Q-factor by the relation $\Omega/(2Q) = \gamma_{\rm res}\,c/\sqrt{\epsilon}$.

The corresponding complex version of (2.6) can be simplified under the assumption that $\omega \approx \omega_0$ and $\gamma \ll \omega$ holds. Setting $\Omega = \omega$, one obtains the equation

$$\partial_t\hat{\mathbf{P}} = -\left(\gamma + i\Delta\omega\right)\hat{\mathbf{P}} - \frac{2i}{\hbar}\mathbf{M}\mathbf{M}^T\hat{\mathbf{E}}\,(N - N_{\rm tr}) \tag{2.13}$$

where we introduced the *frequency detuning* term $\Delta\omega = \omega - \Omega$ which is quantifying the difference between the optical mode frequency Ω and the transition frequency ω of the two-level system. This equation is equivalent to the polarisation part of the optical Bloch-equations [46, 47] which emerge from Heisenberg's equations of motion of a two level-system coupled to the light-field. The complete set of equations for N and $\hat{\mathbf{P}}$ including the light-field $\hat{\mathbf{E}}$ are commonly known as *Maxwell-Bloch equations* [34, 35, 48]. This pays respect to the fact that the electric-field equation is entering in a classical way. We point out that these equations describing the spectral dynamics of our full time-domain equations are situated half in frequency-, half in time-domain.

In the case of $\partial_t\hat{P} \ll \gamma\hat{P}$ the independent dynamics of $\hat{P}$ can be neglected. This step of approximation is called the *adiabatic elimination* of $\hat{P}$ and leads to the relation

$$\hat{\mathbf{P}} = \epsilon_0\,\chi(\Omega, N)\,\hat{\mathbf{E}} \tag{2.14}$$

with

$$\chi(\Omega, N) = -\epsilon_0^{-1}\frac{\xi}{\Omega}\frac{1}{\gamma}\mathcal{D}(\Omega)(N - N_{\rm tr})\,, \tag{2.15}$$

$$\mathcal{D}(\Omega) = \frac{i\gamma}{\gamma + i\Delta\omega}\,, \quad \mathcal{L}(\Omega) = {\rm Im}\left[\,D(\Omega)\,\right] = \frac{\gamma^2}{\gamma^2 + \Delta\omega^2}\,. \tag{2.16}$$

$\mathcal{D}(\Omega)$ and $\mathcal{L}(\Omega)$ are the complex and real Lorentzians, respectively. $g(\Omega, N)$ the *differential gain* function is the derivation of the *spectral gain* $G(\Omega, N) := -{\rm Im}\left[\,\chi(\Omega, N)\,\right]$ with respect to N. For the two-level system the gain function is proportional to a Lorentz-line function $\mathcal{L}$ which contains the independent parameters ξ, ω and γ. The spectral gain turns out to be a linear function of the density N. Another important quantity, the *alpha* or *line-width enhancement factor*, is defined as

$$\alpha(\Omega, N) = \frac{\partial{\rm Re}\left[\,\chi\,\right]}{\partial N}\Big/\frac{\partial{\rm Im}\left[\,\chi\,\right]}{\partial N}\,. \tag{2.17}$$

A high alpha-factor means that in comparison to the differential gain the refractive index is strongly dependent on the density. A positive alpha-factor in combination with a spatially extended system leads to *filamentation* as gain and induced diffraction are competing effects [49–51]. For the two-level model we see that α takes an density-independent value, $\alpha = \Delta\omega/\gamma$.

By averaging over some oscillation periods one easily prooves that the dynamics of the dipole density N (2.8) is given by

$$\partial_t N = -\gamma_{\rm nr} N + \Lambda - \frac{2}{\hbar}{\rm Im}\left[\hat{\mathbf{P}}^* \cdot \hat{\mathbf{E}}\right] . \tag{2.18}$$

After separating the amplitude from the phase and by neglecting the polarisation dynamics, the system of equations (2.12), (2.13) and (2.18) can be further reduced to a system of two coupled equations for the real valued intensity $I = |\hat{\mathbf{E}}|^2$ and the carrier density N:

$$\frac{\sqrt{\epsilon}}{c}\partial_t I = -2\gamma_{\rm res} I + 2\kappa g(\Omega)(N - N_{\rm tr})I , \tag{2.19}$$

$$\partial_t N = -\gamma_{\rm nr} N + \Lambda - \epsilon_0^{-1}\frac{2}{\hbar} g(\Omega) I (N - N_{\rm tr}) . \tag{2.20}$$

The phase ϕ which has been defined by the ansatz $\hat{E} = \sqrt{I}\exp(-i\phi)\hat{\mathbf{e}}$ turn out to be a functional of N,

$$\partial_t \phi = -\frac{c}{\sqrt{\epsilon}}\kappa g(\Omega)\alpha(\Omega)(N - N_{\rm tr}) . \tag{2.21}$$

The above model is generally classified as a *class-B* laser model or the *rate-equation* model. Although phase sensitive effects are completely removed it is still useful to explain some of the more fundamental characteristics of a laser. First of all, we define the *threshold density* $N_{\rm thr}$ as the quasi-equilibrium density where the photon loss and the gain processes are balanced, $\partial_t I = 0$. It follows

$$N_{\rm thr} = N_{\rm tr} + \frac{\gamma_{\rm res}}{\kappa g(\Omega)} . \tag{2.22}$$

The threshold density is connected to the *threshold pump* $\Lambda_{\rm thr}$ which is the carrier injection rate needed to reach the threshold density for $I = 0$ asymptotically,

$$\Lambda_{\rm thr} = \gamma_{\rm nr} N_{\rm thr} . \tag{2.23}$$

Applying the stationary condition $\partial_t N = 0$ to (2.20) one can deduce a relation between N and I,

$$N - N_{\rm tr} = \frac{\Lambda/\gamma_{\rm nr} - N_{\rm tr}}{1 + I/I_{\rm sat}} \quad \text{with} \quad I_{\rm sat} = \gamma_{\rm nr}\frac{\hbar}{2} g^{-1}(\Omega) . \tag{2.24}$$

$I_{\rm sat}$ is called the *saturated intensity*. This means that the gain $G = g(\Omega)(N - N_{\rm tr})$ associated with (2.24) obviously diminishes for $I \to \infty$. The gain saturates and the density stays close to threshold value. A situation that is commonly referred to as *gain clamping*.

Inserting $N = N_{\rm st} = N_{\rm thr}$ and defining $\tilde{\Lambda} = \Lambda - \Lambda_{\rm thr}$ we can exploit the above relation and obtain the stationary solution of the intensity $I_{\rm st}$,

$$I_{\rm st} = \frac{\hbar}{2}\frac{\kappa}{\gamma_{\rm res}}\tilde{\Lambda}\,. \tag{2.25}$$

This equation is valid for $\Lambda > \Lambda_{\rm thr}$ only. Below threshold the laser is off. The effective carrier pump Λ itself is a function of the injected current j. The *threshold current*, defined by $I_{\rm st}(j_{\rm thr}) = 0$ and the *slope-efficiency* $\partial I_{\rm st}/\partial j$ at $j_{\rm thr}$ might be the most prominent performance parameters of a laser as they quantify the conversion-efficiency between injected carriers and out-coupled photons.

We go back to the equations (2.19), (2.20) and insert $I = I_{\rm st} + \tilde{I}$ and $N = N_{\rm st} + \tilde{N}$. Subsequently dropping all nonlinear terms one is left with a linear system of two equations,

$$\frac{\sqrt{\epsilon}}{c}\partial_t \tilde{I} = 2\kappa g(\Omega)\tilde{N} I_{\rm st}\,, \tag{2.26}$$

$$\partial_t \tilde{N} = -\gamma_{\rm nr}\tilde{N} - \frac{2}{\hbar}g(\Omega)I_{\rm st}\tilde{N} - \tilde{I}/I_{\rm st}\tilde{\Lambda}\,. \tag{2.27}$$

The associated eigenvalues $\lambda_{1/2}$ are given by

$$\lambda_{1/2} = -\Gamma_{\rm rel} \pm i\,\Omega_{\rm rel} = -\Gamma_{\rm rel} \pm i\sqrt{\Omega_{\rm rel,0}^2 - \Gamma_{\rm rel}^2}\,, \tag{2.28}$$

$$\Gamma_{\rm rel} = \frac{1}{2}\left(\gamma_{\rm nr} + g(\Omega)\tilde{\Lambda}\frac{\kappa}{\gamma_{\rm res}}\right)\,, \quad \Omega_{\rm rel,0} = \sqrt{\Gamma_z \epsilon^{-1}\Omega g(\Omega)\tilde{\Lambda}}\,. \tag{2.29}$$

Both, the damping $\Gamma_{\rm rel}$ and the relaxation frequency $\Omega_{\rm rel}$ quantify how fast the system relaxes back to the point of stationary equilibrium $(I_{\rm st}, N_{\rm st})$. During this so-called *relaxation oscillation* I and N stay phase-locked with a phase difference of $\Delta\Phi = \pi/2$. This dynamical behaviour governs all switch-on and -off processes of semiconductor lasers and dominates the dynamics of the laser under the influence of current modulation. We note, that for $\Gamma_{\rm rel} > \Omega_{\rm rel,0}$ the relaxation is over-damped.

2.4 The Full Time-Domain Laser-Langevin Equations

As the FTD-MBE equations are based on a classical picture the question arises in which sense these equations are different from their quantum-mechanical counterparts. Although it has been shown that the dynamics of P reproduces the *coherent dipole-light*

interaction described by the Maxwell-Bloch equations there are two major modifications to be made to extend the above model to suit to the quantum-mechanical picture of light-matter interaction. The first correction is to include decay of carriers by spontaneous emission. Spontaneous emission is arising from the fact that the vacuum ground-state of the electro-magnetic field is interacting with the dipole-moment of the two-level system [52, 53]. A second correction has to be made to counter-balance the various loss channels by stochastic Langevin-forces . This is necessary as the laser is a thermodynamically system in constant flux as energy is redistributed between external and internal reservoirs [44, 54–57].

In order to understand these corrections one has to take a look at the corresponding quantum-mechanical equations of motion. For a single longitudinal mode with frequency Ω which is resonantly coupled to a two-level system (e.g. atomic transitions) the Hamiltonian reads

$$\hat{\mathcal{H}} = \frac{1}{2}\hbar\omega\left(\hat{c}^\dagger\hat{c} + \hat{d}^\dagger\hat{d}\right) + \hbar\Omega\left(\hat{a}^\dagger\hat{a} + \frac{1}{2}\right) - \hbar\left(g\,\hat{c}^\dagger\,\hat{d}^\dagger\,\hat{a} + g^*\hat{d}\,\hat{c}\,\hat{a}^\dagger\right) . \tag{2.30}$$

Contained are the energy contributions accounting for the potential energy of the two-level system, the electromagnetic-field energy, and the electron light-field interaction energy. $\hat{c}^\dagger$ and $\hat{c}$ are the electron creation and electron annihilation operators for the upper levels of the two-level system. $\hat{d}^\dagger$ and $\hat{d}$ are the respective hole operators for the lower levels. The bosonic operator $\hat{a}^\dagger$ creates a photon, $\hat{a}$ destroys a photon occupying the laser-mode Ω. As the vector-potential was quantised the following relationship between the photon operators and the electric field operator holds,

$$\hat{E} = i\,\mathcal{E}_\Omega\,\hat{a}\,\mathrm{e}^{iKz}\,\mathrm{e}^{-i\Omega t} . \tag{2.31}$$

The complex *mode-coupling constant* g, and the electric field per photon $\mathcal{E}_\Omega$ are

$$g = i\hbar^{-1}M\mathcal{E}_\Omega\,\mathrm{e}^{iKz} , \quad \mathcal{E}_\Omega = \sqrt{\frac{\hbar\Omega}{\epsilon_0\epsilon V}} \tag{2.32}$$

respectively. M denotes the dipole matrix-element.

The above second-quantisation Hamiltonian is similar to the Hamiltonian of the *Jayne-Cummings model* which describes a two-level systems coupled to a single light-mode [58]. The upper level and the lower level can be independently populated by electrons and holes. Writing down Heisenberg's equation of motion for the particle number operators $\hat{n^{\mathrm{e}}} = \hat{c}^\dagger\hat{c}$, $\hat{n^{\mathrm{h}}} = \hat{d}^\dagger\hat{d}$, the polarisation operator $\hat{p} = \hat{d}\,\hat{c}\,\exp(-i\Omega t)$, and the field-operator $\hat{b} = i\hat{a}\,\exp(-i\Omega t)$ one obtains by exploiting the appropriate commutator and anti-commutator rules

$$\begin{aligned}
&\partial_t\langle\hat{b}\rangle = -g^*\langle\hat{p}\rangle ,\\
&\partial_t\langle\hat{p}\rangle = -(\gamma + i\Delta\omega)\langle\hat{p}\rangle - g\,\langle\hat{b}\left(\hat{n}^{\mathrm{e}} + \hat{n}^{\mathrm{h}} - 1\right)\rangle ,\\
&\partial_t\langle\hat{n}^{\mathrm{e}}\rangle = g\langle\hat{p}^\dagger\hat{b}\,\rangle + g^*\langle\hat{b}^\dagger\hat{p}\rangle ,\\
&\partial_t\langle\hat{n}^{\mathrm{h}}\rangle = g\langle\hat{p}^\dagger\hat{b}\,\rangle + g^*\langle\hat{b}^\dagger\hat{p}\rangle .
\end{aligned} \tag{2.33}$$

$\Delta\omega = \omega - \Omega$ is the frequency-detuning term and the brackets indicate either quantum-mechanical or later-on quantum-statistical expectation values. These equations are exact apart from the phenomenological dipole relaxation term ($\sim \gamma$) which was introduced to remove the singularity at resonance and is attributed to carrier-carrier and carrier-phonon scattering processes [35, 59, 60]. However, the system of equations of motion is not closed. Due to the quantisation of the optical field moments of order three appear on the rhs of $\partial_t\langle\hat{n}^{\mathrm{e}}\rangle$, $\partial_t\langle\hat{n}^{\mathrm{h}}\rangle$, and $\partial_t\langle\hat{p}\rangle$ which are combination of three-particle operators. The factorisation of the three-particale operators into operators of the two-particle states whose time-derivates are given on the lhs leads to the *optical Bloch-equations*.

Instead of *factorising* the three-particle operator $\langle\hat{b}^\dagger\hat{p}\rangle = \langle\hat{b}^\dagger\hat{c}\,\hat{d}\,\rangle$ directly into $\langle\hat{b}^\dagger\rangle\langle\hat{p}\rangle$ one might first take a look at the next higher order equation of motion [43],

$$\partial_t\langle\hat{b}^\dagger\hat{p}\rangle = -(\gamma + i\Delta\omega)\langle\hat{b}^\dagger\hat{p}\rangle - g\langle\hat{b}^\dagger\hat{b}\,(\hat{n}^{\mathrm{e}} + \hat{n}^{\mathrm{h}} - 1)\rangle + g\langle\hat{n}^{\mathrm{e}}\,\hat{n}^{\mathrm{h}}\rangle\,, \tag{2.34}$$

which describes a quantum-mechanical light-dipole correlation. By adiabatically eliminating $\langle\hat{b}^\dagger\hat{p}\rangle$ and assuming that the electric field is in its vacuum state one derives the following expression

$$\langle\hat{b}^\dagger\hat{p}\rangle_{\mathrm{vac}} = \frac{g\langle\hat{n}^{\mathrm{e}}\,\hat{n}^{\mathrm{h}}\rangle_{\mathrm{vac}}}{\gamma + i\Delta\omega}\,. \tag{2.35}$$

Plugging this result back into (2.33) reveals the decay of our carrier system due to the dipole-coupling of the two-level system with the electro-magnetic vacuum-state. By extending our Hamiltonian (2.30) from a single mode to a single laser-mode $\hat{b} = \hat{b}_\Omega$ plus a bath of non-resonant optical modes $\hat{b}_{\Omega'}$ in vacuum ground-state, we obtain

$$\partial_t\langle\hat{n}^{\mathrm{e}}\rangle = \Big(g\langle\hat{p}^\dagger\langle\hat{b}\rangle\rangle + g^*\langle\hat{b}^\dagger\rangle\langle\hat{p}\rangle\Big) - \sum_{\Omega'} B_{\Omega'}\langle\hat{n}^{\mathrm{e}}\hat{n}^{\mathrm{h}}\rangle_{\mathrm{vac}} \tag{2.36}$$

for the electrons.

$$B_{\Omega'} = |g'|^2\frac{2\gamma}{\gamma^2 + (\omega - \Omega')^2}\,, \quad g' = i\hbar^{-1}M\mathcal{E}_{\Omega'}\exp(iKz) \tag{2.37}$$

appears on the rhs of this equation. Usually one will factorise the spontaneous emission term and assume that *all* modes are in vaccum state, that is $\langle\hat{n}^{\mathrm{e}}\,\hat{n}^{\mathrm{h}}\rangle_{\mathrm{vac}} \approx \langle\hat{n}^{\mathrm{e}}\rangle\langle\hat{n}^{\mathrm{h}}\rangle$. This effectively means, that we neglect the influence of the lasing-mode itself on the non-coherent carrier-decay. If we assume the two-level system being coupled to free-space modes, the sum over all Ω' can be analytically calculated This is best true for a planar resonator with perfect mirrors attached to it at the ends. The result of the summation using the free-space density of states is the famous *Weisskopf-Wigner constant* [43, 61] of spontaneous emission,

$$B^0 = (\tau^0)^{-1} = \sum_{\Omega'} B_{\Omega'} = \frac{\omega^3|M|^2\sqrt{\epsilon}^3}{3\pi\hbar c^3\epsilon_0}\,. \tag{2.38}$$

However, within a cavity the spontaneous emission life-time $\tau = B^{-1}$ is different as the electro-magnetic mode-density appears to be modified. In case of a Al-GaAs/GaAs VCSEL with dipoles oriented perpendicular to the z-Axis τ is $1-2$ times τ^0 the fraction between the rate of photons spontaneously emitted into the lasing-modes to those emitted into the non-lasing modes is defined as the *spontaneous emission coupling efficiency* β [52, 53, 61–65]. For VCSELs β is known to be around 0.2 [62, 66] depending on the number of Bragg-layers and the dielectric contrast. Suppression of spontaneous emission is one of the most prominent features of microcavity structures and has been successfully exploited to build resonant cavity high-power LEDs (RC-LEDs) [67].

B quantifies the complete loss of carriers due to coupling of the two level-system to *all* the vacuum modes. A fraction β of these photons are emitted into the lasing mode. The quantum-optical equations of this order lack a term describing how the spontaneously emitted photons contribute to the electrical field of the lasing mode. In fact, higher order correlations of the photon-operators like $\langle \hat{b}^\dagger \hat{b} \rangle$ or $\langle \hat{b}\, \hat{b} \rangle$ would have to be take into account. The equations emerging from such considerations would describe phase-correlations and explain how spontaneous emission enters the optical field equations [68]. Another, more pragmatic way, is to introduce Langevin noise-forces to our set of equations. In that case the loss of carriers due to spontaneous emission couples back into the optical-field as fluctuations. This will be discussed now.

A laser can be regarded as a thermodynamically open system which is in a state of dynamic quasi-equilibrium with its environment: In cw-operation there is a constant flow of energy between the baths, from the source (carrier pump), through the system, to the sinks (vacuum photon bath, lattice phonons). The coupling terms to the various baths have bene introduced to the quantum-mechanical equations in a phenomenological way. This destruction of the Hermiticity of the Hamiltonian reflects itself in a decay of the fundamental bosonic and fermionic commutation relations. It can be shown , that it is possible to restore the commutation relations to their original form by compensating each damping term with an appropriate noise term [54]. This is known as the quantum-mechanical *Dissipation-Fluctuation Theorem*. By introducing loss and noise terms to the Bloch equations (2.33), we end up with the corresponding *Laser Langevin-equations* which take the form

$$\begin{aligned}
\partial_t \hat{b} &= -\Omega/(2Q)\, \hat{b} - g^*\, \hat{p} + F_b(t)\,, \\
\partial_t \hat{p} &= -(\gamma + i\Delta\omega)\hat{p} - g\, \hat{b}\, \left(\hat{n}^{\mathrm{e}} + \hat{n}^{\mathrm{h}} - 1\right) + F_p(t)\,, \\
\partial_t \hat{n}^{\mathrm{e}} &= \lambda - \gamma_{\mathrm{nr}} \hat{n}^{\mathrm{e}} - B \hat{n}^{\mathrm{e}} \hat{n}^{\mathrm{h}} + \left(g\, \hat{p}^\dagger \hat{b} + g^*\, \hat{b}^\dagger \hat{p}\right) + F_n(t)\,, \\
\partial_t \hat{n}^{\mathrm{h}} &= \lambda - \gamma_{\mathrm{nr}} \hat{n}^{\mathrm{h}} - B \hat{n}^{\mathrm{e}} \hat{n}^{\mathrm{h}} + \left(g\, \hat{p}^\dagger \hat{b} + g^*\, \hat{b}^\dagger \hat{p}\right) + F_n(t)\,.
\end{aligned} \tag{2.39}$$

Here, γ is the loss of polarisation coherence due to a coupling to the phonon- and carrier-bath and is caused by scattering processes. $\Omega/(2Q)$ is the photon loss rate due to out-coupling of laser light. γ_{nr}, the non-radiative recombination of carriers, and λ, the carrier pump, are associated with a coupling of the carrier-system to the phonon-bath

and the external carrier source, respectively. The strengths of the Markovian stochastic forces are given by the corresponding diffusion constants (see (B.4)). Their calculation is briefly sketched in Appendix B: by eliminating the dynamics of the polarisation, equations for $\hat{b}$ and $\hat{n}^{\mathrm{e/h}}$ emerge containing effective noise terms (B.8). One finds that in the case of steady-state $\partial_t \langle \hat{b}^\dagger \hat{b} \rangle = 0$ the energy balance

$$\left[\Omega/Q - \left(\langle r_{\mathrm{em}} \rangle - \langle r_{\mathrm{abs}} \rangle\right)\right] \langle \hat{b}^\dagger \hat{b} \rangle = \Omega/Q\, \bar{n}_\Omega + \langle r_{\mathrm{em}} \rangle \,. \tag{2.40}$$

must be fulfilled. $\langle r_{\mathrm{em}} \rangle$ and $\langle r_{\mathrm{abs}} \rangle$ are the rates of emission and absorption rate as defined by (B.9). The lhs of this expression – which is proportional to the field intensity – explains the difference of the resonator's photon losses and the stimulated field amplification processes. As one can see from the rhs expression, the usually small photon number fluctuations and the not so small spontaneous emission of photons are responsible for this mismatch. With increasing pumping current Λ, the output intensity $\langle \hat{b}^\dagger \hat{b} \rangle$ grows steadily. However, as the density is pinned to its threshold value, the rhs of the equation must be considered constant. Hence, the gain asymtotically approaches the cavity losses with increasing power.

Below threshold, the laser spectrum is broadened due to both intensity and phase fluctuations. However, above threshold the intensity will be constrained due to condition (2.40) and the laser line-width is mainly broadened due to phase-fluctuations. According to a calculation outlined in Appendix B, [43] the intensity spectrum of the laser above threshold is described by the equation

$$\begin{aligned} \mathcal{S}(\omega) = I_{\mathrm{st}} \exp\left(-\frac{\alpha^2 \langle r_{\mathrm{em}} \rangle \cos(3\delta)}{4\Gamma I_{\mathrm{st}} \cos(\delta)}\right) \cdot \quad & \int_{-\infty}^{+\infty} \mathrm{e}^{-i\omega t} \\ \times \exp\left(-\frac{\langle r_{\mathrm{em}} \rangle}{4 I_{\mathrm{st}}} \left[(1+\alpha^2)|t| - \frac{\alpha^2 \exp(-\Gamma|t|/2)\cos(\Omega_{\mathrm{rel}}|t| - 3\delta)}{\Gamma \cos(\delta)}\right]\right) \mathrm{d}t \,. \end{aligned} \tag{2.41}$$

The centre peak at $\omega = 0$ has an approximate width of

$$\delta\omega = \frac{1}{2}(1+\alpha^2)\delta\omega_0 \,. \tag{2.42}$$

$\delta\omega_0 = \langle r_{\mathrm{em}} \rangle / I$ is the traditional Shawlow-Townes line-width. For semiconductor lasers the line-width is reduced by a factor one-half due to the amplitude stabilisation and is increased by an factor $(1+\alpha^2)$ as carrier fluctuation cause refractive index fluctuations which add on top of the phase fluctuations of the optical field. The impact of the α factor is particularly strong for semiconductor lasers as the carrier densities are high and the induced refractive index resulting from density fluctuations cannot be neglected. In depth treatments of the laser line-width of semiconductor-lasers can be found in [25,57,68–70].

The analogy between the Laser Langevin-equations (2.39) and the adiabatically eliminated FTD-MBE equations (2.12), (2.13), (2.18) becomes obvious if we translate the dimensionless microscopic quantities to the macroscopic field variables,

$$\begin{aligned}
&\hat{\mathbf{E}} = \mathcal{E}_\Omega \langle \hat{b} \rangle \cdot \hat{\mathbf{e}}_\perp \,, \\
&\hat{\mathbf{P}} = N_0 \mathbf{M} \langle \hat{p} \rangle \,, \\
&N = N_0 \left\langle \hat{n}^{\mathrm{e}} \right\rangle = N_0 \left\langle \hat{n}^{\mathrm{h}} \right\rangle \,, \\
&N_{\mathrm{tr}} = N_0/2 \,, \\
&\Lambda = N_0 \lambda \,,
\end{aligned}$$

with $N_0 = V^{-1}$ and $\hat{\mathbf{e}}_\perp$ being a the unit-vector with $\hat{\mathbf{e}}_\perp \cdot \hat{\mathbf{e}}_z = 0$. Using these conversion rules we can modify equations (2.3), (2.6), (2.8) by adding the missing quantum-mechanical corrections to our classical equations. This completes the FTD-MBE equations to become the *full time-domain Laser Langevin equations* (FTD-LLE). In one dimension they read

$$\begin{aligned}
&\partial_t \mathbf{H} = \epsilon_0 \, c \, \partial_z \mathbf{E} \,, \\
&\epsilon_0 \, \epsilon \cdot \partial_t \mathbf{E} = c \, \partial_z \mathbf{H} - \partial_t \mathbf{P} + \mathbf{J} + F_E(t) \,, \\
&\partial_t^2 \mathbf{P} + 2\gamma \, \partial_t \mathbf{P} + \omega_0^2 \mathbf{P} = -2 \, \xi \cdot \mathbf{E} \, (N - N_{\mathrm{tr}}) + F_P(t) \,, \\
&\partial_t N = \Lambda - \gamma_{\mathrm{nr}} N - N_0^{-1} B N^2 + \frac{1}{\hbar\omega} (\partial_t \mathbf{P}) \cdot \mathbf{E} + F_N(t) \,.
\end{aligned} \tag{2.43}$$

The macroscopic noise forces $F_P(t)$, and $F_N(t)$ can be derived from the expressions $F_p(t)$, and $F_n(t)$,

$$\begin{aligned}
&F_P(t) = -4i\Omega N_0 \mathbf{M} \mathrm{Im} \left[\, F_p(t) \exp(-i\Omega t) \, \right] \,, \\
&F_N(t) = N_0 F_n(t) \,.
\end{aligned} \tag{2.44}$$

In resonance Ω can be replaced with ω. An explicit calculation of the correlation functions delivers,

$$\begin{aligned}
&D_{PP^\dagger} = D_{P^\dagger P} = 4\omega |M|^2 \gamma \left(2N^2 - 2N_0 N + N_0^2 \right) \,, \\
&D_{NN} = N_0 \Lambda/2 + N_0 \gamma_{\mathrm{nr}}/2\bar{N} + BN^2 \,,
\end{aligned} \tag{2.45}$$

where all non-resonant terms were dropped. At threshold $N = \bar{N} = N_{\mathrm{tr}} = N_0/2$ the diffusion coefficients read:

$$\begin{aligned}
&D_{PP^\dagger} = D_{P^\dagger P} = 8\omega |M|^2 \gamma N_{\mathrm{tr}}^2 \,, \\
&D_{NN} = \Lambda N_{\mathrm{tr}} + \gamma_{\mathrm{nr}} N_{\mathrm{tr}}^2 + B N_{\mathrm{tr}}^2 \,.
\end{aligned} \tag{2.46}$$

The calculation of $F_E(t)$ turns out to be more complicated as the diffusion coefficient (B.4) of $F_b(t)$ is associated with the modal loss but the Maxwell equations give a spatially resolved local description of the electrical field-variable. There is no straight forward way of including the optical mode fluctuations into the electrical field equation. However, assuming cavities with a low modal loss we can usually neglect the influence of the field fluctuations $F_E(t)$

2.5 The Single-Lorentzian Fit and the Effective Bloch-Equations in Time-Domain

In the previous sections we approximated the active material with a a two-level system. However, the active semiconductor material bears a complex electronic band and level structure which depends on various parameters like the chosen material-system, the dimensionality (bulk or well structures) or the size of the structure elements (thickness of quantum-well). Its susceptibility can be derived from the *semiconductor-Bloch* equations and is formed by a superposition of k-dependent Lorentz-line functions weighted with the k-dependent carrier inversion (see also CHAPTER 4 or [71, 72]),

$$\chi(\Omega, N) = -\epsilon_0^{-1}\hbar^{-1}\sum_k |M_{\mathrm{cv},k}|^2\gamma_k^{-1}\mathcal{D}_k(\Omega)\,\left[f_k^{\mathrm{e}}(N,T) + f_k^{\mathrm{h}}(N,T) - 1\right]\cdot Q_k\,. \quad (2.47)$$

$f_k^{\mathrm{e/h}}(N,T)$ are the Fermi-functions of electrons and holes respectively. In parabolic band approximation the line-function $\mathcal{D}_k$ is given by

$$\mathcal{D}_k(\Omega) = \frac{i\gamma_k}{\gamma_k + i\Delta\omega_k}\,, \qquad \Delta\omega_k = \left(\omega_{\mathrm{g}} + \frac{\hbar k^2}{2m_r} - \Omega\right)\,, \quad (2.48)$$

where the γ_k are the k-dependent polarisation scattering rate. Q_k is the Coulomb-enhancement factor. This already relies on an approximation as the polarisation has been adiabatically eliminated and an equilibrium ansatz for the carrier distribution functions has been used. Hence, the gain appears to be homogeneously broadened and spectral hole-burning effects are no longer contained. This level of approximation is generally considered to hold for timescales longer than the intraband-scattering rates (~ 100 fs).

For an efficient numerical implementation of complex material systems, the first task would be to fit the Lorentzian gain-function F to the gain-function $G = -\mathrm{Im}\,[\,\chi\,]$ as well as possible. For the moment we assume the density N to be fixed, and, as we want to implement the material response in full time-domain, we define

$$\tilde{\chi}(\Omega) = -\epsilon_0^{-1}\frac{i\omega^{-1}\beta}{\gamma + i(\omega - \Omega)} \quad (2.49)$$

for the susceptibility. This is the complex Lorentzian line-shape function. From the equations we derived in SECTION 2.3 and SECTION 2.2 we know that the differential equation correlated with this frequency response is that of a driven damped harmonic oscillator,

$$\partial_t^2\mathbf{P} + 2\gamma\,\partial_t\mathbf{P} + \omega_0^2\mathbf{P} = -2\,\beta\,\mathbf{E}\,. \quad (2.50)$$

β, γ, and ω are interpreted as density-dependent fit parameters which shall be chosen in a way such that

$$F = -\mathrm{Im}\,[\,\tilde{\chi}\,] = \epsilon_0^{-1}\frac{\omega^{-1}\beta\gamma}{\gamma^2 + (\omega - \Omega)^2} \quad (2.51)$$

provides a good approximation to $G = -\mathrm{Im}\,[\,\chi\,]$ in the vicinity of a given frequency Ω.

With $\Delta\omega = \omega - \Omega$ and

$$B = \frac{2\Delta\omega}{\gamma^2 + \Delta\omega^2}\,, \quad B' = B^2 - \Delta\omega^{-1}B \tag{2.52}$$

it is easy to show, that the first two derivatives of F with respect to Ω can be written as

$$F' = FB\,, \tag{2.53}$$

$$F'' = \left(F' - \Delta\omega^{-1}F\right)B + FB^2\,. \tag{2.54}$$

By eliminating B we extract an expression for the centre-frequency ω of the Lorentzian

$$\Delta\omega = \omega - \Omega = \kappa F'\,, \quad \kappa = \frac{F}{2F'^2 - FF''}\,. \tag{2.55}$$

Inserting this result into (2.53), the width of the Lorentzian is determined to be

$$\gamma = \kappa\sqrt{3F'^2 - 2FF''}\,. \tag{2.56}$$

As we know the value of ω and γ, we are now in position to calculate the strength of the Lorentzian. β can be expressed as

$$\beta = \epsilon_0 F\omega\gamma^{-1}\left(\gamma^2 + (\omega - \Omega)^2\right)\,. \tag{2.57}$$

In order to fit the semiconductor gain G with F the values of F, F' and F'' will be chosen to match the corresponding derivatives of G. As the semiconductor-gain is a function of N, all the fit parameters are density-dependent entities. The most sensible frequency where to fit the semiconductor gain is at the position of the gain-maximum Ω_{max}. Here, the bandwidth of the Lorentzian is comparable with the width of the material gain. This means, $F' = 0$ and we obtain

$$\Delta\omega = 0\,, \quad \gamma = -\frac{\sqrt{-2FF''}}{F''}\,, \quad \beta = \epsilon_0 F\Omega\gamma\,. \tag{2.58}$$

$$\gamma = \Delta\omega\left[2\frac{\Omega}{\Delta\omega} - 1\right]^{1/2}\,. \tag{2.59}$$

A solution exists for $FF'' < 0$ which means that local minima of G can not be fitted with a Lorentzian if $G > 0$. For maxima with $G < 0$ the situation is the same.

The major drawback of this single-Lorentzian approximation is that the Lorentzian is symmetric and that F will be positive for all frequencies as long as $N > N_{\mathrm{tr}}$. In reality the semiconductor gain is highly asymmetric with an absorbing high-frequency tail. As we will see in the next section this problem can be addressed by using a series of Lorentzians rather than a single one. Another point to keep in mind is, that the real and the imaginary part of the complex susceptibility are connected via the Kramers-Kronig

relation. This means, that a good local fit of the gain in frequency space does not guarantee that the induced refractive index is fitted well at the same time. We conclude, that the single-Lorentzian approximation is applicable to single-mode microcavities where effects of an induced refractive index, e.g. self-focusing, are negligible. For laser systems supporting a broad spectrum of longitudinal modes it may be very ainaccurate, however.

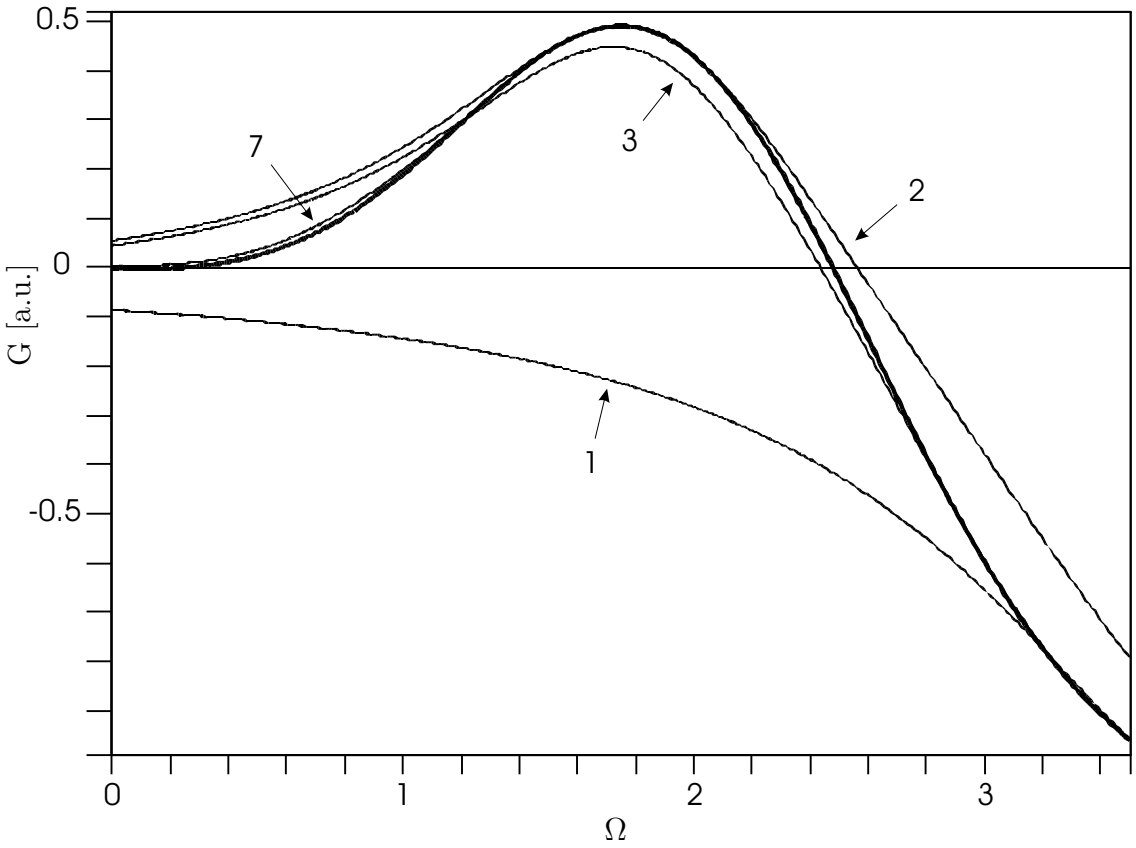

Figure 2.1: Fit of a series of Lorentzians to an artificial gain-curve $G(\Omega) = -0.5 * \arctan(\Omega - 2.0) + \exp(-(\Omega - 2.0)^2)$ (thick line) within a certain frequency range. The labels indicate the number of superposed Lorentzians. While the first one covers the absorbing high-frequency tail of the gain additional Lorentzians remove the deviations. Two Lorentzians are sufficient to qualitatively describe an asymmetric gain. After a superposition of 7 Lorentzians the fit-function is almost indistinguishable from the original gain-curve.

In order to get a better global agreement in frequency space we approximate the homogeneously broadened, material gain $G(\Omega, N)$ by a superposition of Lorentzians $f(\Omega, N), i = 1 \ldots n$. A straight forward solution for this would be to set up the semiconductor-Bloch equations for the interband polarisations p_k transform them to full time-domain and solve the coupled system of harmonic oscillator equations. However, the typical number of Lorentzians needed to achieve a sufficient k-space resolution would count 50-100. In combination with a sub-fs time-step the computational effort for solving this equa-

tions would be huge. Another, approximative, but much more efficient solution of this problem is to look for a small set of Lorentzians with varying bandwidth. While the first Lorentzians could cover thehigh-frequency tail and the broad maximum of the gain-curve smaller deviations could be contained in additional Lorentzians, which are weaker or more narrow. Such a method was firstly proposed by [73]. The susceptibility associated with the semiconductor-Bloch equations is effectively mimiced by a reduced set of *effective Bloch equations*. This concept can be extended to full time-domain. In contrast to the complex variant of this method described in [73] it is not possible to add a frequency-independent offset $\chi_0(N)$ as no time-domain representation for a static frequency independent gain exists. Instead, we apply the ansatz

$$F(\Omega,N)=\sum_{i=1}^{n}F_i(\Omega,N)\,,\qquad F_i(\Omega,N)=\epsilon_0^{-1}\frac{\omega_i^{-1}\beta_i(N)\gamma_i(N)}{\gamma_i(N)^2+(\omega_i(N)-\Omega)^2}\,. \tag{2.60}$$

which forms the basis of a multi-Lorentzian gain-fit which can be implemented in full time-domain. The functions $\beta_i(N)$, $\gamma_i(N)$, and $\omega_i(N)$ are to be chosen in a way to provide a *good* fit for the gain $G(\Omega,N)$ for a given density N and within a certain frequency range $[0,\Omega_{\rm cut}]$. There is no distinct method to determine the fit-parameters. The rule is: the fewer Lorentzians needed, the better. We suggest the following iterative procedure:

1. $i=0$; $D_0(\Omega,N)=G(\Omega)$; $l_0(\Omega)=0$
2. find Ω_i, being the absolute maximum of $|D_i(\Omega)|$ within $[\Omega_{\rm min},\Omega_{\rm max}]$.
3. determine the parameters β_i, γ_i and ω_i of $F_i(\Omega)$ so that $F_i(\Omega)=D_i(\Omega_i)$, $F_i'(\Omega)=D_i'(\Omega_i)$, $F_i''(\Omega)=D_i''(\Omega_i)$.
4. $D_{i+1}(\Omega)=D_i(\Omega)-F_i(\Omega)$; $l_{i+1}(\Omega)=l_i(\Omega)+F_i(\Omega)$
5. $i=i+1$; if $i<n$ then goto 2)

By successively removing the left-over maxima the quality of the fit $F_i(\Omega)$ improves with the number of applied iterations i. After n iterations we know the positions $(\Omega_i, i=1,\dots n)$ in frequency space where the local fits have been applied. To obtain the functional dependence of the parameters $\beta_i(N)$, $\gamma_i(N)$, $\omega_i(N)$ we repeat the above algorithm for a range of densities and record the functional dependence of the parameters for each of the n Lorentzians. The combined response $\mathbf{P}$ can be coupled to Maxwell's equations (2.3) by summing up the parts $\mathbf{P}_i$ associated with each of the fit Lorentzians,

$$\mathbf{P}=\sum_i\mathbf{P}_i\,. \tag{2.61}$$

For the density N, the $(h\omega)^{-1}(\partial_t\mathbf{P})\cdot\mathbf{E}$ term which is accounting for the carrier generation in equation (2.8) has to be replaced by the compound generation rate

$$G=\sum_i\frac{1}{h\omega_i(N)}(\partial_t\mathbf{P}_i)\cdot\mathbf{E}\,. \tag{2.62}$$

It becomes obvious, that this effective Bloch-equation approach introduces nonlinear terms to the differential equation for $\mathbf{P}$. In general, these dependencies can be considered weak especially as long as the density N is a relatively slowly varying quantity. For ultrashort and intense pulses, however, we might expect deviations from the semiconductor gain as given by (2.47). It has been demonstrated by [73] that a small number of five Lorentzians can be sufficient to describe the amplification of short pulses passing through active material in good agreement with k-resolved material models.

3 Light-field and Resonator: Revisited

3.1 Introduction

In principle there are two different approaches that can be taken in order to calculate the optical modes inside laser cavities: The first one is assuming that the E and the B field amplitude of the optical field can be (at least approximately) expressed as $A = A_0 \exp(i\Omega t)$ with A_0 being constant in time. This ansatz leads to the problem of a linear eigenvalue equation that has to be solved for a given dielectric cavity-structure[1]. In the special case of VCSEL structures various algorithms for such *static mode* calculations have been developed and can be successfully applied in good agreement with experiment [29]. It has to be noted, however, that such calculations either are based on the assumption of an empty (or cold) optical cavity [26, 27] or incorporate predefined static gain profiles [28, 74–76]. For laser operation far from equilibrium – e.g. pulse-propagation experiments – or in the case of a pronounced multi-mode activity such an approach turns out to be insufficient as they fail to explain various dynamic and nonlinear aspects of the dynamics [9, 11, 33, 72, 77]. The main reason for this is that coexistent cavity-modes are strongly coupled in a nonlinear fashion as they compete with each other for the available active material gain [10, 78].

A time-domain description, on the other hand, makes it possible to incorporate dynamic and nonlinear effects as the interactions between optical modes and the active laser material can be addressed in a inherent natural way. The major drawback of approach, however, is that because of a minimum resolution of 20 grid-points per wavelength and the *Courant* criterion[2] three dimensional calculations of devices based on an FDTD approach quickly become impracticable and computationally expensive. To overcome these constraints, we use a mixed frequency-, time-domain approach that separates off the longitudinal direction oriented along the optical axis z from the transversal spatial directions. The field-equations used are mostly based on the assumption of a travelling-wave [79]. The derivation is approximative, but pays full respect to the characteristic longitudinal DBR-structure of VCSEL cavities. The result that we give at the end of this chapter is a polarisation resolved two-dimensional equation of motion for the transverse field components. Longitudinal details of the structure enter this equation in an effective, parametric way.

[1] in this chapter we use *structure* as synonym for the dielectric structure in combination with the imposed boundary conditions.

[2] For a laser simulations with wavelengths around 800 nm the time-steps we use are of the order of 10^{-17} s

The following calculations are a generalisation of the *paraxial approximation*[3] specifically adapted to systems featuring dominant longitudinal structure elements. The model we present applies to a broad class of multi-layer and microcavity structures. It also constitutes the optical part of the equations used for the transversely resolved dynamical simulations of VCSEL devices which we discuss in CHAPTER 5.

3.2 Improved Paraxial Approximation for Longitudinally Structured Microcavities

Our starting point are Maxwell's equations. Assuming non-magnetic materials one can derive the following wave-equation for the electric field vector $\mathbf{E}$:

$$\mathcal{L}[\mathbf{E}] := \frac{\epsilon}{c^2}\partial_t^2\mathbf{E} - \nabla^2\mathbf{E} + \nabla\nabla\cdot\mathbf{E} = -\frac{\epsilon_0^{-1}}{c^2}\partial_t^2\mathbf{P}[\mathbf{E}]\,. \tag{3.1}$$

$\mathbf{E}$ and the polarisation $\mathbf{P}$ are vector-fields defined in space and time, $\mathbf{E},\mathbf{P}:\mathbb{R}\times\mathbb{R}^3\to\mathbb{R}^3$. ρ, the macroscopic charge density of carriers injected into the structure has to obey the continuum equation (particle conservation). While $\mathcal{L}[\mathbf{E}]$ is a vector-valued linear functional operator acting on $\mathbf{E}$ with respect to the space and time arguments, $\mathbf{P}$ – the polarisation of the active material – has to be considered a nonlinear functional of $\mathbf{E}$. In addition to the above equation, the divergence of the dielectric displacement vector $\mathbf{D}$ has to be equal to the macroscopic charge density ρ, i.e.

$$\nabla\cdot\mathbf{D} = \nabla\cdot(\epsilon_0\epsilon\mathbf{E} + \mathbf{P}) = \rho\,. \tag{3.2}$$

Without loss of generality we will disregard the impact of the carrier-flow on the optical field and set $\rho\approx 0$[4]. We define the dielectric constant ϵ be related to the static linear response of the passive dielectric material only (inner electrons), while $\mathbf{P}$ covers the dynamical response of the laser active material as a response to the local electric field (valence electrons). In a formal way one can expand the full functional response $\mathbf{P}$ in a Volterra series [82]

$$\mathbf{P}[\mathbf{E}] = \mathbf{P}_1[\mathbf{E}] + \mathbf{P}_2[\mathbf{E},\mathbf{E}] + \mathbf{P}_3[\mathbf{E},\mathbf{E},\mathbf{E}] + \ldots \tag{3.3}$$

of functionals $\mathbf{P}_m$ which are multi-linear in $\mathbf{E}$ and defined by the convolution

$$P_m[\mathbf{E},\ldots,\mathbf{E}](t) = \int_0^\infty \mathrm{d}t_1 \ldots \int_0^\infty \mathrm{d}t_m\, \boldsymbol{\chi}_m(t-t_1,\ldots,t-t_m)\circ\mathbf{E}(t-t_1)\ldots\mathbf{E}(t-t_m)\,. \tag{3.4}$$

[3] the paraxial approximation was introduced as a more systematic way to derive a first order wave-equation for the complex electric field amplitude [80]. This approach has been refined by [35, 81] to fully include the non-linear light-matter interaction. Previous derivations were based on the slowly varying amplitude approximation which turns out to be inaccurate and inconsistent.

[4] This is well justified as a the modulation speed of the pump current is much lower than the optical field frequency.

The shortcut symbol '$\circ$' is used to express the fact, that the Volterra kernels χ_m, namely the nonlinear susceptibilities, are tensors of order $m+1$ acting on the m vectors $\mathbf{E}$, that is

$$\boldsymbol{\chi}_m\circ\ : \underbrace{\mathbb{R}^3 \times \cdots \times \mathbb{R}^3}_{m} \to \mathbb{R}^3\,. \tag{3.5}$$

The principle of causality manifests itself in the conditions $\boldsymbol{\chi}_m(t-t_1,\ldots,t-t_m)=0$ if $t_i > t$ for any i.

Following our aim to describe the propagation of fields in a longitudinally structured waveguide or resonator with ϵ being at least dependent on z, we proceed as in [80] and split the field vectors into a longitudinal part E_z and a transverse part $\mathbf{E}_\perp$,

$$\mathbf{E} = \mathbf{E}_\perp + \mathbf{e}_z E_z \quad \text{with} \quad \mathbf{E}_\perp, \mathbf{E}, \mathbf{e}_z : \mathbb{R}\times\mathbb{R}^3 \to \mathbb{R}^3\,, \quad E_z : \mathbb{R}\times\mathbb{R}^3 \to \mathbb{R}\,. \tag{3.6}$$

By doing this, we obtain two coupled equations of motion for $\mathbf{E}_\perp$ and E_z, namely,

$$\begin{aligned}\mathcal{L}_\perp[\mathbf{E}_\perp, E_z] :=& \frac{\epsilon}{c^2}\partial_t^2\mathbf{E}_\perp - \nabla_\perp^2\mathbf{E}_\perp - \partial_z^2\mathbf{E}_\perp + \nabla_\perp\nabla_\perp\cdot\mathbf{E}_\perp + \nabla_\perp\partial_z E_z \\ =& -\frac{1}{c^2}\partial_t^2\mathbf{P}_\perp[\mathbf{E}_\perp]\,,\end{aligned} \tag{3.7}$$

$$\mathcal{L}_z[\mathbf{E}_\perp, E_z] := \frac{\epsilon}{c^2}\partial_t^2 E_z - \nabla_\perp^2 E_z + \partial_z\nabla_\perp\cdot\mathbf{E}_\perp = -\frac{1}{c^2}\partial_t^2 P_z[E_z]\,. \tag{3.8}$$

At this point isotropy of $\mathbf{P}$ has been presumed. Additionally, the condition

$$\nabla_\perp\cdot(\epsilon_0\epsilon\mathbf{E}_\perp) + \partial_z(\epsilon_0\epsilon E_z) + \nabla_\perp\cdot\mathbf{P}_\perp + \partial_z(P_z) = 0 \tag{3.9}$$

for the divergences has to be satisfied.

The first step to be performed, is to split the fields into slow oscillating amplitude ($\hat{\mathbf{E}}$) and fast oscillating phase (Φ) components. For a single (longitudinal) frequency Ω the ansatz

$$\mathbf{E} = \hat{\mathbf{E}}\,\Phi(z,t) + c.c. = \hat{\mathbf{E}}\,g(z)\,\mathrm{e}^{-i\Omega t} + c.c.\,, \tag{3.10}$$

applies with $g(z) = g^*(z)$ being the longitudinal envelope function. In the case of $\epsilon = \text{const.}$ we set $g(z) = \exp(+iK_z z)$ and obtain the phase-factor $\Phi(z,t)$ of a plane wave travelling in positive z direction.

Similar to (3.10) one has to split $\mathbf{P}$ into an amplitude and phase part, yet, consider that $\mathbf{P}$ is a nonlinear functional of $\mathbf{E}$ with respect to time. Using the following rules for the derivatives,

$$\partial_t^2\mathbf{E} = \Phi(z,t)\left(\partial_t^2 - 2i\Omega\partial_t - \Omega^2\right)\hat{\mathbf{E}}\,, \tag{3.11}$$

$$\partial_z\mathbf{E} = \Phi(z,t)\left(\partial_z + g'/g\right)\hat{\mathbf{E}}\,, \quad \partial_z^2\mathbf{E} = \Phi(z,t)\left(\partial_z^2 + 2g'/g\,\partial_z + g''/g\right)\hat{\mathbf{E}}\,, \tag{3.12}$$

we can transform the wave equation (3.1) into

$$\tilde{\mathcal{L}}[\hat{\mathbf{E}}]\, g\, \mathrm{e}^{-i\Omega t} + \tilde{\mathcal{L}}^*[\hat{\mathbf{E}}^*]\, g\, \mathrm{e}^{+i\Omega t} = -\frac{\epsilon_0^{-1}}{c^2}\partial_t^2 \mathbf{P}\left[\hat{\mathbf{E}}\, g\, \mathrm{e}^{-i\Omega t} + \hat{\mathbf{E}}^*\, g\, \mathrm{e}^{+i\Omega t}\right] , \tag{3.13}$$

with $\tilde{\mathcal{L}}$ being a linear differential operator acting on the slowly varying field amplitudes. Higher orders of $\mathbf{P}$ will mix $\hat{\mathbf{E}}$ and $\hat{\mathbf{E}}^*$. We identify the parts of $\mathbf{P}$ which oscillate with a phase factor $\exp(-i\Omega t)$ as only these parts have a dominant influence on the dynamics of $\hat{\mathbf{E}}$. Including term up to third order, we write

$$\mathbf{P}\left[\hat{\mathbf{E}}\, g\, \mathrm{e}^{-i\Omega t} + \hat{\mathbf{E}}^*\, g\, \mathrm{e}^{+i\Omega t}\right] \approx \underbrace{\left(\hat{\mathbf{P}}_1[\hat{\mathbf{E}}] + \hat{\mathbf{P}}_3[\hat{\mathbf{E}}]\right)}_{=:\,\hat{\mathbf{P}}[\hat{\mathbf{E}}]}\, g(z)\, \mathrm{e}^{-i\Omega t} \tag{3.14}$$

including the linear response term

$$\hat{\mathbf{P}}_1[\hat{\mathbf{E}}] = \int_0^\infty \mathrm{d}t_1 \boldsymbol{\chi}_1(t-t_1) \circ \hat{\mathbf{E}}(t_1)\, \mathrm{e}^{+i\Omega(t-t_1)} \tag{3.15}$$

and the cubic response term

$$\hat{\mathbf{P}}_3[\hat{\mathbf{E}}] = 3\, g^2 \int_0^\infty \mathrm{d}t_1 \ldots \int_0^\infty \mathrm{d}t_2\, \boldsymbol{\chi}_3(t-t_1, \ldots t-t_3) \circ \hat{\mathbf{E}}(t_1)\hat{\mathbf{E}}(t_2)\hat{\mathbf{E}}^*(t_3)\, \mathrm{e}^{+i\Omega(t-t_1-t_2+t_3)} . \tag{3.16}$$

The above approximation is justified as $\boldsymbol{\chi}_m$ can be expanded in derivatives of delta functions describing the fading memory of the material [83]. Thus, the kernel of the integral is getting smaller for times $t_1, \ldots, t_m$ far away in the past of t. We therefore look for the appearance of the $\exp(-i\Omega t)$ phase factor in the limit $t_1, \ldots, t_m \to t$. In that context even orders can be completely neglected due to fast rotating phases. This is the *rotating wave approximation* (RWA) which allows us to write

$$\tilde{\mathcal{L}}[\hat{\mathbf{E}}] \approx -\mathrm{e}^{+i\Omega t}\frac{\epsilon_0^{-1}}{c^2}\partial_t^2 \left(\hat{\mathbf{P}}\, \mathrm{e}^{-i\Omega t}\right) . \tag{3.17}$$

For now we assumed that $\mathbf{P}$ is a functional in time only and that $\mathbf{P}$ couples to $\mathbf{E}$ at all spatial points[5].

We recall that it is our aim to decouple the equations (3.8) and (3.7) in order to find a closed equation of motion for the transverse field amplitudes $\hat{\mathbf{E}}_\perp$ which no longer includes the longitudinal field components $\hat{E}_z$ in an explicit way. This problem can be solved by applying the paraxial approximation which we have to generalise in order to address some important characteristics typical for VCSEL cavity-structures. The key concept of

[5] we will modify this term later by introducing the longitudinal confinement function.

the paraxial approximation [80] consists in introducing a smallness parameter f and to formally expand $\hat{\mathbf{E}}$ and $\hat{\mathbf{P}}$ in such a way that (3.7) and (3.8) split up into a consistent hierarchy of equations describing the transverse and longitudinal wave-dynamics. The usual approach assumes, that a Gaussian pulse of width w travels along the longitudinal axis z. Then, the characteristic length of diffraction is given by $\ell = K_{\text{eff}}\, w^2$ and the time needed to pass that length is $\tau = \ell n_{\text{eff}}\,/c$. K_{eff} and n_{eff} are the effective wavelength and the effective refractive index experienced by the pulse while propagating through the waveguide structure. τ, ℓ and w are used to rescale the independent variables x, y, z and t,

$$t = \tau\tilde{t}\,, \quad z = \ell\tilde{z}\,, \quad x = w\tilde{x}\,, \quad y = w\tilde{y}\,. \tag{3.18}$$

The space and time derivatives acting on the amplitude functions $\hat{\mathbf{E}}$, $\hat{\mathbf{P}}$ can then be expressed in terms of the rescaled coordinates,

$$\partial_{x/y} = f\; K_{\text{eff}}\,\partial_{\tilde{x}/\tilde{y}}\,, \qquad \partial_z = f^2\; K_{\text{eff}}\,\partial_{\tilde{z}}\,, \qquad \partial_t = f^2\; cK_{\text{eff}}/n_{\text{eff}}\,\partial_{\tilde{t}} \tag{3.19}$$

where we introduce

$$f = \frac{w}{\ell} = (K_{\text{eff}} w)^{-1}\,. \tag{3.20}$$

Constant terms of the amplitudes are associated with f^0, while derivatives with respect to the transverse coordinates x, y are associated with f^1. Derivatives with respect to z or t are weighted with f^2. This ansatz is justified as long as $\Phi(z,t)$ covers the substantial variation of $\mathbf{E}$ over z and t. Although, more formal in its deviation the resemblance with the *slowly varying amplitude approximation* (SVAA) is obvious.

By applying the rules (3.11) and (3.12) to the equations (3.7), (3.8) and (3.9) we deduce an equation for the transverse field components,

$$\begin{aligned}
& -\epsilon\, c^{-2}\partial_t^2\hat{\mathbf{E}}_\perp - c^{-2}\epsilon_0^{-1}\partial_t^2\hat{\mathbf{P}}_\perp + 2ic^{-1}\epsilon_0^{-1}K_0\partial_t\hat{\mathbf{P}}_\perp \\
[f^3]\quad & -\nabla_\perp\partial_z\hat{E}_z \\
[f^2]\quad & +2ic^{-1}K_0\,\epsilon\,\partial_t\hat{\mathbf{E}}_\perp + \nabla_\perp^2\hat{\mathbf{E}}_\perp - \nabla_\perp\nabla_\perp\cdot\hat{\mathbf{E}}_\perp + 2g'/g\,\partial_z\hat{\mathbf{E}}_\perp + \epsilon_0^{-1}K_0^2\hat{\mathbf{P}}_\perp \\
[f^1]\quad & -\; g'/g\,\nabla_\perp\hat{E}_z \\
[f^0]\quad & +\; g''/g\,\hat{\mathbf{E}}_\perp + \epsilon K_0^2\hat{\mathbf{E}}_\perp \qquad\qquad = 0\,,
\end{aligned} \tag{3.21}$$

and for the longitudinal field components,

$$\begin{aligned}
& -\epsilon\, c^{-2}\partial_t^2\hat{E}_z - c^{-2}\epsilon_0^{-1}\partial_t^2\hat{P}_z + 2ic^{-1}\epsilon_0^{-1}K_0\partial_t\hat{P}_z \\
[f^3]\quad & -\nabla_\perp\cdot\partial_z\hat{\mathbf{E}}_\perp \\
[f^2]\quad & +2ic^{-1}K_0\,\epsilon\,\partial_t\hat{E}_z + \nabla_\perp^2\hat{E}_z + \epsilon_0^{-1}K_0^2\hat{P}_z \\
[f^1]\quad & -\; g'/g\,\nabla_\perp\cdot\hat{\mathbf{E}}_\perp \\
[f^0]\quad & +\; \epsilon K_0^2\hat{E}_z \qquad\qquad = 0\,.
\end{aligned} \tag{3.22}$$

The $\nabla \cdot \mathbf{D} = 0$ condition results in

$$\begin{aligned} & \epsilon_0^{-1}\partial_z P_z + \epsilon_0^{-1}\nabla_\perp \cdot \hat{\mathbf{P}}_\perp \\ [f^2] \quad & + \epsilon\, \partial_z \hat{E}_z + \epsilon_0^{-1} g'/g\, \hat{P}_z + \hat{\mathbf{E}}_\perp \cdot \nabla_\perp \epsilon \\ [f^1] \quad & + \epsilon\, \nabla_\perp \cdot \hat{\mathbf{E}}_\perp \\ [f^0] \quad & + (\, \partial_z \epsilon + g'/g\, \epsilon\,)\, \hat{E}_z \qquad\qquad = 0\,. \end{aligned} \tag{3.23}$$

$K_0 = \Omega/c$ denotes the vacuum wave-number.

As we want to compare orders of f we have to expand the field amplitudes $\hat{\mathbf{E}}_\perp$ and $\hat{E}_z$ by

$$\begin{aligned} \hat{\mathbf{E}}_\perp &= \underbrace{\hat{\mathbf{E}}_\perp^{(0)}}_{\sim f^0} + \underbrace{\hat{\mathbf{E}}_\perp^{(1)}}_{\sim f^1} + \underbrace{\hat{\mathbf{E}}_\perp^{(2)}}_{\sim f^2} + \dots \\ \hat{E}_z &= \underbrace{\hat{E}_z^{(0)}}_{\sim f^0} + \underbrace{\hat{E}_z^{(1)}}_{\sim f^1} + \underbrace{\hat{E}_z^{(2)}}_{\sim f^2} + \dots\,. \end{aligned} \tag{3.24}$$

The superscript indices in parentheses indicate the associated order of f. In the limit $f \to 0$ we are left with the zero'th order solution of a plane wave. This solution can only exist if the polarisation $\mathbf{P}$ vanishes and ϵ remains independent on x and y. We therefore assume that

$$\mathbf{P} \to f^2 \mathbf{P} \tag{3.25}$$

and

$$\epsilon = \epsilon^{(0)}(z) + \epsilon^{(2)}(x, y, z)\,. \tag{3.26}$$

This way we ensure that terms containing $\mathbf{P}$ are always smaller by two orders of magnitude than $\mathbf{E}$. In addition, any transverse dependence $\nabla_\perp \epsilon$ is a factor f^2 smaller than ϵ itself. We can now perform a classification of the different order terms as indicated in equation (3.22), (3.21) and (3.23) according to their order in f (as indicated in brackets).

In order zero of f it follows, that (3.21) the relation

$$(g''/g + \epsilon^{(0)} K_0^2)\, \hat{\mathbf{E}}_\perp^{(0)} = 0\,. \tag{3.27}$$

$E_\perp^{(0)}$ is of arbitrary value as long as the expression in parentheses vanishes. This means that $g(z)$ has to fulfil the time independent wave-equation

$$g''(z) + K_0^2 \epsilon^{(0)} g(z) = 0\,. \tag{3.28}$$

Which is an eigenvalue equation associating $g(z)$ with K_0. From (3.22) we deduce $E_z^{(0)} = 0$. This solution corresponds to the case of plane wave-fronts propagating through

the media with a dielectric constant $\epsilon^{(0)}(z)$. The associated phase function is then given by $g(z)\exp(-i\Omega t)$. The order zero of the divergence relation can be satisfied without further restrictions.

For the first order we derive the relation

$$E_z^{(1)} = R\,\nabla_\perp \cdot \mathbf{E}_\perp^{(0)}\,, \qquad R = 1/\epsilon^{(0)}\,K_0^{-2} g'/g \tag{3.29}$$

emerges from the longitudinal part. Furthermore, the divergence relation leads to the equation

$$\epsilon^{(0)}\,\nabla_\perp \cdot \hat{\mathbf{E}}_\perp^{(0)} + (\,\partial_z \epsilon^{(0)} + g'/g\,\epsilon^{(0)}\,)\hat{E}_z^{(1)} = 0\,. \tag{3.30}$$

By eliminating $\hat{E}_z^{(1)}$ from the two above equations we see that the condition

$$F\,\nabla_\perp \cdot \hat{\mathbf{E}}_\perp^{(0)} = 0, \quad F = (1 + g'/g\,R)\,\epsilon^{(0)} + R\,\partial_z \epsilon^{(0)} \tag{3.31}$$

has to be satisfied. In general F is not equal zero which means $\nabla_\perp \cdot \hat{\mathbf{E}}_\perp^{(0)} = 0$ and $\hat{E}_z^{(1)} = 0$. The transverse equation of first order is fulfilled due to (3.28).

Eventually, the second order of (3.21) constitutes an evolution equation for $\hat{\mathbf{E}}_\perp^{(0)}$. It reads

$$2ic^{-1}K_0\epsilon^{(0)}\,\partial_t \hat{\mathbf{E}}_\perp^{(0)} + 2g'/g\,\partial_z \hat{\mathbf{E}}_\perp^{(0)} = -\nabla_\perp^2 \hat{\mathbf{E}}_\perp^{(0)} - \epsilon^{(2)} K_0^2 \hat{\mathbf{E}}_\perp^{(0)} - \epsilon_0^{-1} K_0^2 \hat{\mathbf{P}}_\perp^{(2)}\,. \tag{3.32}$$

Similar to the first order we obtain the longitudinal relation

$$\hat{E}_z^{(2)} = R\,\nabla_\perp \cdot \hat{\mathbf{E}}_\perp^{(1)}\,, \tag{3.33}$$

while the divergence relation now demands

$$\epsilon^{(0)}\,\nabla_\perp \cdot \hat{\mathbf{E}}_\perp^{(1)} + (\,\partial_z \epsilon^{(0)} + g'/g\,\epsilon^{(0)}\,)\hat{E}_z^{(2)} + \hat{\mathbf{E}}_\perp^{(0)} \cdot \nabla_\perp \epsilon^{(2)} = 0\,. \tag{3.34}$$

The last two equations show that in contrast to $\hat{\mathbf{E}}_\perp^{(0)}$ the transverse divergence of $\hat{\mathbf{E}}_\perp^{(1)}$ does not vanish as we can rewrite these equations to

$$F\,\nabla_\perp \cdot \hat{\mathbf{E}}_\perp^{(1)} = -\hat{\mathbf{E}}_\perp^{(0)} \cdot \nabla_\perp \epsilon^{(2)}\,. \tag{3.35}$$

Equation (3.32) describes how $\hat{\mathbf{E}}_\perp^{(0)}$ develops in time, yet, we have to keep in mind that (3.31) restricts the space of possible solutions at all times to those consistent with the $\nabla \cdot \hat{\mathbf{E}}_\perp^{(0)} = 0$ condition. In cylindrical coordinates this means, that

$$\partial_r \left(r \hat{E}_r^{(0)} \right) + \partial_\phi \hat{E}_\phi^{(0)} = 0\,. \tag{3.36}$$

By extending the approximation to the third order the equation

$$\begin{aligned} &2ic^{-1}K_0\epsilon^{(0)}\,\partial_t \hat{\mathbf{E}}_\perp^{(1)} + 2g'/g\,\partial_z \hat{\mathbf{E}}_\perp^{(1)} = \\ &\quad - \nabla_\perp^2 \hat{\mathbf{E}}_\perp^{(1)} - \epsilon^{(2)} K_0^2 \hat{\mathbf{E}}_\perp^{(1)} - F^{-1}\,(1 + g'/g\,R)\,\nabla_\perp \left(\hat{\mathbf{E}}_\perp^{(0)} \cdot \nabla_\perp \epsilon^{(2)} \right) - \epsilon_0^{-1} K_0^2 \hat{\mathbf{P}}_\perp^{(3)} \end{aligned} \tag{3.37}$$

for the amplitude $\hat{\mathbf{E}}_\perp^{(1)}$ drops out. This equation is similar to (3.32) but contains an additional term that adds a contribution which is important in case of a spatially dependent dielectric structure. After adding (3.32) to (3.37) and a multiplication by $-iD_p$ we finally obtain the equation

$$\begin{aligned}&\frac{n^2}{n_{\text{eff}}^2}\, v_{\text{eff}}^{-1}\, \partial_t \hat{\mathbf{E}}_\perp + \eta\, \partial_z \hat{\mathbf{E}}_\perp = \\ &\quad iD_p \nabla_\perp^2 \hat{\mathbf{E}}_\perp + iK_0 \nu \delta n\, \hat{\mathbf{E}}_\perp + 2iD_p\, \sigma \nabla_\perp \left(\hat{\mathbf{E}}_\perp \cdot \nabla_\perp \delta n\right) + i\kappa \hat{\mathbf{P}}_\perp\,.\end{aligned} \tag{3.38}$$

where we defined $\hat{\mathbf{E}}_\perp = \hat{\mathbf{E}}_\perp^{(0)} + \hat{\mathbf{E}}_\perp^{(1)}$.

For the sake of a more lucid style we performed the substitutions

$$\begin{aligned} &v_{\text{eff}} = c/n_{\text{eff}}\,, && K_{\text{eff}} = K_0 n_{\text{eff}}\,, \\ &D_p = (2K_{\text{eff}})^{-1}\,, && \kappa = \epsilon_0^{-1} K_0^2 D_p = \epsilon_0^{-1} K_0 (2n_{\text{eff}})^{-1} \end{aligned} \tag{3.39}$$

which introduce the effective velocity v_{eff}, the effective k-vector K_{eff} the diffraction constant D_p and the media coupling constant κ. Furthermore, we replaced the dielectric constants $\epsilon^{(0)}(z)$ and $\epsilon^{(2)}(x,y,z)$ with the refractive index values $n(z)$ and $\delta n(x,y,z)$. From $(n+\delta n)^2 = \epsilon^{(0)} + \epsilon^{(2)}$ and $n^2 = \epsilon^{(0)}$ one can show that

$$n = \sqrt{\epsilon^{(0)}} \qquad \text{and} \qquad \delta n \approx \epsilon^{(2)}/(2n)\,. \tag{3.40}$$

Finally, the following three z-dependent parameters have been introduced:

$$\nu = \frac{n}{n_{\text{eff}}}\,, \quad \sigma = \frac{1}{n}\left(\frac{1}{1+L}\right)\,, \quad L = \frac{g'/g}{(nK_0)^2 + (g'/g)^2}\left(\frac{\partial_z n^2}{n^2}\right)\,. \tag{3.41}$$

As the denominator of L turns out to be greater than one we can neglect L in the denominator of σ and assume $\sigma \approx n^{-1}$.

The electrical field amplitude $\hat{\mathbf{E}}_\perp = \hat{\mathbf{E}}_\perp^{(0)} + \hat{\mathbf{E}}_\perp^{(1)}$ is exact up to an error of order two. We can now exploit the fact that

$$\nabla_\perp \left(\hat{\mathbf{E}}_\perp \cdot \nabla_\perp \epsilon^{(2)}\right) \approx \nabla_\perp \left(\hat{\mathbf{E}}_\perp^{(0)} \cdot \nabla_\perp \epsilon^{(2)}\right) + o(f^4) \tag{3.42}$$

and use

$$\hat{\mathbf{P}}_\perp = \hat{\mathbf{P}}_\perp^{(2)} + \hat{\mathbf{P}}_\perp^{(3)} = \Phi^{-1}\mathbf{P}[\hat{\mathbf{E}}_\perp \Phi] + o(f^4) \tag{3.43}$$

for the dielectric polarisation of the medium. This means that if we insert the full polarisation response function the error is of order f^4 which is well beyond the order of our approximation.

As mentioned before, the phase function g has to be chosen as a solution of the longitudinal equation

$$g''(z) + K_0^2 n(z)^2 g(z) = 0 \ . \tag{3.44}$$

In Appendix A we give solutions for this equation for the most simple resonator, the dielectric Fabry-Pérot. In Section 3.4 solutions for the more complicated structure of a VCSEL structure will be discussed.

We note, that in the special case $n \to n_{\text{eff}}$ and $\delta n = 0$ the equation of motion (3.38) takes the well known form

$$v_{\text{eff}}^{-1}\, \partial_t \hat{\mathbf{E}}_\perp + \eta\, \partial_z \hat{\mathbf{E}}_\perp = i D_p \nabla_\perp^2 \hat{\mathbf{E}}_\perp + i\kappa \hat{\mathbf{P}}_\perp \ . \tag{3.45}$$

This equation is commonly accepted in literature to describe the phase-sensitive dynamics of the optical field (see e.g. [**?**,84]). Two of the associated solutions are

$$g^\pm = \exp(\pm i K_{\text{eff}} z) \quad \text{for} \quad \eta = \pm 1 \ , \tag{3.46}$$

which are equivalent to plane waves propagating in $\pm z$ direction. Note, that without appropriate boundary conditions this result does not apply to any resonator structure as it is based on the assumption of an infinite sized system with an homogeneous refractive index.

3.3 Longitudinal Mean-Field Approximation

According to ansatz (3.10), $\hat{\mathbf{E}}$ is the envelope function of a wave-packet which shows a relatively weak dependence on z and t. The phase function $g(z)$, on the other hand, is the solution of the one dimensional wave equation (3.44) and therefore oscillates fast with varying z. Without loss of generality we assume the resonator structure extending from $z = z^-$ to $z = z^+$ with length $L = z^+ - z^-$. In order to eliminate the direction of propagation from the wave equation we have to perform the average over a resonator round-trip. For this purpose we introduce the (averaging) operator

$$\big\langle \dots \big\rangle_z = \frac{1}{L} \int_{z^-}^{z+} |g(z)|^2 dz \dots \quad ; \qquad z^+ - z^- = L \ , \tag{3.47}$$

with $g(z)$ being normalised to 1. This means $< 1 >= 1$ or

$$\frac{1}{L} \int_{z^-}^{z+} |g(z)|^2 dz = 1 \ . \tag{3.48}$$

After applying $\langle \dots \rangle_z$ to (3.38) and assuming $\partial_z \hat{\mathbf{E}}_\perp \approx 0$ or $\hat{\mathbf{E}}_\perp = \hat{\mathbf{E}}_\perp(x,y,t)$ the equation of motion simplifies to

$$\begin{aligned} \left\langle \frac{n^2}{n_{\text{eff}}^2} \right\rangle_z v_{\text{eff}}^{-1}\, \partial_t \hat{\mathbf{E}}_\perp &= iD_p \nabla_\perp^2 \hat{\mathbf{E}}_\perp + iK_0 \langle \nu \delta n \rangle_z\, \hat{\mathbf{E}}_\perp \\ &+ 2iD_p\, \nabla_\perp \left(\hat{\mathbf{E}}_\perp \cdot \nabla_\perp \langle \sigma \delta n \rangle_z \right) + i\kappa \langle \zeta \rangle_z \hat{\mathbf{P}}_\perp \,. \end{aligned} \tag{3.49}$$

A possible functional dependence of $\hat{\mathbf{P}}_\perp$ on z was separated into a *confinement* function. Consequently, $\zeta(z)$ is one at all z points where active material is present, otherwise it is zero.

Up to now n_{eff} has been an arbitrary parameter. We chose to fix n_{eff} by assuming

$$n_{\text{eff}}^2 = \frac{1}{L} \int_{z^-}^{z+} |g(z)|^2 n^2(z) dz \tag{3.50}$$

and obtain the a simple expression for the energy density integrated over z,

$$\mathcal{E}_\perp := \frac{1}{L} \int_{z^-}^{z+} |\, \hat{\mathbf{E}}_\perp\, g(z)\, \mathrm{e}^{-i\Omega t}\, |^2 \epsilon(z) dz = n_{\text{eff}}^2 |\hat{\mathbf{E}}_\perp|^2 \,. \tag{3.51}$$

Concerning the longitudinal and the transverse components, the original dynamics of the electromagnetic fields appears utterly decoupled . $g(z)$, the longitudinal phase function is calculated from

$$g''(z) + K_0^2 n(z)^2\, g(z) = 0 \,, \tag{3.52}$$

an eigenvalue equation with eigenvalue being $\Omega = cK_0$. The eigenfunction $g(z)$ reflects the longitudinal dielectric structure via its z-dependent phase and intensity values. It is important to note, that Ω is always complex until we have a prefect lossless resonator. We set

$$\Omega = \omega - i\,\gamma \tag{3.53}$$

with γ being the damping value associated with the mode characterised by the frequency ω. In paricular, Ω enters the ansatz (3.10) as a complex quantity. In order to describe the resonator losses explicitly we modify this ansatz by writing

$$\mathbf{E}_\perp = \hat{\mathbf{E}}_\perp g(z) \mathrm{e}^{-i\,\omega\, t} \mathrm{e}^{-\gamma\, t} = \bar{\mathbf{E}}_\perp g(z) \mathrm{e}^{-i\,\omega\, t} \,, \tag{3.54}$$

which means that $\bar{\mathbf{E}}_\perp$ comprises an explicit decay over time. For the field amplitude $\bar{\mathbf{E}}_\perp$ we can derive from (3.49) the equation

$$\begin{aligned} v_{\text{eff}}^{-1}\, \partial_t \bar{\mathbf{E}}_\perp &= -\gamma_{\text{res}} \bar{\mathbf{E}}_\perp + iD_p \nabla_\perp^2 \bar{\mathbf{E}}_\perp + iK_0 \langle \nu \delta n \rangle_z\, \bar{\mathbf{E}}_\perp \\ &+ 2iD_p\, \nabla_\perp \left(\bar{\mathbf{E}}_\perp \cdot \nabla_\perp \langle \sigma \delta n \rangle_z \right) + i\kappa \Gamma_z \bar{\mathbf{P}}_\perp \,. \end{aligned} \tag{3.55}$$

The resonator losses per length unit and the *longitudinal confinement factor* are defined by

$$\gamma_{\mathrm{res}} = v_{\mathrm{eff}}^{-1}\gamma\,, \quad \Gamma_z = \langle\zeta\rangle_z\ . \tag{3.56}$$

Having in mind the picture of a resonator of length L and two mirrors with reflectivities R_1, R_2 at the ends one can write

$$\gamma_{\mathrm{res}} = -\frac{\ln R}{L} = -\frac{\ln(R_1 R_2)}{2L} \tag{3.57}$$

and thereby associate a reflectivity R with the decay rate γ_{res}. Another common entity which quantifies the resonator quality is the *cavity Q-factor*, $Q = \omega/\gamma$.

Because of (3.53) all the Ω dependent parameters in (3.55) like e.g. D_p have to be considered being complex quantities. For well confined modes one can assume $\gamma \ll \omega$. In this case it is possible to neglect the influence of the imaginary part of Ω on the parameters by setting $\Omega \approx \omega$.

An analytic solution of the eigenvalue equation (3.52) is only possible for some simple cases like for the dielectric Fabry-Pérot covered in Appendix A. Solutions associated with more complex dielectric structures are numerically accessible with the help of generic eigenvalue solver, transfer-matrix methods [85] or even time domain solvers [37, 39]. In the following section we will use the longitudinal mode solver described in Appendix C.3 in order to calculate the modes of a VCSEL structure.

3.4 Application to VCSEL Resonators

The resonator of a VCSEL – like depicted in Figure 3.1 – consists of two stacks of Bragg-reflecting $\lambda/4$-layers, the top and bottom DBR (*distributed Bragg reflectors*). With the insertion of a defect of length $m\lambda$ in between these two DBR stacks an optical microcavity is formed. Typically, $m = 1$, but higher values are also common. In order to enhance the optical confinement and to concentrate the pumping current closer to the axis, an *oxide-aperture* is embedded in the top DBR stack. The oxide-aperture represents one of the important optical elements, which is taken into consideration by the δn terms which appears in our equation of motion.

In difference to bulk material, edge-emitting lasers, quantum-well layers positioned at the mode maxima are constituing the active-material. Hence, only a small part of the defect-zone consists of active material, a fact, which we pay respect to by the calculation of the longitudinal confinement factor Γ_z.

We setup $g(z)$ as the lowest order defect-mode is the mode with the best longitudinal optical confinement. In the transmission spectra this mode appears as the *cavity-dip*. An analytical calculation of $g(z)$ is not practical as the system of equations to be solved

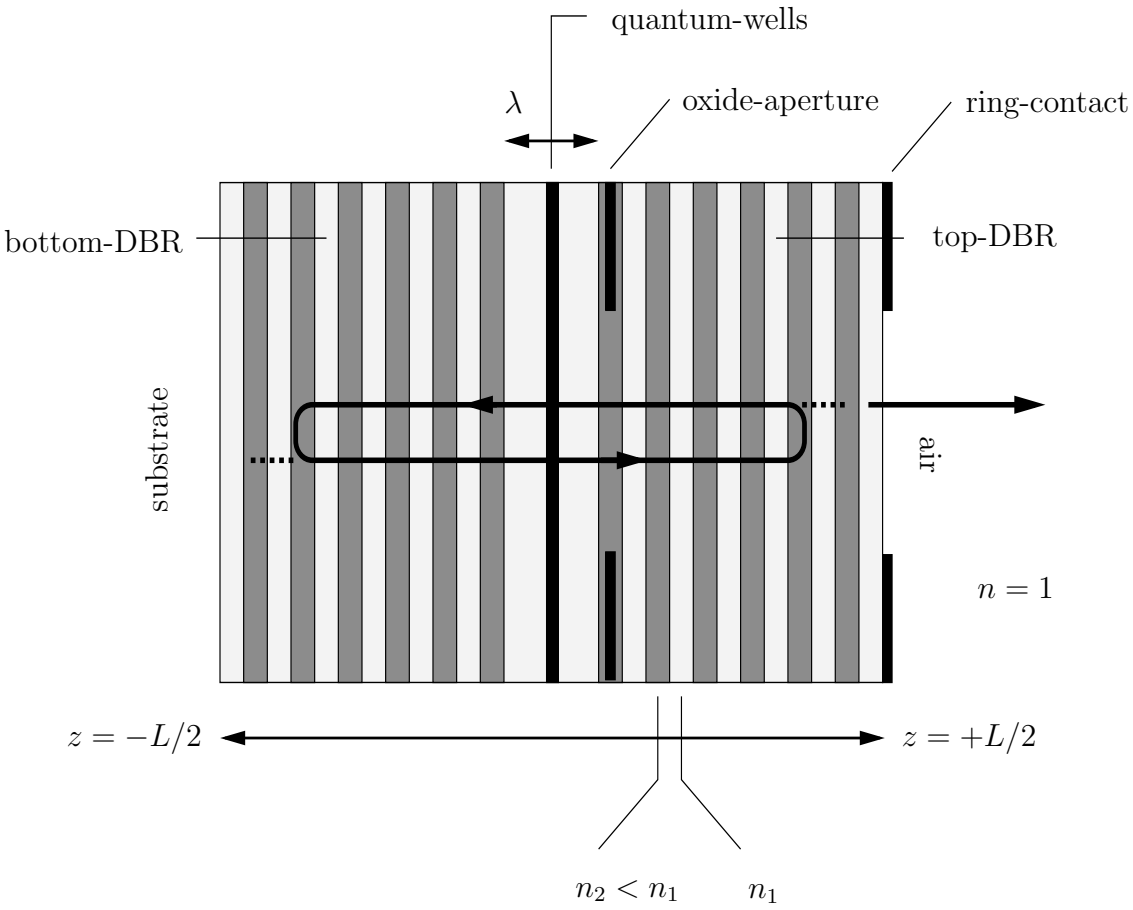

Figure 3.1: Schematic cut through a VCSEL resonator structure. A defect of length λ is enclosed in between the top- and bottom-DBR. Positioned in the mode maxima there are one or more active quantum-well layers (typically 1-5). Depending on application Al-GaAs-VCSELs feature several (10 to 30) Al-GaAs/GaAs mirror pairs with $n_1 \approx 3.5$ and $n_2 \approx 3.1$. The oxide aperture serves both, to confine the carriers injected by the ring-contact to the centre of the structure and to confine the optical field via a radial refractive index change (index guiding).

may become large depending on the number of layers. Instead, we utilise the numeric eigenvalue solver presented in APPENDIX C.3 to obtain $g(z)$ from (3.52). Together with $g(z)$ we can calculate the effective parameters γ_{res}, Γ_z, $\langle \nu \delta n \rangle_z$ and $\langle \sigma \delta n \rangle_z$ for various structures (see FIGURE 3.2, FIGURE 3.4).

The oxide-aperture is a thin, transversely structured layer. Firstly, we separate the functional dependencies, substitute

$$\delta n \to \Theta(z) \delta n^{\text{g}}(x, y) \, . \tag{3.58}$$

$\Theta(z)$ is a step function which is one at z-points where the layer is localised and equal to

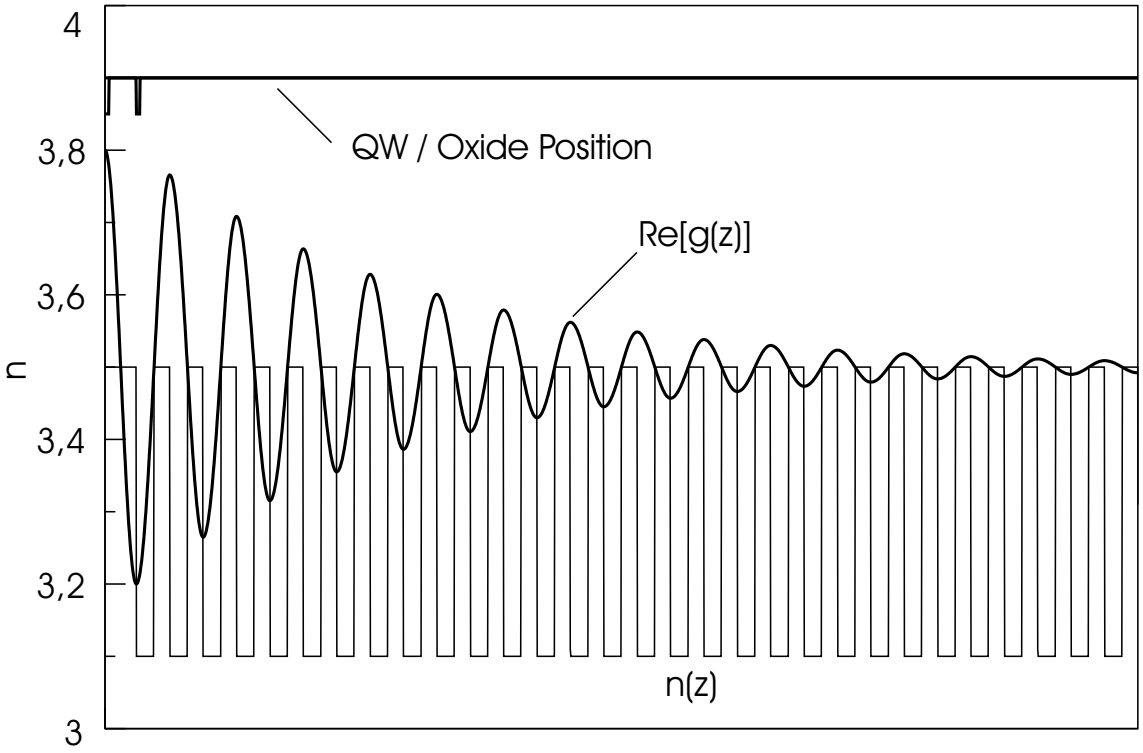

Figure 3.2: Longitudinal optical mode $g(z)$ plotted together with the index structure for one half of a VCSEL resonator. Refractive index contrast is $n_1/n_2 = 3.5/3.1$. The line with the two small dips mark the position and the width of the active material (left dip) and the oxide aperture (right dip). The oxide aperture is positioned at the maximum of the mode (anti-node position).

zero at all the other z-points. This enables us to simplify the respective averages to

$$\langle \nu \delta n^{\mathrm{g}} \rangle_z (x,y) = \langle \nu \Theta \rangle_z \, \delta n^{\mathrm{g}}(x,y) \,, \tag{3.59}$$

$$\langle \sigma \delta n^{\mathrm{g}} \rangle_z (x,y) = \langle \sigma \Theta \rangle_z \, \delta n^{\mathrm{g}}(x,y) \approx \left\langle n^{-1} \Theta \right\rangle_z \delta n^{\mathrm{g}}(x,y) \,. \tag{3.60}$$

Moving the oxide-aperture closer towards a node of the mode $g(z)$ (*node position*), the above averages will shrink. FIGURE 3.5 shows the calculated results which illustrate the dependence of these paramters on the number of mirrors and the exact position of the oxide-aperture.

3.5 Influence of the Crystal Structure: Birefringence and Dichroism

Up to this point we assumed the dielectric constant ϵ to be a scalar-valued function of space. Depending on the crystal structure of the optically passive material the dielectric function can also be a tensor. Although Gallium Arsenide, like most semiconductor materials has a cubic zinc-blend crystal structure and usually does not feature intrinsic

birefringence, the dielectric tensor becomes anisotropic if an electric field is imposed. This is due to the well-known linear electro-optic effect, which can be exploited to build Gallium Arsenide beam modulators in the near-infrared [86]. In VCSEL cavities the electro-optic is claimed to be responsible for linear birefringence and influences the polarisation suppression and switching behaviour [87, 88]. As the carriers injected along the z-axis are driven by a static electric field $\mathcal{E}$ (typically $\sim 10^7\,\mathrm{V\,m^{-1}}$) and strong static fields emerge from the doping-levels of the Bragg mirrors the dielectric tensor becomes anisotropic and destroys the intrinsic rotational symmetry of the optical field [89, 90]. The transverse field components E_x and E_y become directly coupled.

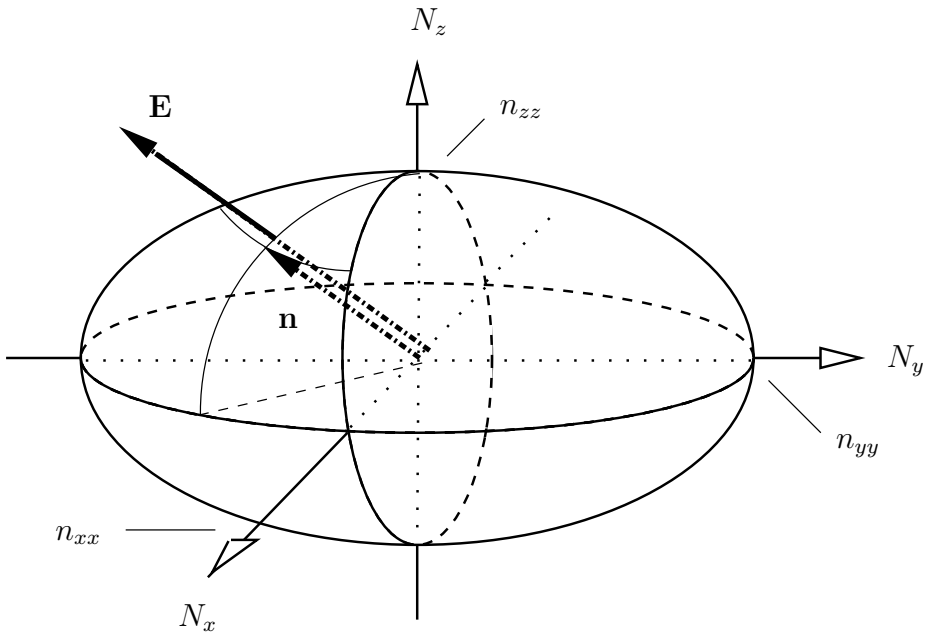

Figure 3.3: Sketch of the index ellipsoid as given by equation (3.65). GaAs becomes optically biaxial if an electric field $\mathcal{E}_z$ is applied along the z-axis. The refractive index for waves propagating along the z-direction is $(n_0 + 1/2n^3 r_{41}\mathcal{E}_z)$ for the x-polarised part and $(n_0 - 1/2n^3 r_{41}\mathcal{E}_z)$ for the y-polarised part of the E-vector.

In order to incorporate anisotropy into our model, we assume the anisotropic parts of ϵ to be relatively small compared to the isotropic part. In that case $\epsilon^{(0)} = n^2$ which we introduced by equation (3.40) is still considered a scalar entity, while we split $\epsilon^{(2)}$ into a scalar geometrical part $\delta\epsilon^{\mathrm{g}}(x, y, z)$ – accounting for a transverse refractive index structure, e.g. for the oxide-aperture – and into a tensor-valued crystallographic part $\delta\boldsymbol{\epsilon}^{\mathrm{c}}$ which is anisotropic yet homogeneous in space

$$\boldsymbol{\epsilon}(x, y, z) = \boldsymbol{\epsilon}^{(0)} + \boldsymbol{\epsilon}^{(2)}(x, y, z) = \underbrace{\big(\epsilon + \delta\epsilon^{\mathrm{g}}(x, y, z)\big)}_{=:\,\epsilon_0}\,\mathbf{1} + \delta\boldsymbol{\epsilon}^{\mathrm{c}}\,. \tag{3.61}$$

For structures grown on a [001] substrate (surface of epitaxial growth), we assume the optical axis $\mathbf{e}$ to be aligned along the [001]-axis. For Gallium Arsenide material the $\delta\boldsymbol{\epsilon}^{\mathrm{c}}$

part vanishes without an external electrical field $\mathcal{E}$ and the indicatrix at a given point in space is given by

$$\frac{N_x^2}{\epsilon_0} + \frac{N_y^2}{\epsilon_0} + \frac{N_z^2}{\epsilon_0} = 1\,. \tag{3.62}$$

The electro-optic effect causes changes of the dielectric constants by the magnitude

$$\Delta\left(\frac{1}{\epsilon}\right)_i = \sum_{j=1,2,3} r_{ij}\mathcal{E}_j\,, \qquad i = 1\ldots 6 \tag{3.63}$$

with ($\mathcal{E}_1$, $\mathcal{E}_2$, $\mathcal{E}_3$) being the components of the electric field ($\mathcal{E}_x$, $\mathcal{E}_y$, $\mathcal{E}_z$) [91]. The index $j = 1\ldots 6$ enumerates the entries of the symmetric $\Delta(1/\epsilon)$ matrix ($1 \leftrightarrow xx$, $2 \leftrightarrow yy$, $3 \leftrightarrow zz$, $4 \leftrightarrow yz$, $5 \leftrightarrow xz$, $6 \leftrightarrow xy$). r_{ij} are the components of the electro-optic tensor $\mathbf{R}$. In the case of III-V semiconductors with cubic zinc-blend structure ($\bar{4}3m$ symmetry) like GaAs or InP there are three identical non-vanishing components, $r_{41} = r_{52} = r_{63}$ [91]. Another literature value for Gallium Arsenide is $r_{41} \sim 1.4 \cdot 10^{-3}\,\mathrm{nm/V}$. Assuming $\mathcal{E}_x = \mathcal{E}_y = 0$ and $\mathcal{E}_z \neq 0$, the index ellipsoid is given by

$$\frac{N_x^2}{\epsilon_0} + \frac{N_y^2}{\epsilon_0} + \frac{N_z^2}{\epsilon_0} + 2\frac{N_x N_y}{\epsilon_0} r_{41}\mathcal{E}_z = 1\,. \tag{3.64}$$

According to [89], [91] we can perform a transformation to a coordinate system where $\mathbf{e}_x$ and $\mathbf{e}_y$ are oriented along the [011] and [01$\bar{1}$] axes (the cleavage planes) instead of [100] and [010]. In that coordinate frame the indicatrix reads

$$\left(\frac{1}{\epsilon_0} + r_{41}\mathcal{E}_z\right) N_x^2 + \left(\frac{1}{\epsilon_0} - r_{41}\mathcal{E}_z\right) N_y^2 + \frac{N_z^2}{\epsilon_0} = 0\,. \tag{3.65}$$

The resulting index ellipsoid is drafted in FIGURE 3.3 and shows three different optical axes. By identifying the denominators with the squares of the refractive index components we obtain in good approximation

$$(\delta\mathbf{n}^{\mathrm{c}})_{xx} = -\frac{1}{2}n^3 r_{41}\mathcal{E}_z\,, \quad (\delta\mathbf{n}^{\mathrm{c}})_{yy} = +\frac{1}{2}n^3 r_{41}\mathcal{E}_z\,, \quad \text{but} \quad (\delta\mathbf{n}^{\mathrm{c}})_{ij} = 0 \quad \text{otherwise.} \tag{3.66}$$

We may now split the refractive index into a sum of parts

$$\mathbf{n}(x,y,z) = \big(n + \Theta(z)\delta n^{\mathrm{g}}(x,y)\big)\mathbf{1} + \delta\mathbf{n}^{\mathrm{c}}\,, \tag{3.67}$$

with $n^2 = \epsilon$ and

$$\Theta\,\delta n^{\mathrm{g}} = \delta\epsilon^{\mathrm{g}}/(2n)\,. \tag{3.68}$$

By inserting this result into equation (3.55) one can show that

$$\begin{aligned} v_{\mathrm{eff}}^{-1}\,\partial_t\bar{\mathbf{E}}_\perp = {} & -\gamma_{\mathrm{res}}\bar{\mathbf{E}}_\perp + iD_p\nabla_\perp^2\bar{\mathbf{E}}_\perp + iK_0\,\langle\nu\Theta\rangle_z\,\delta n^{\mathrm{g}}\,\bar{\mathbf{E}}_\perp + iK_0\,\langle\nu\rangle_z\,\delta\mathbf{n}^{\mathrm{c}}\cdot\bar{\mathbf{E}}_\perp \\ & + 2iD_p\,\langle\sigma\Theta\rangle_z\,\nabla_\perp\big(\bar{\mathbf{E}}_\perp\cdot\nabla_\perp\delta n^{\mathrm{g}}\big) + i\kappa\Gamma_z\bar{\mathbf{P}}_\perp\,. \end{aligned} \tag{3.69}$$

This equation includes both, the impact of the oxide aperture as well as the influence of birefringence due to the electro-optic effect. Most structural and material specific parts known to be relevant for the optical field dynamics in VCSEL cavities are combined in this equation.

We do not fail to mention, that it is not only the electro-optic effect which gives reason to symmetry-breaking. Several other mechanisms like stress [92], anisotropies [75], asymmetric current injection [93], or aperture shape have been identified to have an impact on polarisation-dynamics in particular in cases where the internal or the applied electrical fields are comparatively weak. An effect that always has to be taken into consideration is the nonlinear birefringence due to spin-polarisation of the medium. This will be a topic of Chapter 4.

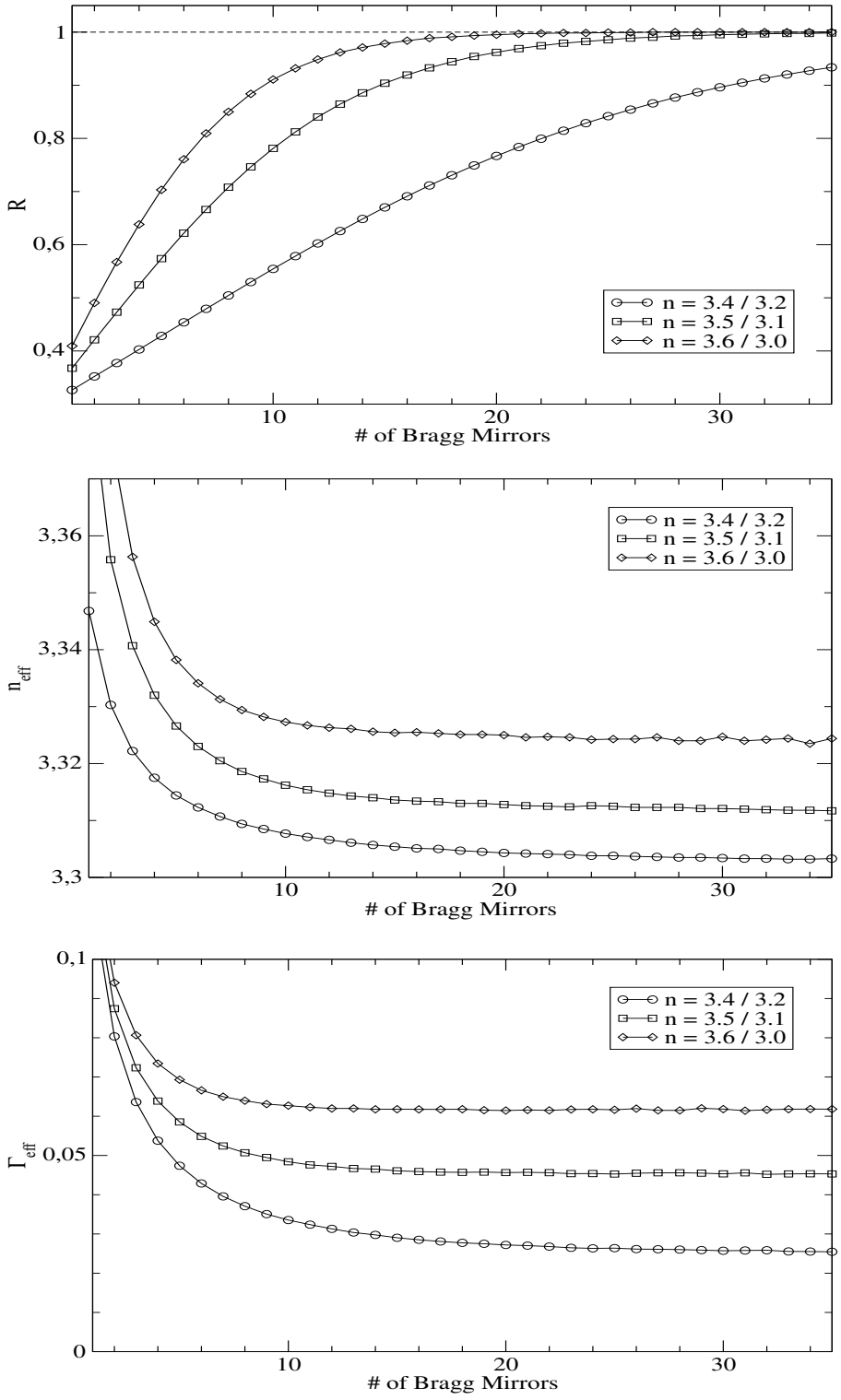

Figure 3.4: Numerically calculated values for the reflectivity R, the effective refractive index n_{eff} and the longitudinal confinement factor Γ_z. The x-axis labels the number of Bragg layers of the top and bottom mirror. The graphs shown were calculated for three different index contrasts $n_1 = 3.6 - 0.1 \cdot x$ and $n_2 = 3.0 + 0.1 \cdot x$ with $x = 0, 1, 2$.

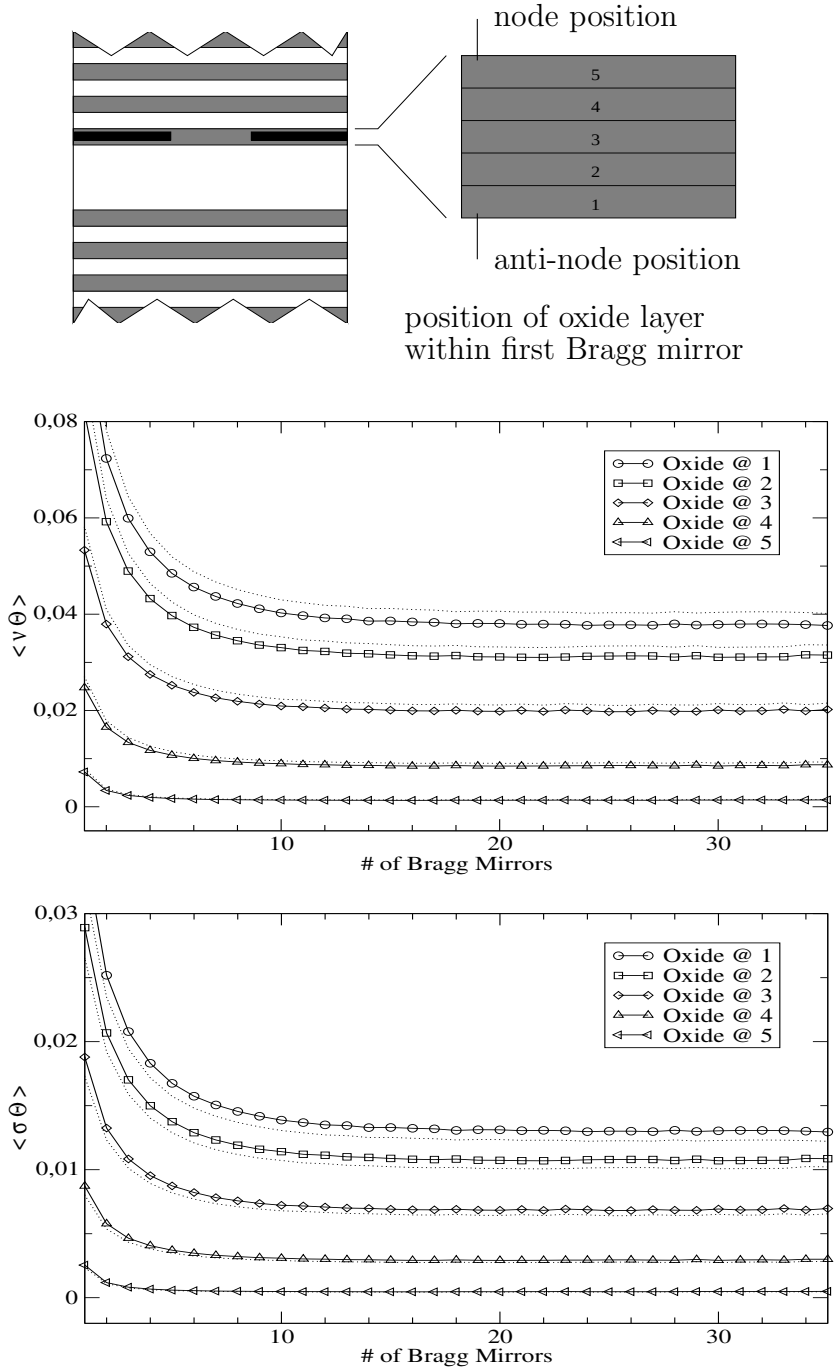

Figure 3.5: Numerically calculated values for $\langle \nu\Theta \rangle_z$ and $\langle \sigma\Theta \rangle_z$ plotted over the number of Bragg layers. Depending on the position of the oxide-aperture (see top illustration) the results vary. The closer the oxide-aperture is positioned towards a node (position 5) the smaller the resulting values. Clearly, the largest values are found for position 1 (close to the mode maxima). The dashed line indicates the values of the factorised averages, that is $\langle \nu \rangle_z \langle \Theta \rangle_z$ and $\langle \sigma \rangle_z \langle \Theta \rangle_z$. Their deviation from the exact values is within a few percent.

4 Carrier Dynamics of Quantum-Well VCSELs

4.1 Introduction

In CHAPTER 2 a Lorentzian material model had been introduced in order to describe the active laser material response. Generally, such an approach is suitable for lasers characterised by isolated weakly interacting active lasing centres (e.g. gas lasers) for which it can be assumed that the optical transitions occur between discrete energetic levels [94]. A semiconductor laser, however, is a solid state laser with the atoms of the active material being tightly bound together to form a crystal. With the atoms being in strong interaction with each other a separate treatment of individual laser centres is inadequate: The outer, optically active electrons no longer occupy individual atomic orbits but are delocalised over the valence and conduction energy-bands. High electron densities and the strong exchange- and Coulomb-interaction between the electrons call for a more adequate description of the active material which is inherently capable of explaining effects caused by and associated with spectral hole burning and carrier-carrier scattering.

The material model presented here, is based on the quantum-mechanical many-particle picture. Aspects of the underlying theory – including quantum-field theory of solids, many-body theory, quantum-kinetic theory or mesoscopic quantum-optics – can be found summarised in textbooks [43, 46, 47, 58, 95] and a series of publications [35, 72, 81, 96, 97]. We will unify parts of the theory to build a microscopic dynamical model for the carriers of the active semiconductor quantum-well material of a VCSEL. The resulting equations, the *4-band semiconductor Bloch equations* are an extension of the traditional semiconductor-Bloch equations as they include the influence of spin and angular momentum. On this level, the description is not only limited to the mesoscopic response functions, that is how the polarisation $\mathbf{P}[\mathbf{E}, N]$ and the carrier generation rate $G[\mathbf{E}, N]$ evolve in time but give, in combination with the numerical simulations carried out in the next chapter, a deep and instructing insight in the dynamics of the underlying microscopic processes and effects.

The basic semiconductor-Bloch equations may be derived from the Hamiltonian

$$\hat{\mathcal{H}} = \hat{\mathcal{H}}_0 + \hat{\mathcal{H}}_{\text{c-L}} + \hat{\mathcal{H}}_{\text{I}} \tag{4.1}$$

and the wave-function $\Psi(\mathbf{r}, t)$ whose dynamics is determined by the corresponding Schrödinger equation. $\hat{\mathcal{H}}_0$ is the sum of the kinetic and potential energy of an electron trapped

in the quantum-well structure,

$$\hat{\mathcal{H}}_0 = \frac{\hat{\mathbf{p}}^2}{2m_0} + \mathcal{V}_0(\hat{\mathbf{r}}) + \mathcal{V}(\hat{z})\,. \tag{4.2}$$

$\mathcal{V}_0(\mathbf{r}) = \mathcal{V}_0(\mathbf{r}+\mathbf{R})$ is the periodic lattice potential and $\mathcal{V}(z)$ the confinement-potential of the quantum-well which is assumed to be a step-function in z. We introduced the three-dimensional vector-operators $\mathbf{r} = (\mathbf{r}_\perp, \mathbf{r}_z)$ and $\hat{\mathbf{p}} = (\hat{p}_\perp, \hat{p}_z)$. Further parts of $\hat{\mathcal{H}}$ account for electron-light interaction, $\hat{\mathcal{H}}_{\text{c-L}}$, and all kinds of many-particle interaction of electrons with other particle states such as electrons or phonons, $\hat{\mathcal{H}}_{\text{I}}$. The first section will give an overview over the solution of the Schrödinger equation for the $\hat{\mathcal{H}}_0$-part using $\mathbf{k}\cdot\mathbf{p}$-theory. This explains the important details of the band-structure which we need to consider for the derivation of our model. Subsequent to this section, we briefly discuss the carrier-carrier and carrier-phonon interaction parts which complete the 4-band semiconductor-Bloch equations. In combination with the optical equations derived in Chapter 3 these equations constitute the backbone of the VCSEL simulations discussed in Chapter 5.

In the last section of this chapter, we discuss the mesoscopic response function which can be extracted by summing-up the k-solved equations. The resulting effective mesoscopic material model allows us to perform simulations of VCSEL devices on comparatively long time-scales of more than 10 ns.

4.2 $\mathbf{k}\cdot\mathbf{p}$-Method, Envelope Approximation Method, and Band-Mixing

The Hamiltonian $\hat{\mathcal{H}}_0$ is the Hamiltonian of a free electron moving in the crystal potential of a semiconductor with a grown in quantum-well structure. In order to calculate the associated wave-function $\phi_\lambda(\mathbf{r}) = \langle \mathbf{r} | \phi_\lambda \rangle$ and the energy eigenvalue ϵ_λ of a single electron confined to the quantum-well hetero-structure one has to solve the time-independent Schrödinger equation

$$\left(\frac{\hat{\mathbf{p}}^2}{2m_0} + \mathcal{V}_0(\hat{\mathbf{r}}) + \mathcal{V}(\hat{z}) \right) |\phi_\lambda\rangle = \epsilon_\lambda |\phi_\lambda\rangle \ . \tag{4.3}$$

Assuming that the confinement potential $\mathcal{V}(\hat{z})$ is sufficiently small one can expand the eigenstate $|\phi_\lambda\rangle$ in terms of the bulk eigenstates $|\psi_{n,\mathbf{k}}\rangle$. The latter are the solutions of the eigenvalue equation,

$$\left(\frac{\hat{\mathbf{p}}^2}{2m_0} + \mathcal{V}_0(\hat{\mathbf{r}}) \right) |\psi_{n,\mathbf{k}}\rangle = \epsilon_{n,\mathbf{k}} |\psi_{n,\mathbf{k}}\rangle \ . \tag{4.4}$$

As this Hamiltonian bears full translational symmetry, that is $\mathcal{V}_0(\mathbf{r}+\mathbf{R}) = \mathcal{V}_0(\mathbf{r})$, the bulk eigenfunction obeys the *Bloch-theorem*:

$$\langle \mathbf{r} | \psi_{n,\mathbf{k}} \rangle = \mathrm{e}^{i\mathbf{k}\cdot\mathbf{r}} \langle \mathbf{r} | n\,\mathbf{k} \rangle \ . \tag{4.5}$$

Here $\langle \mathbf{r}\,|\,n\,\mathbf{k}\rangle = \langle \mathbf{r}+\mathbf{R}\,|\,n\,\mathbf{k}\rangle$ are the lattice-periodic Bloch-functions which fulfil a) the orthonormality relation $\langle m\,\mathbf{k}\,|\,n\,\mathbf{k}\rangle = \delta_{m,n}$ and b) provide a complete set of eigenfunctions for each $\mathbf{k}$. Expanding the quantum-well eigenfunction in terms of the bulk eigenfunctions at $\mathbf{k}=0$ one obtains (see [43])

$$\phi_\lambda(\mathbf{r}) = \langle \mathbf{r}\,|\,\phi_\lambda\rangle = \sum_m W_{\lambda m}(\mathbf{r})\,\langle \mathbf{r}\,|\,m\rangle \;, \quad W_{\lambda m}(\mathbf{r}) = \sum_{\mathbf{k}} \mathrm{e}^{i\mathbf{k}\cdot\mathbf{r}} W_{\lambda m\mathbf{k}} \;, \tag{4.6}$$

and

$$W_{\lambda m\mathbf{k}} = \sum_n \langle m\,|\,n\,\mathbf{k}\rangle\,\langle \psi_{n,\mathbf{k}}\,|\,\phi_\lambda\rangle \;. \tag{4.7}$$

$W_{\lambda m}(\mathbf{r})$ is the envelope function which, compared to $\langle \mathbf{r}\,|\,m\rangle$, varies slowly in $\mathbf{r}$. $|m\rangle$ and ϵ_m are shortcut notations for $|m\mathbf{k}\rangle$ and $\epsilon_{n,\mathbf{k}}$ at $\mathbf{k}=0$. Inserting the expansion (4.6) into the Schödinger equation (4.3) the equation

$$\sum_{n,\mathbf{k}} W_{\lambda n\mathbf{k}} \frac{1}{V} \int \mathrm{d}^3 r\, \mathrm{e}^{i(\mathbf{k}-\mathbf{k}')\cdot\mathbf{r}}\,\langle \mathbf{r}\,|\,m\rangle \left(\frac{\hbar^2 k^2}{2m_0} + \epsilon_n - \epsilon_\lambda - \frac{i\hbar^2}{m_0}\mathbf{k}\cdot\nabla + \mathcal{V}(z) \right) \langle \mathbf{r}\,|\,n\rangle = 0 \tag{4.8}$$

can be deduced [43]. Using the orthonormality of the Bloch-function states the integration over the volume can be evaluated for each of the terms in the parenthesis. The evaluation of the last integral, encompassing the z-dependend confinement potential, affords an additional approximation which is well justified provided that the confinement potential varies little over a unit cell of the lattice. Details can be found in [43]. In that case the above equation can be approximated by

$$\left(\frac{\hbar^2 k^2}{2m_0} + \epsilon_n \right) W_{\lambda n\mathbf{k}} + \frac{\hbar}{m_0} \sum_m \mathbf{k}\cdot\mathbf{p}_{nm} W_{\lambda n\mathbf{k}} + \sum_{\mathbf{k}'} \mathcal{V}_{\mathbf{k}-\mathbf{k}'} W_{\lambda n\mathbf{k}'} = \epsilon_\lambda W_{\lambda n\mathbf{k}} \;, \tag{4.9}$$

where the abbreviations

$$\mathbf{p}_{mn} = \langle m\,|\,\hat{\mathbf{p}}\,|\,n\rangle \;, \quad \mathcal{V}_{\mathbf{k}-\mathbf{k}'} = \frac{1}{N} \sum_{l=1}^{N} \mathrm{e}^{i(\mathbf{k}-\mathbf{k}')\cdot\mathbf{R}_l} \mathcal{V}(Z_l) \tag{4.10}$$

for the momentum matrix-elements and the confinement potential, respectively, were used. $\mathbf{R}_l = (X_l, Y_l, Z_l)$ are the N unit vectors of the lattice. Note, that due to the approximation applied here, the confinement potential does not mix states associated with a different band-index n.

The $\mathbf{k}\cdot\mathbf{p}$-method aims to solve equation (4.9) in the vicinity of a band minimum by treating the $\mathbf{k}\cdot\mathbf{p}$-term as a perturbation. Like many other III-V semiconductors Gallium Arsenide has a direct band-gap at $\mathbf{k}=0$ (Γ-point). From tight-binding theory one knows that the conduction band is s-like and has a 2-fold degeneracy due to the electron's spin while the valence band is p-like and thus is 6-fold degenerated [43,98,99]. So far, the spin-orbit coupling has been neglected. $\hat{\mathcal{H}}_0$. This adds a term, $\xi\mathbf{L}\cdot\mathbf{S}$, to the Hamiltonian

which induces major modifications on the electronic states: Assuming a *Russel-Saunders* type L-S coupling, the eigenfunctions $|ls; jm_j\rangle$ of the Hamiltonian are classified by the quantum numbers of the total angular momentum rather than by the magnetic quantum numbers of the orbital angular momentum and the spin $|ls; m_l m_s\rangle$. For the $l = 0$ conduction band nothing changes: The two degenerate states $|j\, m_j\rangle = |1/2\ \pm 1/2\rangle$ remain energetically degenerate and do not shift. In contrast to this, the degeneracy of the $l = 1$ valence-states is lifted. Treating the spin-orbit coupling term as a perturbation one finds that the 4-fold degenerated valence band states $|3/2\ \pm 3/2\rangle$, $|3/2\ \pm 1/2\rangle$ are separated from the $|1/2\ \pm 1/2\rangle$ states by $\Delta_{\mathrm{so}} \approx 9/8\,\langle\,\xi\,\rangle$ where $\langle\,\xi\,\rangle$ is the expectation value of the spin-orbit function ξ. The 2-fold degenerated $j = 1/2$ states are called the *split-off* band as the associated states are energetically lowered. For Gallium Arsenide numerical calculations show that $\Delta_{\mathrm{so}} \approx 0.341\mathrm{eV}$ [3].

Keeping the electronic structure at $k = 0$ in mind, equation (4.9) serves as a valid starting point for a $\mathbf{k}\cdot\mathbf{p}$-expansion. For the conduction-band n one can apply non-degenerate perturbation theory and finds

$$\left(-\frac{\hbar^2\nabla_\perp^2}{2m_n^*} - \partial_Z\frac{\hbar^2}{2m_n^*}\partial_Z + \mathcal{V}(Z)\right) W_{\lambda n}(\mathbf{R}) = \epsilon_{\lambda n} W_{\lambda n}(\mathbf{R})\,. \tag{4.11}$$

$W_{\lambda n}(\mathbf{R})$ is the slowly varying envelope function, $\mathcal{V}(Z)$ the discrete Fourier-transform of $\mathcal{V}_{\mathbf{k}-\mathbf{k}'}$, and $\epsilon_{\lambda n} = \epsilon_\lambda - \epsilon_n$. m_n^* the effective band mass. Because of the symmetry of the conduction band the matrix-elements for the momentum components have all the same value. Thus, the effective mass is a scalar quantity, which can be calculated from

$$\frac{1}{m_n^*} = \frac{1}{m_0} + \frac{2}{m_0^2}\sum_{m\neq n}\frac{|\langle n|\hat{p}_x|m\rangle|^2}{\epsilon_n - \epsilon_m}\,. \tag{4.12}$$

One has to keep in mind, that the effective mass is a z-dependent quantity and the derivative has to be symmetrised with respect to z in order to assure that the Hamiltonian is Hermitian. E.g. (4.11) can be solved by separation of the vertical z- and the in-plane ($\perp$) components,

$$W_{\lambda n}(\mathbf{R}) = A_{in}(Z) B_{\mathbf{k}_\perp\lambda}(\mathbf{R}_\perp)\,. \tag{4.13}$$

i and $\mathbf{k}_\perp$ are the quantum-numbers of the sub-band and the in-plane k-vector. The energy states ϵ_{in} are the eigenvalues of the one-dimensional equation

$$\left(-\partial_Z\frac{\hbar^2}{2m_n^*}\partial_Z + \mathcal{V}(Z)\right) A_{in}(Z) = \epsilon_{in} A_{in}(Z)\,, \tag{4.14}$$

while $\mathbf{k}_\perp$ is associated with the kinetic-energy in the plane of the quantum-well

$$\epsilon_{\mathbf{k}_\perp} = \frac{\hbar^2 k_\perp^2}{2m_n^*}\,. \tag{4.15}$$

In case of Gallium Arsenide the value for the effective mass of the conduction band is known to be $m_e^*/m_0 \approx 0.067$ [3,100]. The total energy of the quantum-well state is the sum of the energy of the bulk-band n, the sub-band i, and the in-plane motion $k_\perp$:

$$\epsilon_\lambda = \epsilon_n + \epsilon_{in} + \epsilon_{\mathbf{k}_\perp n} \,. \tag{4.16}$$

For the valence band degenerative perturbation theory has to be applied. Labelling the four $j = 3/2$ valence-band states with $n = 1 \ldots 4$ and neglecting the influence of the split-off and the conduction band one obtains:

$$\left(-\frac{\hbar^2 \nabla_\perp^2}{2m^*_{\mathrm{hh},\perp}} - \partial_Z \frac{\hbar^2}{2m^*_{\mathrm{hh},Z}} \partial_Z + \mathcal{V}(Z) \right) W_{\lambda n}(\mathbf{R}) + \hat{\mathcal{D}}(k_\perp) W_{\lambda m}(\mathbf{R}) = \epsilon_{\lambda 1} W_{\lambda n}(\mathbf{R}) \,, \tag{4.17}$$

for $(n, m) = (1, 2)$ and $(4, 3)$ and

$$\left(-\frac{\hbar^2 \nabla_\perp^2}{2m^*_{\mathrm{lh},\perp}} - \partial_Z \frac{\hbar^2}{2m^*_{\mathrm{lh},Z}} \partial_Z + \mathcal{V}(Z) \right) W_{\lambda n}(\mathbf{R}) + \hat{\mathcal{D}}(k_\perp) W_{\lambda m}(\mathbf{R}) = \epsilon_{\lambda 2} W_{\lambda n}(\mathbf{R}) \,, \tag{4.18}$$

for $(n, m) = (2, 1)$ and $(3, 4)$ where

$$\hat{\mathcal{D}}(k_\perp) = \frac{\sqrt{3}\hbar^2 k_\perp}{2m_0} \left(\gamma_2 k_\perp - 2\gamma_3 \partial_Z \right) \tag{4.19}$$

was used. These system of equations constitutes the degenerate equivalent to (4.11). The bands labelled with $n = 1, 4$ are associated with the heavy-hole states while $n = 2, 3$ account for the light hole states. For GaAs the relation $\gamma_1 > \gamma_2 \approx \gamma_3$ for the *Luttinger-parameters* holds true. In that case the effective masses can be expressed in terms of γ_1 and γ_2 ($\gamma_1 \approx 6.85$, $\gamma_2 \approx 2.1$) only,

$$\begin{aligned}
m^*_{\mathrm{hh},\perp}/m_0 &= (\gamma_1 + \gamma_2)^{-1} \approx 0.112 \,, \\
m^*_{\mathrm{lh},\perp}/m_0 &= (\gamma_1 - \gamma_2)^{-1} \approx 0.211 \,, \\
m^*_{\mathrm{hh},Z}/m_0 &= (\gamma_1 - 2\gamma_2)^{-1} \approx 0.377 \,, \\
m^*_{\mathrm{lh},Z}/m_0 &= (\gamma_1 + 2\gamma_2)^{-1} \approx 0.091 \,.
\end{aligned} \tag{4.20}$$

Along the Z-direction the effective masses of the heavy- and the light-hole are the same than the ones calculated for the bulk case. In transverse direction, however, the *heavy*-whole has the smaller effective mass than the *light*-hole. This is known as *mass-reversal*. As $m^*_{\mathrm{hh},Z} > m^*_{\mathrm{lh},Z}$ the hole band associated with the heavy-holes is lower than the one for the light-holes. A sketch of the resulting in-plane band structure in the vicinity of $k = 0$ is given in FIGURE 4.1. Band crossing would occur at some value $k_\perp > 0$. As this is unphysical *band-mixing* occurs in the transverse direction [43,98] in order to avoid the

crossing. In practice we are considering merely the top-valence band and use a parabolic band-approximation. The influence of band-mixing can be implemented by defining a slightly modified heavy-hole mass.

The band-structure of a quantum-well can be modified by means of external and internal fields. One method which has significant effect on both, the effective masses as well as on the energetic offset between light- and heavy-hole band is the introduction of tensile or compressive elastic strain [101]. As we concentrate on the well lattice-matched Al-GaAs material-system we can neglect such effects.

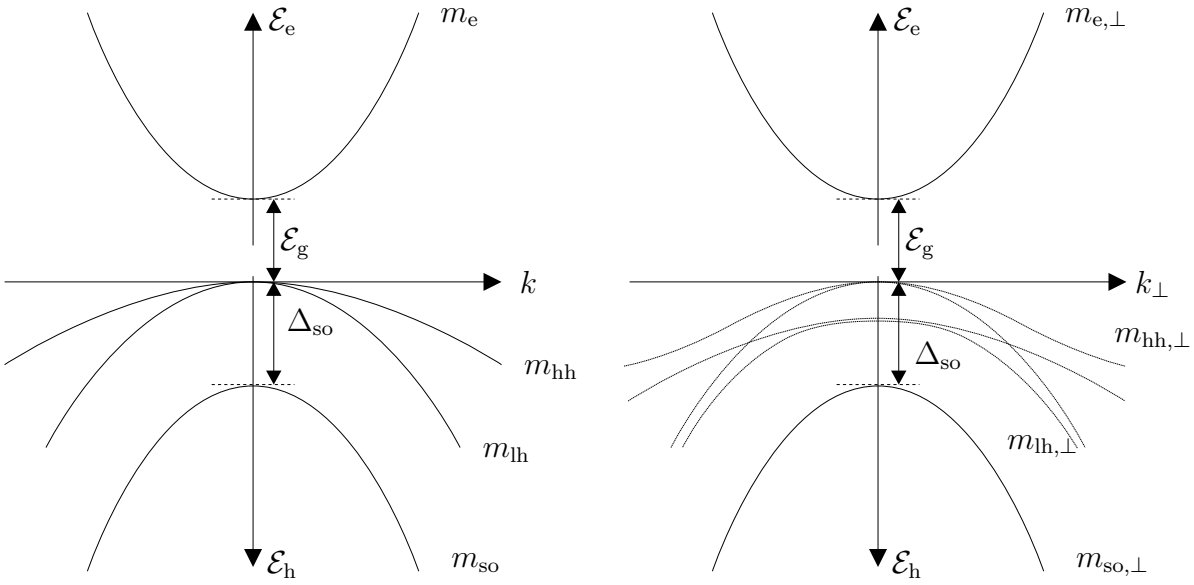

Figure 4.1: Lowest conduction and valence bands of Gallium Arsenide in the vicinity of the Γ-point (k=0) for the bulk case (left) and the quantum-well case (right). At $T = 300K$ the band-gap energy is $\mathcal{E}_g \approx 1.519\,\text{eV}$ and the split-off energy is $\Delta \approx 0.34\,\text{eV}$. The effective masses of the conduction, the heavy-hole and the light-hole bands are $m_e = 0.067m_0$, $m_{hh} = 0.377m_0$ and $m_{lh} = 0.09m_0$ for the bulk case. In the quantum-well case masses along the z-direction stay same as in the bulk case. In the plane with the quantum well $k_\perp$ the situation is different: The heavy-hole turns out to be lighter ($m_{hh,\perp} = 0.112$) and the light-hole to be more heavy ($m_{lh,\perp} = 0.211$). In order to avoid band-crossing the light- and heavy-hole bands mix for $k_\perp \neq 0$.

4.3 Many-Body Interactions

We switch back to the complete Hamiltonian (4.1) but consider the electrons of the lowest conduction ($n = c$) and the heavy-holes of the lowest valence ($n = v$) band only.

For this simplified case one may write down the wave function

$$\Psi(\mathbf{r},z) = 1/\sqrt{A}\sum_{\mathbf{k}} \mathrm{e}^{i\mathbf{k}\cdot\mathbf{r}} A_c(z)\hat{c}_{\mathbf{k}} + 1/\sqrt{A}\sum_{\mathbf{k}} \mathrm{e}^{i\mathbf{k}\cdot\mathbf{r}} A_v(z)\hat{d}^{\dagger}_{-\mathbf{k}}\,, \tag{4.21}$$

which introduces the particle operators typical for second quantisation. $\hat{c}$ is the electron annihilation operator of the conduction band and $\hat{d}^{\dagger}$ the hole creation operator of the valence band. Furthermore, $\mathbf{k}$ and $\mathbf{r}$ were used as abbreviations for $\mathbf{k}_{\perp}$ and $\mathbf{r}_{\perp}$.

The kinetic and the light-field interaction parts of the Hamiltonian read [46]

$$\hat{\mathcal{H}}_{\text{kin}} = \sum_{\mathbf{k}} \epsilon^{\text{e}}_{\mathbf{k}} c^{\dagger}_{\mathbf{k}} c_{\mathbf{k}} + \sum_{\mathbf{k}} \epsilon^{\text{h}}_{\mathbf{k}} d^{\dagger}_{\mathbf{k}} d_{\mathbf{k}}\,, \tag{4.22}$$

$$\hat{\mathcal{H}}_{\text{c-L}} = -\sum_{\mathbf{k}} \left(\mathbf{M}_{cv,\mathbf{k}} \cdot \mathbf{E}^{(+)}(t)\, \hat{c}^{\dagger}_{\mathbf{k}} \hat{d}^{\dagger}_{-\mathbf{k}} + \mathbf{M}^{*}_{cv,\mathbf{k}} \cdot \mathbf{E}^{(-)}(t)\, \hat{d}_{-\mathbf{k}} \hat{c}_{\mathbf{k}} \right) \tag{4.23}$$

with $\epsilon^{\text{e}}_{\mathbf{k}} = \epsilon_{c,\mathbf{k}}$ and $\epsilon^{\text{h}}_{\mathbf{k}} = \epsilon_{v,\mathbf{k}}$. Splitting the driving electric field $\mathbf{E}(t)$ into positive and negative frequency components one can write

$$\mathbf{E}(t) = \mathbf{E}^{(+)}(t) + \mathbf{E}^{(-)}(t) = \mathbf{E}_0\, \mathrm{e}^{-i\Omega t} + \mathbf{E}^{*}_0\, \mathrm{e}^{+i\Omega t}\,. \tag{4.24}$$

This is only possible for a longitudinal single-mode system. All non-resonant parts of the excitation have been dropped in rotating-wave approximation. Note, that the electric field was introduced as a classical observable, an approximation which is well justified because of the high level of coherence which is typical for laser systems above threshold. $\mathbf{M}_{ij,\mathbf{k}}$ is the dipole transition matrix-element of the quantum-well which can in principle be calculated from the bulk dipole transition matrix and the z-dependent envelope functions $A_n(z)$ [43, 59, 60].

Beside the interaction of carriers with the light-field one should consider at least two more interactions which are distinctive features of semiconductors: the carrier-carrier interaction due to Coulomb-scattering and the interaction of carriers with longitudinal optical phonons (LO-phonons) due to the *Fröhlich-interaction*. Without derivation we write down the respective interaction Hamiltonians [14, 46, 59]:

$$\begin{aligned}\hat{\mathcal{H}}_{\text{c-c}} =& \frac{1}{2}\sum_{\mathbf{k},\mathbf{k}',\mathbf{q}} W_{cc}(\mathbf{q})\, \hat{c}^{\dagger}_{\mathbf{k}+\mathbf{q}} \hat{c}^{\dagger}_{\mathbf{k}'-\mathbf{q}} \hat{c}_{\mathbf{k}'} \hat{c}_{\mathbf{k}} + \frac{1}{2}\sum_{\mathbf{k},\mathbf{k}',\mathbf{q}} W_{vv}(\mathbf{q})\, \hat{d}^{\dagger}_{\mathbf{k}+\mathbf{q}} \hat{d}^{\dagger}_{\mathbf{k}'-\mathbf{q}} \hat{d}_{\mathbf{k}'} \hat{d}_{\mathbf{k}} \\ & - \sum_{\mathbf{k},\mathbf{k}',\mathbf{q}} W_{cv}(\mathbf{q})\, \hat{c}^{\dagger}_{\mathbf{k}+\mathbf{q}} \hat{d}^{\dagger}_{\mathbf{k}'-\mathbf{q}} \hat{d}_{\mathbf{k}'} \hat{c}_{\mathbf{k}}\end{aligned} \tag{4.25}$$

and

$$\begin{aligned}\hat{\mathcal{H}}_{\text{c-LO}} =& \sum_{\mathbf{k},\mathbf{q},q_z} \left(\gamma_c(\mathbf{q},q_z) \hat{c}^{\dagger}_{\mathbf{k}+\mathbf{q}} \hat{b}_{\mathbf{q},q_z} \hat{c}_{\mathbf{k}} + \gamma^{*}_c(\mathbf{q},q_z) \hat{c}^{\dagger}_{\mathbf{k}} \hat{b}^{\dagger}_{\mathbf{q},q_z} \hat{c}_{\mathbf{k}+\mathbf{q}} \right) \\ & + \sum_{\mathbf{k},\mathbf{q},q_z} \left(\gamma_v(\mathbf{q},q_z) \hat{d}^{\dagger}_{\mathbf{k}+\mathbf{q}} \hat{b}_{\mathbf{q},q_z} \hat{d}_{\mathbf{k}} + \gamma^{*}_v(\mathbf{q},q_z) \hat{d}^{\dagger}_{\mathbf{k}} \hat{b}^{\dagger}_{\mathbf{q},q_z} \hat{d}_{\mathbf{k}+\mathbf{q}} \right).\end{aligned} \tag{4.26}$$

Here, W_{cc}, W_{vv}, and W_{cv} denote the matrix-elements of the Coulomb-interaction which are given by

$$W_{nm}(\mathbf{q}) = \frac{1}{2\pi A} \int_{-\infty}^{+\infty} \mathrm{d}z \int_{-\infty}^{+\infty} \mathrm{d}z' \; |A_n(z)|^2 |A_m(z')|^2 \cdot \int_{-\infty}^{+\infty} \mathrm{d}q_z \; \frac{1}{V} \frac{e^2}{\epsilon_0 \epsilon \sqrt{|\mathbf{q}|^2 + q_z^2}} \mathrm{e}^{iq_z(z-z')} \; . \tag{4.27}$$

For the γ matrix-elements of the electron-phonon scattering one can show [46] that for electrons

$$\begin{aligned} \gamma_c(\mathbf{q}, q_z) &= -4\pi i \sqrt{\frac{e^2\hbar}{2\gamma\omega_{\mathrm{LO}} A L}} \frac{1}{\sqrt{|\mathbf{q}|^2 + q_z^2}} \int_{-\infty}^{\infty} \mathrm{d}z \; A_c^*(z) A_c(z) \mathrm{e}^{iq_z z} \; , \\ \gamma &= \frac{4\pi}{\omega_{\mathrm{LO}}^2} \left(\frac{1}{4\pi\epsilon_0\epsilon_\infty} - \frac{1}{4\pi\epsilon_0\epsilon} \right)^{-1} \end{aligned} \tag{4.28}$$

holds. γ_v can be calculated from a similar expression but with a positive sign in front.

4.4 Two-Band Semiconductor-Bloch Equations

In order to find an effective kinetic description of the processes taking place in the quantum-well, we will concentrate on the lowest electronic sub-bands only, one for the electrons (conduction band) and one for the holes (valence band). The electronic state of the system can be described by single-particle density matrices for the electrons $n^{\mathrm{e}}_{\mathbf{k}\mathbf{k}'}$, the holes $n^{\mathrm{h}}_{\mathbf{k}\mathbf{k}'}$ and the interband-polarisation $p_{\mathbf{k}\mathbf{k}'}$, which are

$$n^{\mathrm{e}}_{\mathbf{k}\mathbf{k}'} = \left\langle \hat{c}^\dagger_{\mathbf{k}} \hat{c}_{\mathbf{k}'} \right\rangle , \quad n^{\mathrm{h}}_{\mathbf{k}\mathbf{k}'} = \left\langle \hat{d}^\dagger_{\mathbf{k}} \hat{d}_{\mathbf{k}'} \right\rangle , \quad p_{\mathbf{k}\mathbf{k}'} = \left\langle \hat{d}_{-\mathbf{k}} \hat{c}_{\mathbf{k}'} \right\rangle . \tag{4.29}$$

These density-matrices can be transformed to the *Wigner representation* [102, 103] by applying a Fourier-transformation to the relative momentum $\mathbf{q}$,

$$A_{\mathbf{k}}(\mathbf{r}) = \sum_{\mathbf{q}} A_{\mathbf{k}-\frac{1}{2}\mathbf{q}, \mathbf{k}+\frac{1}{2}\mathbf{q}} \, \mathrm{e}^{i\mathbf{q}\cdot\mathbf{r}} \; . \tag{4.30}$$

$A_{\mathbf{k}\mathbf{k}'}$ is a placeholder for one of the density-matrices (4.29) and $\mathbf{r}$, $\mathbf{k}$ and $\mathbf{q}$ are two-dimensional vectors in-plane with the quantum-well.

The Wigner functions $n^{\mathrm{e}}_{\mathbf{k}}(\mathbf{r})$, $n^{\mathrm{h}}_{\mathbf{k}}(\mathbf{r})$ and $p_{\mathbf{k}}(\mathbf{r})$ are the dynamical variables of our semiconductor system. The corresponding equations of motion can be obtained by plugging the respective operators (4.29) into Heisenberg's equation of motion. After substituting $\mathbf{k} \to \mathbf{k} - \frac{1}{2}\mathbf{q}$ and $\mathbf{k}' \to \mathbf{k} + \frac{1}{2}\mathbf{q}$ one can apply the transformation (4.30) and retrieve an hierarchy of equations for the Wigner-Functions. In general, it is not even for the $\hat{\mathcal{H}}_{\mathrm{kin}} + \hat{\mathcal{H}}_{\mathrm{c\text{-}L}}$ part of $\hat{\mathcal{H}}$ possible to derive local equations in $\mathbf{r}$ and $\mathbf{k}$. Yet, in lowest order

of a Taylor-expansion with respect to $\mathbf{r}$ and $\mathbf{k}$, one obtains from the $\hat{\mathcal{H}}_{\text{kin}} + \hat{\mathcal{H}}_{\text{c-L}}$ part of the Hamiltonian the equations [81]

$$\partial_t n^{\text{e}}_{\mathbf{k}}(\mathbf{r},t) = g_{\mathbf{k}}(\mathbf{r},t)\,, \tag{4.31}$$

$$\partial_t n^{\text{h}}_{\mathbf{k}}(\mathbf{r},t) = g_{-\mathbf{k}}(\mathbf{r},t)\,, \tag{4.32}$$

$$\partial_t p_{\mathbf{k}}(\mathbf{r},t) = -i\,\Delta\omega_{\mathbf{k}}\,p_{\mathbf{k}}(\mathbf{r},t) - \frac{i}{\hbar}\mathbf{M}_{\text{cv},\mathbf{k}}\cdot\mathbf{E}^{(+)}(\mathbf{r},t)\left[n^{\text{e}}_{\mathbf{k}}(\mathbf{r},t) + n^{\text{h}}_{-\mathbf{k}}(\mathbf{r},t) - 1\right]\,. \tag{4.33}$$

The *spectral carrier generation rate* $g_{\mathbf{k}}$ which is defined by the expression

$$g_{\mathbf{k}}(\mathbf{r},t) = 2\text{Im}\left[\frac{1}{\hbar}\mathbf{M}_{\text{cv},\mathbf{k}}\cdot\mathbf{E}^{(+)}(\mathbf{r},t)\,p^{*}_{\mathbf{k}}(\mathbf{r},t)\right] \tag{4.34}$$

quantifies the work the electric field exerts to the microscopic dipoles. The k-dependent *frequency detuning*, $\Delta\omega_{\mathbf{k}} = \omega_{\mathbf{k}} - \Omega$, results from the fact that we transformed to a coordinate frame which is rotating with the light-field frequency Ω. $\omega_{\mathbf{k}}$ is related to the energy of an electron-hole pair at a particular $\mathbf{k}$-value. Its value is given by the formula

$$\hbar\omega_{\mathbf{k}} = \epsilon^{\text{e}}_{\mathbf{k}} + \epsilon^{\text{h}}_{-\mathbf{k}} = \mathcal{E}_{\text{g}} + \frac{\hbar^2|\mathbf{k}|^2}{2m_{\text{r}}}\,. \tag{4.35}$$

Here, $\mathcal{E}_{\text{g}}$ denotes the band-gap energy, $\epsilon^{\text{e}}_{\mathbf{k}} + \epsilon^{\text{h}}_{-\mathbf{k}}$ at $\mathbf{k} = 0$ and m_{r} is the reduced effective mass of the electron-hole system,

$$m_{\text{r}} = \frac{m_{\text{e}}\cdot m_{\text{h}}}{m_{\text{e}} + m_{\text{h}}}\,. \tag{4.36}$$

Equations (4.31)-(4.33) are the *coherent optical Bloch equations* [8, 43, 47] applied to a semiconductor material. These equations feature the coherent interaction of the incident light-field with the electron-hole dipoles, the stimulated emission and absorption of photons, and the affiliated generation and recombination of carriers. However, they fail to describe the dynamics in a semiconductor by quantity. The reason for this is, that the density of carriers in a semiconductor laser is high compared to other laser types (e.g. gas lasers) and therefore particle interactions play an important role. Additionally, the light-field couples not solely to a two-level system but to a whole band of transitions. Many-particle effects, like scattering processes are fast ($\sim 100fs$) and distinct, and thus the intraband carrier distributions show a strong tendency to attain a thermalised state. By taking into account the carrier interaction terms, one can extend the above Bloch equations to the so-called *semiconductor-Bloch equations* [47, 104, 105],

$$\partial_t n^{\text{e}}_{\mathbf{k}} = g_{\mathbf{k}} + \Lambda^{\text{e}}_{\mathbf{k}}(1 - n^{\text{e}}_{\mathbf{k}}) - w_{\text{sp},\mathbf{k}} - \gamma_{\text{nr}} n^{\text{e}}_{\mathbf{k}} + \partial_t n^{\text{e}}_{\mathbf{k}}\big|^{\text{sc}}\,, \tag{4.37}$$

$$\partial_t n^{\text{h}}_{\mathbf{k}} = g_{-\mathbf{k}} + \Lambda^{\text{h}}_{\mathbf{k}}(1 - n^{\text{h}}_{\mathbf{k}}) - w_{\text{sp},\mathbf{k}} - \gamma_{\text{nr}} n^{\text{h}}_{\mathbf{k}} + \partial_t n^{\text{h}}_{\mathbf{k}}\big|^{\text{sc}}\,, \tag{4.38}$$

$$\partial_t\, p_{\mathbf{k}} = -i\,\Delta\bar{\omega}_{\mathbf{k}}\,p_{\mathbf{k}} - i\mathcal{U}^{(+)}_{\mathbf{k}}\left[n^{\text{e}}_{\mathbf{k}} + n^{\text{h}}_{-\mathbf{k}} - 1\right] + \partial_t\, p_{\mathbf{k}}\big|^{\text{sc}}\,. \tag{4.39}$$

Using this simplified notation one should keep in mind, that all the quantities are still dependent on $\mathbf{r}$ and t. Here, we have set $\Delta\bar{\omega}_{\mathbf{k}} = \bar{\omega}_{\mathbf{k}} - \Omega$ and $\bar{\omega}_{\mathbf{k}} = \mathcal{E}^{\text{e}}_{\mathbf{k}} + \mathcal{E}^{\text{h}}_{-\mathbf{k}}$ with the renormalised electron and hole energies

$$\mathcal{E}^{\text{e/h}}_{\mathbf{k}} = \epsilon^{\text{e/h}}_{\mathbf{k}} + \Delta\mathcal{E}^{\text{e/h}}_{\mathbf{k}}\,. \tag{4.40}$$

The electric field has been replaced by the *generalised Rabi-frequencies*

$$\mathcal{U}_{\mathbf{k}}^{(+)} = \hbar^{-1}\,\mathbf{M}_{\mathrm{cv},\mathbf{k}} \cdot \mathbf{E}^{(+)} + \Delta\mathcal{U}_{\mathbf{k}}^{(+)} \tag{4.41}$$

which include the *screening* of the internal fields due to Coulomb-interaction. This modified expression for the electric field enters the microscopic generation rates $g_{\mathbf{k}}$ which are now defined by

$$g_{\mathbf{k}} = 2\mathrm{Im}\left[\mathcal{U}_{\mathbf{k}}^{(+)} p_{\mathbf{k}}^{*}\right] . \tag{4.42}$$

Both, the energy and field renormalisations are coherent corrections that emerge from the *Hartree-Fock* terms of the Coulomb potential. This will be briefly discussed in the next section.

The impact of electron-electron and electron-phonon scattering processes to the dynamics is described by *Boltzmann collision* terms. If the electron- and hole-densities are close to their equilibrium Fermi-distributions, these collision terms can be approximated by

$$\partial_t n_{\mathbf{k}}^{\mathrm{e/h}}\Big|^{\mathrm{sc}} = -\gamma_k^{\mathrm{e/h}}\left(n_{\mathbf{k}}^{\mathrm{e/h}} - f_{\mathbf{k}}^{\mathrm{e/h}}\right) , \qquad \partial_t\, p_{\mathbf{k}}|^{\mathrm{sc}} = -\gamma_k^{\mathrm{p}}\, p_{\mathbf{k}} , \tag{4.43}$$

where $f_{\mathbf{k}}^{\mathrm{e/h}}$ are the equilibrium Fermi-functions of a two-dimensional system,

$$f_{\mathbf{k}}^{\mathrm{e/h}}(N,T) = \left(\exp\left[\beta\mathcal{E}_{\mathbf{k}}^{\mathrm{e/h}} - \beta\mu^{\mathrm{e/h}}(N,T)\right] + 1\right)^{-1} , \quad \mathcal{E}_{\mathbf{k}}^{\mathrm{e/h}} = \frac{\hbar^2 k^2}{2m_{\mathrm{e/h}}} . \tag{4.44}$$

Note, that the Fermi-functions are functionally dependent on the temperature parameter $\beta = 1/(k_{\mathrm{B}}T)$ and on the total carrier density of the band, N. N equals the sum over the two-dimensional microscopic carrier densities

$$N = 2A^{-1}\sum_{\mathbf{k}} n_{\mathbf{k}}^{\mathrm{e}} = 2A^{-1}\sum_{\mathbf{k}} n_{\mathbf{k}}^{\mathrm{h}} . \tag{4.45}$$

This ansatz is called *ambipolar approximation* as the total charge density concentrated in a spacial cell is assumed to be vanishing due to internal electrostatic forces which keep electrons and holes together. Note, that the "2" appearing in front of the sum accounts for the spin degeneracy of the electrons. $\mu^{\mathrm{e/h}}(N,T)$ are the two-dimensional chemical potentials which can be calculated analytically from the expression [43, 106]

$$\mu^{\mathrm{e/h}}(N,T) = \beta^{-1}\ln\left[\exp(\hbar^2\beta\pi N/m_{\mathrm{e/h}}) - 1\right] . \tag{4.46}$$

The k-dependent *dephasing rate* γ_k^{p} appearing in (4.39) quantifies how fast the polarisation $p_{\mathbf{k}}$ decays due to scattering processes. $\gamma_k^{\mathrm{e/h}}$ are the *Coulomb-scattering rates* of electrons and holes. The carrier-carrier scattering rates are responsible for the distribution functions $n_{\mathbf{k}}^{\mathrm{e/h}}$ to be pulled back towards their respective quasi-equilibrium Fermi distribution functions. Their theoretical evaluation will be briefly sketched in SECTION 4.6.

Two more terms have been introduced along with (4.37) and (4.38). $w_{\mathrm{sp},\mathbf{k}}$, the carrier loss rate due to spontaneous emission,

$$w_{\mathrm{sp},\mathbf{k}} = B_{\mathbf{k}} n^{\mathrm{e}}_{\mathbf{k}} n^{\mathrm{h}}_{-\mathbf{k}} \,, \tag{4.47}$$

and $\Lambda^{\mathrm{e/h}}_{\mathbf{k}}$, the carrier injection rate. The latter, a phenomenological modification to the pump-term is describing the carrier thermalisation and Fermi-blocking which occuris during the relaxation process of electrons and holes down from the barrier-states to the conduction- and valence-band. A expression commonly used, is [35]

$$\Lambda^{\mathrm{e/h}}_{\mathbf{k}} = \Lambda_0 \, f^{\mathrm{e/h}}_{\mathbf{k}} \left[2A^{-1} \sum_{\mathbf{k}} f^{\mathrm{e/h}}_{\mathbf{k}} \left(1 - n^{\mathrm{e/h}}_{\mathbf{k}} \right) \right]^{-1} \quad \text{with} \quad f^{\mathrm{e/h}}_{\mathbf{k}} = f^{\mathrm{e/h}}_{\mathbf{k}}(T_l, N) \,. \tag{4.48}$$

The semiconductor-Bloch equations contain the kinetic part and the coherent interaction of the charge carriers with the optical laser field (single-particle Hamiltonians), the mean-field part of the many-body Hamiltonians (see SECTION 4.5), and the scattering processes (see SECTION 4.6). The strong influence of many-body interaction is one of the distinct features of semiconductor laser material. Apart from the Coulomb-interaction among carriers which is responsible for screening effects and a thermalisation of non-equilibrium distribution functions due to carrier-carrier scattering, the interaction with phonons, in particular with polar optical phonons has to be taken into account. The *Fröhlich-interaction* is resulting in an energy transfer between the *hot* carrier subsystem and the colder crystal lattice [35, 49, 107].

In the next section we discuss the origin of and how to calculate the various corrections entering (4.37)-(4.39).

4.5 Mean-Field Corrections: Hartree-Fock Terms

By inserting the Hamiltonian (4.1) and the density-matrices (4.29) into Heisenberg's equation of motion one is confronted with the following problem: as the many-particle interaction Hamiltonians (4.25) and (4.26) contain products of operators of the interacting particles, higher order correlations appear on the rhs of the equations of motion. One can formally split the interaction Hamiltonians $\hat{\mathcal{H}}_{\mathrm{I}}$ into a mean-field part, the *Hartree-Fock* contribution $\hat{\mathcal{H}}^{\mathrm{HF}}_{\mathrm{I}}$, and into $\hat{\mathcal{H}}^{\mathrm{corr}}_{\mathrm{I}}$, which contains all of the remaining higher order correlations. The Hartree-Fock part of the Coulomb interacting $\hat{\mathcal{H}}^{\mathrm{HF}}_{cc}$ contains single-particle correlations only and causes (see [35, 59]) a *renormalisation* of the energy terms,

$$\begin{aligned} \Delta\mathcal{E}^{\mathrm{e}}_{\mathbf{k}} &= -\sum_{\mathbf{k}'} W_{cc}(\mathbf{k}-\mathbf{k}')\, n^{\mathrm{e}}_{\mathbf{k}} \,, \\ \Delta\mathcal{E}^{\mathrm{h}}_{\mathbf{k}} &= -\sum_{\mathbf{k}'} W_{hh}(\mathbf{k}-\mathbf{k}')\, n^{\mathrm{h}}_{\mathbf{k}} \,, \end{aligned} \tag{4.49}$$

and a modification of the Rabi-frequencies,

$$\Delta\mathcal{U}_{\mathbf{k}} = -1/\hbar \sum_{\mathbf{k}'} W_{cv}(\mathbf{k}-\mathbf{k}')\, p_{\mathbf{k}'} \,. \tag{4.50}$$

The internal field corrections are the result from the carrier exchange interaction and are responsible for excitonic effects and the Coulomb-enhancement. However, the bare Coulomb-potential does not describe the physical situation correctly: As densities are high the Coulomb-interaction between the carriers is *screened*. The simplest way to include the plasma screening is to use a modified Coulomb potential $W^{\mathrm{s}}_{mn}(\mathbf{k}-\mathbf{k}')$ which includes a screening term on a phenomenological level. A good model for this, including spatial and spectral dispersion, is the *Lindhard-formula* [108]. For many numerical applications, however, the Lindhard-formula is too complicated and might be replaced by the *static* plasmon-approximation. In that case, the screened Coulomb-potential is given by

$$W^{\mathrm{s}}_{mn}(q) = W_{mn}(\mathbf{k}-\mathbf{k}')\left(1-\frac{\omega_{\mathrm{pl}}}{\omega_q}\right), \quad \omega_q^2 = \omega_{\mathrm{pl}}^2\left(1+\frac{q^2}{\kappa^2}\right) + C\left(\frac{\hbar q^2}{4m^*_{\mathrm{r}}}\right)^2 . \tag{4.51}$$

In this equation ω_{pl} denotes the electron-hole plasma frequency, ω_q the effective plasmon frequency and κ the inverse static screening length.

Inserting the screened potential into the energy renormalisation terms (4.49) it turns out that the transition energy is shifted. For small deviations from the equilibrium carrier distribution functions, the *Debye-shift* or *Coulomb-hole self-energy* can be approximated by the a formula derived by *Zimmermann* [109, 110]:

$$\begin{aligned} &\Delta\mathcal{E}^{\mathrm{e/h}}_{\mathbf{k}} = \Delta\mathcal{E}^{\mathrm{e/h}} = \mp\frac{a}{2}\mathcal{E}_0\left(1+\frac{b^2}{\beta^2 N a_0^2 \mathcal{E}_0}\right)^{-1/4}, \\ &\text{with} \qquad a_0 = \frac{\hbar^2\epsilon_0}{e^2 m_{\mathrm{r}}}, \quad \mathcal{E}_0 = \frac{e^2}{2\epsilon_0 a_0} \,. \end{aligned} \tag{4.52}$$

a_0 and $\mathcal{E}_0$ are the Bohr radius and the excitonic binding energy, respectively. a and b are fit parameters, which turn out to be $a = 4.64$ and $b = 0.107$. This formula describes, how, with increasing carrier densities, the transition energies decrease due to an increasing screening of the potential.

In contrast to the Coulomb-interaction, the Fröhlich-interaction does not contribute a Hartree-Fock term. The reason is, that for quantum-well structures coherent phonons can only exist at $q = 0$ [60].

4.6 Second Order Corrections: Scattering Processes

By neglecting memory effects (Markov approximation) and all nonlinear terms in the polarisation Boltzmann collision terms can be introduced to the microscopic equations

of motion [35]:

$$\partial_t n_{\mathbf{k}}^{\mathrm{e/h}}|^{\mathrm{sc}} = -\Gamma_k^{\mathrm{e/h,out}} n_{\mathbf{k}}^{\mathrm{e/h}} + \Gamma_k^{\mathrm{e/h,in}}(1 - n_{\mathbf{k}}^{\mathrm{e/h}}) \,, \tag{4.53}$$

$$\partial_t p_{\mathbf{k}}^{\pm}|^{\mathrm{sc}} = -\frac{1}{2}\left(\Gamma_k^{\mathrm{e,out}} + \Gamma_k^{\mathrm{e,in}} + \Gamma_k^{\mathrm{h,out}} + \Gamma_k^{\mathrm{h,in}}\right) p_{\mathbf{k}}^{\pm} \,. \tag{4.54}$$

From the calculations it becomes obvious that for the polarisation, both, out- and in-scattering processes, are decay processes. The respective Γ scattering matrices reveal typical Fermi's golden rule expressions. For the Coulomb-interaction the result is [35, 97, 111]

$$\begin{aligned}
&\mathbf{k} \to \mathbf{k} - \mathbf{q}: \\
&\Gamma_k^{\mathrm{e,out}} = \sum_{\mathbf{k}',\mathbf{q},\circ} \frac{2\pi}{\hbar}\delta\left(E_k^{\mathrm{e}} - E_{k-q}^{\mathrm{e}} + E_{k'}^{\circ} - E_{k'+q}^{\circ}\right)|W^s(q)|^2\, n_{k'}^{\circ}(1 - n_{k'+q}^{\circ})(1 - n_{k-q}^{\mathrm{e}}) \,, \\
&\mathbf{k} - \mathbf{q} \to \mathbf{k}: \\
&\Gamma_k^{\mathrm{e,in}} = \sum_{\mathbf{k}',\mathbf{q},\circ} \frac{2\pi}{\hbar}\delta\left(-E_k^{\mathrm{e}} + E_{k-q}^{\mathrm{e}} - E_{k'}^{\circ} + E_{k'+q}^{\circ}\right)|W^s(q)|^2\, (1 - n_{k'}^{\circ}) n_{k'+q}^{\circ} n_{k-q}^{\mathrm{e}} \,,
\end{aligned} \tag{4.55}$$

where we used the shortcut symbol $\circ = \mathrm{e}, \mathrm{h}$. The Delta-function guarantees for energy conservation during the interaction and $W^s(q)$ quantifies the strength of the interaction. Note, that the bare 2D Coulomb potential is weakened due to plasma screening as given by the static Lindhard formula. Additionally, $W^s(q)$ contains quantum-well specific corrections. The scattering probability is proportional to the population of the initial state and to the open states of the final state (Pauli principle). By evaluating the sum over all possible scattering processes one finally obtains the k-dependent scattering matrices.

The Fröhlich interaction leads to a similar result [35, 59]. Here, the number of carriers is conserved as for the Coulomb-scattering but there is no conservation of momentum and energy. As the phonon bath is not part of our Hamiltonian the energy and momentum transferred to the phonon subsystem is considered *lost*[1]. There are two possible scattering processes to consider [59]. One of them is accounting to the emission and one to the absorption of a phonon,

$$\begin{aligned}
&\mathbf{k} \to \mathbf{k} - \mathbf{q}: \\
&\Gamma_k^{\mathrm{e,out}} = \sum_{\mathbf{q},q_z} \sum_{\pm} \frac{2\pi}{\hbar}\delta\left(E_k^{\mathrm{e}} - E_{k-q}^{\mathrm{e}} \pm \hbar\omega_{\mathrm{LO}}\right)|\gamma(q,q_z)|^2\, (n_{q,q_z} + \frac{1}{2} \mp \frac{1}{2})(1 - n_{k-q}^{\mathrm{e}}) \,, \\
&\mathbf{k} - \mathbf{q} \to \mathbf{k}: \\
&\Gamma_k^{\mathrm{e,in}} = \sum_{\mathbf{q},q_z} \sum_{\pm} \frac{2\pi}{\hbar}\delta\left(-E_k^{\mathrm{e}} + E_{k-q}^{\mathrm{e}} \pm \hbar\omega_{\mathrm{LO}}\right)|\gamma(q,q_z)|^2\, (n_{q,q_z} + \frac{1}{2} \mp \frac{1}{2}) n_{k-q}^{\mathrm{e}} \,.
\end{aligned} \tag{4.56}$$

[1] we will later discuss a temperature-model that relates the transferred energy to the lattice temperature.

The phonon dispersion relation ω_{LO} is assumed to be momentum-independent. For the phonon system being close to equilibrium, one can approximate n_{q,q_z} with a Bose-Einstein function.

Because of the typically high carrier-sheet densities in quantum-well lasers we assume that the distributions show only small deviations from the quasi-equilibrium Fermi-Dirac functions. It is therefore possible to linearise the equations (4.53) and (4.54) in the vicinity of the equilibrium state. One obtains the following expressions for the rates appearing in the collision terms (4.43) [35]:

$$\gamma_k^{\mathrm{e/h}} = \Gamma_k^{\mathrm{e/h,out}} + \Gamma_k^{\mathrm{e/h,in}}\Big|^{\mathrm{eq}} , \qquad \gamma_k^{\mathrm{p}} = \frac{1}{2}(\gamma_k^{\mathrm{e}} + \gamma_k^{\mathrm{h}}) . \tag{4.57}$$

These rates quantify how fast the carrier densities relax towards their quasi-equilibrium state and how fast the state of polarisation is destroyed. This loss of phase information is generally associated with a decay of coherence.

In FIGURE 4.2, the polarisation relaxation rates for both the Coulomb- and the Fröhlich-interaction are plotted as functions of the carrier-sheet density and the momentum. They were calculated by *K. Böhringer* for a quantum-well width of 5 nm by direct integration of the corresponding Boltzmann-integrals.

4.7 The Four-Band Model for the VCSEL

Due to the efficient carrier confinement multi quantum-well structures have widely replaced bulk material as gain media for VCSELs. As a consequence of the reduced dimensionality of the quantum-wells the degeneracy along the z-axis is lifted and we are left with several discrete electronic sub-levels for the bandstructure. In SECTION 4.2 we did already give a picture of the bandstructure in the vicinity of the band-edge. Around $k = 0$ the atomic quantum number of the angular moment J can be considered as a sufficently good quantum number and one knows from $\mathbf{k}\cdot\mathbf{p}$-theory that we have to deal at least with four bands, with each of them being two-fold degenerated: The s-like conduction $|j\, m_j\rangle = |1/2\ \pm 1/2\rangle$, the p-like heavy-hole $|3/2\ \pm 3/2\rangle$, the p-like light-hole $|3/2\ \pm 1/2\rangle$, and the s-like split-off band, $|1/2\ \pm 1/2\rangle$. For optical dipole radition with $E_z \approx 0$, the carrier transitions have to obey the selection rules $\Delta J = 0$ and $\Delta J_z = 0$. This, in principle, allows the heavy- and light-hole bands to participate the stimulated emission and absorption processes. For strained quantum-wells the light-hole's energy is lowered and we can assume that the only transition active is the one between the conduction and the heavy-hole band. As each band has an bears a certain angular momentum we associate this model with the picture of two spin-baths[2] which we denote '+' and '−' according to the sign of $J_z = \pm 1$. FIGURE 4.3 visualised the 4-band model. A reduction of this model to a 4-level model would lead to the *SFM model* first proposed by

[2] the expression *spin-bath* is slightly misleading. What is meant is the total angular momentum resulting from spin-orbit coupling.

San Miguel et al. [99]. Extensions incorporating band-resolved dynamics can be found in [112–114].

Instead of introducing a *spin-flip* rate at a microscopic level. we asssume that there is an implicit spin-exchange between the '+' and the '−' baths as carriers are in- and out-scattered from the k-values $k_{\rm op}$ where the optical transition takes place. The actual spin-flip is implemented on a mesoscopic level by splitting the mesoscopic density into two,

$$N = N^+ + N^- \,, \tag{4.58}$$

$$N^\sigma = A^{-1} \sum_{\mathbf{k}} n_{\mathbf{k}}^{\mathrm{e},\sigma} = A^{-1} \sum_{\mathbf{k}} n_{\mathbf{k}}^{\mathrm{h},\sigma} \,. \tag{4.59}$$

N^+ and N^- are entering the respective Fermi-distribution functions.

We apply the discussed modifications and extend the semiconductor-Bloch equations (4.37)-(4.39) to the *4-band semiconductor-Bloch equations*

$$\partial_t n_{\mathbf{k}}^{\mathrm{e},\pm} = g_{\mathbf{k}}^{\pm} + \Lambda_{\mathbf{k}}^{\mathrm{e}} \left(1 - n_{\mathbf{k}}^{\mathrm{e},\pm}\right) - w_{\mathrm{sp},\mathbf{k}}^{\pm} - \gamma_{\mathrm{nr}}\, n_{\mathbf{k}}^{\mathrm{e},\pm} - \gamma_k^{\mathrm{e}} \left(n_{\mathbf{k}}^{\mathrm{e},\pm} - f_{\mathbf{k}}^{\mathrm{e},\pm}\right) \,, \tag{4.60}$$

$$\partial_t n_{\mathbf{k}}^{\mathrm{h},\pm} = g_{\mathbf{k}}^{\pm} + \Lambda_{\mathbf{k}}^{\mathrm{h}} \left(1 - n_{\mathbf{k}}^{\mathrm{h},\pm}\right) - w_{\mathrm{sp},\mathbf{k}}^{\pm} - \gamma_{\mathrm{nr}}\, n_{\mathbf{k}}^{\mathrm{h},\pm} - \gamma_k^{\mathrm{h}} \left(n_{\mathbf{k}}^{\mathrm{h},\pm} - f_{\mathbf{k}}^{\mathrm{h},\pm}\right) \,, \tag{4.61}$$

$$\partial_t p_{\mathbf{k}}^{\pm} = -\left(i\,\Delta\bar{\omega}_{\mathbf{k}} + \gamma_k^{\mathrm{p}}\right) p_{\mathbf{k}}^{\pm} - i\mathcal{U}^{\pm} \left(n_{\mathbf{k}}^{\mathrm{e},\pm} + n_{-\mathbf{k}}^{\mathrm{h},\pm} - 1\right) \,, \tag{4.62}$$

which include the expressions

$$\mathcal{U}_{\mathbf{k}}^{\pm} = 1/\hbar\, M_{\mathrm{cv},\mathbf{k}}^{\pm} E^{\pm} + \Delta\mathcal{U}_{\mathbf{k}} \,, \tag{4.63}$$

$$g_{\mathbf{k}}^{\pm} = 2\,\mathrm{Im}\left[\mathcal{U}_{\mathbf{k}}^{\pm} p_{\mathbf{k}}^{\pm *}\right] \,, \tag{4.64}$$

$$w_{\mathrm{sp},\mathbf{k}}^{\pm} = B_{\mathbf{k}}\, n_{\mathbf{k}}^{\mathrm{e},\pm} n_{\mathbf{k}}^{\mathrm{h},\pm} \,, \tag{4.65}$$

$$\Lambda_{\mathbf{k}}^{\mathrm{e/h}} = \Lambda_0 f_{\mathbf{k}}^{\mathrm{e/h}} \left[A^{-1} \sum_{\mathbf{k},\sigma=\pm} f_{\mathbf{k}}^{\mathrm{e/h}} \left(1 - n_{\mathbf{k}}^{\mathrm{e/h},\sigma}\right)\right]^{-1} \,, \tag{4.66}$$

for the renormalised field, the stimulated carrier generation rate, the loss of free carriers due to spontaneous emission, and the pump-term accounting for carrier-thermalisation and pump-blocking effects. The equilibrium Fermi-functions are associated with the mesoscopic density N and the temperature T,

$$f_{\mathbf{k}}^{\mathrm{e},\pm} = f_{\mathbf{k}}^{\mathrm{e}}(N^{\pm}, T) \,, \tag{4.67}$$

$$f_{\mathbf{k}}^{\mathrm{h},\pm} = f_{\mathbf{k}}^{\mathrm{h}}(N^{\pm}, T) \,. \tag{4.68}$$

E_+ and E_- are the right- and left-circular polarised field components, which induce transitions in the '+' and '−' baths respectively.

Equations (4.60)-(4.62) feature the dynamic impact of all the relevant scattering processes: the non-radiative recombination of carriers, the dephasing of polarisation due

to carrier-carrier scattering and the scattering of carriers with LO-phonons and finally the redistribution of the carrier distributions $n_k^{\mathrm{e/h}}$ to the equilibrium Fermi-Dirac functions by carrier-carrier scattering. Carrier-carrier scattering is the mechanism which is rebalancing the spectral distribution of carriers towards the thermal quasi-equilibrium functions. As this is a spin-conserving process each reservoirs '+' and '−' are relaxating to their own associated equilibrium fermi-functions.

Summing up the above microscopic quantities one gets the respective mesoscopic source- and loss-terms,

$$G^{\pm} = A^{-1} \sum_{\mathbf{k}} g_{\mathbf{k}}^{\pm} \,, \tag{4.69}$$

$$\Gamma_{\mathrm{sp}}^{\pm} = A^{-1} \sum_{\mathbf{k}} w_{\mathrm{sp},\mathbf{k}}^{\pm} \,, \tag{4.70}$$

$$P^{\pm} = n_{\mathrm{QW}} (A \cdot d)^{-1} \sum_{\mathbf{k}} M_{\mathrm{cv},\mathbf{k}}^{\pm} \, p_{\mathbf{k}}^{\pm} \,, \tag{4.71}$$

which represent the total coherent carrier generation rate G, the total carrier loss by spontaneous emission Γ_{sp} and the total polarisation of the active medium $P^{\pm}$. In contrast to the carrier generation and spontaneous emission rate which are summed up to carrier-sheet densities of the individual quantum-well layers, it is important to note, that the polarisation is multiplied with the well-number n_{QW} and divided by the active region width d (see FIGURE 4.4).

In isotropic approximation the sums can be converted to a scalar k-integration, thereby introducing the isotropic two-dimensional density of states $D(k) = A(2\pi)^{-1}k$,

$$A^{-1} \sum_{\mathbf{k}} \cdots = A^{-1} \int_0^{k_{\max}} \mathrm{d}k \, D(k) \ldots \,; \tag{4.72}$$

$k_{\max}$ is a numerical cut-off k-value used for numeric integration ($f_{k_{\max}}^{\mathrm{e/h}} \ll 1$).

The given band- or k-resolved semiconductor-Bloch equations are to be coupled to the mesoscopic equations. This leads to a closed set of equations which can be numerically solved in time and space in a selfconsistent way [43, 50, 115]. This will be subject of CHAPTER 5. We note, that many typical effects in semiconductor lasers like spectral hole burning as well as propagation effects of extremely short and intense pulses [116] require band-resolved models.

4.8 Adiabatic Elimination and Static Gain Response

The k-resolved description of the gain medium is coupled with the laser light field via the induced susceptibility. The microscopic variables depend on the momentum and

on the mesoscopic fields, the carrier density, the optical field, and the temperatures. If we assume that these variables instantly follow the mesoscopic field variables (because of the fast time scales involved in the microscopic scattering processes) the complex susceptibiliy depending on N, T and Ω can be calculated as following:

$$\begin{aligned}\chi_{\Omega}^{\pm} &= \chi_{\Omega}(N^{\pm}, T) \\ &= -\epsilon_0^{-1} n_{\mathrm{QW}} (A \cdot d)^{-1} \sum_{\mathbf{k}} \frac{|M_{\mathrm{cv},\mathbf{k}}|^2}{\hbar} \frac{\Delta\bar{\omega}_k + i\gamma_k^{\mathrm{p}}}{(\Delta\bar{\omega}_{\mathbf{k}})^2 + (\gamma_k^{\mathrm{p}})^2} (f_{\mathbf{k}}^{\mathrm{e},\pm} + f_{-\mathbf{k}}^{\mathrm{h},\pm} - 1) \cdot Q_{\mathbf{k}}\end{aligned} \tag{4.73}$$

where $Q_{\mathbf{k}}$ is the interband Coulomb-enhancement factor. In Padé-Approximation it reads [117]

$$Q_{\mathbf{k}} = \frac{1}{1 - q(\mathbf{k})}\,, \qquad q(\mathbf{k}) = \frac{1}{M_{\mathrm{cv},\mathbf{k}}} \sum_{\mathbf{k}' \neq \mathbf{k}} W(\mathbf{k} - \mathbf{k}')\,. \tag{4.74}$$

For the Fermi-functions the abbreviation $f^{\mathrm{e},\pm} = f^{\mathrm{e}}(N^{\pm}, T)$ and $f^{\mathrm{h},\pm} = f^{\mathrm{h}}(N^{\pm}, T)$ have been used.

Taking a phenomenological model for the energy renormalisation and assuming an equilibrium of temperatures – that is by equalising setting lattice and plasma temperatures – one can calculate the small signal gain as shown in FIGURE 4.5 from the k-resolved polarisation scattering rates. It turns out, that in many cases, where light- and density dynamics are slow enough, such a static response function is sufficiently accurate. Concerning the simulation time, a mesoscopic approach is often more practical, as the time- and space-resolved k-space integrations of the microscopic equations (4.60) - (4.62) can be dropped. For a simplified numerical implementation further local approximations can be applied in the to the static gain to mimic the behaviour of the material in the vicinity of predefined operation conditions [71].

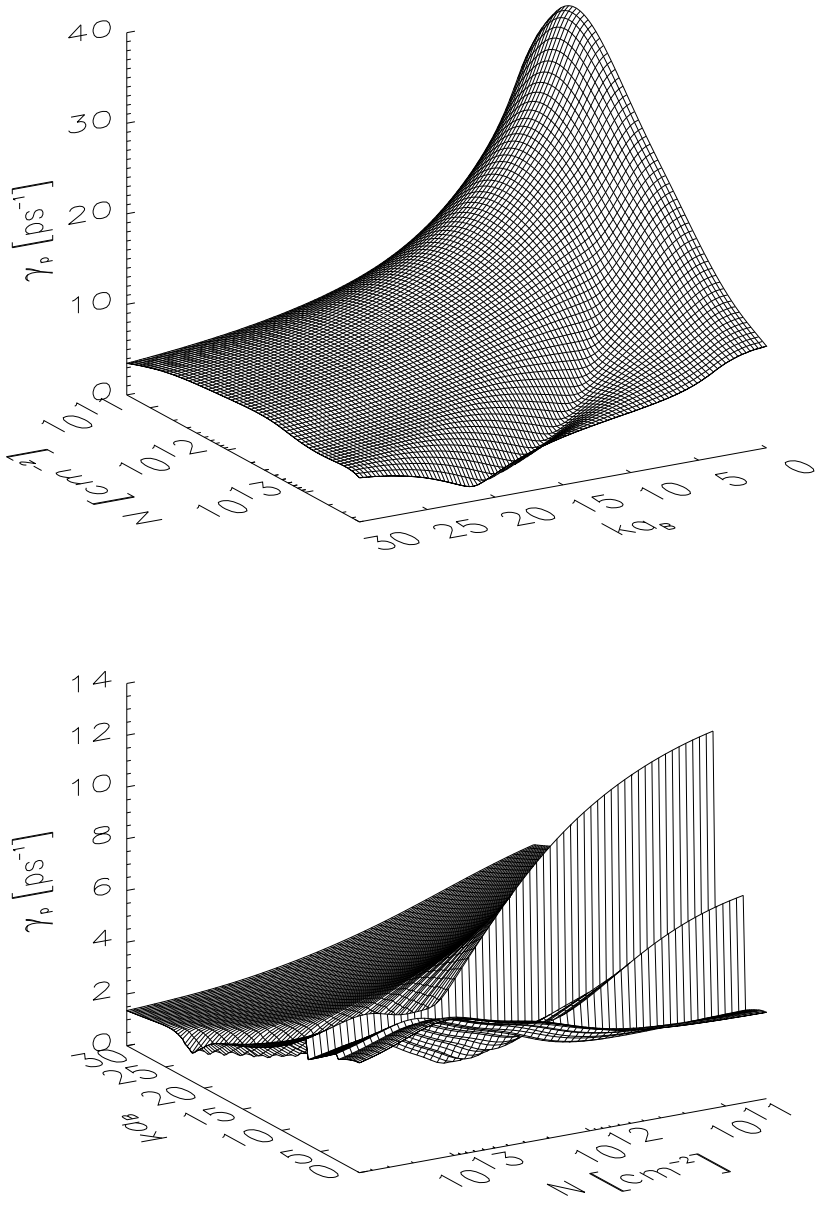

Figure 4.2: The dephasing rates of the carrier interband-polarisation, plotted over density and momentum, for the carrier-carrier (left) and the carrier-phonon (right) interaction. For the Fröhlich-interaction there exist a threshold momentum k. For energies lower than $\hbar\omega_{\mathrm{LO}}$ the creation of phonons is almost impossible. This edge is associated with electron-phonon scattering, while the second edge, at the higher momentum, is due to hole-phonon scattering. At laser operation typical scattering times near the band-edge are about 50 fs for the Coulomb- and about 200 fs for the Fröhlich-interaction – with friendly permission of *K. Böhringer*.

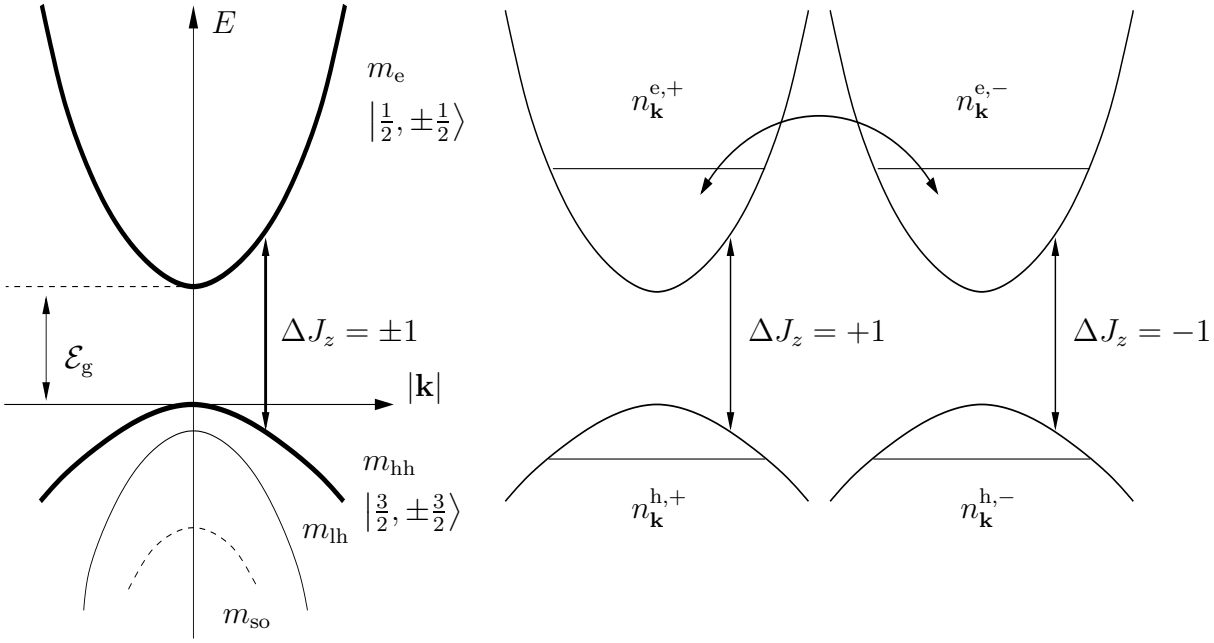

Figure 4.3: Left: Energetic scheme of a strained GaAs quantum-well structure. The optical $J_z = \pm 1$ transition is assumed to take place between the conduction and the heavy-hole band. The light-hole band is energetically lowered due to the influence of strain. Right: Spin-bath picture. Carriers of different angular momentum are created by the optical transitions. The curved arrow indicates an exchange mechanism between the carrier baths.

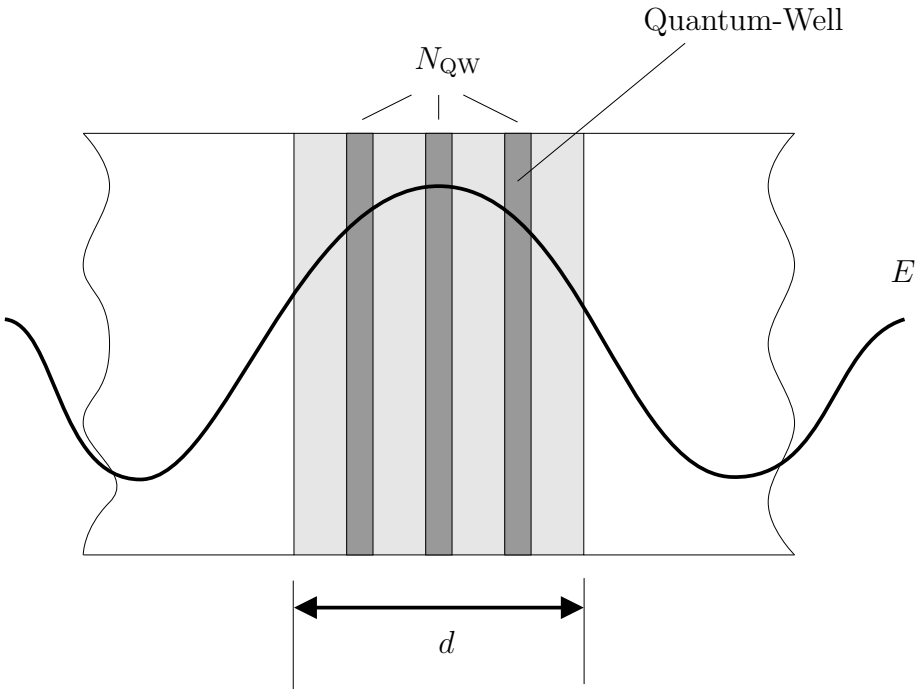

Figure 4.4: Sketch of the active area of a three quantum-well VCSEL. d, the active zone thickness, and n_{QW}, the number of quantum-wells are used to convert the polarisation sheet density to the three-dimensional polarisation which couples to the electric field equation. Most of the carrier related quantities are related to the individual quantum-wells, which are treated to be in an identical state.

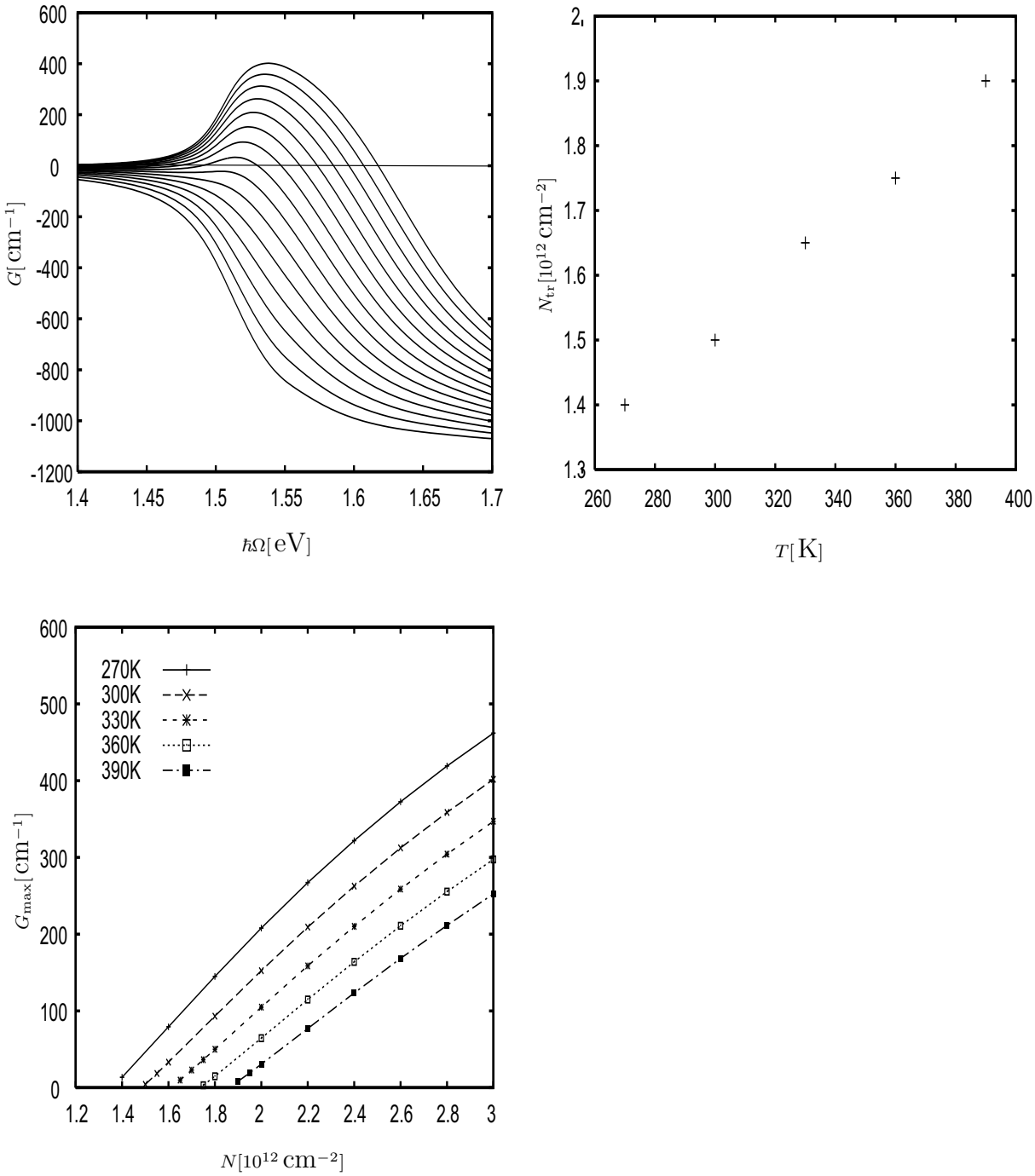

Figure 4.5: Parameter dependence of the gain and the threshold density for a 5 nm GaAs quantum-well structure. Top left: small-signal gain G plotted over the light field energy for different carrier-sheet densities N within the range $[2\cdot10^{11}\,\mathrm{cm}^{-2}, 3\cdot10^{12}\,\mathrm{cm}^{-2}]$ (at $T = 300\,\mathrm{K}$). Top right: transparency density N_{tr} in dependence of temperature. Bottom: Peak gain value G_{max} over density N for different temperatures – with friendly permission of *K. Böhringer*.

5 Transverse Multi-Mode VCSEL Dynamics

5.1 Introduction

In this chapter we put the equations for the optical, carrier, and lattice together and establish a solver schema which is subsequently used to simulate the transversal mode-dynamics of VCSEL structures. The dynamics of the optical subsystem is described by the paraxial wave-equation (3.69) which we deduced in CHAPTER 3. This first order equation describes the evolution of the transverse resolved electromagnetic modes within the cavity in a phase- and polarisation sensitive way. Terms accounting for diffraction, resonator losses, optical birefringence and material polarisation are contained. We complement the optical field by adequate material equations describing the behaviour of the induced material polarisation in response to the optical field. The material model comprises the dynamics of electrons and holes of the lowest conduction and valence subband within the active GaAs quantum-well layers. Calculations are consistently based on the microscopic considerations presented in CHAPTER 4. As the polarisation is dependent on both the electric field and the carrier's density we have to add an equation accounting for the ambipolar diffusion of the carriers in the plane of the quantum-well sheet. The resulting dynamical model includes the features of other well-established semiconductor models [9, 99, 105, 112, 118, 119]. However, the combination of transverse resolved optical wave-equation adapted to structured microcavities in combination with a k-resolved quantum-well material model enables us to give a more complete dynamical description of a VCSEL than all the previous models did. Due to the fast time-scales imposed by the mode-beating of transverse mdoes, a combination of spectral and spatial hole-burning effects have to be taken into account in order to explain the basic system characteristics [115, 115, 120, 121]. Furthermore, the bottom-up approach provides an easy interface and allows integrate dynamic temperature effects which are responsible for a effects like *thermal lensing* and *thermal rollover* in a consistent way. Depending on the scope of the studies we are able to activate or deactivate the intraband carrier dynamics and the temperature dynamics. This possibility to rebalance the model offers some flexibility to adapt it to the specific problem.

The dynamic model is applied to predefined VCSEL structures which are subject of a detailed numerical investigations. This includes the analysis of the state of polarisation, the mode-dynamics, temperature and the spectral properties and the k-resolved dynamics. Information can be extracted on a broad range of timescales, revealing various levels

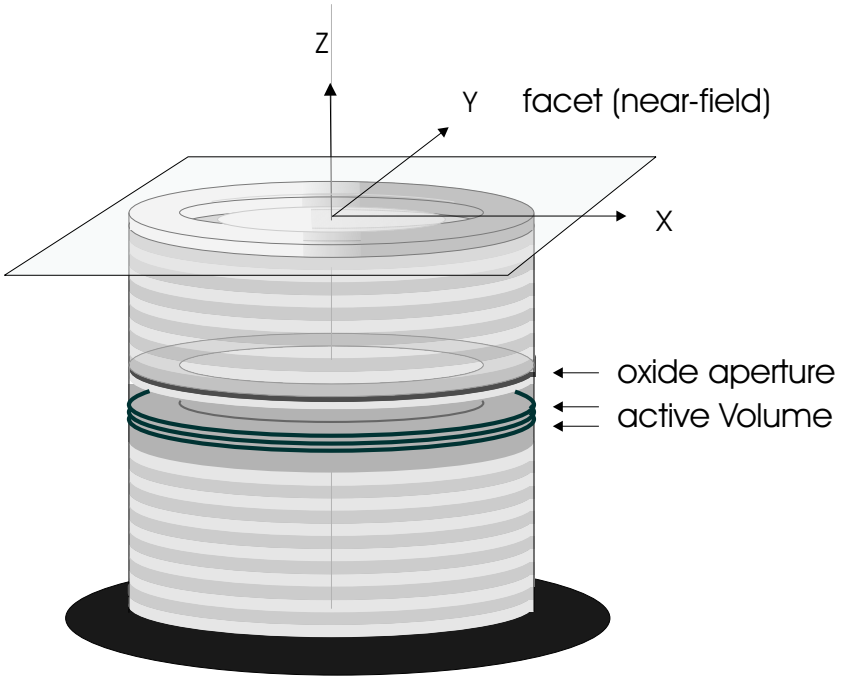

Figure 5.1: Schematic view of VCSEL with applied coordinate system. The x-y-plane indicates the simulation domain. To avoid boundary effects the integration domain for the PDEs is usually chosen to be twice the diameter of the oxide aperture.

and aspects of interaction. They range from intraband processes which are typically sub-picosecond to carrier relaxation and diffusion times are situated on a nanosecond scale. By comparing numerical simulations based on this theory with time-resolved experiments [122] we are able to show how far our VCSEL model coincides with the real dynamics of real VCSEL devices.

5.2 Basic Set of Equations

The equations needed for a description of time-resolved transverse laser dynamics can be classified in equations for the light-field and equations describing the state of the semiconductor material as far as relevant for the laser activity. Equation (3.69), which is already well adapted for VCSEL-like structures, serves as a starting point. The bars on top, indicating the mean-field average and the subscript symbol '$\perp$', symbolising the transverse nature of the polarisation vector are omitted from now on. In compact notation the optical field equation for the electrical field vector $\mathbf{E} = (E_x, E_y)$ reads

$$\begin{aligned} v_{\text{eff}}^{-1}\,\partial_t \mathbf{E} = &-\gamma_{\text{res}}\mathbf{E} + iD_p\nabla^2\mathbf{E} + iK_0\Theta_z\,\delta n^{\text{g}}\,\mathbf{E} + iK_0\,\delta\mathbf{n}^{\text{c}}\cdot\mathbf{E} \\ &+ 2iD_p\Theta_z\,n_{\text{eff}}^{-1}\nabla\left(\mathbf{E}\cdot\nabla\delta n^{\text{g}}\right) + i\kappa\Gamma_z\mathbf{P} \end{aligned} \tag{5.1}$$

with $\nabla = (\partial_x, \partial_y)$ and $\Theta_z = \langle\Theta\rangle_z$. Furthermore, the following factorisations have been applied which are justified by the calculations presented in FIGURE 3.5: $\langle\nu\Theta\rangle_z \approx$

$\langle\nu\rangle_z \langle\Theta\rangle_z$ and $\langle\sigma\Theta\rangle_z \approx \langle\sigma\rangle_z \langle\Theta\rangle_z$. In addition, the numerical analysis shows, that for common GaAs VCSEL it is sufficient to assume $\langle n\rangle_z \approx n_{\text{eff}}$, $\langle n^{-1}\rangle_z \approx n_{\text{eff}}^{-1}$. Besides the field quantities $\mathbf{E}$ and $\mathbf{P}$ a series of parameters (3.39), (3.41), (3.56), (3.58) enter this equation being either related to the dielectric structure or of physical nature.

In order to include ambipolar diffusion within the quantum-well sheets into our model the optical field equation and the material equations derived in CHAPTER 4 have to to be supplemented with a phenomenological equation accounting for the electron / hole densities of the lowest conduction and valence sub-band. We use equation an equation similar to (2.8) but extend it by a couple of phenomenological terms: The spontaneous emission rate Γ_{sp}, an Auger-recombination term Γ_{aug}, an ambipolar diffusion term D_f and last but not least the carrier pump Λ. This leads to

$$\partial_t N^{\pm} = G^{\pm} - D_f \Delta N^{\pm} - \gamma_{\text{s}} \left(N^{+} - N^{-} \right) - \gamma_{\text{nr}} N^{\pm} + \Lambda^{\pm} - \Gamma_{\text{sp}}^{\pm} - \Gamma_{\text{aug}}^{\pm} \,. \tag{5.2}$$

G is the carrier generation rate, which already appeared in CHAPTER 2 and CHAPTER 4. It is generally defined by

$$G^{\pm} = -\epsilon_0^{-1} n_{\text{QW}}^{-1} d \frac{2}{\hbar} \text{Im} \left[P^{\pm *} \cdot E^{\pm} \right] \,. \tag{5.3}$$

Further terms include the spin-relaxation time $\tau_{\text{s}} = 1/\gamma_{\text{s}}$ [123] and the non-radiative recombination-time $\tau_{\text{nr}} = 1/\gamma_{\text{nr}}$ which is related to carrier capturing in the deep-trap levels of impurities; a process which is followed by dark recombination with a hole of the valence band. For GaAs this so-called *Shockley-Read recombination-mechanism* gives the dominant contribution to dark recombination. The associated decay time is know to be around $\tau_{\text{nr}} \sim 5\,\text{ns}$ depending on the impurity level. However, for longer near-infrared wavelength, narrow narrow band-gap material is used and the situation becomes different. For these materials Auger-recombination processes are significant loss channels. The origin of the Auger-recombination are triple collisions where the energy of the recombining electron-hole pair is transfered to a third electron which is then excited into a higher sub-band. For low densities the Auger-processes lead to an decay term proportional to N^3. Thus, both, the Auger-recombination and the rate of spontaneous emission serve as additional nonlinear damping channels in equation (5.2). However, as we are mainly interested in the Al-GaAs/GaAs material system, we will usually neglect the influence of Auger-processes in our simulations.

We want to mention, that the calculation of the carrier pump Λ for VCSEL structures is a task of its own. The relation

$$\Lambda = \frac{\eta}{e} j \tag{5.4}$$

relates the carrier pump to the current density j, the total quantum-efficiency η and the active zone's thickness d. However, a complete description of the carrier transport would request a three-dimensional treatment of carriers which are injected at the top

(ring-)contact and the bottom contact of the VCSEL. The equations to solve are drift-diffusion equations for electrons and holes coupled to a Poisson equation. The field potential arises as a consequence of free carriers, the doping levels and the externally applied fields. In quasi-equilibrium the current density takes a stationary profile. One consequence of the drift-diffusion is that the spatial profile of the carriers injected into the quantum-wells does not appear to have sharp defined boundaries. For our model we apply predefined carrier pump profiles like the one shown in FIGURE 5.2 to the active zone.

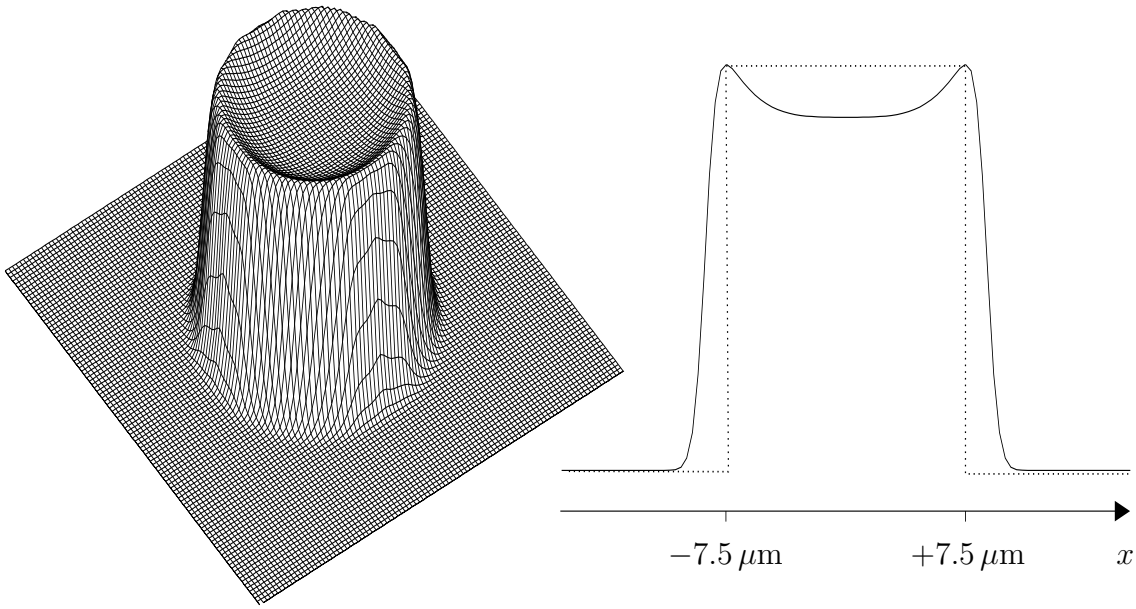

Figure 5.2: Transverse pump profile of a VCSEL $\Lambda_0(x, y)$. The borders are smoothed out by successive application of a diffusion algorithm to a rectangular profile. The carrier pump is set higher at the edge of the oxide-aperture in order to adapt the model to the specific ring-contact / oxide-aperture constellation.

The missing link between the optical equation and the carrier density equation are the active material equations. As previously discussed, the response functions entering the above equations can be calculated from microscopic semiconductor-Bloch equations (4.60)-(4.62). The respective sums enter the rhs of (5.2) and (5.1) and are connected to the microscopic variables via the equations (4.71). The complex electric field vector couples to the two spin-baths of microscopic dipoles with its circular polarised components. This means one has to perform a transformation between circular and cartesian coordinates,

$$E^{+}\mathbf{e}_{+} + E^{-}\mathbf{e}_{-} = E_x\mathbf{e}_x + E_y\mathbf{e}_y \tag{5.5}$$

where the component transformation rules given by (D.10), (D.11) apply. This also holds, for the polarisation which emerges in circular polarised coordinates from the material equations and has to be transformed back to cartesian coordinates in order to suit

to (5.1).

The sum over $\mathbf{k}$ in (4.71) is transformed into an integration weighted with the two-dimensional density of states (4.72). This was discussed in section SECTION 4.7. On the other hand the microscopic equations are itself functionally dependent on N and $\mathbf{E}$. This leads to a recursion which can not be analytically solved anymore. For an iterative procedure we have to consider the timescales which are intrinsically connected with the various equations. This is depicted in FIGURE 5.3. The approach is justified as long as the microscopic dynamics takes place on much faster timescales than e.g. the dynamics described by (5.1), (5.2). This means, that concerning the Semiconductor-Bloch equations, N and E to take the role of slowly varying parameters.

The replacement of the microscopic densities $n_{\mathbf{k}}^{\mathrm{e},\pm}$ and $n_{\mathbf{k}}^{\mathrm{h},\pm}$ by their respective Fermi-function equivalents enables – after the adiabatic elimination of $\partial_t p_{\mathbf{k}}^{\pm}$ – a transition from dynamic sources (5.5) to response functions. Instead of the functional response character we obtain simple response functions in $N^{\pm}$ and $\mathbf{E}$

$$\begin{aligned} P^{\pm} &= \epsilon_0 \chi_\Omega(N^{\pm}, T) E^{\pm} \,, \\ \Gamma_{\mathrm{sp}}^{\pm} &= A^{-1} \sum_{\mathbf{k}} B_{\mathbf{k}} f_{\mathbf{k}}^{\mathrm{e},\pm} f_{\mathbf{k}}^{\mathrm{h},\pm} \,, \end{aligned} \tag{5.6}$$

as described in section (4.8) of CHAPTER 4. For the pump Λ we substitute $\Lambda = \Lambda_0$. The polarisation and the spontaneous emission are functions of N, T, and Ω. The functional dependence of the static gain response χ is defined by (4.73). One has to be aware that intraband processes, which are conserving the particle number (e.g. intraband scattering) do not contribute to carrier leakage and that both carrier-carrier and carrier-phonon scattering processes are spin-conserving.

In cases where the fields are varying rather slowly a more radical approximation can be chosen. If we linearise $\mathbf{P}$ around the threshold density $N = N_{\mathrm{thr}}$ we can write

$$P^{\pm}(\Omega, N^{\pm}, E^{\pm}) = -g(\Omega, N_{\mathrm{thr}})[i + \alpha(\Omega, N_{\mathrm{thr}})](N^{\pm} - N_{\mathrm{thr}}) E^{\pm} \,. \tag{5.7}$$

The differential gain and the alpha-factor independent of the spin-state and are defined by

$$\begin{aligned} g(\Omega, N_{\mathrm{thr}}) &= -\operatorname{Im}[\,\partial\chi/\partial N\,]\big|_{N=N_{\mathrm{thr}}} \,, \\ \alpha(\Omega, N_{\mathrm{thr}}) &= \left.\frac{\operatorname{Re}[\,\partial\chi/\partial N\,]}{\operatorname{Im}[\,\partial\chi/\partial N\,]}\right|_{N=N_{\mathrm{thr}}} . \end{aligned} \tag{5.8}$$

Nevertheless, the above k-resolved processes are the source for a spin-resolved spectral redistribution of energy within the band and therefore play an important role for experiments where the spectral hole-burning is a strong effect [124]. If we are interested in such sub-picosecond effects the microscopic band-resolved equations (4.60)-(4.62) have to be solved. In fact, the k-resolved simulations are computationally expensive. However, the

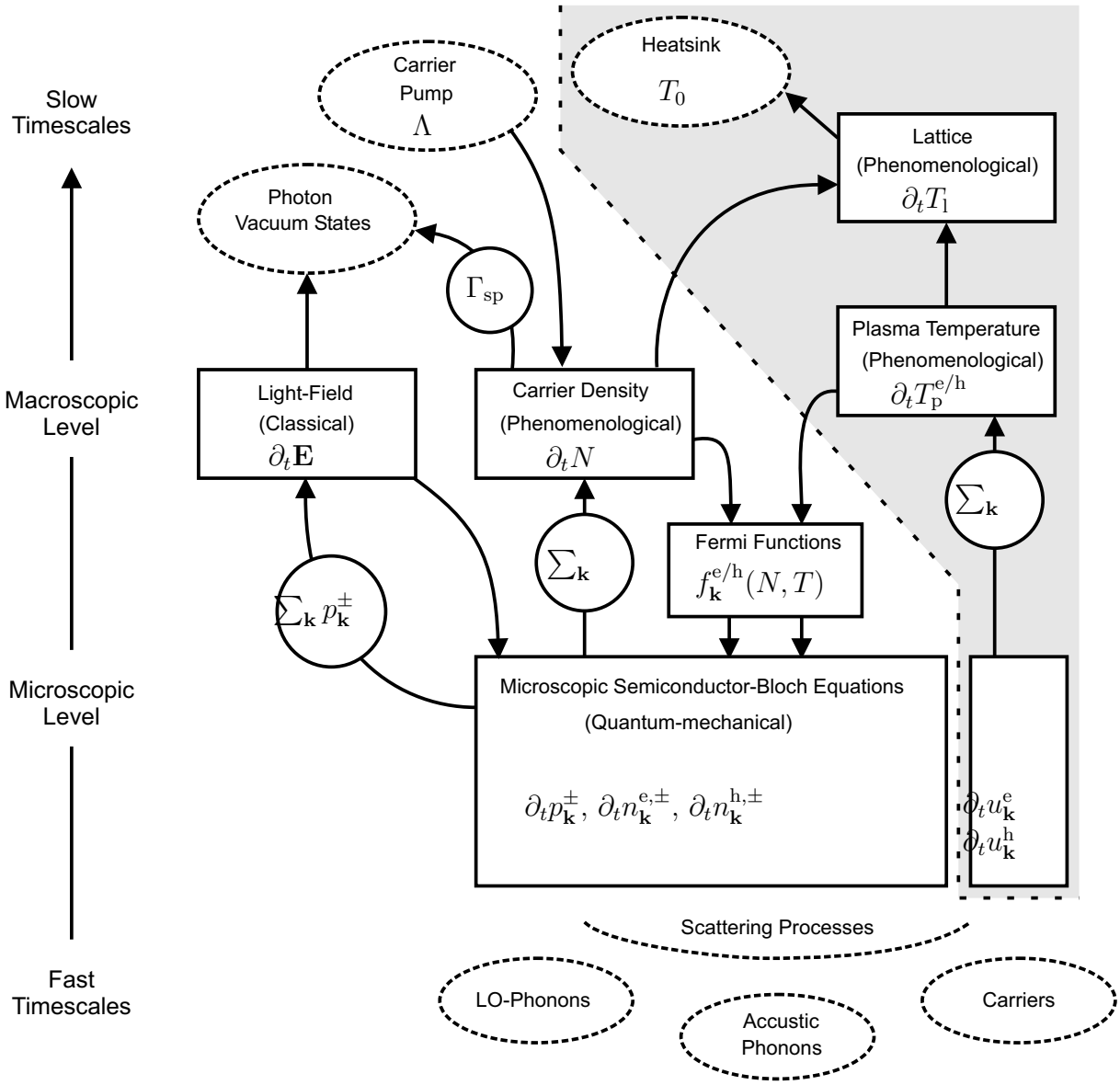

Figure 5.3: Interaction of the different levels of the VCSEL model. The macroscopic light-field $\mathbf{E}$ and carrier density N are considered as slowly varying variables that enter the fast oscillating band resolved Semiconductor-Bloch equations. The microscopic quantities feedback into the macroscopic equations via the summed up (dynamic) sources (5.5). The temperature parts are included on the right hand side of the diagram.

much more efficent mesoscopic model can be used prepare the relaxed system state taken after some nanoseconds time and then be followed by a microscopic simulation. The possibility to switch between different levels of material responses can also help to identify the origin of effects. A good example is SECTION 5.13 where the direct comparision of the polarisation intensities reveals that the polarisation mode suppression can partially

be attributed to spectral carrier polarisation.

5.3 Scale Invariance

In order to gain a deeper understanding for the equations (5.1) and (5.2), we assume $N = 2N^+ = 2N^-$ and a linear relation $P = \epsilon_0\chi(N)E$ between polarisation and electric field vector. Neglecting the Auger-recombination and the spontaneous emission term in (5.2), one obtains

$$\begin{aligned} v_{\text{eff}}^{-1}\,\partial_t\mathbf{E} &= -\gamma_{\text{res}}\mathbf{E} + iD_p\nabla^2\mathbf{E} + iK_0\Theta_z\,\delta n^{\text{g}}\,\mathbf{E} + iK_0\,\delta\mathbf{n}^{\text{c}}\cdot\mathbf{E} \\ &\quad + 2iD_p\Theta_z\,n_{\text{eff}}^{-1}\nabla\left(\mathbf{E}\cdot\nabla\delta n^{\text{g}}\right) + i\kappa\Gamma_z\chi(N)\mathbf{E}\,, \\ \partial_t N &= D_f\nabla_\perp^2 N + \Lambda - \gamma_{\text{nr}}N - \frac{2}{\hbar}\text{Im}(\chi)(N)\cdot|\mathbf{E}|^2\,. \end{aligned} \tag{5.9}$$

After rescaling the space and time coordinates,

$$x \to \tilde{x} = x/\alpha\,, \quad t \to \tilde{t} = t/\alpha^2 \tag{5.10}$$

we can define new field quantities

$$\tilde{\mathbf{E}}(\tilde{x},\tilde{t}) = \alpha\mathbf{E}(\alpha\tilde{x},\alpha^2\tilde{t}\,) \tag{5.11}$$

$$\tilde{N}(\tilde{x},\tilde{t}) = N(\alpha\tilde{x},\alpha^2\tilde{t}\,) \tag{5.12}$$

which are considered to be dependent on the new coordinates $\tilde{x}$ and $\tilde{y}$. The transformation of (5.9) to new field quantities and the new coordinates leads to

$$\begin{aligned} v_{\text{eff}}^{-1}\,\partial_{\tilde{t}}\tilde{\mathbf{E}} &= -\alpha^2\gamma_{\text{res}}\tilde{\mathbf{E}} + iD_p\tilde{\nabla}^2\tilde{\mathbf{E}} + i\alpha^2K_0\Theta_z\,\delta n^{\text{g}}\,\tilde{\mathbf{E}} + i\alpha^2K_0\,\delta\mathbf{n}^{\text{c}}\cdot\tilde{\mathbf{E}} \\ &\quad + 2iD_p\Theta_z\,n_{\text{eff}}^{-1}\tilde{\nabla}\left(\mathbf{E}\cdot\tilde{\nabla}\delta n^{\text{g}}\right) + i\alpha^2\kappa\Gamma_z\chi(\tilde{N})\tilde{\mathbf{E}}\,, \end{aligned} \tag{5.13}$$

$$\partial_{\tilde{t}}\tilde{N} = D_f\tilde{\nabla}_\perp^2 N + \alpha^2\Lambda - \alpha^2\gamma_{\text{nr}}\tilde{N} - \frac{2}{\hbar}\text{Im}(\chi)(\tilde{N})\cdot|\tilde{\mathbf{E}}|^2\,. \tag{5.14}$$

It is possible to retain the old shape (5.9) if we simultaneously perform a transformation of the parameters,

$$\begin{aligned} &\Gamma_z \to \tilde{\Gamma}_z = \alpha^2\Gamma_z\,, \\ &\Theta_z \to \tilde{\Theta}_z = \alpha^2\Theta_z\,, \\ &\delta\tilde{\mathbf{n}}^{\text{c}} = \alpha^2\delta\mathbf{n}^{\text{c}}\,, \\ &\gamma_{\text{res}} \to \tilde{\gamma}_{\text{res}} = \alpha^2\gamma_{\text{res}}\,, \\ &\Lambda \to \tilde{\Lambda} = \alpha^2\Lambda\,, \\ &\gamma_{\text{nr}} \to \tilde{\gamma}_{\text{nr}} = \alpha^2\gamma_{\text{nr}}\,. \end{aligned} \tag{5.15}$$

This means that the equations (5.9) are invariant under a combined scaling of coordinates, fields and parameters. Λ scales with α^2. However, the pump in units of the

threshold pump Λ_{thr} stays unscaled. It is well known, that multi-mode dynamics depends critically on the transverse systems size [125, 126]. However, instead of blowing up the geometric size by a factor α it is possible to achieve the same multi-mode behaviour on a shorter timescale by scaling up the parameters (5.15) with a factor α^2. It turns out, that from the above parameters it are mainly Λ, Γ_z and γ_{res} which have a dominant influence on the multi-mode dynamics. In general, the dynamic influence of γ_{nr} (which is material dependent) is rather weak. From this we understand, that if we aim at constructing a small multi-mode laser device, we have to assure, that the pump is high above threshold, the resonator is lossy, and the active material coupling is as good as possible.

5.4 The Influence of Temperature

VCSEL structures, in general, have to be attached to good heat-sinks as both output power and the number of active transverse near-field modes are very sensitive to a change of temperature conditions. In contrast to edge emitting devices, one has to be aware that the heat produced in the active zone has to be effeciently drained from the quantum-wells, the barriers and the bottom-DBR which are of some μm thickness together.

Our material model of Section 4.7 applies to the active quantum-well structures and but contains no longitudinal information. It is therefore reasonable to distinguish three different temperatures: the plasma temperatures of the free carriers in the active zone, the temperature of the lattice in the active zone and the temperature of the structure encompassing the active zone. To shorten the notation we will speak of lattice temperature, plasma temperatures and ambient temperature and denote them with T_{l}, $T_{\mathrm{p}}^{\mathrm{e/h}}$ and T_0. As our dynamic description is essentially reduced to the active zone, the ambient temperature T_0 has to be interpreted as a temperature parameter of the structure itself rather than of the heat-sink alone. We note that Spoken more explicitly: T_0 would only be the temperature of the heat-sink if the structure is a perfect heat conductor. In this section the temperatures T_{l} and $T_{\mathrm{p}}^{\mathrm{e/h}}$ will be considered as dynamic field variables. This holds as long as we can attribute temperatures to the individual sub-systems (carrier, phonon) and a local thermal quasi-equilibrium exists.

A dynamic temperature model is essentially an energy transfer model [107, 127]. Energy transfer occurs between the light field and the carriers, between carriers and the LO-phonons of the active zone and finally, due to heat transport, to the surrounding structure elements. We include temperatures on the microscopic level by replacing temperature parameters with the appropriate variables and by formulating equations of motion for T_{l} and $T_{\mathrm{p}}^{\mathrm{e/h}}$. Equations (5.1) and (5.2) are not explicitly dependent on temperatures. However, the Semiconductor-Bloch equations include a couple of temperature dependent terms. Within the microscopic equations (4.60) - (4.62) we have to take into account

that the band-gap renormalisation (4.52)

$$\Delta\mathcal{E}^{\mathrm{e/h}} = \Delta\mathcal{E}^{\mathrm{e/h}}(N, T_{\mathrm{l}}) \tag{5.16}$$

is a function of the lattice temperature and that the carrier-carrier scattering-terms

$$\gamma_k^{\mathrm{e/h}} \left(n_{\mathbf{k}}^{\mathrm{e/h},\pm} - f_{\mathbf{k}}^{\mathrm{e/h}} \right) = \gamma_k^{\mathrm{e/h}} \left(n_{\mathbf{k}}^{\mathrm{e/h},\pm} - f_{\mathbf{k}}^{\mathrm{e/h}}(T_{\mathrm{p}}^{\mathrm{e/h}}, N) \right) \tag{5.17}$$

are dependent on the plasma temperatures. We also have to introduce temperatures to the pumping term $\Lambda_{\mathbf{k}}^{\mathrm{e/h}}$, which models the injection of thermalised carriers,

$$\Lambda_{\mathbf{k}}^{\mathrm{e/h}} = \Lambda_0 \, f_{\mathbf{k}}^{\mathrm{e/h}}(T_{\mathrm{l}}, N) \left[2(A \cdot d)^{-1} \sum_{\mathbf{k},\sigma=\pm} f_{\mathbf{k}}^{\mathrm{e/h}}(T_{\mathrm{p}}^{\mathrm{e/h}}, N) \left(1 - n_{\mathbf{k}}^{\mathrm{e/h},\sigma} \right) \right]^{-1} . \tag{5.18}$$

We assume that the carriers arrive at the lowest lasing bands in a thermalised state and insert the lattice temperature into the Fermi-function which appears in the nominator. The distribution function attributed to the participating lasing bands contains the plasma temperatures of electrons and holes respectively. In addition, we note, that the calculated carrier scattering rates $\gamma_k^{\mathrm{e/h}}$ itself are dependent on both, the lattice and the plasma temperature. This effect, however, is considered relatively weak.

In order to conceive the plasam temperature dynamics, an equation similar to (5.2) but for the carrier energy densities $U^{\mathrm{e/h}}$ has to be derived. This can be done by building the appropriate higher order moments of the equations (4.60)-(4.62) [49], via

$$A^{-1} \sum_{\mathbf{k}} \frac{\hbar^2 k^2}{2m_{\mathrm{e/h}}} \cdots = A^{-1} \int_0^{k_{\max}} \mathrm{d}k \, D(k) \frac{\hbar^2 k^2}{2m_{\mathrm{e/h}}} \ldots \tag{5.19}$$

One obtains

$$\partial_t U^{\mathrm{e/h}} = D_f \Delta U^{\mathrm{e/h}} + G_U^{\mathrm{e/h}} - \gamma_{\mathrm{nr}} \, U^{\mathrm{e/h}} + \Lambda_U^{\mathrm{e/h}} - \Gamma_{\mathrm{sp},U}^{\mathrm{e/h}} - \Delta U_{\text{c-ph}}^{\mathrm{e/h}} \, . \tag{5.20}$$

This equation contains terms which are the analogue to (5.2), except, that a phenomenological energy transfer term

$$\Delta U_{\text{c-ph}}^{\mathrm{e/h}} = \gamma_{\text{c-ph}}^{\mathrm{e/h}} \big(U^{\mathrm{e/h}} - U_{\mathrm{eq}}^{\mathrm{e/h}}(T_{\mathrm{l}}, N) \big) \, . \tag{5.21}$$

has been added. $U_{\text{c-ph}}^{\mathrm{e/h}}$ accounts for the amount of energy transfered from the plasma to the lattice due to carrier-phonon scattering processes. The inverse of $\gamma_{\text{c-ph}}^{\mathrm{e/h}}$ gives the time, which is needed for the carrier system to be thermalised to the lattice.

Once again, the various terms on the rhs of (5.20) can be calculated from the sums over microscopic quantities,

$$\begin{aligned} G_U^{\mathrm{e/h}} &= A^{-1} \sum_{\mathbf{k},\sigma=\pm} \frac{\hbar^2 k^2}{2m_{\mathrm{e/h}}} g_{\mathbf{k}}^{\sigma} \,, \\ \Gamma_{\mathrm{sp},U}^{\mathrm{e/h}} &= A^{-1} \sum_{\mathbf{k},\sigma=\pm} \frac{\hbar^2 k^2}{2m_{\mathrm{e/h}}} B_{\mathbf{k}} n_{\mathbf{k}}^{\mathrm{e},\sigma} n_{\mathbf{k}}^{\mathrm{h},\sigma} \\ \Lambda_U^{\mathrm{e/h}} &= A^{-1} \sum_{\mathbf{k},\sigma=\pm} \frac{\hbar^2 k^2}{2m_{\mathrm{e/h}}} \Lambda_{\mathbf{k}}^{\mathrm{e/h}} (1 - n_{\mathbf{k}}^{\mathrm{e},\sigma}) \,. \end{aligned} \tag{5.22}$$

The Auger-processes are destroying an electron-hole pair, but the energy is transfered to a hot electron (or hole). As long as no higher sub-bands are involved, we can assume that no plasma energy change is caused by these processes.

Equation is a energy balance equation for the hot carrier system. From a thermodynamical point of view both $N^{\mathrm{e/h}} = N$ and $U^{\mathrm{e/h}}$ are extensive variables. Associated with them are the intensive values of the chemical potential $\mu^{\mathrm{e/h}}$ and the plasma temepratures $T^{\mathrm{e/h}}$. In particular, we are interested in the change of the plasma temperatures over time. By eliminating $\mathrm{d}\mu$ from the respective total differentials of $N(\mu, T)$ and $U(\mu, T)$ the relation [107, 128]

$$\left(\frac{\partial U}{\partial \mu} \frac{\partial N}{\partial T} - \frac{\partial N}{\partial \mu} \frac{\partial U}{\partial T} \right) \mathrm{d}T = \frac{\partial U}{\partial \mu} \mathrm{d}N - \frac{\partial N}{\partial \mu} \mathrm{d}U \tag{5.23}$$

arises [128]. Inserting equilibrium values for the factors in front of the total derivatives, this relation can be used to express the change of the two plasma temperatures $\mathrm{d}T_{\mathrm{p}}^{\mathrm{e/h}}$ in dependence on the changes $\mathrm{d}N$ and $\mathrm{d}U^{\mathrm{e/h}}$ as described by equations (5.2) and (5.20), that is

$$\dot{T}^{\mathrm{e/h}} = J_N^{\mathrm{e/h}} \dot{N} - J_U^{\mathrm{e/h}} \dot{U}^{\mathrm{e/h}} \tag{5.24}$$

with

$$\begin{aligned} J_N^{\mathrm{e/h}} &= \left(\frac{\partial U^{\mathrm{e/h}}}{\partial \mu^{\mathrm{e/h}}} \frac{\partial N}{\partial T_p^{\mathrm{e/h}}} - \frac{\partial N}{\partial \mu^{\mathrm{e/h}}} \frac{\partial U^{\mathrm{e/h}}}{\partial T_p^{\mathrm{e/h}}} \right)^{-1} \frac{\partial U^{\mathrm{e/h}}}{\partial \mu^{\mathrm{e/h}}} \,, \\ J_U^{\mathrm{e/h}} &= \left(\frac{\partial U^{\mathrm{e/h}}}{\partial \mu^{\mathrm{e/h}}} \frac{\partial N}{\partial T_p^{\mathrm{e/h}}} - \frac{\partial N}{\partial \mu^{\mathrm{e/h}}} \frac{\partial U^{\mathrm{e/h}}}{\partial T_p^{\mathrm{e/h}}} \right)^{-1} \frac{\partial N}{\partial \mu^{\mathrm{e/h}}} \,. \end{aligned} \tag{5.25}$$

Eventually, an equation for the lattice temperature of the active zone is required. Our description is restricted to the dynamics of the carrier system rather than on the lattice. This is why we have to provide a phenomenological equation for the lattice temperature [49, 107, 118, 128],

$$\partial_t T_{\mathrm{l}} = -\gamma_{\mathrm{amb}} \big(T_{\mathrm{l}} - T_0 \big) + c_{\mathrm{q,V}}^{-1} n_{\mathrm{QW}} d^{-1} \left(\Delta U_{\text{c-ph}}^{\mathrm{e}} + \Delta U_{\text{c-ph}}^{\mathrm{h}} + \hbar \omega_{\mathrm{op}} \gamma_{\mathrm{nr}} N \right) + c_{\mathrm{q,V}}^{-1} \rho j^2 \tag{5.26}$$

Here, $c_{\mathrm{q,V}}$ is the specific heat per volume, ρ the specific resistivity, and j the injection current density. One has to be aware, that the sheet densities N and $U^{\mathrm{e/h}}$ have to be transformed to a volume densitiy. As a consequence the factor $n_{\mathrm{QW}}d^{-1}$ appears in front of the plasma energy and the density terms. γ_{amb}, the ambient relaxation rate is closely related to the strength of longitudinal transport and the heat conductivity of the encompassing structure elements. It can be calculated with the help of quasi three-dimensional boundary value solver for the heat equation [129]. The last two terms pay respect to the fact that the non-radiative recombination of carriers is associated with an energy transfer to the lattice, and to the fact that – as a result of electrical pumping – the lattice temperature increases due to Joule heating [127].

5.5 Reference Parameter Sets

The following simulation scenarios are categorised according to predefined setups. *Default parameter sets* are used to specify the device parameters which will not be changed. A change of operation conditions is indicated by the respective simulation name (e.g. **V6**) and qualifiers: subscript 'm' for the microscopic scenario, subscript 'T' for the temperature scenario, and – in square brackets – the carrier pump value in units of the estimated *intrinsic threshold-pump*. For example: $\mathbf{V6}_{\mathrm{mT}}\{2\}$ refers to simulation scenario **V6**, which is resolving spectral k-dynamics, is including temperature dynamics, and performed at a pump value $\Lambda = 2 \cdot \Lambda_{\mathrm{thr},0}$. The parameters are device specific (dependent on device geometry, quantum-well design, doping levels, etc.) or tied to operating conditions (carrier pump, ambient temperature. Material specific parameters can be found in Appendix E.

Examples of parameters which have a severe impact on the picosecond dynamics are: the diameter of the aperture $\varnothing$, the vacuum wavelength λ, the longitudinal confinement factor Γ_z, and the birefringence parameter $\mathbf{n}^{\mathrm{c}}$. Although, the system seems to be relatively insensitve against changes of some parameters, one always has to consider the timescales on which these terms are inducing changes to the system. Good examples are the non-radiative recombination rate γ_{nr} and the carrier diffusion D_f which are crucial system parameters but are associated with nanosecond timescale. As a rule of thumb, we never assume the system being completely settled below 10 nanoseconds. In fact, we can observe reconfiguration of modes and qualitative changes of the dynamics up to these timescales. In terms of the optical field, however, the output intensity is usually stabilised between 500 ps to 1 ns. Concerning *cw*-operation, some additional explanations are needed: cw-operation, in terms of a stationary solution of the field intensity can only be achieved in single-mode operation. For complete stationarity, one would have to wait till the slowest parts – these are processes and effects related to either the density or to the temperature – of the equations settle down to their quasi-equilibrium solutions. In spite of this, we will use the expression *quasi cw-operation* when 1 the carrier pump is constant, 2) the total averaged optical intensity has settled to a constant value. *Total averaged* intensity means, that we take the sum over all spatial points of the near-field and that we apply a time-average of roughly $10 - 50$ ps to eliminate mode-beating effects. In other words, the state of quasi cw-operation is obtained after all remnants of the relaxation oscillation have vanished.

The intrinsic threshold-density is calculated from the condition[1]

$$\gamma_{\mathrm{res}} = \kappa \Gamma_z G(N) \,, \qquad G(N) = \mathrm{Im}\,[\,\chi(N)\,] \,. \tag{5.27}$$

A numerical solution of this equation gives the intrinsic threshold density $N_{\mathrm{thr},0}$. Ne-

[1] This means, that the threshold carrier density is calculated for the situation where the gain equals the longitudinal resonator losses. The actual threshold density N_{thr} is greater than $N_{\mathrm{thr},0}$ due to additional transverse diffraction losses.

glecting both, the carrier diffusion and spontaneous emission in (5.2), we obtain

$$\Lambda_{\mathrm{thr},0} = \gamma_{\mathrm{nr}} N_{\mathrm{thr},0} \tag{5.28}$$

for the intrinsic threshold-pump.

It has to be noted, that as the value of $\Lambda_{\mathrm{thr},0}$ is derived from (5.1) and (5.2) implicitly relies on the existence of a stationary solution of these equations. Coexistent higher-order transverse modes cause mode beating which automatically implies a non-stationary solution, that is $\partial_t \mathbf{E} \neq 0$.

Default Parameter Set		
Symbol	*Value*	*Meaning*
$\varnothing$	-	diameter of oxide-aperture
d	60 nm	well-width
n_{QW}	5	number of quantum-wells
λ	810 nm	optical vacuum wavelength
Γ_z	0.0772	confinement factor, active zones
Θ_z	0.0189	confinement factor, oxide-aperture
n_{eff}	3.31	effective refractive index
n_{ox}	3.1/1.6	refractive index contrast, oxide-aperture
$\delta\mathbf{n}^{\mathrm{c}}$	$5 \cdot 10^{-3}$	birefringence
T_0	300 K	ambient temperature

V6	
Symbol	*Value*
$\varnothing$	6μm
$\delta\mathbf{n}^{\mathrm{c}}$	$5 \cdot 10^{-3}$

V15	
Symbol	*Value*
$\varnothing$	15μm
$\delta\mathbf{n}^{\mathrm{c}}$	$5 \cdot 10^{-3}$

Scenario **V6** represents a small 6 μm VCSEL. This VCSEL is running single mode up to relatively high injection currents ($\sim 2 \cdot \Lambda_{\mathrm{thr},0}$). In this regine, relaxation oscillations are very regular and the polarisation suppression is total. In contrast to this scenario, **V15**, with more than twice the aperture diameter of **V6**, displays a pronounced multi-mode behaviour with many transverse modes above threshold. The polarisation modes are coupled due to linear birefringence. In the following sections, we perform an in depth analysis and extract aspects of the dynamics which are characteristic for these two devices.

Time series of the field variables are recorded for a range of time-windows between 300 ps (shortest) and 9600 ps (longest). The multi-mode behaviour of **V15** shortens the observed relaxation oscillation to roughly 300 ps. After this time the output intensity can be considered *quasi cw*. However, we see that the mode dynamics and in particular

the polarisation composition is changing on nanosecond time-scale. To which degree this is an artifact of a non-equilibrium density profile which is still subject to diffusion or related to other intrinsic time-scales requires further analysis.

The full microscopic simulations presented here are performed with a time-step of 0.6 fs. Mesoscopic calculations, on the other hand, are utilising precalculated gain- and temperature response tables. The advantage of this is that a 5 times bigger time-step of 3 fs can be used. The output parameters are stable for a transverse resolution of 100x100 grid-points and carrier pump levels up to 10 times threshold. Microscopic calculations are performed on a local $60-100$ point k-space grid. A mesoscopic simulation of 9600 ps requires roughly 2,000,000 time-steps and takes 3 hours user time on a 8 CPU node of a *Hitachi SR-8000* supercomputer. Depending on the output load the code is performing 2-3 GFlop and running with 84% parallel efficiency. With the exponential growth of computing power, we dare to predict, that spatially resolved time-domain simulations will gain more importance in the future because of their high degree of parallelisability and and their comprehensive physical nature.

The near-field intensity images we will present here are either retrieved as instantaneous snapshots of the optical field variables at a certain time or by averaging over a predefined time period. The latter is in close analogy to experiment as every detector (e.g. streak camera, CDD-camera) has a certain shutting time which is the direct equivalent to a time integration. In order to obtain time-averaged fields on-the-fly from our numerical simulations we proceed as follows: at $t = 0$ we start our simulation. At each time t that is at every time-step i ($t = i\Delta t$) we add-up the field $E_i^{\pm}(x, y)$ to an averaged field $\bar{E}^{\pm}(x, y)$ which, after n time-steps ($\Delta T = n\Delta t$), can be written as

$$\bar{E}^{\pm}(x, y) = \sum_{i=1}^{n} \bar{E}_i(x, y) \, . \tag{5.29}$$

After that we dump $\bar{E}^{\pm}(x, y)$ to as a file to disk we can reinitialise it to zero. By doing this, we circumvent extensive memory requirements, and are able to sample our time-interval $[0, T = N \cdot \Delta t]$ into $T/\Delta T = N/n$ *"detector"* shots, each one integrated over a time-interval of ΔT.

In agreement with other publications [122, 130–132] we consider modes as spectrally filtered near-field patterns. The process of spectral filtering involves to identify the eigenfrequencies of the linearised system [77]. These frequencies appear as peaks in the total intensity spectrum. After extracting the transverse mode frequencies from the (scalar) spectrum we can apply a spatial resolved Fourier-transformation for the identified peak-frequencies to the time series of the optical field. This technique has several advantages which will be explained in more detail in Section 5.11. Due to the nonlinear character of the set of equations the modes do not constitute a complete base system nor do they obey a orthonormality relation. Moreover, a strict mathematical description and classification of the modes in terms of simple functions of Gaussian-

Laguerre type is not possible as the pump-profile is a smeared out ring profile rather than a clean step-function. The inversion density which either feeds or drains energy from the optical field does not stay constant in time but changes its shape due to the impact of the optical field. This change is a much slower process than the actual mode-dynamics and it turns out, that even after 10 ns mode-transitions occur and change the character of the near-field pattern. Our simulations reveal how – in this complex nonlinear interplay – the spatial, temporal, spectral and polarisation characteristics change and how the shape of the carrier profile affects the type and the shape of the modes over time. This clearly exhibit the weaknesses and limitations of the mode picture. Because of similarities, we classify the spectral components of the electric field as Gaussian-Laguerre modes TEM_{pl}, as far a possible. As linear polarised modes are the dominant polarisation modes in VCSELs we also label them as linear polarised LP_{pl} modes. In agreement with [133] we show that VCSELs with a pronounced ring shaped carrier pump and a smeared-out index profile are favouring such *daisy modes*, radially deformed TEM modes of high azimuthal order but low radial order which concentrate the field intensity to the rim of the carrier density profile.

5.6 Transverse Single-Mode Operation at a Low Pump-Level

VCSEL structures with an aperture diameter around $5\,\mu$m tend to exhibit transverse single-mode behaviour. This is particularily true if they are operated at pump rates close to threshold. One main difference between a VCSEL and an edge-emitting laser is that the optical field of a VCSEL features two orthogonal polarisation states. In a transverse single-mode VCSEL these polarisation states compete for the same spatially distributed material gain. If – by any means – one of the two polarisation states gets favoured, this polarisation state will gain dominatation over the discriminated one [134, 135]. One possible source of this is cavity birefringence which shifts the x- and y-polarised parts of the optical field against each other in the frequency spectrum [87]. Dependent on the position of the gain maximum one of the polarisation modes experiences either less material gain or higher cavity losses than the other and will switch-off over time with a characteristic decay constant that depends on the level of gain discrimination. A shift of the gain maximum with temperature can change the favoured polarisation mode.

This kind of behaviour is demonstrated in FIGURE 5.4. **V6** $\{1.3\}$ has an aperture of 6 μm diameter and is pumped close to threshold at $\Lambda = 1.3 \cdot \Lambda_{\mathrm{thr},0}$. As one can see from the top graph the relaxation oscillation is very distinct and regular with a time period of roughly 150 ps. The picture in the middle displays the near-field trace of the total optical intensity resolved along the transverse x-axis. 300 ps after the switch-on the profile of a TEM_{00} mode remains stable. The spatially summed up total intensity of the x-polarised state is constantly decaying during the simulation time (lower dash-dotted line in top graph) while at the same time the y-polarised state approaches the cw-value

of the total intensity. The relaxation oscillations are perfectly synchronised between the x- and y-parts of the field polarisation. The bottom picture of FIGURE 5.4 shows the carrier density profile. The first peak of the relaxation oscillation digs in a deep and broad valley into the density which is subsequently filled up again. During the next period of the relaxation oscillation the optical field experiences the modified refractive index structure: with a calculated alpha-factor of 0.612 the carrier profile produces an induced waveguide structure which causes the field profile to narrow. In equilibrium state diffraction and gain of the optical field are balanced. Stable transverse profiles for both the optical field and the carrier density are formed.

We should not fail to mention, that increasing pumping currents can cause polarisation-switching in transverse single-mode lasers. The origin of this effect is the nonlinear birefringence imposed by the spin-flip model [136].

5.7 Transverse Multi-Mode Operation at a Low Pump-Level

The impact of aperture diameter can be explained best when performing a simulation identical to the previous one but for a $15\,\mu$m diameter. This scenario **V15** $\{1.3\}$ is depicted in FIGURE 5.5. Due to the increased aperture size higher order transverse modes are now supported. Compared to compared to FIGURE 5.4 the period of the relaxation oscillation remains almost unchanged. However, it is not regular anymore. Polarisation suppression is partial: the x-polarised state takes roughly 33% and the y-polarised 67% of the total intensity. A comparision of the time averaged transverse near-field patterns reveals that the x- and the y-polarised states take complementary spatial intensity distributions. This configuration seems to be advantageous as the coverage of the gain area is maximised. However, the stronger mode has a higher probability of covering spatial regions where the pump is highest, that is areas of of high gain. The following simulations show that for the dominant polarisation daisy-modes, whose intensity concentrates to the rim-region of the carrier-profile are much more probable than modes of low azimuthal order covering the centre area. The spatial resolved time-trace of the carrier density shows another characteristic feature: during the first relaxation oscillation the Gaussian mode is dominant. Its width is limited rather by an intrinsic length scale of approximately $5-6\,\mu$m than by the aperture size itself. The first relaxation oscillation peak is smooth and regular. After the first peak of thesituation is very much different than in the previous case. With the first Gaussian flare failing to deplete the carriers in the rim higher order modes are developing as they are more profitable in exploiting the gain during the next relaxation oscillation. Just before the second intensity flare sets in a characteristic high-frequency oscillation superposes the total field intensity. The Gaussian mode contracts and is decreasing its width until at $t \approx 290$ ps the flare of higher order modes gets over-amplified and imprints its trace in the density profile. After the second peak of the relaxation oscillation the mode composition seems to converge. Al-

though the intensity has settled to its quasi cw-value, the system has not settled in terms of the composition of eigenmodes.

5.8 Transverse Multi-Mode Operation at a Moderate Pump-Level

For the following simulations we increase the pump-level to $3 \cdot \Lambda_{\mathrm{thr},0}$. Again the spatially resolved dynamics of the fields are recorded over time along a one-dimensional cut. FIGURE 5.6 and FIGURE 5.6 display the results for the **V6** {3} and **V15** {3} respectively. To simplify the comparison the correspong near-fields are displayed separatly for both polarisations but colour-coded with the same intensity colour-bar. The small-aperture system **V6** (FIGURE 5.6) performs a transition from the lowest order mode to a higher order mode. As the gain area is very limited and comparable to the width of the fundamental mode we see no distinct multi-mode behaviour for both of the polarisations but a transition to a deformed LP_{00} cross-shaped mode for the y-polarised mode and to a PL_{02} mode for the x-polarised mode. This transition allows the y-polarised state to deplete the low diffraction centre area more effectively and leaves space for the x-polarised state to access the rim area at the same time. The transition itself is a rather slow process: During the first 300 ps both modes occupy the fundamental PL_{00} mode only. After this period of time the x-polarised mode slowly drifts into a PL_{02} like state ($t = 300 \ldots 1200$). After a rather long period of 1200 ps the x-mode concentrates on the PL_{02} mode, while the y-mode has its maximum close to the centre occupying a deformed, cross-shaped fundamental mode. From the one-dimensional time-series it becomes evident that the intersection planes of the PL_{02} modes must be turning in time. The reason for this behaviour is, that the y-polarised mode tries to deplete the carriers more efficiently. Using a shorter integration time in our calculation we would reveal that the y-polarised cross-shaped (master) mode turns around the axis of symmetry while the x-polarised PL_{02} mode follows this movement in order to align its node planes to the areas where the y-polarised mode is strong. This behaviour seems to be characteristic for small apertures system and only few transverse modes above threshold.

FIGURE 5.7 visualises the simulation results for the 15 μm aperture system. Two differences are immediately obvious: 1) The discrimination of the x-polarised state is weaker than in for the **V6** system, and 2) the time-resolved transition to transverse multi-mode operation takes place in a much faster way. Although the integrated spatially resolved intensities display the same complementary behaviour than we observed for the smaller system the superposition of intensities do not completely cover the gain area: Along the radial node plane the total field intensity remains lower than in the centre and the rim of the aperture. A possible explanation for this could be that although the gain is high at the rim and low within the plateau-like centre area, the diffraction losses are low in the centre but high at the rim. A detail analysis of the radial dependence of gain and diffraction would be necessary to reveal the correlation between density profile and the

intensity pattern.

The direct comparison of the one-dimensional field patterns of **V6** {3} and **V15** {3} reveals another interesting detail: the conspicuous switching behaviour from the $LP_0 0$ to the $LP_0 2$ mode which is shown in FIGURE 5.6 can also be observed within the larger system but embedded into the much more complex dynamics (compare with FIGURE 5.7). The fact that the x-polarised mode changes its composition in terms of transverse modes and clears the centre within roughly the same time scale (1200 ps) gives strong indication that this dynamics is not only and artifact of boundary conditions but reflects intrinsic length- and timescales of the modal interplay.

5.9 Behaviour on Longer Timescales: Polarisation Dynamics and Stokes Parameters

By extending the time-window of our simulation to 9.2 ns we recognise another dynamical features of **V15** {3} related to the state of polarisation. In order to analyse the state of polarisation we use the Stokes parameter representation of the complex optical field: The state of the field polarisation which may be described by 4 real variables which correspond to the amplitudes and the phase of the complex amplitudes E_x and E_y can alternatively be expressed by the set of Stokes parameters (see [137–139] and APPENDIX D). The Stokes parameters give the degree of field-polarisation in terms of the total intensity (S_0), the intensity of linearly polarised light (S_1), circular polarised light (S_2) and diagonally polarised light (S_3). In order to receive a scalar measure for the degree of polarisation of the spatially extended system we perform a field-average over the normalised Stoke parameters $\hat{S}_1(x,y)$, $\hat{S}_2(x,y)$, and $\hat{S}_3(x,y)$ which take values between -1 and 1 and are well defined at each spatial point. At each spatial point the system is in a state of complete polarisation, that is the equality

$$P_{\mathrm{pol}} = \sqrt{\hat{S}_1^2 + \hat{S}_2^2 + \hat{S}_3^2} = 1 \tag{5.30}$$

holds. The corresponding spatially averaged quantities $\bar{S}_1$, $\bar{S}_2$, and $\bar{S}_3$, however, do not obey this equation. Instead,

$$0 \leq \bar{P}_{\mathrm{pol}} = \sqrt{\bar{S}_1^2 + \bar{S}_2^2 + \bar{S}_3^2} \leq 1\,. \tag{5.31}$$

This justifies to use $\bar{P}_{\mathrm{pol}}$ as a measure for the overall degree of polarisation in spatially extended multi-mode system. FIGURE 5.8 is a comparison of the two systems **V6** and **V15**. The smaller system features both, a higher degree of polarisation and stronger fluctuations concerning the polarisation state. The Stokes parameter $\bar{S}_0$ levels off close to -0.5 which is in good agreement with the previously observed result of a stronger y-polarisation. In contrast to this, we observer oscillations of high high-frequency on the circular and diagonally polarised state of the optical field. Although not single-mode, the number of modes above threshold is small. *Inter-mode polarisation switching* can be

observed on slow time-scales around $200 - 400$ ps: A reconfiguration process takes place during which the favoured mode is drifting from one mode to another in order to improve its modal-gain. This process is conducted by a modified carrier density which induces a change of the refractive index and the available gain. It is remarkable, that the broad aperture system behaves initially in a more regular way. After 2.4 ns the relative intensities of the polarisation states seems to be levelled around $\bar{S}_1 \approx 0.2$. The amplitudes of the fluctuations imposed on the circular and the diagonally polarised Stokes parameters are much weaker during that period. We ascribe this behaviour to the fact that the transitions between modes can be performed much easier as the number of transverse modes above threshold is higher. Reconfiguration of modes is particularly distinct during the first 2 ns. During this time the intensity settles to its cw-value and the density profile takes an almost stationary profile. For the bottom picture we extended the time axis to 9.6 ns. The reconfiguration and transformation of modes is a persistent process throughout this time-window. Around $t = 5$ ns we see a dip in the $\bar{S}_1$ (≈ -0.15) variable which marks a point of low polarisation discrimination. The following 1.8 ns are characterised by a constant drop of $\bar{S}_1$ till it reaches a level of -0.5. During this drop the degree of polarisation rises to a value close to 50% while the oscillations of the circular and diagonal state almost vanish. In the same way in which we attribute modes to the linearised equations we attribute the change of intensity and polarisation between the these modes to the inherent nonlinearities. It will be the subject of further research to analyse the imposed motion of the polarisation resolved modal amplitudes and whether or not they can be attributed to either the non-radiative recombination rate or the carrier pump-rate.

5.10 The Time Averaged Dynamics

A practical tool for studying the modal interplay is to integrate the two-dimensional near-field patterns to polarisation resolved averaged intensity patterns. The result for the **V15** {3} is presented in FIGURE 5.9 where the fast axis is running top-down, and the slow left-right. Here, the near-field dynamics is recorded during a total of 8256 ps with a sample rate of 48 frames. The field averages are calculated on-the-fly using an integration time of 172 ps. While the intensity distributions are synchronised during the first relaxation oscillation peak (first snapshot) this initial symmetry is broken and replaced by complementary field patterns. This means, that the x- and the y-polarised states try to divide the gain area among each other in a way that minimises the overlap between the two of them. The preferred modes are modes with a high azimuthal node count LP_{0l} ($l \sim 6$) which cover the high gain at the rim well, and low order modes with minimal diffraction losses focused around the centre. The LP_{06}-like daisy-mode is recognisable during the whole time window but underlies significant changes in intensity. For the x-polarisation the intensity is lowest between the 32nd and the 40th frame. This coincides with the period of increased average polarisation we see in FIGURE 5.8. During this period ring-shaped modes with low azimuthal node count are a distinctive feature of the spectrum. We finally note, that the calculation of time-series of the averaged near-

field intensities is closely related to experimental setups where a detector is integrating the photons during its exposure time. An adjustment of sampling rates to the time-scales under investigation may reveal effects correlated with intrinsic time-scales of the equations and help to understand the nonlinear character of the light-field dynamics.

5.11 Spectral Transverse Multi-mode Dynamics

We analyse the spectral dynamics of the transverse multi-mode device given by **V15** {3}. As a full 2D 100x100 grid-point Fourier transform of our time series (typically 300,000 time steps) would consume an immense amount of memory and disk space we perform a discrete Fourier-transforms (DFT) on-the-fly. Ringing effects are suppressed with a Hanning-filter. The technique we use in order to record spatio-spectral information is to divide the full time-interval T into N sub-*frames* denoted by $f = 1 \ldots N$. In each frame f a DFT is determining a scalar spectrum of the electric field vector $E^{x/y}_{i(r),j(r)}(\omega)$ at R random grid points $[i(r), j(r)]$ $(r = 1 \ldots R)$ on-the-fly. At the end of each frame we sum-up the individual spectra to a polarisation resolved pseudo-power spectrum

$$\tilde{I}^{(f)x/y}(\omega) = \sum_{r=1\ldots R} |E^{(f)x/y}{}_{i(r),j(r)}(\omega)|^2 \tag{5.32}$$

Even though this spectrum does not display the right intensities it will feature the same peak characteristics as the real spectrum ,

$$I^{(f)x/y}(\omega) = \sum_{ij} |E^{(f)x/y}{}_{i,j}(\omega)|^2 \,. \tag{5.33}$$

but can be calculated with a factor $100 - 1000$ less computational effort depending on the choice of R (we used $R = 32$). After calculating $\tilde{I}^{(f)x/y}(\omega)$ at the end of frame f we run a simple peak detection over the spectra for the x- and y- polarised fields. From all the detected peaks the L (we use 16) strongest are identified. The corresponding frequencies $\omega_l^{(f)}$ ($l = 1 \ldots L$) serve as frequency channels set up for a spatial DFT which is performed on-the-fly during the following frame $(f + 1)$:

$$I^{(f)x/y}_{i,j}(\omega_l^{(f)}) = |E^{(f)x/y}{}_{i,j}(\omega_l^{(f)})|^2 \,. \tag{5.34}$$

A simple summation allows to extract the real mode intensities

$$I^{(f)x/y}(\omega_l^{(f)}) = \sum_{ij} I^{(f)x/y}_{i,j}(\omega_l^{(f)}) \tag{5.35}$$

for the L channels so that they can be compared with the intensities of the estimated spectrum $\tilde{I}^{(f)x/y}(\omega)$. This method enables us to trace the changes of the polarisation-resolved spectral composition of the optical field during a simulation.

FIGURE 5.10 shows the trace of the spectral intensities of **V15** {3} recorded over a time-window of 9600 ps. The upper picture gives the graphs for the total (solid), and

the polarisation resolved (dash-dotted) intensities. The dashed line is an inset of the carrier density. The two logarithmic colour-coded intensity diagrams visualise the spectral channels together with the real intensities of the strongest components (16 for each polarisation). The x-polarised components can be found at higher relative frequencies $\delta\omega = \Omega - \omega$ while the y-components fill the lower part (compare with FIGURE 5.11 which shows the spectra separated according to polarisation).

The first 600 ps are dominated by the relaxation oscillation: the fundamental mode gets over-amplified, breaks down and is followed by broad band of spectral components which fade out after a while. FIGURE 5.11 shows the dominant modes for both linear polarisations during switch-on ($192 - 384$ ps). The fundamental mode is still strongest for x but is closely followed by two daisy-modes of the type LP_{06} and LP_{04}. For the y-polarisation both LP_{06} and LP_{04} are stronger than the fundamental mode. The preference of modes with high azimuthal order but low radial order is observed in both theory [50, 133] and experiment [89,122,126]. Our simulation show that daisy-modes are present from switch-on time ($t = 0$ ps) till the end of the integration ($t = 9600$ ps). Among the 10 strongest y-polarised modes we identify 8 daisy-modes of LP_{0l} type with $l = 3 \ldots 10$.

After the first relaxation oscillation, the intensity fractions of the two polarisation-projections x and y split. Polarisation discrimination of the x-polarised state becomes strong. The y-component is occupying the modes featuring the strongest overlap with the inverted media (dominant modes) but the x-polarised state seems to randomly switch between various transverse modes to access the remaining gain areas. Between 6000 and 8000 ps the intensity of the x-polarised state drops significantly to almost half of the y-intensity. This can also be seen from the averaged time series in FIGURE 5.9. The explanation for this behaviour is that some of the daisy-modes of the y-polarisation are replaced by donut shaped modes with a higher radial order. However, three of the daisy-modes that are observed during the initial relaxation oscillation are still present (LP_{03}-LP_{06}). The dominant y modes completely cover the rim of the density profile where the gain is highest. We observe a combination between polarisation dynamics and mode transitions on long time-scales of up to 1 ns. As it is known that spatial hole-burning can induce polarisation switching [140] we suspect a combination of these two effects.

FIGURE 5.11 and FIGURE 5.12 visualise another feature which seems to be typical for the modal dynamics: while some of the spatial modes are oriented along the same angle for x- and y-polarisation others are complementary. During the relaxation oscillation period (FIGURE 5.11) the LP_{03} and LP_{08} modes are *locked* in the sense that two modes of the same kind but different polarisation bear the same orientation while the LP_{04} and LP_{06} modes are *conjugated*. This means, that two transverse modes of the same kind cover complementary spatial regions for different linear polarisations. Other higher order modes which can not be easily classified due to their more complex shape show the same behaviour. At the end of our time series for $t = 9408 \ldots 9600$ ps the situation is slightly different. From FIGURE 5.12 we see that LP_{02} and LP_{04} and LP_{05} are locked

while LP_{03} and LP_{06} are complementary. In our simulations we experience the dominant modes more often in a state of conjugation while the weaker modes frequently appear to be locked. The observed locking behaviour does not seem to be a feature that can be attributed to a class of modes but rather seems to be the consequence of a inherent dynamical process.

5.12 Impact of Temperature

The previously discussed simulation data were obtained by using static but non-homogeneous temperature profiles. This means, that we calculated quasi-equilibrium temperature profiles using (5.26) with $\partial_t T_\mathrm{l} = 0$ and $N = N_{\mathrm{thr},0}$. Furthermore, we assume that there is no effective energy transfer between lattice and plasma, that is $\Delta U^{\mathrm{e/h}}_{\text{c-ph}} = 0$, so that we can set the plasma to the same temperature as the lattice. Although, the temperature of the carrier system, in particular of the electrons is higher than the lattice temperatures we can justify this approximation for low field-intensities, that is for a low pump over threshold. In order to capture temperature dynamics we implement an algorithm which solves the equations of both, the lattice and plasma-temperatures in a dynamic fashion. As our model describes the physics within the active zone and for transverse coordinates only, we have to use a precalculated relaxation time τ_{amb} which reflects the effective coupling of the active-zone to the heat-sink. Other time-scales involved are the LO-phonon scattering rate $\tau_{\text{c-LO}}$ which is a measure for the energy transfer between the carrier system and the lattice. As the energy transfer is not instantaneous and involves its own time-scales the temperatures of lattice and phonons do not match. Due to the high mobility of electrons and holes the carrier system is thermalising much faster than the lattice. The energy transferred from the hot carriers to the LO-phonons is stored in vibrational degrees of freedom and eventually drained along a longitudinal temperature gradient towards the heat-sink on which the VCSEL is mounted.

We now put the the dynamical temperature calculations $\mathbf{V15}_{\mathrm{T}}\{3\}$ in comparison with the simulations $\mathbf{V15}\,\{3\}$ based on precalculated static temperature profiles. FIGURE 5.13 gives the intensities for both polarisation states during the first relaxation oscillations. The relaxation oscillation set in at the same time. The first relaxation peak is comparable in both height and width. During the second peak of the relaxation oscillation we already observe strong deviations. The first peak is characterised by a Gaussian mode burst but the second by inset of higher order modes. We conclude that 1) the material gain is not significantly altered, but 2) the temperature have a certain impact on the induced refractive index. The first observation is related to the fact that the carrier pump is still relatively low. A thermal rollover of the L-I curve – dependent on the specific VCSEL model – typically becomes visible at carrier pumps of $5-10$ times the threshold value. The temperatures we calculate are too low to have a significant impact on the gain. The modal gain of the transverse modes, however, is extremely sensitive to changes of the induced refractive index. Both lattice and plasma temperature enter the nonlinear susceptibility and cause the optical field to experience modified effective

dielectric guidance. This is known as *thermal lensing* [141]. From the simulations we see that the lattice temperature is dominantly influenced by the Joule heating of carriers and the coupling to the heat-sink. Both are static processes and, although there is a dynamical transfer of energy from the carrier plasma, the lattice is relatively inert and does not cause a big difference. On the other hand, we do observe distinct sub-ps dynamics on the plasma temperatures. The middle and bottom picture of FIGURE 5.13 show the electron and hole temperature profile recorded over time. Black is ambient temperature 300K for both and white accounts for a temperature of 320K for the electrons and 307K for the holes. On longer time-scales we recognise that the total intensity of the low-energy x-polarised state matches well with that of the static temperature calculation. In contrast to this, the intensity output of the y-polarised state is almost 20% stronger. We can not attribute this to fluctuations of the polarisation as the total intensity has settled. The mechanism and the reason, why only the y-polarisation state gets enhanced by a dynamical temperature calculation, is not understood yet.

5.13 Impact of Intraband Carrier Dynamics

In situations where the local light-field intensity changes on timescales similar to the intraband scattering rates band-resolved carrier dynamics are known to have a strong impact on the mode dynamics. Under this circumstances carrier distribution functions can not thermalise fast enough to settle to their equilibrium Fermi-functions ($\sim$ 100 fs). Although, we do not study ultra-fast pulse generation and amplification with the VCSEL simulations the superposed mode frequencies are are coupled in a nonlinear fashion which excite higher harmonics and cause *mode-beating*. Systems with an aperture size $> 10\,\mu$m which are pumped significantly over threshold display an intrinsic ps-dynamic even though they are pumped with a constant current. The significance of incorporating microscopic degrees of freedom into our calculations can be understood best from FIGURE 5.14. Even so the pump is of moderate strength substantial qualitative deviations become visible, in particular when comparing the mesoscopic ($\mathbf{V15}\,\{3\}$) and the microscopic ($\mathbf{V15}_{\mathrm{m}}\{3\}$) switch-on behaviour. At first glance, one recognises that for the microscopic simulation the relaxation oscillation sets in delayed by roughly 15 ps. After some periods of the relaxation oscillation the level of the overall carrier density is with $0.0435\mathrm{nm}^{-2}/0.0399\mathrm{nm}^{-2}$ approximately 10% percent higher than that obtained from mesoscopic simulations. The output field intensities match within a range of 2%. This discrepancy can be understood from the way the k-resolved gain is calculated: as pump-blocking effects are entering the k-resolved equations but are not included on a mesoscopic level, we effectively added an additional loss channel to equations (4.60), (4.61). The results is a higher threshold density in case of the dynamically calculated gain.

More important is the impact of the band-resolved carrier dynamics on the polarisation modes. As the frequency splitting of polarisation-modes (typically $\sim$ 10 GHz) is of the same order of magnitude than intra-band carrier effects we expect a significant change in

the relative intensities of the polarisation modes. The bottom picture of FIGURE 5.14 gives indication of such a resonance phenomena. While the intensities of the linear polarisation modes deviate within less than 10% for the mesoscopic simulation we observe an almost 80% suppression of the weaker x-polarisation mode in our band-resolved calculations.

Spectral hole-burning [142] and the resulting modifications of the spectral gain and the spectral refractive index may explain the differences we encounter in a direct comparision of the two models. The deviations of the electron- and hole-densities from their quasi-equilibrium Fermi-functions together with the k-resolved interband polarisation are depicted in FIGURE 5.15. For the graphs shown we recorded the k-dimension against the time axis for the centre point of the VCSEL. The dips in the carrier distribution and the peaks in the k-resolved polarisation mark the position in k-space where the optical transition takes place. On the high-energetic side of the dip we see – in particular for the electrons – increased carrier densities. This is due to a combination of pump-blocking and the increased density of states for higher k-values.

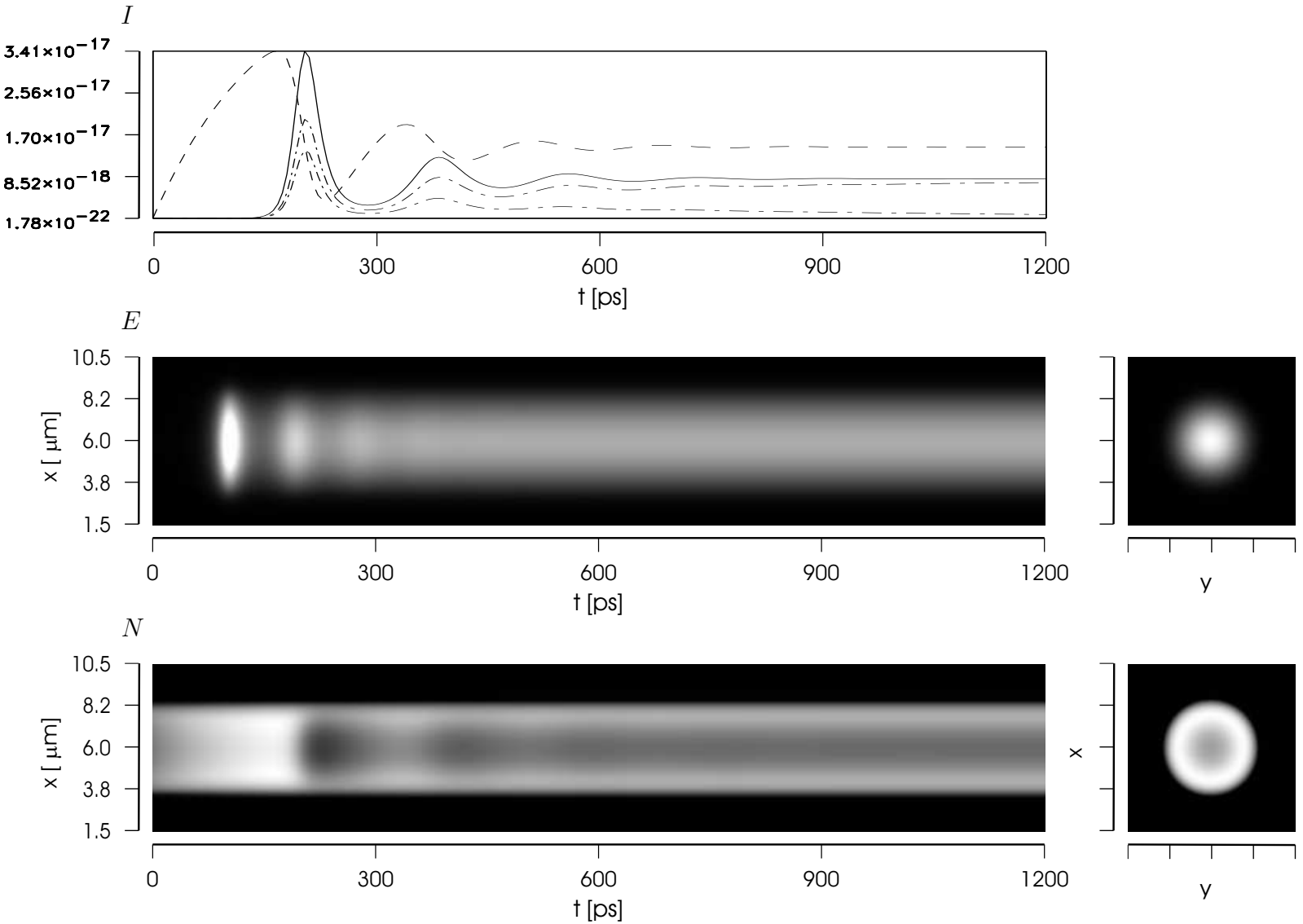

Figure 5.4: **V6** {1.3} – Single mode switch-on dynamics at low pump-level. Top: total field energy (solid line) together with the x- and the y-polarised fractions (dashed lines). The total inversion density is given for comparision as an inset (dashed line).

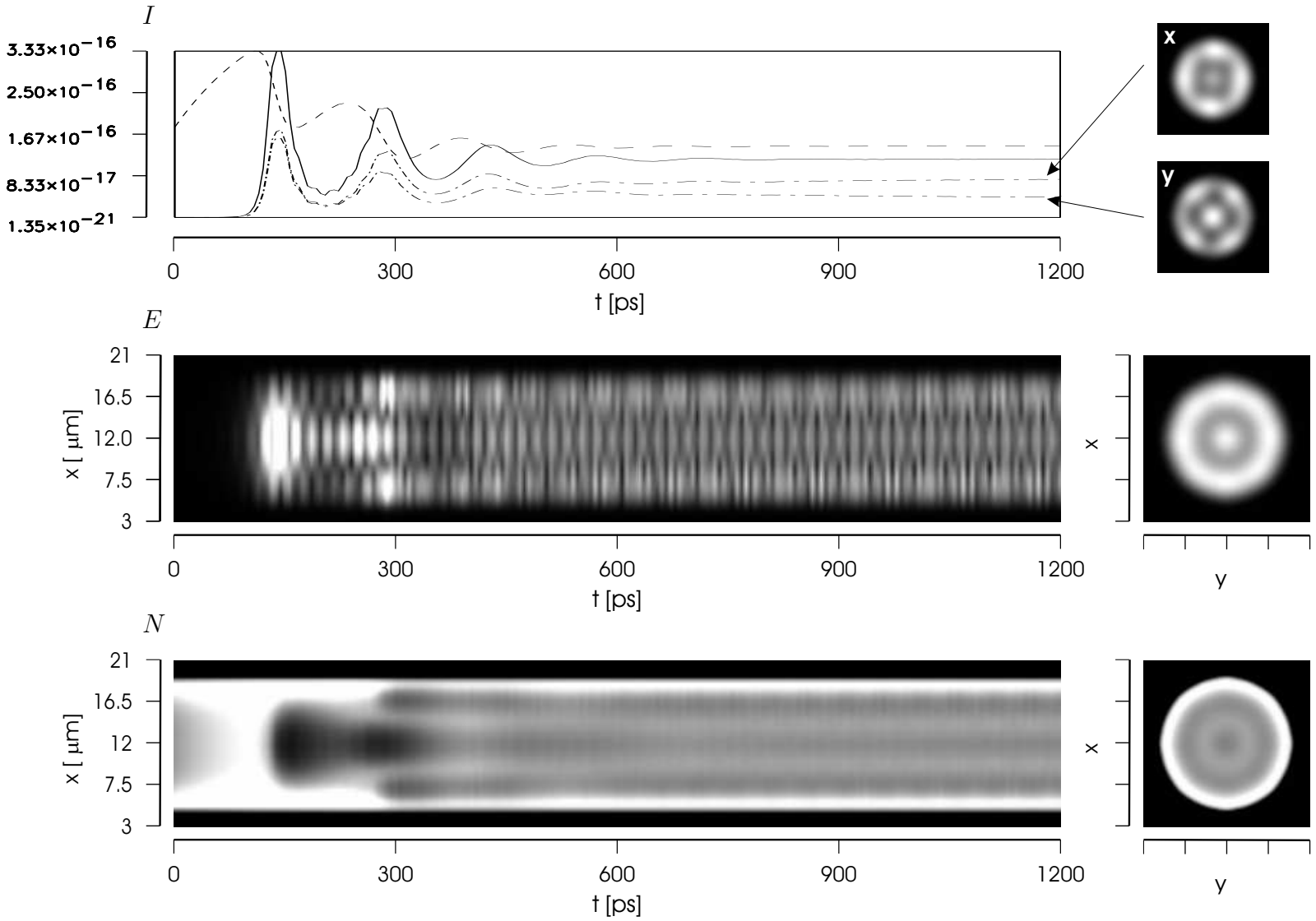

Figure 5.5: **V15** {1.3} – Multi-mode switch-on dynamics at low pump-level. Top: total field energy (solid line) together with the x- and the y-polarised fractions (dashed lines). The total inversion density is given for comparision as an inset (dashed line).

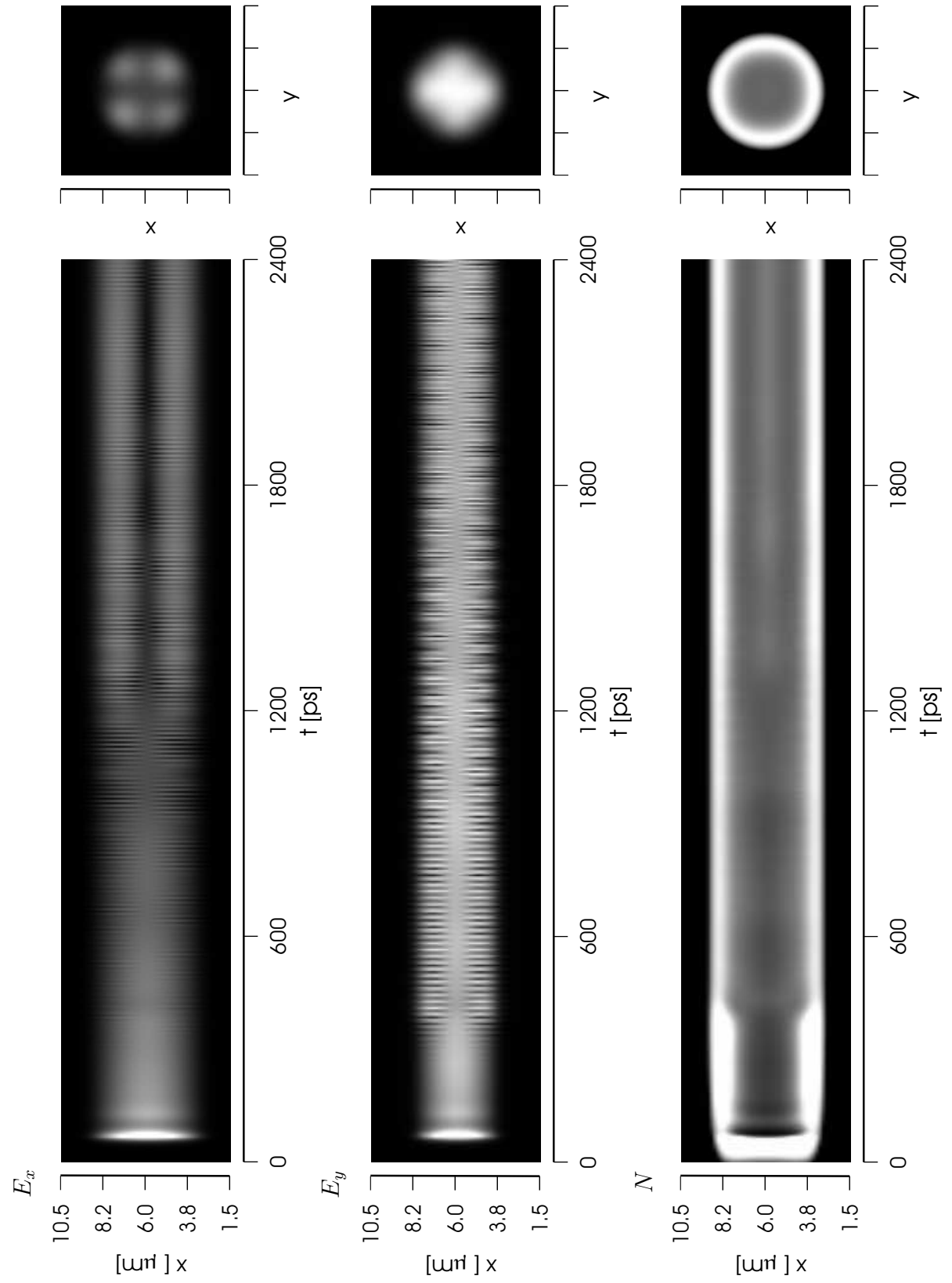

Figure 5.6: **V6** {3} – Inset of higher order modes and polarisation-competition for a small device at a moderate pump-level.

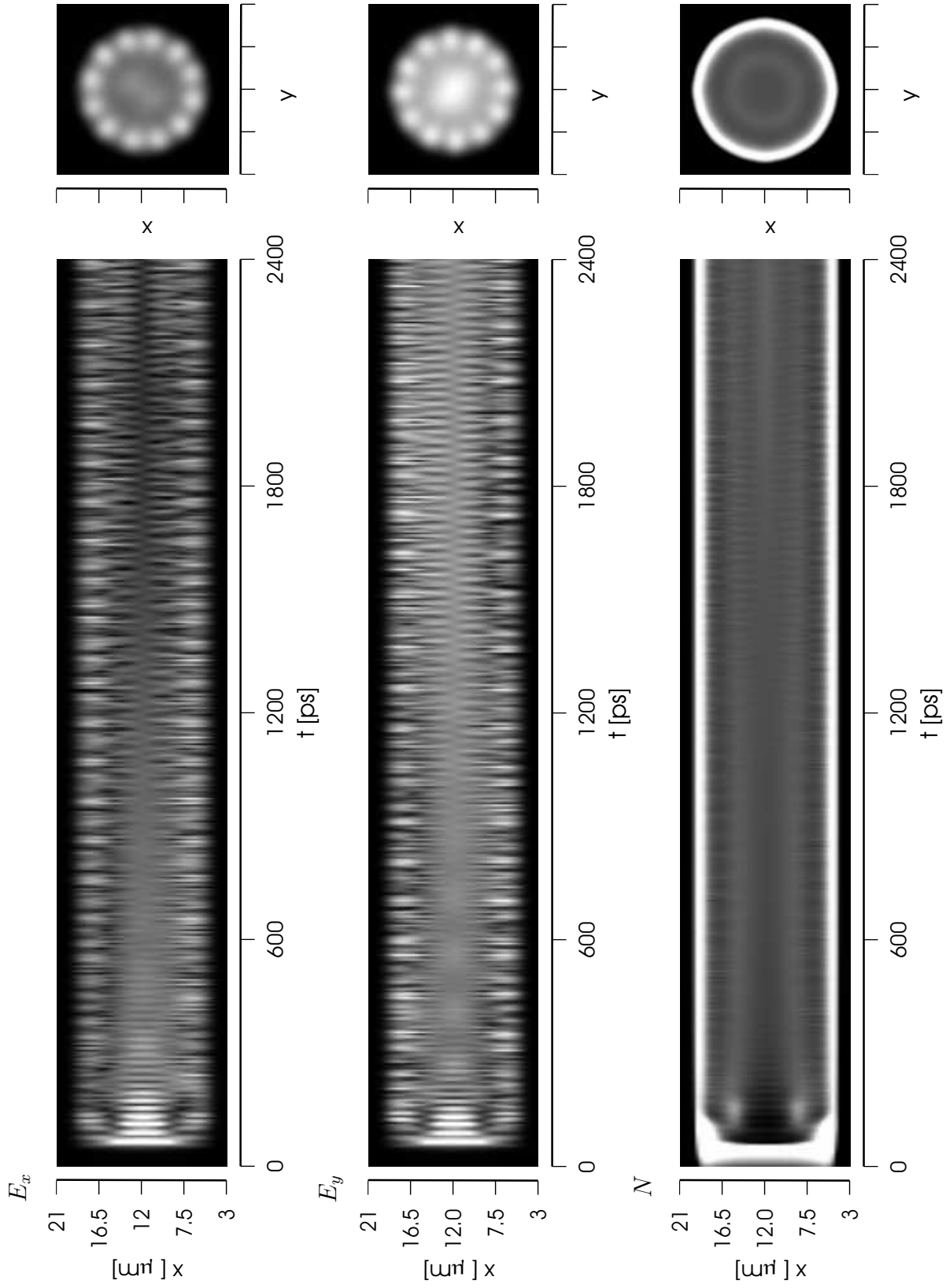

Figure 5.7: **V15** {3} – Higher order mode-dynamics and polarisation-competition for a broad device at a moderate pump-level.

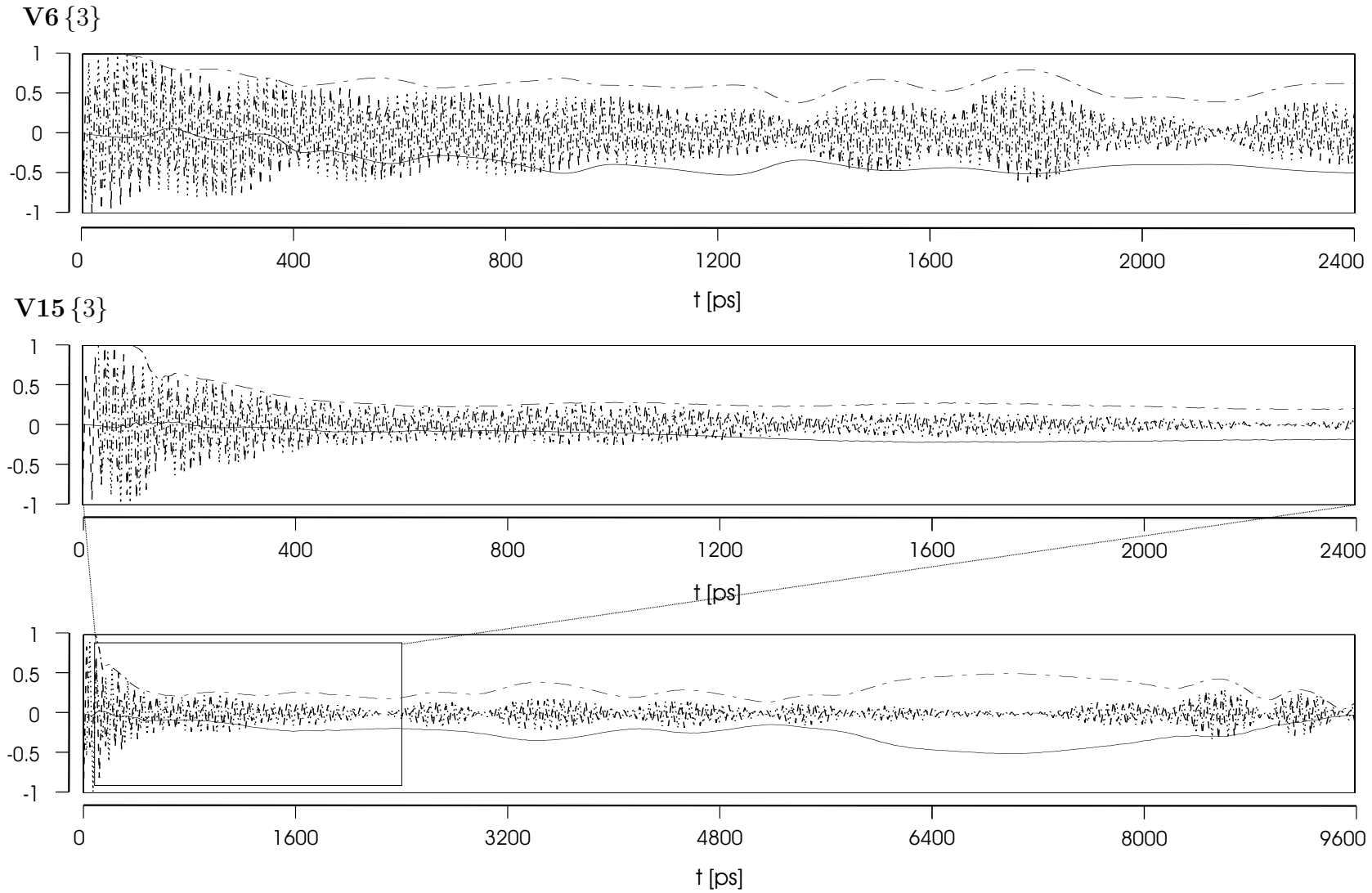

Figure 5.8: Comparison of polarisation dynamics **V6** {3} (top), **V15** {3} (middle and bottom). Plotted is the dynamics of the summed up stokes parameters $\bar{S}_1$ (solid), $\bar{S}_2$ (dashed) and $\bar{S}_3$ (dotted) and the averaged degree of polarisation $\bar{P}_{\mathrm{pol}}$ (dash-dotted).

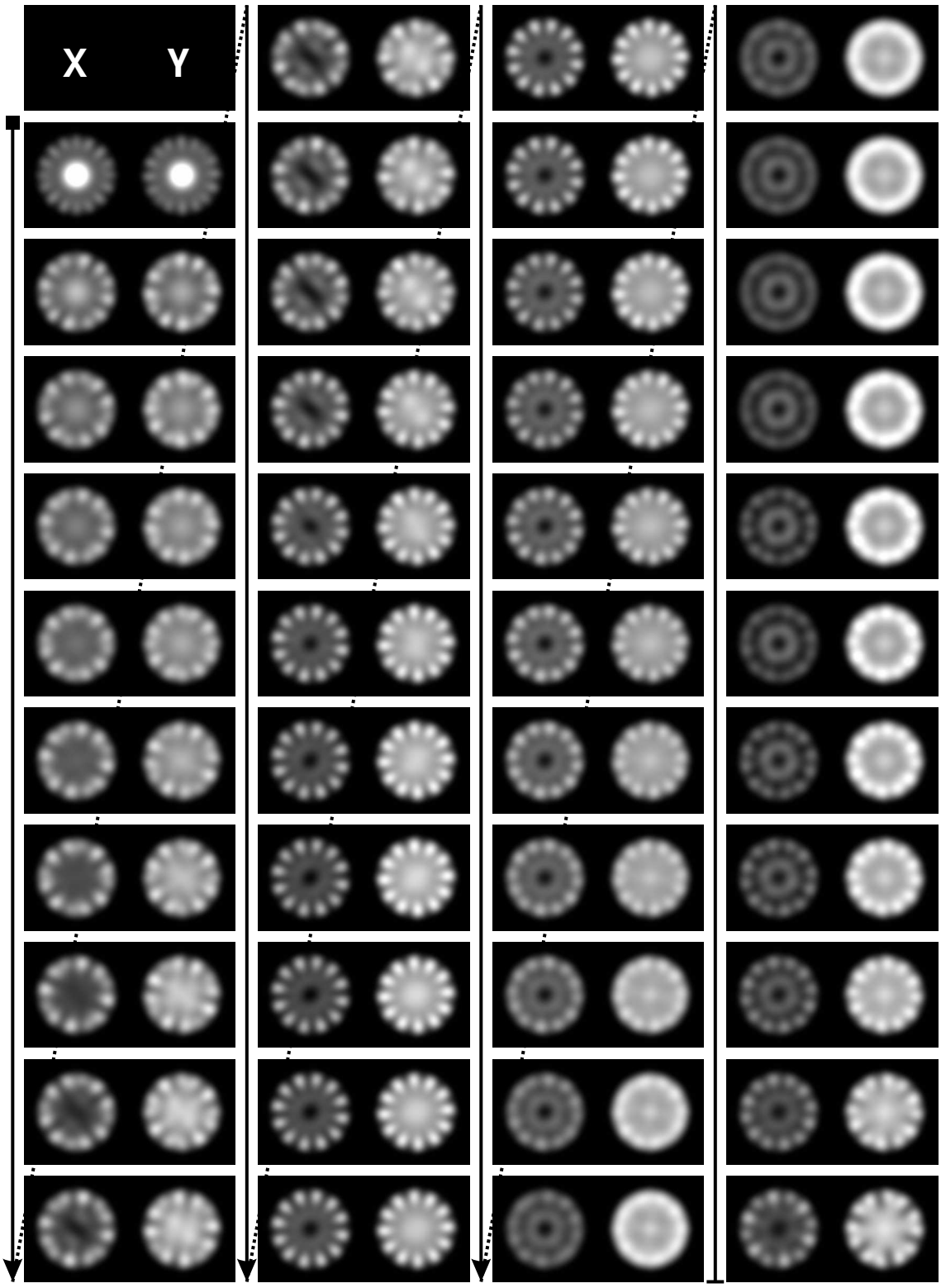

Figure 5.9: **V15** {3} – Averaged dynamics and relative intensities of the orthogonal polarisation-modes during 8258 picoseconds. Each frame represents field intensities averaged over 192 ps.

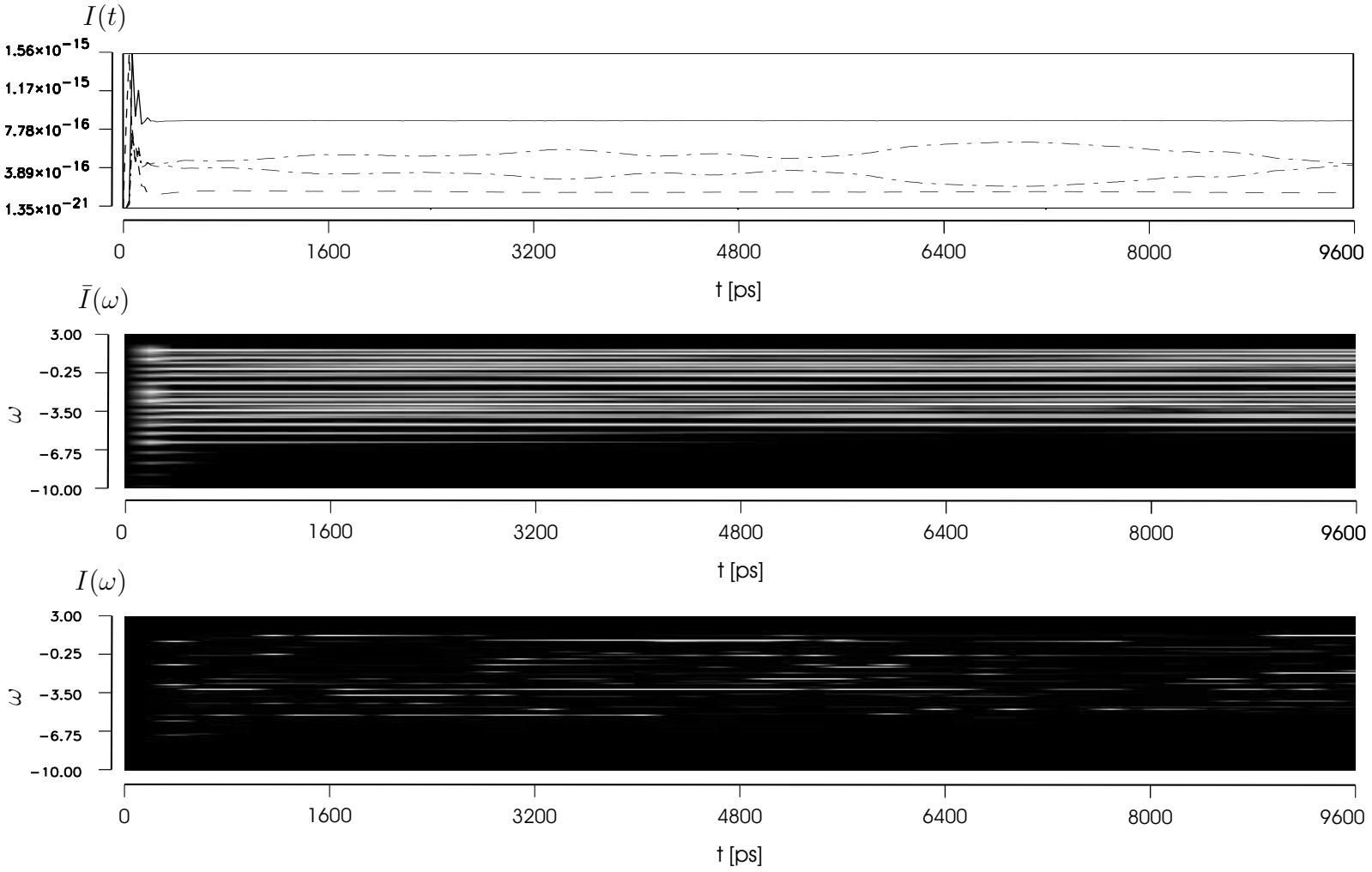

Figure 5.10: **V15** {3} – Spectral fingerprint of the Fourier components during $T = 9600\,\text{ps}$. The time-series is divided into 50 frames of 192 ps length. See SECTION 5.11 for details.

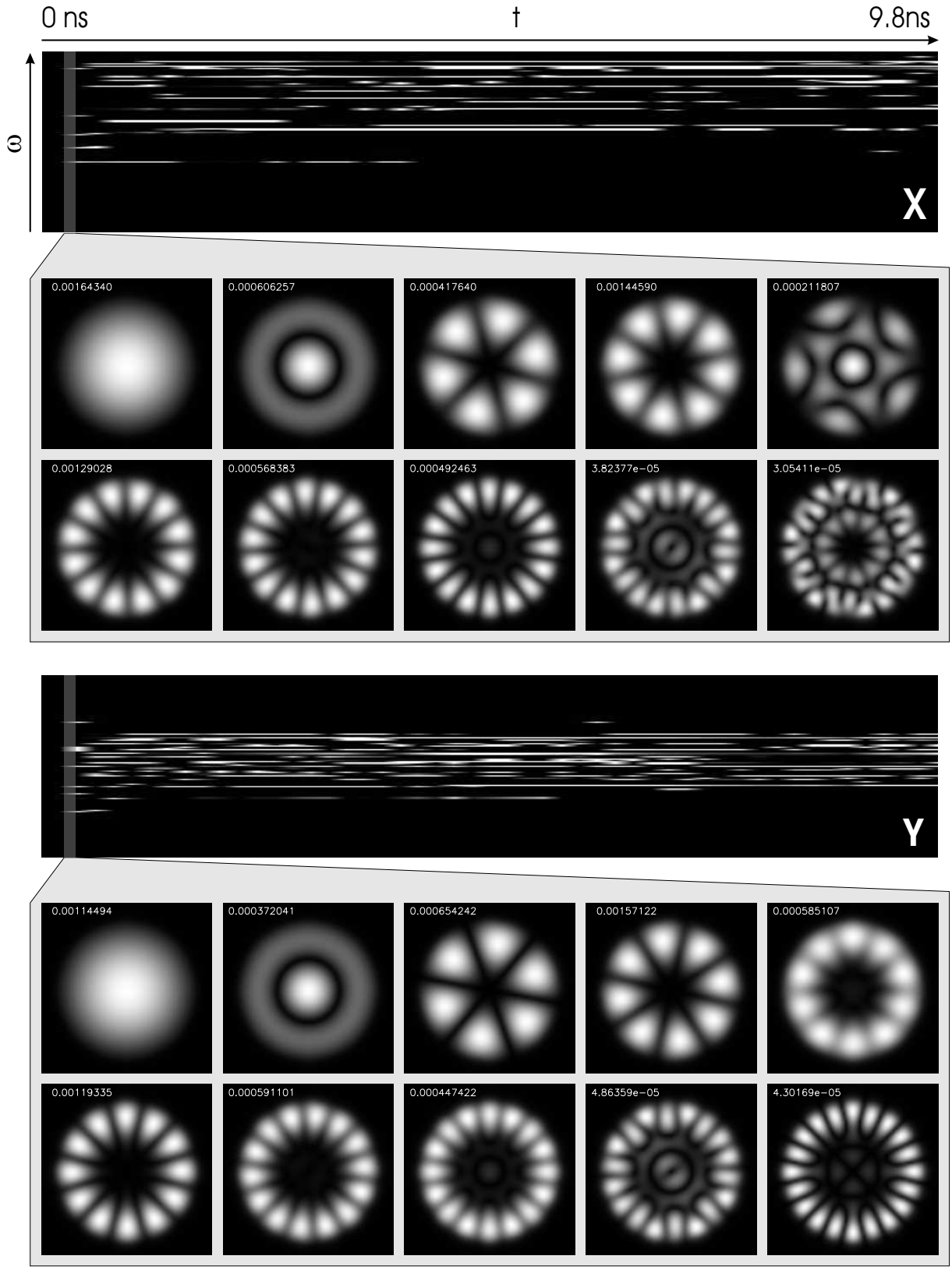

Figure 5.11: **V15** {3} – Spectral composition of the near-field of the second frame (192 – 384 ps). For a detailed explanation see Section 5.11.

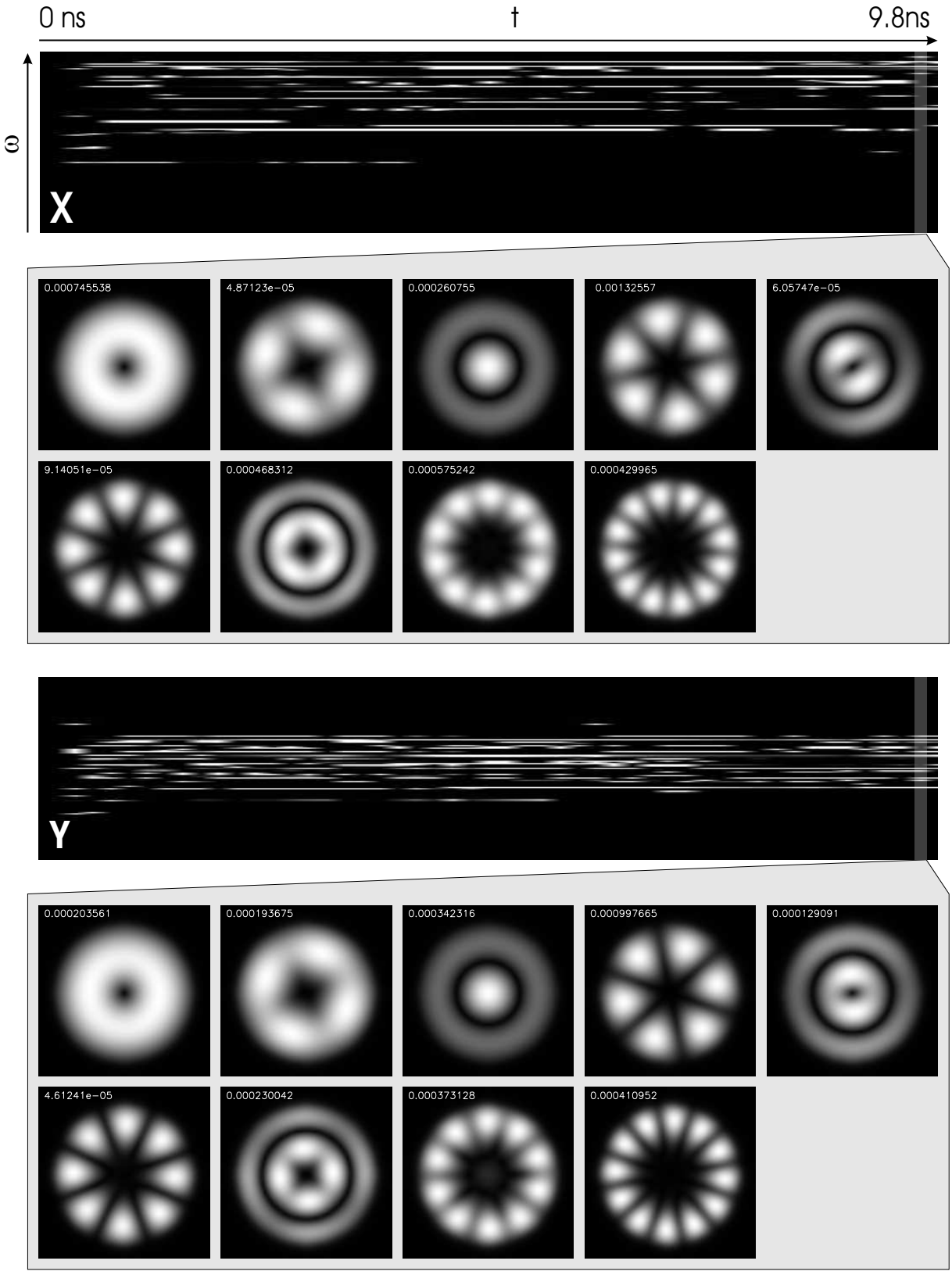

Figure 5.12: **V15** {3} – Spectral composition of the near-field of the 50th frame (9408 – 9600 ps). For a detailed explanation see Section 5.11.

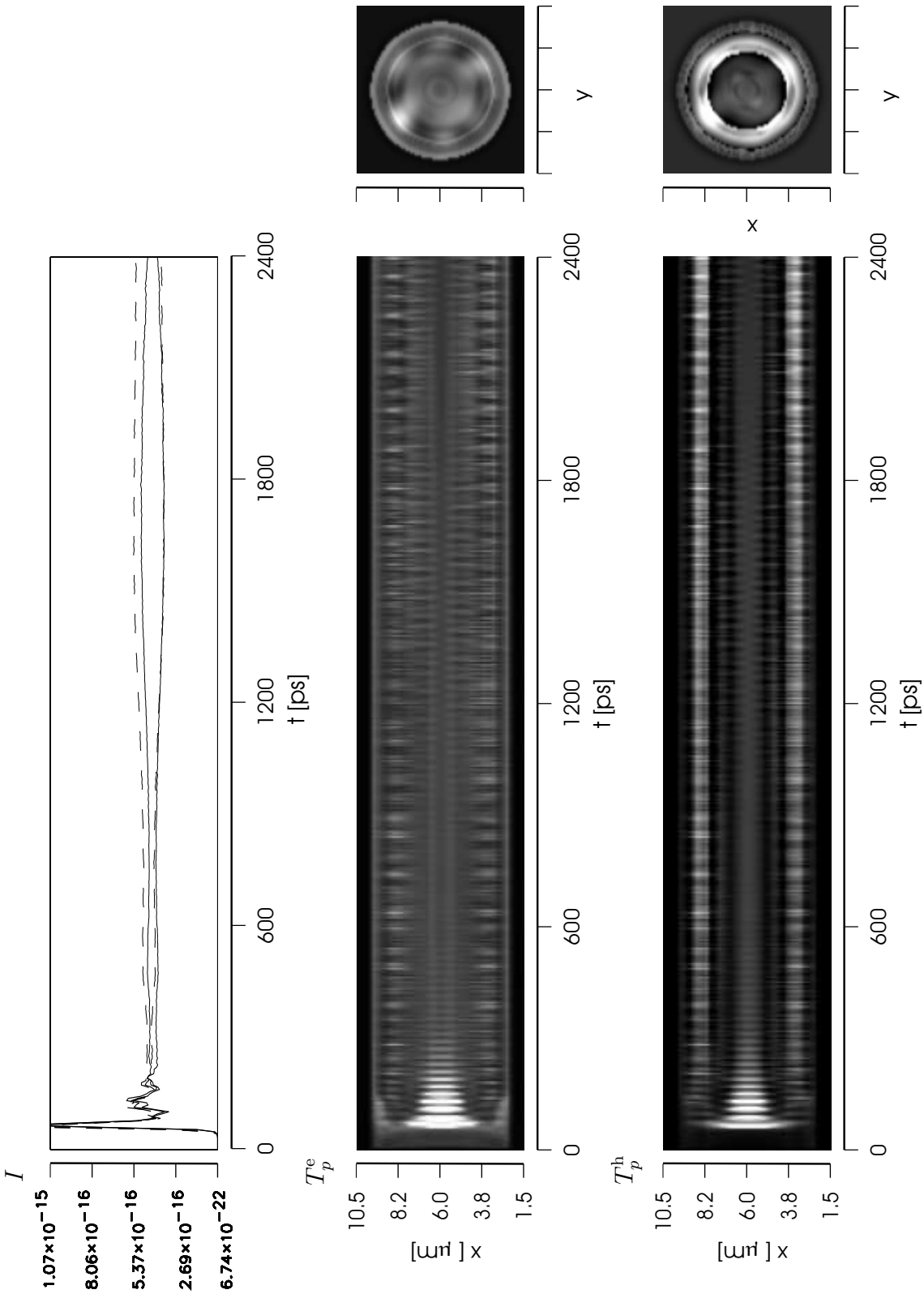

Figure 5.13: $\mathbf{V15}_{\mathrm{T}}\{3\}$ – Temperature dynamics. Top graph is a direct comparison between dynamic (solid) and static (dashed) polarisation resolved output intensities. Bottom colour plots show spatial-resolved cuts of the electron/hole plasma temperatures.

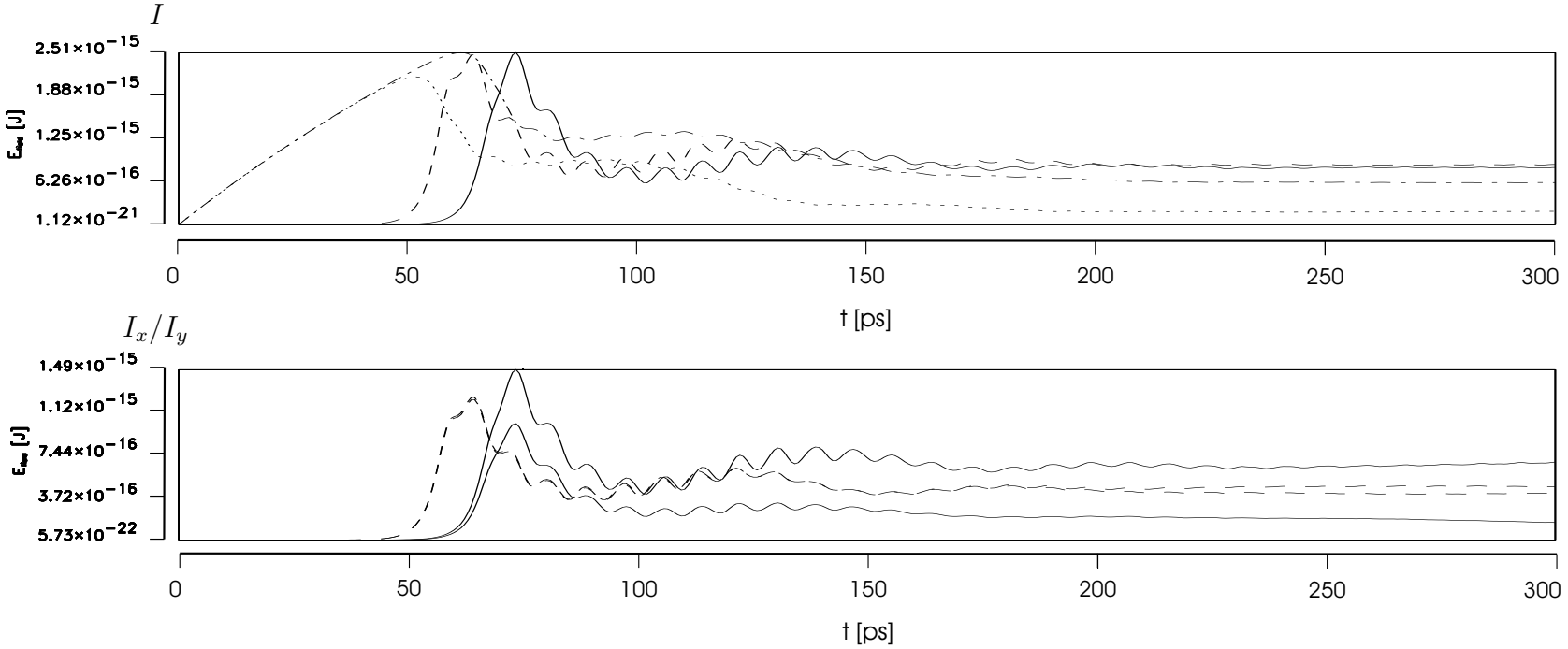

Figure 5.14: $\mathbf{V15}_{\mathrm{m}}\{3\}$ – Microscopic switch-on dynamics. The top graph shows the total intensities of $\mathbf{V15}_{\mathrm{m}}\{3\}$ (solid) and the mesoscopic model $\mathbf{V15}\{3\}$ (dashed). The corresponding densities (dash-dotted and dotted lines) are given as an inset. The graphs below show the output intensities for each polarisation and reveal a dominant y-polarisation. The ones drawn in solid lines are resulting from the full microscopic simulation while the dashed ones are attributed to the mesoscopic model.

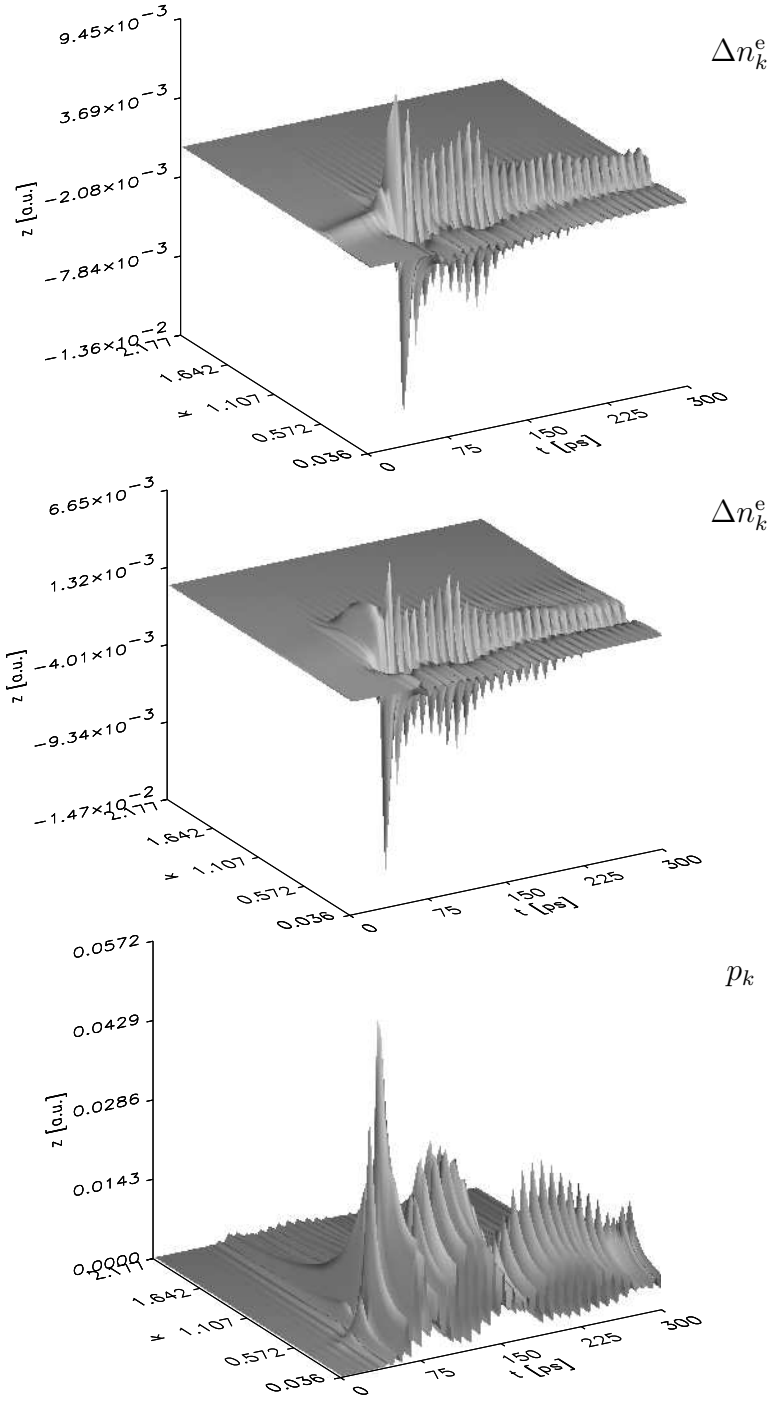

Figure 5.15: $\mathbf{V15}_{\mathrm{m}}\{3\}$ – Dynamics of the band-resolved electron (top) and hole (middle) densities. Bottom graph shows the microscopic interband-polarisation. See SECTION 5.13 for discussion.

5.14 Comparison with Experimental Results

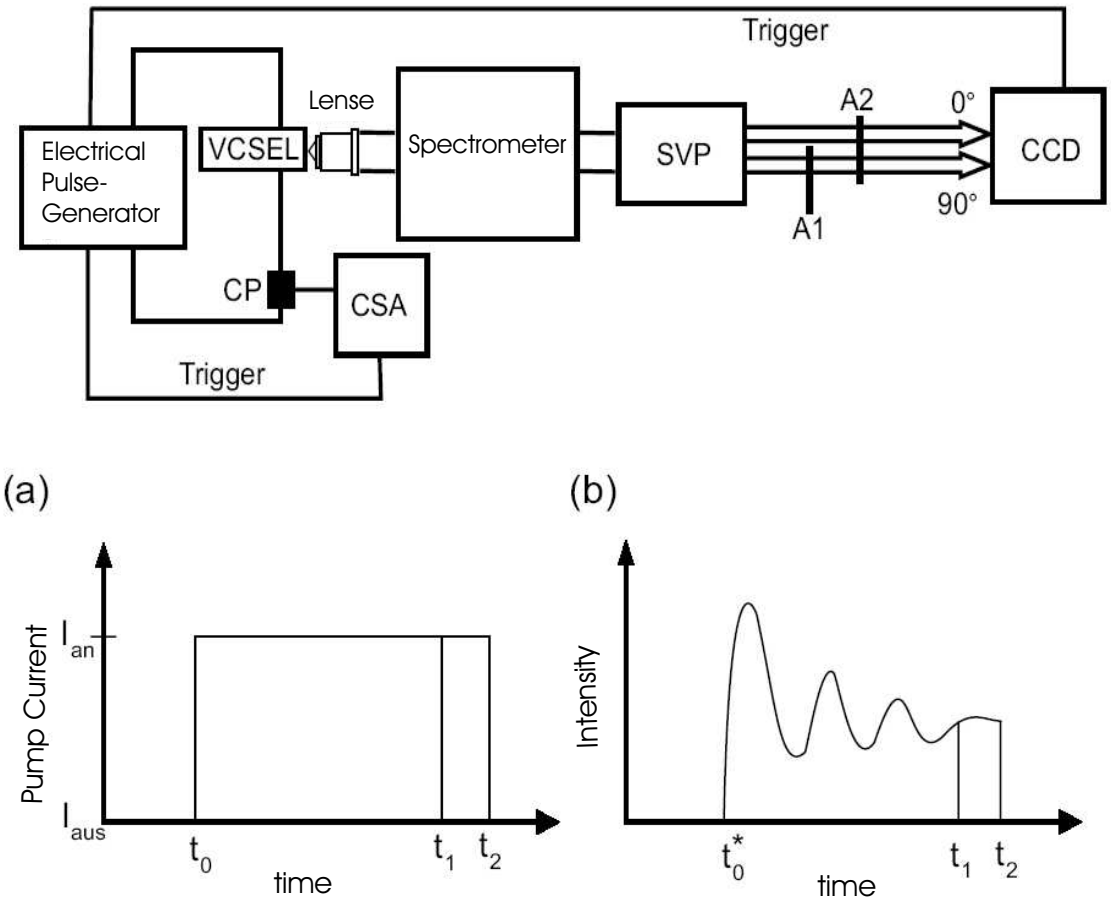

Figure 5.16: Experimental TRIDA setup as used for recording of the repetitive VCSEL dynamics down to a 10 ps resolution.

Due to the close analogy we will set our simulations into context with experimental data obtained from near-field measurements of VCSELs. The experiments were carried out by *Andreas Barchanski* from TU Darmstadt and involve polarisation resolved near-field measurements and TRIDA experiments on VCSELs [122]. As we do not want to go to much into the details of the experimental setup we refer to [143] which gives a good overview over the measument methods and their results. The Al-GaAs VCSEL under investigation is of 14 μm aperture and has a 28 layer top- and a 34 layer bottom-DBR. Emission wave-length is 850 nm.

Polarisation resolved near-field measurements of VCSELs can be performed by projecting the facet of the VCSEL via a set of lenses to the opening of a streak camera. The spatially resolved intensity patterns are integrated field intensities with the minimum integration time limited by the shutter-time of the streak camera (typically $> 10\mu$s). By putting a spectrometer into the beam path it is possible to decompose the averaged field

pattern into its spectral components [131]. Such measurements have been performed by *Degen et al.*. The integration time and the frame rate of the streak camera clearly make it impossible to analyse the ps-dynamics of a VCSEL with a standard setup. To tackle this problem an approach is chosen which is based on the assumption that two experiments with the same VCSEL, carried out with identical (as far as possible) operating conditions, reproduce (at least partially) the same output characteristics: the VCSEL is pumped with square shaped pump-pulses generated with a 10 ps resolution pulse-generator. For any given pulse length T the integration is repeated and averaged over a predefined number N (e.g. 1000) of *shots*. Then the pulse-length is increased by $\Delta t = 10\,\text{ps}$ – which is the minimum step-length resolution of the pulse-generator – and repeated N times. The averaged near-field images obtained from this second ensemble of averaged shots differ from the first by the *repetitive* part of the dynamics that took place within 10 ps. Thus, by subtracting the averaged integrated intensities of two successive sets a differential snapshot of the near-field can be obtained which is integrated over both the ensemble and the 10ps time window $[T, T + \Delta t]$ (see FIGURE 5.18). This measurement method is known as *Temporally Resolved Imaging by Differential Analysis* (TRIDA). FIGURE 5.16 illustrates the principle of the experimental setup that has been realised by the *Semiconductor Optics Group* at the TU Darmstadt.

While a simple integration over the spatial resolved images gives the total polarisation resolved intensities which are shown in FIGURE 5.17, a spectrometer can be integrated into the beam path in order to obtain spatial, temporal and spectral resolved images of the near-field FIGURE 5.19.

The relaxation oscillation shown in FIGURE 5.17 indicates a strong suppression of the x-polarisation which is only around 25% the value of the y-polarisation. The first peak is very distinct. A spectral temporal analysis shows that it is dominated by the LP_{00} ground mode and low order axial symmetric modes. Sample snapshots at $T = 2100\,\text{ps}$ and $T = 2260\,\text{ps}$ (see FIGURE 5.18) recorded with the TRIDA method (10 ps integration) reveal that the dominant mode is a LP_{04} daisy-mode. In the centre a donut shaped pattern is visible which is presumably part of another mode. Comparing the two polarisations the conjugation of the patterns is eye-catching. This applies to both the rim area where the maxima of the weaker x-polarised mode match the minima of the y-polarised mode but also applies to the centre area where the y-polarisation is strong and the x-polarisation is very dim. FIGURE 5.19 represents another experiment and displays the near-field decomposed into both, polarisation and spatial modes. Here, the y-polarised ground mode is bright and conjugated by a x-polarised mode of LP_{02} kind. Similar to our simulations the y-polarisation features a much broader spectrum of bright modes.

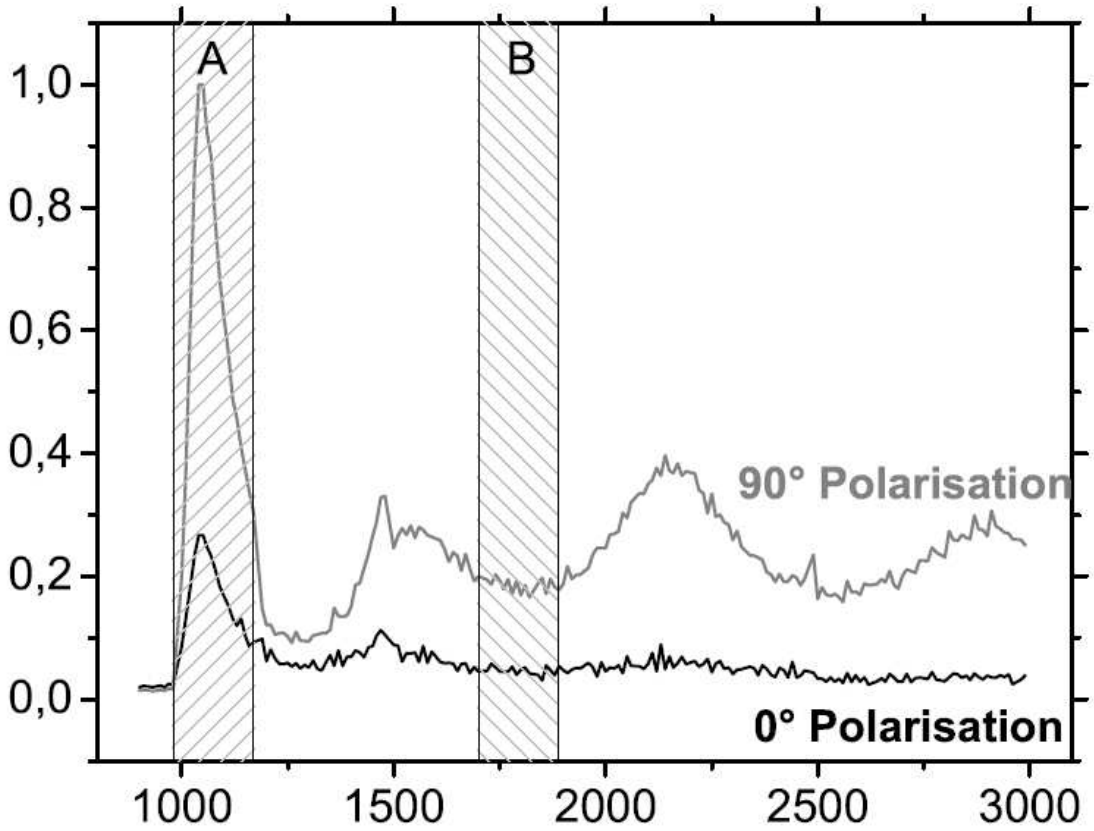

Figure 5.17: Measured relaxation oscillation. The y-axis is in arbitrary units, the x-axis displays time in picoseconds. The first peak of the relaxation oscillation starts at $t = 1000\,\text{ps}$ and is $\sim 400\,\text{ps}$ in width. Peak-intensity of the x-polarisation is approximately 25% of the y-polarisation.

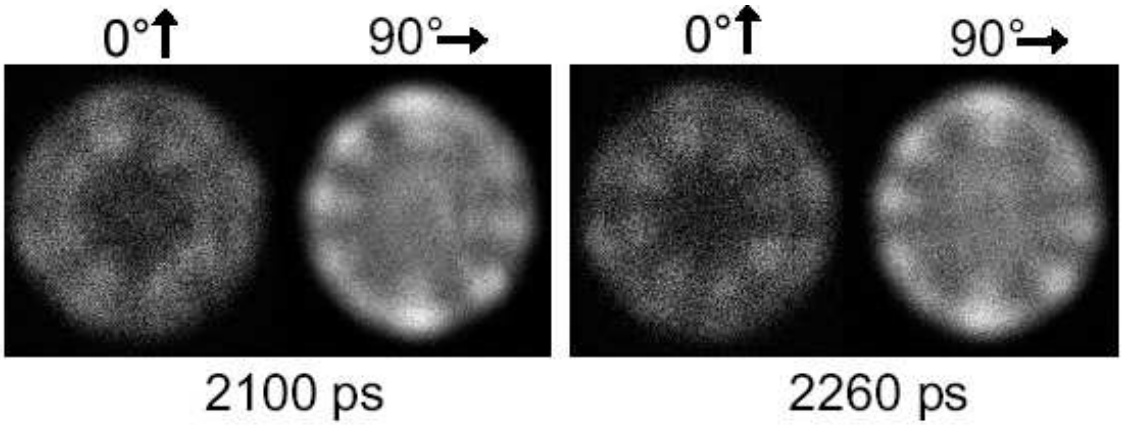

Figure 5.18: Near-field intensity patterns at $t = 2100\,\text{ps}$ and $t = 2260\,\text{ps}$. The pictures show the repetitive differential intensity increase within 20 ps.

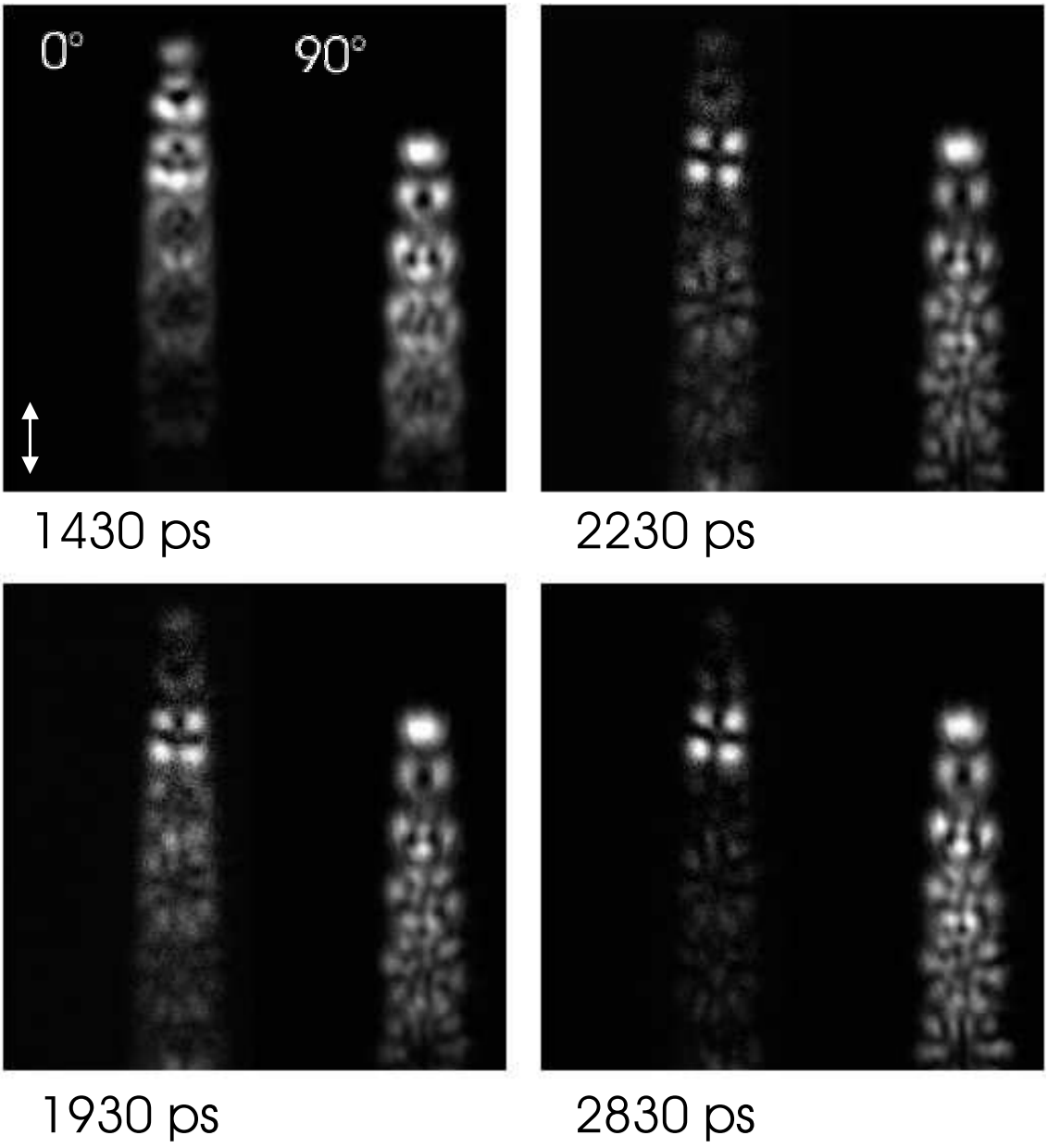

Figure 5.19: Spectral, temporal and polarisation resolved near-field pattern of a 14μm aperture VCSEL. The y-axis is the wavelength λ with increasing values from bottom to top. The small arrow indicates a wavelength delta of $\Delta\lambda \approx 0.1$ nm.

6 Longitudinal Multi-Level VECSEL Dynamics

6.1 Introduction

A straight forward approach to increase the optical power output of a VCSEL would be to make the VCSEL structure broader and to increase the aperture diameter. As we have seen in CHAPTER A.1 this leads to a situation where both, transverse mode and polarisation dynamics become more and more distinct. The mode-beating causes fluctuations which are imposed on the nearfield and degrade the divergence of the farfield. For most applications this is a rather undesirable situation as e.g. the incoupling and the dispersion in fibres becomes worse. Suppression of transverse higher order modes can be achieved by means of an external mirror stabilising low order Gaussian modes. Leading edge projection and display technologies (Laser-TV) which are currently in development would also require a low divergent beam to allow for the highest possible resolutions.

The concept of the *vertical external cavity surface-emitting lasers* (VECSEL) was invented around 1999. Thus, they constitute a relatively young tribe of vertical emitting semiconductor laser devices [144]. In comparision to the weak emission power of VCSELs (~ 10 mW) they are designed for much higher output intensities of 500 mW– 1 W. This is comparable to the output power of broad-area edge-emitting devices but without their high astigmatic poor beam-quality. Recent efforts concentrate on designing more powerful optically pumped vertical extended cavity surface-emitting lasers and on improving their thermal properties. A VECSEL consists of three basic elements. A *chip* mounted on a heat sink, an external mirror, and a pump source. The chip is a grown semiconductor multi-layer structure which is integrating a (bottom) DBR together with a couple of multi quantum-well (MQW) structures placed on top. The multiple quantum-well structures (MQW) are embedded in between *barriers* and put into positions where they match the optical mode maxima best. In optically pumped systems the carriers are either generated within the barrier states or directly within upper levels of the quantum-wells. Graded-index speparate-confinement heterostructures (GRINSCH) help to improve the capturing process of carriers into the wells [24]. In comparision to a VCSEL the external mirror replaces the top-DBR and enforces a transverse Gaussian mode operation (see FIGURE 6.1) [144]. Although, the cavity of a VECSEL is not a typical microcavity, there are some similarities: 1) The bottom DBR mirror is highly frequency selective. 2) The optical coupling between the carriers captured in the quantum-wells and the longitudinal lasing modes is strongly enhanced due to a high longitudinal confinement-factor. This

is because the DBR fixes the field node positions which also increases the spontaneous emission coupling factor β. Various dielectric resonator designs are possible: While some devices use AR-coating on top of the chip in order to completely avoid a chip internal cavity, others are operated in resonance or anit-resonant to the dielectric cavity. The dielectric cavity can be regarded in both cases as a longitudinal microcavity of several μm in length with an external mirror attached in some cm distance from the chip.

As similarities and differences between VCSEL and VECSEL are obvious we aim to develop a theoretical model for optically or electrically pumped systems which allows us to investigate the combined carrier and longitudinal light-field dynamics. The carrier transport is described on base of electronic multi-level equations which model both electron and the hole dynamics based on quasi-equilibrium distribution functions. The spatial carrier dynamics is integrated by a simple transport model. The equations presented are a first step towards a complex tool for the analysis of longitudinal and polarisation dynamics. Polarisation dynamics in optically pumped VCSELs has been recently studied in [145] where the impact of spin-polarisation is analysed by exciting the medium with elliptical polarised pump light. Further scenarios where the presented model can be applied are passive mode-locking and the generation of ultrashort high-intensity pulses by mean of integrated saturable-absorbers (SESAMs). This however, will not be covered within this work.

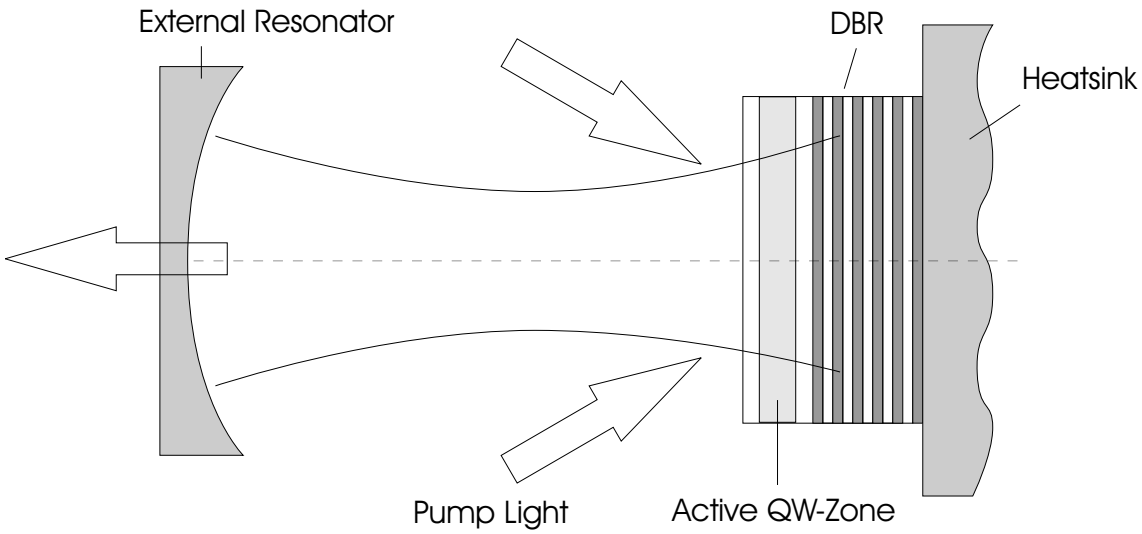

Figure 6.1: Schematic diagram of an optically pumped semiconductor vertical extended cavity surface-emitting laser (VECSEL). The active zone consists of multi-quantum-well layers (MQW) grown in between the barriers. The multi-layer Bragg-mirror which is also a part of the semiconductor chip is directly mounted onto the heat-sink. Depending on the design an anti-reflective coating layer is grown on top of the chip.

Firstly, we present some of the key concepts of our longitudinal model. The first one concerns the effective description of transverse processes, which will be dynamically

neglected as 1) field-profiles are transversely static in quasi-cw and 2) the timescales involved in transverse carrier and temperature diffusion processes are usually much slower than the timescale associated with the carrier light-field coupling. Instead, we chose an effective transverse description which means, that we split the each field-component of any physical entity $A(\mathbf{r}, t)$ (e.g. electric field) into a static radial part and a dynamic longitudinal part:

$$A(\mathbf{r}, t) \rightarrow f(x, y)A(z, t) \,. \tag{6.1}$$

$f(x, y)$ is a valued real function which is normalised on a predefined circular area $[0, R]$. Consequently, we enter the various physical equations (e.g. carrier diffusion) with this ansatz, average from $[0, R]$ over the transverse direction and thereby deduce an effective longitudinal description which then includes all transverse effects in terms of loss terms (e.g. transverse carrier loss).

Another key element of our VECSEL description is the external mirror structure which imposes an optical way-length of several cm. The associated round-trip time is of the order of 100 ps and has to be integrated into the model as it may become resonant with internal processes. Furthermore, it is known that a delayed feedback response of the reflected light can cause additional dynamical effects, e.g. feedback induced instabilities. A full time-domain longitudinal model allows us to describe this delayed feedback in combination with longitudinal multi-mode behaviour. Both elements are elementary for the future simulation of pulse-generation scenarios.

In order to set up a laser model, we start with the classical laser equations introduced in Chapter 2 but supplement them with gain models and appropriate carrier transport equations for an electronic multi-level system. The longitudinal interplay between carrier generation, spatial carrier transport, carrier multi-level dynamics and the interacting light-field under the influence of an external cavity constitute major ingredients of this model. We stress, that the focus of the presented model is on the spatio-temporal dynamic interaction between the carrier and light-field subsystem. It implements some elements of carrier transport theory but on a rather simplified level.

6.2 Light-Field and Quantum-Well Gain

As a first step we want to verify the validaty of the longitudinal optical model (2.3). By applying the generic ansatz (6.1),

$$\mathbf{E}(\mathbf{r}, t) \rightarrow f(x, y)\,\mathbf{E}(z, t) \,, \qquad \mathbf{H}(\mathbf{r}, t) \rightarrow f(x, y)\,\mathbf{H}(z, t) \,, \tag{6.2}$$

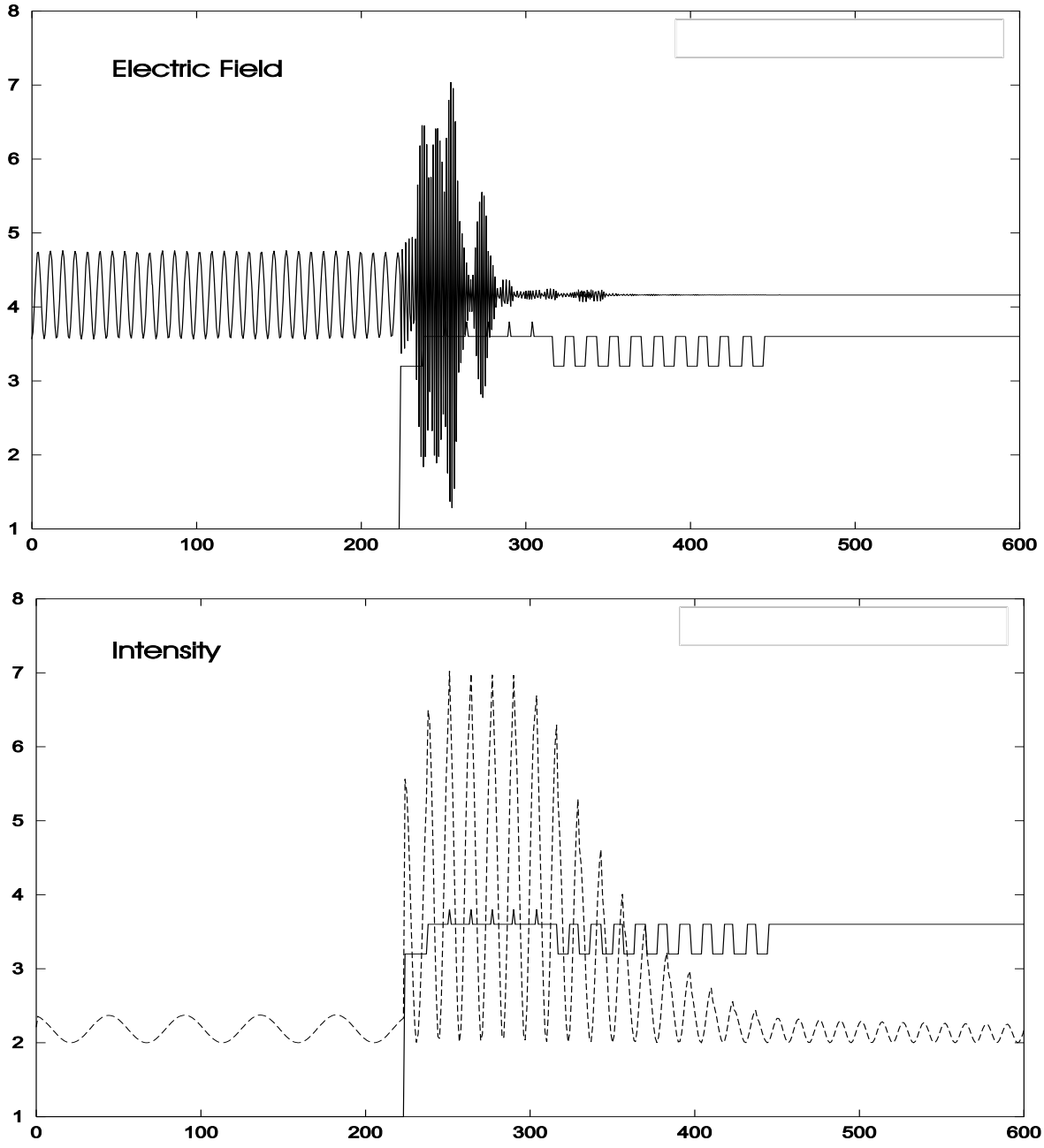

Figure 6.2: Optical field before (top) and after (bottom) the lasing sets in.

we can transform Maxwell's equations (2.1) to

$$-\mathbf{F}^* H_z + f\partial_z \mathbf{H}^* = \epsilon_0 \epsilon \partial_t \mathbf{E} + \partial_t \mathbf{P} \,, \tag{6.3}$$

$$-\mathbf{F} \cdot \mathbf{H}^* = \epsilon_0 \epsilon \partial_t E_z + \partial_t P_z \,, \tag{6.4}$$

$$-\mathbf{F} E_z + f\partial_z \mathbf{E} = \mu_0 \partial_t \mathbf{H}^* \,, \tag{6.5}$$

$$-\mathbf{F}^* \cdot \mathbf{E} = -\mu_0 \partial_t H_z \,, \tag{6.6}$$

where the previously introduced two-dimensional component notation has been used,

$$\mathbf{A} = (A_x, A_y)\,, \quad \mathbf{A}^* = (-A_y, A_z). \tag{6.7}$$

'$*$' marks duality, that is $\mathbf{A}\cdot\mathbf{A}^* = 0$. We defined $\mathbf{F}$ as the gradient of $f(x,y)$. Assuming a standing wave, the time derivatives of the z-components can be neglected. Additionally we set $\partial_t P_z = 0$, which means that $\mathbf{E}$ and $\mathbf{H}^*$ have to be orthogonal to $\mathbf{F}^*$ and $\mathbf{F}$, respectively. To maintain consistency the z components as such have to vanish. An integration over r shows, that in first approximation no transverse losses have to be taken into account which means that the one-dimensional Maxwell-equations (2.3) can be applied. However, we have to incorporate the field profile $f(x,y)$ as a transverse confinement-factor Γ_{xy} whenever we encounter an interaction term which involves the electrical field in combination with another field with a different transverse cross-section. E.g. if the active material would be concentrated in an area marked by a function $\eta(x,y)$, a confinement factor

$$\Gamma_{xy} = \int_A \eta(x,y) f(x,y) \mathrm{d}x\mathrm{d}y\,. \tag{6.8}$$

would have to be introduced in front of the $\dot{\mathbf{P}}\cdot\mathbf{E}$ term of the material equation.

To take into account active dipole-transitions we firstly take a look at the active material equations derived in Chapter 2. These equations constitute the response of an individual two-level system that couples to the electro-magnetic field. A simple Lorentzian material model can be applied as a local gain fit to quantum-well material or may account for an electronic transition between two levels in a quantum-dot. This was discussed in Section 2.5. As we want to treat the dynamics of electrons and holes separatly we label energetic electron states with i and hole states with j. In many cases the equations for electrons and holes are identical in shape. We then will write down only the one for the electrons. The equation

$$\partial_t^2 \mathbf{P}_{ij} + 2\gamma_{ij}\partial_t \mathbf{P}_{ij} + \omega_{0,ij}^2 \mathbf{P}_{ij} = -2\mathcal{V}_{ij}\xi_{ij}\mathbf{E}\big\{w_{ij}N_i^{\mathrm{e}} + (1-w_{ij})N_j^{\mathrm{h}} - 2N_{ij}^{\mathrm{tr}}\big\} \tag{6.9}$$

is the direct analogon to (2.6) but introduces both, electron and hole densities. ij labels a transition between the electronic level i occupied by N_i^{e} electrons and the hole level j occupied by N_j^{h} holes. w_{ij} takes values between 0 and 1. This weight factor takes respect to the fact that the material gain $G_{ij}(N_i^{\mathrm{e}}, N_i^{\mathrm{h}})$ associated with the optical transition $i \leftrightarrow j$ is always a function of both, the electron and the hole density. ξ_{ij} is a matrix proportional to the diade of the dipole matrix element $\mathbf{M}_{ij}\mathbf{M}_{ij}^T$. Equation (6.9) is a first order expansion of the gain around $N_i^{\mathrm{e}} = N_j^{\mathrm{h}} = N_{ij}^{\mathrm{tr}}$. N_{ij}^{tr} is defined by

$$G_{ij}(N_{ij}^{\mathrm{tr}}, N_{ij}^{\mathrm{tr}}) = 0 \tag{6.10}$$

and one can see, that

$$G_{ij}(N_i^{\mathrm{e}}, N_j^{\mathrm{h}}) = \underbrace{\frac{\partial G_{ij}}{\partial N_i^{\mathrm{e}}}}_{g_{ij}^{\mathrm{e}}}(N_i^{\mathrm{e}} - N_{ij}^{\mathrm{tr}}) + \underbrace{\frac{\partial G_{ij}}{\partial N_j^{\mathrm{h}}}}_{g_{ij}^{\mathrm{h}}}(N_j^{\mathrm{h}} - N_{ij}^{\mathrm{tr}})\,. \tag{6.11}$$

This renders the weight factor w_{ij} to be $g^{\mathrm{e}}_{ij}/(g^{\mathrm{e}}_{ij} + g^{\mathrm{h}}_{ij})$.

In a general sense, (6.9) defines the response of the transition ij to the electric field $\mathbf{E}$. $\mathbf{P}_{ij}[\mathbf{E}]$ can be implemented using more complicated material models, using a time-domain equivalent of the k-resolved semiconductor Bloch-equations or an arbitrary gain function by applying the fit-model that was presented in SECTION 2.5. The parameters γ_{ij}, $\omega_{0,ij}$, ξ_{ij} and w_{ij} loose their direct physical meaning. but are considered fit-parameters which conceive a part of a more complicated material response.

One has to keep in mind, that the electron and hole densities which enter (6.9) differ for quantum-dot, quantum-well and bulk densities. If $\mathbf{P}_{ij}$ is calculated as the material polarisation which enters Maxwell-equations (2.3), then we have to correct the dimension in (6.9) depending on the dimension of the electronic structure under consideration. This can be done by applying a *volume correction factor* $\mathcal{V}_{ij} = \mathcal{V}_i = \mathcal{V}_j$. For bulk transitions this factor is 1. For quantum-wells it is n_{QW}/d, with d being the thickness of quantum-well area and n_{QW} being the number of quantum-wells intersecting d. For quantum-dots, $\mathcal{V}_{ij}$ has to be replaced with the average number of quantum-dots per volume.

In FIGURE 6.2 we present snapshots which illustrate the light-field carrier dynamics for a sample VECSEL structure. The top picture shows the situation before the VECSEL starts lasing. The initial electric field is filtered by the bottom-DBR and experiences a delayed feedback from the external mirror attached at the left boundary. Before the lasing sets in the cavity is filled with a superposition of longitudinal modes which do not show a significant alignment of the mode maximas over the quantum wells (marked as little wedges). This situation changes once the coherent amplification sets in. The bottom picture shows a good match of mode-maxima and quantum-well. The emitted wave is very regular which means that the emitted light is occupying a narrow band of longitudinal modes.

6.3 External Mirrors and Delayed Feedback Boundary Conditions

For our simulations we developed and implemented full-time domain delayed feedback boundary conditions (DFBC). The DFBC are usually applied to the top of the simulation regime. These boundary conditions are constructed in such a way that a travelling wave or pulse which is incident to the boundary (e.g. at grid-point 0 in FIGURE 6.2) are absorbed and pushed through a delay line. Each time-step a pointer advances on a *ring*-buffer with T_{ext}/dt elements where T_{ext} is the round-trip time in the external resonator. After this time the pulse is injected back into the system but a) travelling in the opposite direction and b) phase shifted by $\pi/2$. The pulse appears as a mirrored copy of its original. Apart from the delay-time a damping-factor can be applied. This damping factor mimics the outcoupling losses of the external mirror. As a proof of the numeric

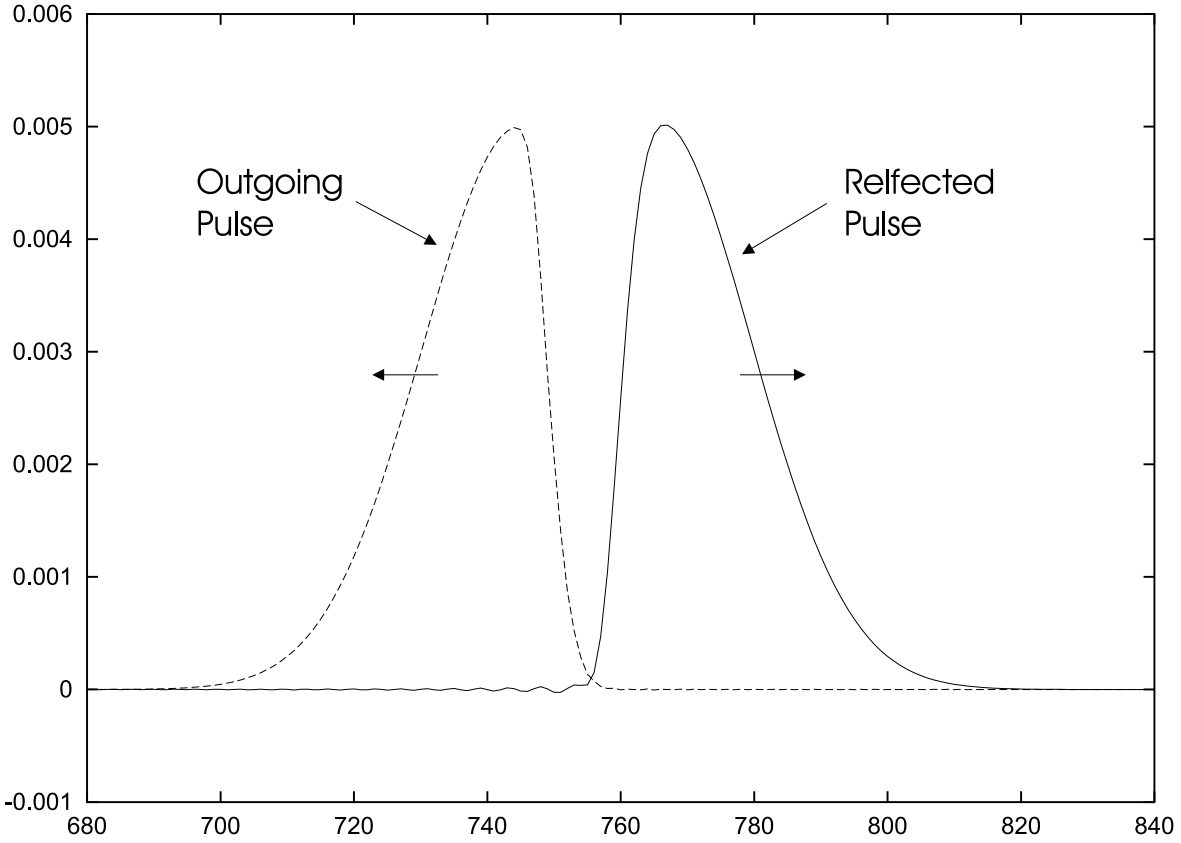

Figure 6.3: Record of the outgoing and reinjected pulse. The reflected pulse becomes phase-shifted and travels backs into the structure. The accuracy of the numerical method is within a promille range. Slight ringing effects are visible at the sharp left flank of the reflected pulse.

stability and accuracy we refer to FIGURE 6.3. Details of the numerical implementation can be found in APPENDIX C.

The big advantage between this method over an explicit simulation of Maxwell's Equations in air is the minimalistic computational effort. In fact, the only operations that have to be performed involve the fields at the boundary itself. Solving Maxwell's equations in air for a cm-length external cavity would mean that approximately $10^6 - 10^7$ timesteps would have to be performed. Even worse, the grid would have to be extended by an additional $10^6 - 10^7$ grid-points. Clearly, most of the computational time would be wasted in handling the extra memory through-put at each timestep. The presented algorithm reduces the memory load to a single store (for recording the pulse) and a load operation (for reinjecting the pulse) for each light-field component.

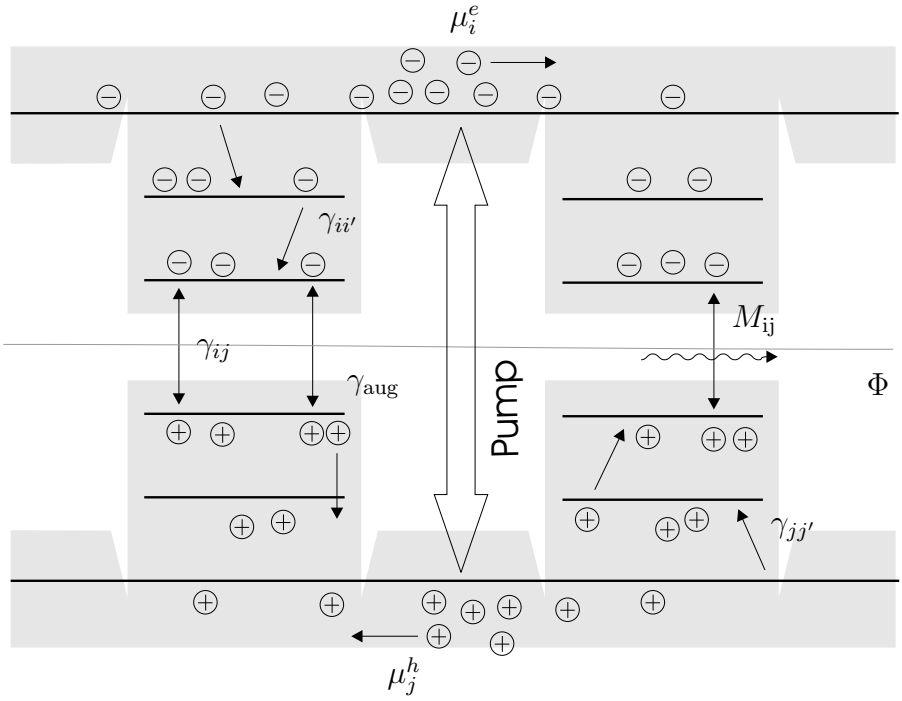

Figure 6.4: Schematic energy diagram of an optically pumped VECSEL showing the energy states of the barrier states an the quantum wells showing the various kinds of relaxation, excitation mechanisms.

6.4 Multi-Level Carrier Dynamics

Within the framework of our model we describe the dynamics of electrons $N_i^{\mathrm{e}}(z)$ and holes $N_j^{\mathrm{h}}(z)$ within the semiconductor structure separatly. While the dependence on z accounts for the spatial dynamics and thereby introduces spatial hole burning and effects of non-ambipolar transport, the indexes i and j comprise the occupation of energetic levels. Some main aspects of multi-level carrier dynamics within a given structure can be described by a set of equations

$$\begin{aligned}\partial_t N_i^{\mathrm{e}} = \partial_t N_i^{\mathrm{e}}|^{\mathrm{ct}} + \sum_j \eta_{ij} G_{ij} - \sum_j \gamma_{ij}^{\mathrm{rec}} B_{ij}(N_i^{\mathrm{e}}, N_j^{\mathrm{h}}) N_i^{\mathrm{e}} \\ - \sum_{i', E_{i'} < E_i} \gamma_{ii'}^{\mathrm{rel}} B_{ii'}(N_i^{\mathrm{e}}, N_{i'}^{\mathrm{e}}) N_i^{\mathrm{e}} + \sum_{i', E_{i'} > E_i} \gamma_{i'i}^{\mathrm{rel}} B_{i'i}(N_i^{\mathrm{e}}, N_{i'}^{\mathrm{e}}) N_{i'}^{\mathrm{e}} \,.\end{aligned} \tag{6.12}$$

The respective hole equation can be obtained from this one by replacing i with j and j with i. With this equation, recombination and relaxation processes are taken into account on a phenomenological level. η_{ij} equals one for an allowed optical transition $i \leftrightarrow j$ and else equals zero. G_{ij} is the associated transition response which can be generally written as a superposition of multiple Lorentzians (see Section 2.5 or Chapter 4),

$$G_{ij} = \sum_l \frac{1}{\hbar \omega_{ij,l}} \mathbf{E} \cdot \partial_t \mathbf{P}_{ij,l} \,. \tag{6.13}$$

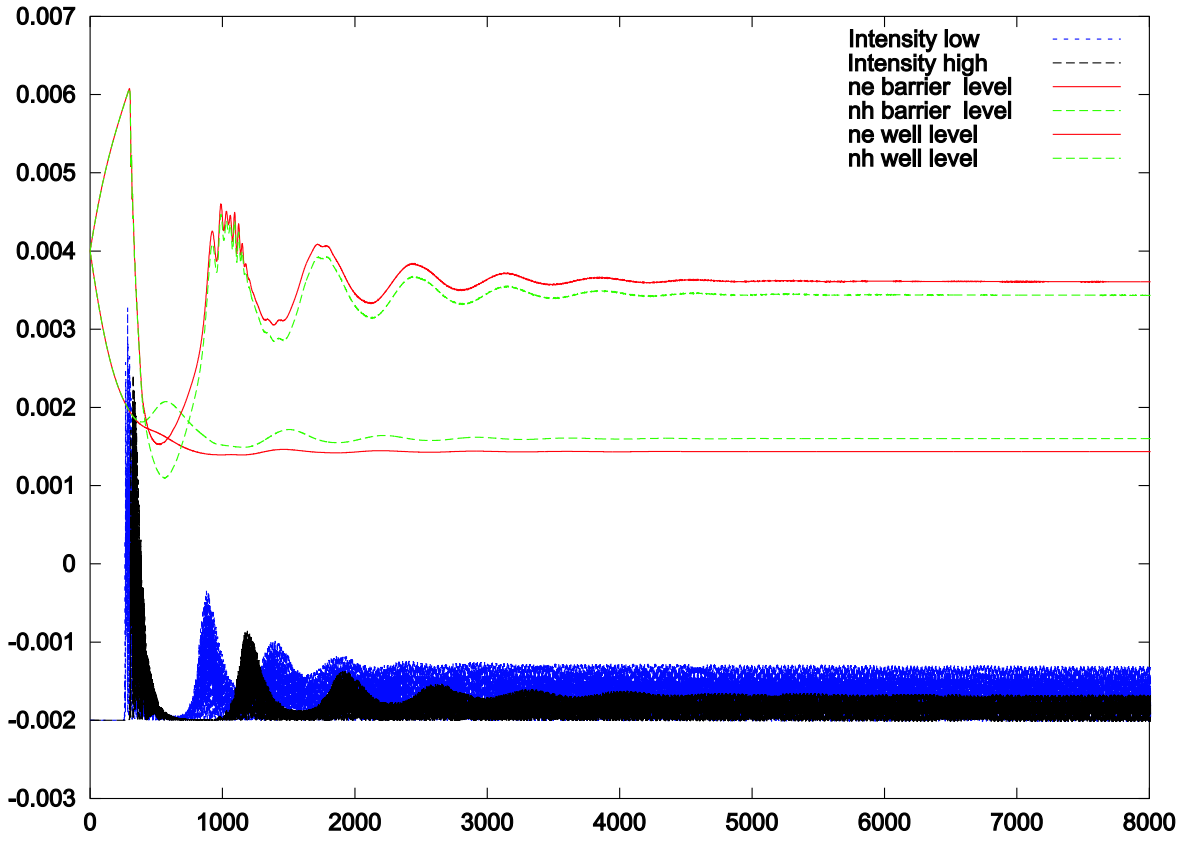

Figure 6.5: Relaxation oscillation of a 2 level VECSEL model. The light-field intensities are drawn in the lower part, where the black one is for a lower pump level and the grey one for a pump twice as high. The four carrier densities in the upper part are for the electron / hole densities of the barrier states and the lowest quantum-well level respectively. The carrier densities and the black intensity graph belong together.

The B coefficients denote level specific transition blocking factors applied to the various recombination and relaxation processes. They take values between one (no blocking,)and zero (full blocking). They generally show a dependence on both the initial and the final level's carrier density. For bulk and quantum-well levels we use factors of the kind

$$B(N_i^{\mathrm{e}}, N_{i'}^{\mathrm{e}}) = 1 \,, \tag{6.14}$$

$$B(N_i^{\mathrm{e}}, N_j^{\mathrm{h}}) = N_j^{\mathrm{h}}/(N_i^{\mathrm{e}} + N_j^{\mathrm{h}}) \,. \tag{6.15}$$

For bulk and quantum-well material we do not introduce blocking for inter-level relaxation. This reflects the assumption that there are always enough empty states for each electron relaxating to another electron level. The second factor describes nonradiative recombination between electrons and holes. This term emerges from the Shockley-Read dark-recombination rate [15] where we neglect the intrinsic carrier densities. In the quantum-dot case a full quantum-mechanical treatment on base of a many-particle description would be necessary to comprise the quantum-statistical aspects of level oc-

cupation. This would include to resolve spin-related effects and to take into account electron-electron exchange- and Coulomb-interactions. However, the above approach in combination with blocking factors

$$B(N_i^{\mathrm{e}}, N_{i'}^{\mathrm{e}}) = 1 - N_i^{\mathrm{e}}/N_i^{\mathrm{deg}}\,, \tag{6.16}$$

$$B(N_i^{\mathrm{e}}, N_j^{\mathrm{h}}) = N_j^{\mathrm{h}}/N_j^{\mathrm{deg}}\,, \tag{6.17}$$

can be considered as an approximation which is incorporating Pauli blocking on a very simplified level. Here, N_i^{deg} and N_j^{deg} are the degeneracies of the electron level i and hole level j, respectively.

$\partial_t N_i^{\mathrm{e}}|^{\mathrm{ct}}$ is the change of the local carrier density due to the carrier drift and diffusion. In good approximation, we assume that this term is zero for energetic states confined in z-direction (quantum-well, quantum-dot). However, the trapped carriers always contribute to the electro-static potential which is experienced by the free moving carriers occupying the bulk states. Equation (6.12) is solved on a one dimensional-grid. Apart from optical pumping we can also inject carriers electrically by using Neumann-type boundary conditions for the drift diffusion equation which will be discussed now.

6.5 Electrostatic Potential and the Carrier Drift-Diffusion Equation

For unconfined carrier states we take into account the impact of drift and diffusion. In three dimensions the change of carrier density due to the carrier flux can be calculated from a simple model,

$$\partial_t N_i^{\mathrm{e}}|^{\mathrm{ct}} = -\nabla \cdot J_i^{\mathrm{e}}\,, \qquad \text{with} \qquad J_i^{\mathrm{e}} = -D_i^{\mathrm{e}} \nabla N_i^{\mathrm{e}} - \mu_i^{\mathrm{e}} N_i^{\mathrm{e}} \nabla(\mathcal{E}_i + \Phi)\,. \tag{6.18}$$

Here, D_i^{e} is the electron diffusion constant and μ_i^{e} is the mobility of electrons. $\mathcal{E}_i$ is the potential energy or the i'th level and $\Phi(z)$ the electrostatic potential. In order to calculate $\Phi(z)$ we must perform the sum over all carriers, confined or unconfined, within this spatial cell. In electro-static approximation, it is sufficient to solve Poissions-equation,

$$\nabla \cdot \epsilon \nabla \Phi = \sum_{ij} q(N_i^{\mathrm{e}} - N_j^{\mathrm{h}})\,. \tag{6.19}$$

Appropriate boundary conditions of either Neumann or Dirichlet type allow to either model the injection of carriers through contact layers or to describe surface recombination.

As we target a one-densional model we enter (6.18) with transverse carrier profiles and a transverse profile for the electro-magnetic potential Φ,

$$\begin{aligned} N_i^{\mathrm{e}}(\mathbf{r}, t) &\to h_i(x, y)\, N_i^{\mathrm{e}}(z, t)\,, \\ \Phi(\mathbf{r}, t) &\to k(x, y)\, \Phi(z, t)\,. \end{aligned} \tag{6.20}$$

After an integration over the transverse coordinates we obtain a one dimensional equation for the one-dimensional transversely averaged field $N_i^{\mathrm{e}}(z,t)$

$$\partial_t N_i^{\mathrm{e}}|^{\mathrm{ct}} = -\partial_z \left(-D_i^{\mathrm{e}} \partial_z N_i^{\mathrm{e}} - \mu_i^{\mathrm{e}} N_i^{\mathrm{e}} \partial_z (\mathcal{E}_i + \Phi)\right) + \partial_t N_i^{\mathrm{e}}|^{\mathrm{ct},\perp} . \tag{6.21}$$

$\partial_t N_i^{\mathrm{e}}|^{\mathrm{ct},\perp}$ contains all the transverse transport effects. If we assume that $\mathcal{E}_i$ is a functions of z only, we can show, that

$$\begin{aligned} \partial_t N_i^{\mathrm{e}}|^{\mathrm{ct},\perp} = & \mu_i^{\mathrm{e}} N_i^{\mathrm{e}} \, \Phi \frac{1}{A} \int\limits_A (h_i \Delta k) \mathrm{d}A + D_i^{\mathrm{e}} N_i^{\mathrm{e}} \frac{1}{A} \int\limits_A (\Delta h_i) \mathrm{d}A \\ & + \mu_i^{\mathrm{e}} N_i^{\mathrm{e}} \frac{1}{A} \int\limits_A (\nabla h_i) \cdot (\nabla k) \mathrm{d}A \, . \end{aligned} \tag{6.22}$$

with $\nabla = (\partial_x, \partial_y)$ and $\Delta = \partial_x^2 + \partial_y^2$. The three-dimensional Poisson equation (6.19) takes the simplified form

$$k \partial_z (\epsilon \, \partial_z \Phi) + \epsilon \, \Phi \Delta k = \sum_{ij} q (h_i N_i^{\mathrm{e}} - h_j N_j^{\mathrm{h}}) \, . \tag{6.23}$$

This equation can only be solved if we use a homogenous transverse carrier profile $h(x,y)$. Applying this approximation, we obtain

$$k \partial_z (\epsilon \, \partial_z \Phi) + \epsilon \, \Phi \Delta k = h \sum_{ij} q (N_i^{\mathrm{e}} - N_j^{\mathrm{h}}) \, . \tag{6.24}$$

The k and h factors drop out after averaging over the area A. Equation (6.24) then becomes a one-dimensional equation which can be solved in a very efficient way with help of the *Thomas-algorithm* (see APPENDIX C).

6.6 The Energy-Transfer Model and the Temperature Equations

For the following we assume that the carrier system is in a state of thermodynamic quasi-equilibrium. This means, that we consider the carriers of a electronic subsystem (bulk or quantum-well band) are distributed according to a Fermi-distribution function. This approach implies that intra-band processes are much faster than inter-band relaxation processes, an approximation, which is usually well justified by experimentally obtained data. Between the various carrier subsystems we assume that the dynamical equilibrium situation is obtained by the time when the number of carriers relaxating into this subsystem equals the number of carriers drained, either via non-radiative recombination, further relaxation to lower levels, radiative-recombination or thermionic emission.

In quasi-equilibrium the plasma energy U_i^{e} can be calculated in the same way than the density N_i^{e} from the distribution functions but incorporates higher order moments. For electrons occupying the subsystem i, we obtain the conditions functions.

$$\begin{aligned} N_i^{\mathrm{e}} &= N_i^{\mathrm{e}}(\mu,T) = \int \mathrm{d}k D_i^{\mathrm{e}}(k) f_k^{\mathrm{e}}(\mu,T)\,, \\ U_i^{\mathrm{e}} &= U_i^{\mathrm{e}}(\mu,T) = \int \mathrm{d}k D_i^{\mathrm{e}}(k)\epsilon_{k,i} f_k^{\mathrm{e}}(\mu,T)\,, \quad \epsilon_{k,i} = \frac{\hbar^2 k^2}{2m_i^*}\,. \end{aligned} \tag{6.25}$$

Within each band we assume a Fermi-distribution of carriers

$$f_k^{\mathrm{e}}(\mu,T) = \frac{1}{1+\exp[\beta(calE_i+\epsilon_{k,i}-\mu)]}\,, \qquad \beta = \frac{1}{k_{\mathrm{B}}T}\,. \tag{6.26}$$

Here, E_i denotes the level energy offset and $\epsilon_{k,i}$ the kinetic energy of the electron. The density of states for two-dimensional quantum-well or three-dimensional bulk structures are $D_i^{\mathrm{e}}(k) = (k/\pi)$ or $D_i^{\mathrm{e}}(k) = (k/\pi)^2$, respectively. The equations (6.6) define the thermodynamic state in quasi-equilibrium. By resolving $N = N_i^{\mathrm{e}}(\mu,T)$ with respect to μ we obtain the chemical potential $\mu_i^{\mathrm{e}}(N,T)$ as a function of N and T. For the two-dimensional case this can be done analytically,

$$\beta\mu_i^{\mathrm{e}}(N,T) = \ln\left[\exp\left(\pi\frac{\hbar^2\beta}{m_i^*}N\right)-1\right]\,. \tag{6.27}$$

while for the three-dimensional (bulk) case it is common to use the *Padé-Approximation* of the chemical potential,

$$\beta\mu_i^{\mathrm{e}}(N,T) = \ln\left(\frac{N}{N_0}\right) + K_1\ln\left(K_2\,\frac{N}{N_0}+1\right) + K_3\,\frac{N}{N_0}\,, \qquad N_0 = \frac{1}{4}\left(\frac{2m_i^*}{\pi\hbar^2\beta}\right)^{3/2} \tag{6.28}$$

which is considered good for $\beta\mu < 30$. The constants can be numerically calculated and are $K_1 = 4.8966851$, $K_2 = 0.04496457$, and $K_3 = 0.1333760$, respectively.

In order to conceive the temperature dynamics for the multi-level system, we set up the energy density as a dynamical variable. based on microscopic considerations (see Chapter 4) the energy density of a bulk or quantum-well band can be independently calculated. We obtain,

$$\begin{aligned} \partial_t U_i^{\mathrm{e}} =& \partial_t U_i^{\mathrm{e}}|^{\mathrm{ct}} + \sum_j \eta_{ij} G_{U,ij} - \sum_j \gamma_{ij}^{\mathrm{rec}} B_{ij}(N_i^{\mathrm{e}}, N_j^{\mathrm{h}}) U_i^{\mathrm{e}} \\ &- \sum_{i',E_{i'}<E_i} \gamma_{ii'}^{\mathrm{rel}} B_{ii'}(N_i^{\mathrm{e}}, N_{i'}^{\mathrm{e}}) U_i^{\mathrm{e}} + \sum_{i',E_{i'}>E_i} \gamma_{i'i}^{\mathrm{rel}} B_{i'i}(N_i^{\mathrm{e}}, N_{i'}^{\mathrm{e}}) U_{i'}^{\mathrm{e}} \\ &- \gamma_{\mathrm{LO},i}\left[U_i^{\mathrm{e}} - U_{\mathrm{eq},i}^{\mathrm{e}}(N_i^{\mathrm{e}}, T_l)\right]\,. \end{aligned} \tag{6.29}$$

$G_{U,ij}$ is the gain or loss of energy due to induced absoption or emission. For its calculation we refer to chapter Chapter 4. The last term comprises the transfer of energy

to the lattice by means of scattering with longitudinal optical phonons. This and the corresponding equation for the lattice temperature have been discussed in Section 5.4.

With an equation for the carrier densities and the energy densities we can use make use of together with the formulas for the chemical potentials in order to derive a plasma temperature. Another way would be to use relation (5.24).

The combined treatment of light-field carrier dynamics together with temperature dynamics would allow to address the temperature problems that are typical for VECSEL structures. In this section we provided a first framework of equations that might be used in combination with the light-field carrier equations. A detail analysis of the energy transfer is necessary to validate the assumptions. In particular, we have to validate the quasi-equilibrium ansatz which is known to become inaccurate in the high carrier density regime [49]. Apart from this there are many supplements that could be made to the presented model. Auger-recombination and a more realistic description of the carrier capturing from the barriers to the wells are just two examples. However, ieven the basic carrier rate equation model is featuring many dynamical aspects. A main focus for future work will be to activate a polarisation sensitive coupling to the active material and thereby include spin-polarisation into the presented model.

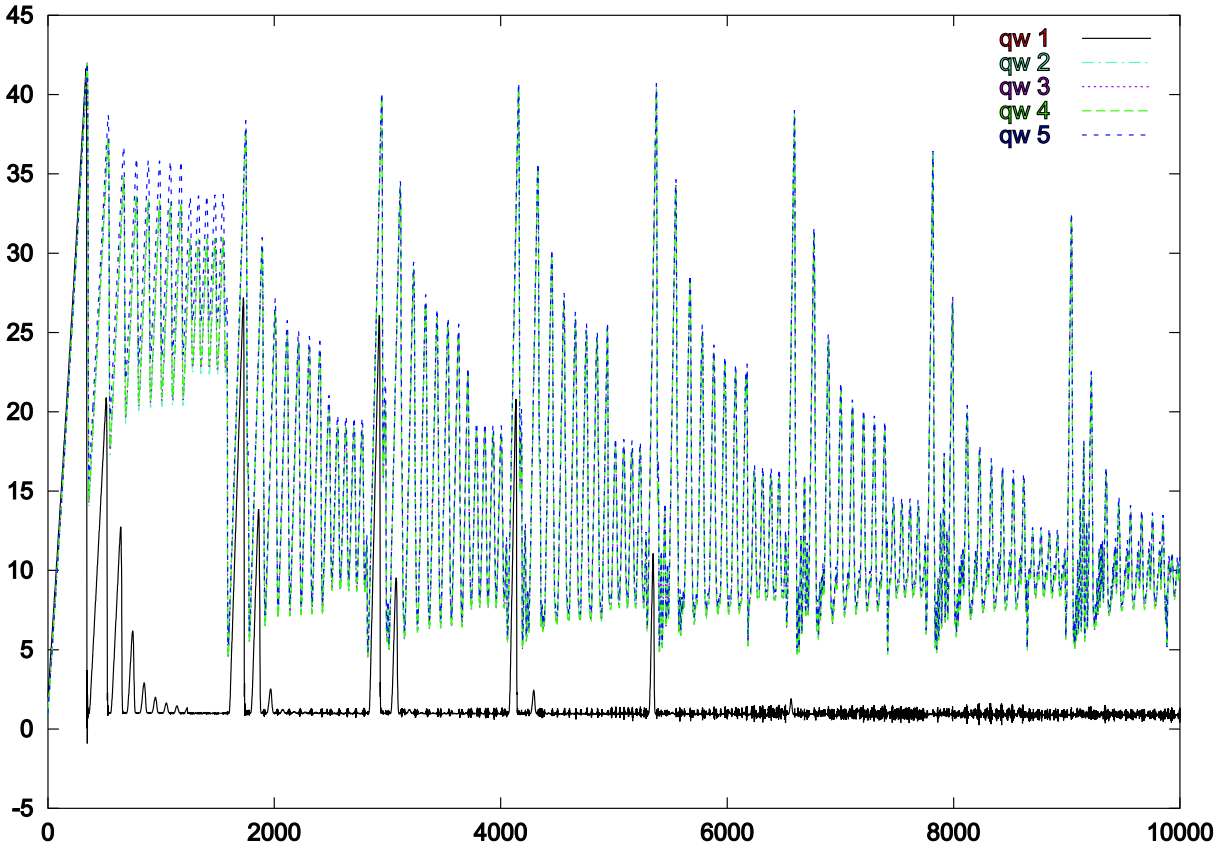

Figure 6.6: Multi-level simulation of a VECSEL. The lowest level corresponds to the energetically lowest level which features the best coupling to the resonant field in the cavity The levels form a relaxation cascade where the top level is optically pumped. The upper levels couple to the longitudinal side-modes which are induced by the external resonator (axes in arbitray units).

A Paraxial Approximation Applied to the Dielectric Fabry-Pérot

A.1 Dispersion Relation

We consider a dielectric resonator of length L and look for the solution $g(z)$ of equation (3.52). For a lossy resonator it is not possible to obtain static modes with real eigenvalues. This means, that in the absense of internal sources which would balance the losses, the eigenvalues of (3.52) render complex

$$K_0 = k_0 - i\alpha\,, \qquad k_0 = \omega/c\,, \quad \alpha = \gamma/c\,. \tag{A.1}$$

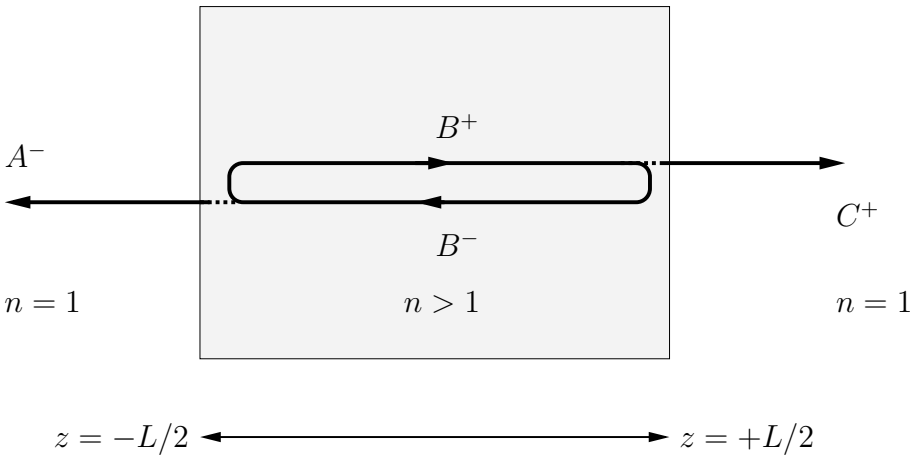

Figure A.1: Sketch: forward and backward propagating cavity modes B^+ / B^- and exterior waves A^- / C^+ for the dielectric resonator of length L.

Starting with equation (3.52), we define the equations

$$g'' = -\begin{cases} K_0^2 g & \text{within area A, C} \\ K_0^2\, n^2\, g & \text{within area B} \end{cases} \tag{A.2}$$

for the three adjacent parts A, B and C. The associated solutions take the functional shape

$$g = \begin{cases} A^- \mathrm{e}^{-ik_0 z} \mathrm{e}^{-\alpha z} & \text{within area A} \\ B^+ \mathrm{e}^{+ikz} \mathrm{e}^{+\beta z} + B^- \mathrm{e}^{-ikz} \mathrm{e}^{-\beta z} & \text{within area B} \\ C^+ \mathrm{e}^{+ik_0 z} \mathrm{e}^{+\alpha z} & \text{within area C}\,. \end{cases} \tag{A.3}$$

By inserting the solutions into the corresponding equations (A.2) the condition

$$k = n\,k_0 \quad \text{and} \quad \beta = n\,\alpha\,. \tag{A.4}$$

arises. We choose $A^- = C^+ = A$ and $B^+ = B^- = B/2$ for the complex amplitudes and thereby ensure that the connection conditions for both g and g' at the points $\pm L/2$ are fulfilled. This results in a complex dispersion relation

$$1/n = (\mathrm{e}^{x} - \mathrm{e}^{-x})/(\mathrm{e}^{x} + \mathrm{e}^{-x})\,, \quad x = (ik + \beta)L/2\,, \tag{A.5}$$

which can be separated into real and imaginary parts,

$$kL = m\pi\,, \quad m \geq 1\,, \tag{A.6}$$

$$n\sinh(\beta L) - \cosh(\beta L) = \cos(kL) = (-1)^m\,. \tag{A.7}$$

$m-1$ specifies the order of the mode. If $n > 1$ all modes with $m = 2, 4, 6, \ldots$ lead to constructive interference. Note, that the ratio of the amplitudes is determined to be

$$\frac{|A|^2}{|B|^2} = \frac{n}{2}\mathrm{e}^{-\alpha L}\sinh\beta L\,. \tag{A.8}$$

A.2 Wave-Equation and Effective Parameters

The damping constant βL is numerically calculated from the above relation. The resulting graph is shown in FIGURE A.2 as function over n. For increasing n, βL approaches $2/\sqrt{\epsilon}$ asymptotically. The associated damping factor per time unit is

$$\gamma = \beta\,c/n\,. \tag{A.9}$$

We can now determine the parameters needed for the transverse equation. Setting $z^{\pm} = \pm L/2$ we calculate the helpful quantities,

$$|g(z)|^2 = \frac{|B|^2}{2}\big[\cosh(2\beta z) + \cos(2kz)\big]\,, \tag{A.10}$$

$$\left(\frac{g'(z)}{g(z)}\right)^2 = (ik+\beta)^2\,\tanh^2\left[(ik+\beta)z\right] = (k-i\beta)^2\,\tan^2\left[(k-i\beta)z\right] \tag{A.11}$$

together with $|B|^2$ which is obtained from normalisation,

$$|B| = \left(\frac{2\beta L}{\sinh(\beta L)}\right)^{1/2}\,. \tag{A.12}$$

Beside the parameters $\Gamma_z = 1$, $n_{\text{eff}} = n$, $\nu = 1$ and $\gamma_{\text{res}} = \beta$ we have to evaluate $\langle\nu\delta n\rangle_z$ and $\langle\sigma\delta n\rangle_z$. Both of them vanish for the case $\delta n \to 0$. Assuming δn being not dependent on z, that is $\delta n = \delta n(x, y)$, we obtain

$$\langle\nu\delta n\rangle_z = \delta n \quad \text{and} \quad \langle\sigma\delta n\rangle_z = \delta n/n\,. \tag{A.13}$$

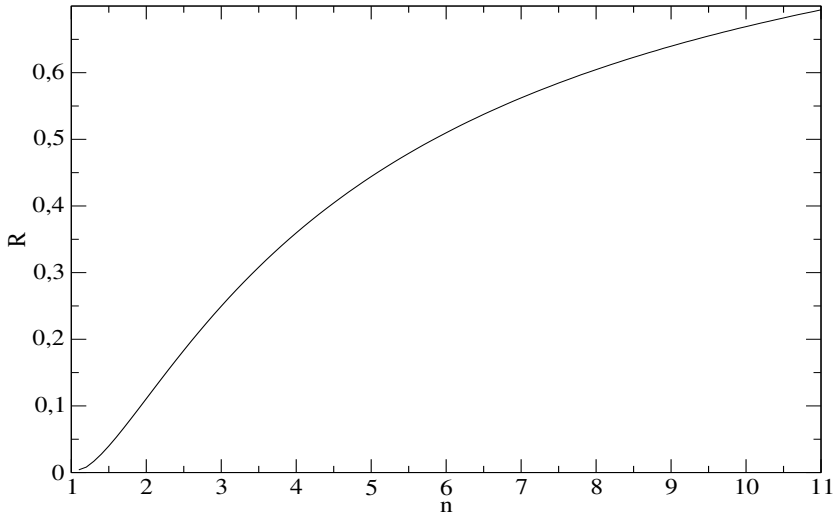

Figure A.2: Numerically calculated reflectivity $R = \exp(-2\gamma_{\mathrm{res}}L)$ of the facets of the dielectric Fabry-Pérot plotted over the refractive index n. For $n = 3.6$ the reflectivity equals $R = 0.3191$, which means that 31.91% of the intensity are reflected at each of the two facets.

For the dielectric Fabry-Pérot Equation (3.55) takes the explicit representation

$$\begin{aligned}\frac{n}{c}\,\partial_t\bar{\mathbf{E}}_\perp &= -\beta\bar{\mathbf{E}}_\perp + iD_p\nabla_\perp^2\bar{\mathbf{E}}_\perp + iK_0\delta n\,\bar{\mathbf{E}}_\perp \\ &\quad + 2iD_p\,\nabla_\perp\left(\bar{\mathbf{E}}_\perp\cdot\nabla_\perp\frac{\delta n}{n}\right) + i\kappa\bar{\mathbf{P}}_\perp\end{aligned} \tag{A.14}$$

with $D_p = (2nK_0)^{-1}$ and $\kappa = K_0/(2n)$.

B Microcavity Quantum Langevin-Equations

B.1 Calculation of Noise Sources

For the following calculations the light-field and atoms are considered as quantum-mechanical systems described in second quantisation by the Hamiltonian (2.30). Following the outline given in SECTION 2.4 one can deduce the corresponding Langevin equations (2.39) from the optical Bloch equations (2.33). The stochastic force terms are related to the different damping channels by the *fluctuation-dissipation theorem* [8]. The fluctuation-dissipation theorem is based on the Markovian assumption that the stochastic forces F_i appearing on the rhs of the Langevin equation

$$\partial_t A_\mu = D_\mu(\{A_\nu\}) + F_{A_\mu}(t) \tag{B.1}$$

can be described by Gaussian noise,

$$\big\langle F_\mu(t)\big\rangle = 0\,, \qquad \big\langle F_\mu(t)F_\nu(t')\big\rangle = 2\big\langle D_{A_\mu A_\nu}\big\rangle\delta(t-t')\,. \tag{B.2}$$

$D_{A_\mu A_\nu}$ are the *diffusion coefficients* which are given by the *generalised Einstein relation*,

$$2\big\langle D_{A_\mu A_\nu}\big\rangle = \mathrm{d}_t\big\langle A_\mu A_\nu\big\rangle - \big\langle A_\mu D_\nu\big\rangle - \big\langle D_\mu A_\nu\big\rangle\,. \tag{B.3}$$

This relation can be used to determine the diffusion coefficients for the noise terms $F_A(t)$, $F_P(t)$, $F_N(t)$ which appear in (2.39) provided that $\mathrm{d}_t\big\langle A_\mu A_\nu\big\rangle$ can be independently calculated. Doing this, one obtains (compare [8, 43])

$$\begin{aligned}
&\big\langle D_{b^\dagger b}\big\rangle = \Omega/(2Q)\bar{n}_\Omega\,,\\
&\big\langle D_{b\,b^\dagger}\big\rangle = \Omega/(2Q)(\bar{n}_\Omega+1)\,,\\
&\big\langle D_{p^\dagger p}\big\rangle \approx \gamma\,\big\langle \hat{n}^{\mathrm{e}}\hat{n}^{\mathrm{h}}\big\rangle\,,\\
&\big\langle D_{p\,p^\dagger}\big\rangle \approx \gamma\,\big\langle (1-\hat{n}^{\mathrm{e}})(1-\hat{n}^{\mathrm{h}})\big\rangle\,,\\
&\big\langle D_{nn}\big\rangle \approx \lambda/2 + \gamma_{\mathrm{nr}}/2\,\bar{n} + B\big\langle \hat{n}^{\mathrm{e}}\hat{n}^{\mathrm{h}}\big\rangle\,,
\end{aligned} \tag{B.4}$$

where it has been assumed that the different reservoirs are uncorrelated. Note, that the bra-kets indicate a quantum-statistical ensemble average. $\bar{n}_\Omega = \big\langle \hat{b}^\dagger\hat{b}\big\rangle$ and $\bar{n} = \big\langle \hat{n}^{\mathrm{e}}\big\rangle = \big\langle \hat{n}^{\mathrm{h}}\big\rangle$ are the mean photon number and the mean carrier density respectively. As usual the equations (2.39) can be simplified by adiabatically eliminating $\hat{p}$, that is

$$\hat{p} \approx \gamma^{-1}\mathcal{D}(\Omega)\left(i\gamma^{-1}g\,\hat{b}\,\left(D_{p^\dagger p} - D_{p\,p^\dagger}\right) - iF_p(t)\right)\,, \tag{B.5}$$

where we inserted the expression

$$D_{p^\dagger p} - D_{p\,p^\dagger} = \gamma\left(\hat{n}^{\mathrm{e}} + \hat{n}^{\mathrm{h}} - 1\right) \tag{B.6}$$

By plugging the adiabatic eliminated polarisation into the dynamic equations (2.39) for $\hat{b}$ and $\hat{n}^{\mathrm{e}}$ one derives the equations

$$\begin{aligned}
\partial_t \hat{b} &= -\Omega/(2Q)\,\hat{b} + 1/2(r_{\mathrm{em}} - r_{\mathrm{abs}})(1 - i\alpha)\,\hat{b} + F_b'(t)\,, \\
\partial_t \hat{n}^{\mathrm{e}} &= \lambda - \gamma_{\mathrm{nr}}\hat{n}^{\mathrm{e}} - B\hat{n}^{\mathrm{e}}\hat{n}^{\mathrm{h}} - (r_{\mathrm{em}} - r_{\mathrm{abs}})\,\hat{b}^\dagger\hat{b} + F_n'(t)\,, \\
\partial_t \hat{n}^{\mathrm{h}} &= \lambda - \gamma_{\mathrm{nr}}\hat{n}^{\mathrm{h}} - B\hat{n}^{\mathrm{e}}\hat{n}^{\mathrm{h}} - (r_{\mathrm{em}} - r_{\mathrm{abs}})\,\hat{b}^\dagger\hat{b} + F_n'(t)\,,
\end{aligned} \tag{B.7}$$

which contain the effective stochastic forces

$$\begin{aligned}
F_b'(t) &= F_b(t) + ig^*\gamma^{-1}\mathcal{D}(\Omega)F_p(t)\,, \\
F_n'(t) &= F_n(t) + i\gamma^{-1}\left(g\mathcal{D}^*(\Omega)F_p^\dagger(t)\hat{b} - g^*\mathcal{D}(\Omega)\hat{b}^\dagger F_p(t)\right)\,.
\end{aligned} \tag{B.8}$$

To keep the expressions compact, the absorption and emission rates

$$\begin{aligned}
r_{\mathrm{em}} &= 2|g|^2\gamma^{-2}\mathcal{L}(\Omega)D_{p^\dagger p}\,, \\
r_{\mathrm{abs}} &= 2|g|^2\gamma^{-2}\mathcal{L}(\Omega)D_{p\,p^\dagger}\,,
\end{aligned} \tag{B.9}$$

were introduced. The correlation functions of the effective noise source F_b' and F_n' give the corresponding diffusion coefficients. With the help of (B.4), we find that

$$\begin{aligned}
2D'_{b^\dagger b} &= 2D_{b^\dagger b} + r_{\mathrm{em}}\,, \\
2D'_{b\,b^\dagger} &= 2D_{b\,b^\dagger} + r_{\mathrm{abs}}\,, \\
2D'_{n^\dagger n} &= 2D_{n^\dagger n} + \hat{b}^\dagger\hat{b}\,(r_{\mathrm{em}} + r_{\mathrm{abs}})\,, \\
2D'_{nb} &= -\hat{b}\,r_{\mathrm{em}}\,, \\
2D'_{nb^\dagger} &= -\hat{b}^\dagger r_{\mathrm{em}}\,.
\end{aligned} \tag{B.10}$$

B.2 Calculation of the Laser Spectrum

In order to determine the noise spectra of lasers we have to linearise the equations of motion for A and N. However, it is necessary to split A into an amplitude $\sqrt{I}$ and phase ϕ. This is done by the ansatz

$$A = \sqrt{I}\exp(-i\phi)\,, \tag{B.11}$$

where $I \cdot \mathcal{E}_\Omega^2$ is the field intensity and $\mathcal{E}_\Omega^2$ the field intensity per photon

$$\mathcal{E}_\Omega = \sqrt{\frac{\hbar\Omega}{\epsilon_0\epsilon V}}\,. \tag{B.12}$$

From the rate equations (B.7) and

$$R = r_{\rm em} - r_{\rm abs} \approx r(N - N_{\rm tr}) \,, \quad R(N_{\rm tr}) = 0 \,, \tag{B.13}$$

we derive equations for the particle number N, the intensity I and the phase ϕ,

$$\begin{aligned} \partial_t N &= \Lambda(1 - N/N_0) - \gamma_{\rm nr} N - \Gamma_{\rm sp} - r(N - N_{\rm tr})I + F_N(t) \,, \\ \partial_t I &= -\Omega/Q I + r(N - N_{\rm tr})I + F_I(t) \,, \\ \partial_t \phi &= \alpha/2 r(N - N_{\rm tr}) + F_\phi(t) \,. \end{aligned} \tag{B.14}$$

The diffusion constants of the stochastic forces F_I and F_ϕ are determined by applying the rule

$$\left\langle D_{B_i B_j} \right\rangle = \sum_{\mu\nu} \left\langle D_{A_\mu A_\nu} \frac{\partial B_i}{\partial A_\mu} \frac{\partial B_j}{\partial A_\nu} \right\rangle \tag{B.15}$$

to the diffusion constant $\left\langle D_{A^\dagger A} \right\rangle$ of the light-field amplitude. Consequently, the diffusion constant of an operator B follows from evaluating

$$\begin{aligned} \left\langle D_{BB} \right\rangle &= \left(\frac{\Omega}{Q}(\overline{N}_\Omega + 1/2) + \frac{1}{2}\big(\langle r_{\rm em}\rangle + \langle r_{\rm abs}\rangle\big) \right) \left\langle \frac{\partial B}{\partial A} \frac{\partial B}{\partial A^\dagger} \right\rangle \\ &\approx \langle r_{\rm em}\rangle \left\langle \frac{\partial B}{\partial A} \frac{\partial B}{\partial A^\dagger} \right\rangle \,. \end{aligned} \tag{B.16}$$

Neglecting the fluctuations $\overline{N}_\Omega$ we have further simplified this expression by inserting the relation (2.40) with the rhs set approximately to zero. Eventually, one obtains for the phase and intensity diffusion constants

$$\left\langle D_{\phi\phi} \right\rangle = 1/(4I)\langle r_{\rm em}\rangle \,, \qquad \left\langle D_{II} \right\rangle = I\langle r_{\rm em}\rangle \,. \tag{B.17}$$

In order to get the intensity and phase noise spectra one has to linearise the equations (B.14). Therefore we have to determine a stationary solution. As stationary density we use the threshold density defined by $\partial_t I = 0$. It is given by

$$N_{\rm thr} = N_{\rm tr} + r^{-1}\Omega/Q \tag{B.18}$$

Dropping the $\Gamma_{\rm sp}$ term at first instance, we find the threshold pump $\Lambda_{\rm thr}$ to be

$$\Lambda_{\rm thr} = \frac{\gamma_{\rm nr} N_{\rm thr}}{1 - N_{\rm thr}/N_0} \,. \tag{B.19}$$

From this we deduce the stationary intensity

$$I_{\rm st} = \frac{\tilde{\Lambda}(1 - N_{\rm thr}/N_0)}{\Omega/Q} \tag{B.20}$$

with $\tilde{\Lambda} = \Lambda - \Lambda_{\rm thr}$ being defined as pump above threshold. With these definitions we expand the system of equations (B.14) in the vicinity of $N_{\rm thr}$ and $I_{\rm st}$. $\tilde{N}$ and $\tilde{I}$ shall

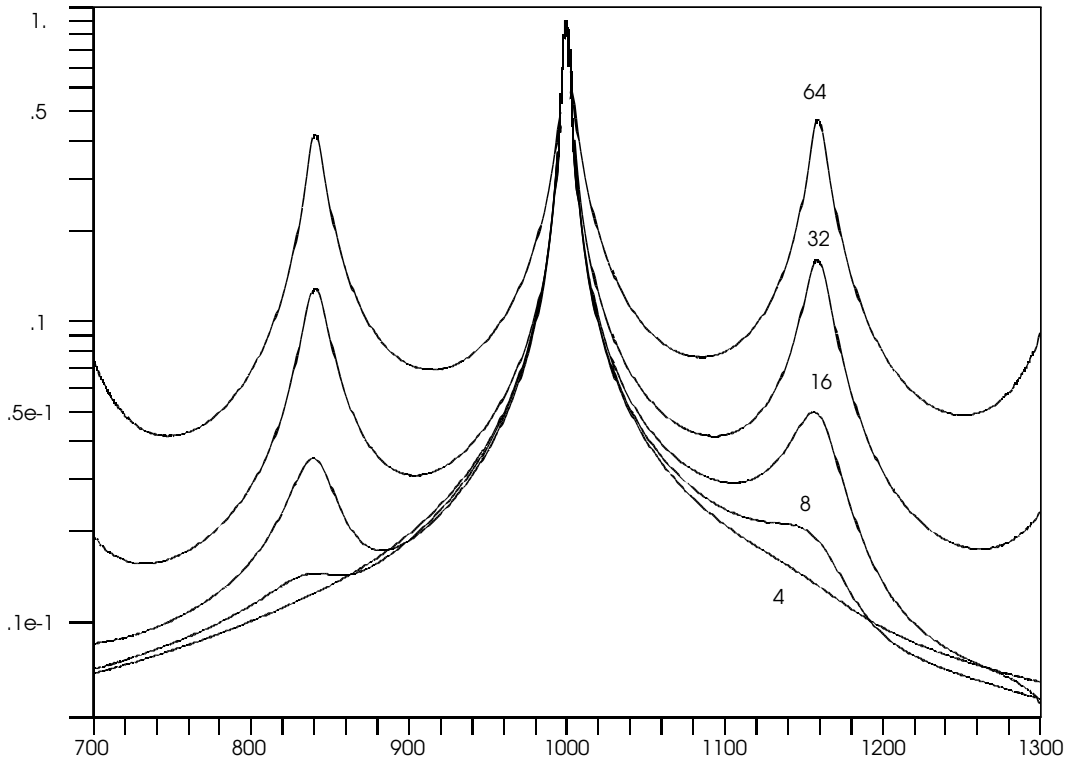

Figure B.1: Plot of the line-shape for different values showing the qualitative behaviour in dependence of Γ. The axis are in arbitrary units. The parameter values are illustrative only: ($\Omega_{\rm rel} = 100.$, $\alpha = 2.$, $\langle r_{\rm em} \rangle = 1.$, $I_{\rm st} = 1.$). Next to the main peak appear the side-peaks of the relaxation oscillation which are more and more suppressed the higher the damping values Γ.

represent the elongation from this steady state solution. After dropping all nonlinear terms we obtain

$$\begin{aligned} \partial_t \tilde{N} &= -\Gamma \tilde{N} - \Omega/Q \tilde{I} + F_N(t) \,, \\ \partial_t \tilde{I} &= r I_{\rm st} \tilde{N} + F_I(t) \,, \\ \partial_t \phi &= \Omega_\phi + \alpha/2 r \tilde{N} + F_\phi(t) \,. \end{aligned} \tag{B.21}$$

Γ and Ω_ϕ are given by

$$\Gamma = \tilde{\Lambda}/N_0 + \gamma_{\rm nr} + r I_{\rm st} \,, \qquad \Omega_\phi = \alpha/2(\Omega/Q) \,. \tag{B.22}$$

By solving this linear system via Fourier-transformation, one obtains expression for $I(\omega)$, $N(\omega)$ and $\phi(\omega)$. The spectrum of the laser is defined according to the *Wiener-Khintchine theorem* as the Fourier-transform of the electric field's auto-correlation function,

$$\mathcal{S}(\omega) = \int_{-\infty}^{+\infty} {\rm d}\omega {\rm e}^{-i\omega t} \big\langle E^*(t) E(0) \big\rangle \,. \tag{B.23}$$

Far above threshold the dominant noise part emerges from phase fluctuations while the influence of amplitude noise can be neglected. In that situation one can rewrite (B.24) to

$$\begin{aligned}\mathcal{S}(\omega) &\approx I_{\mathrm{st}} \int_{-\infty}^{+\infty} \mathrm{d}\omega \mathrm{e}^{-i\omega t} \big\langle \exp(i\Delta\phi(t)) \big\rangle \\ &= I(\omega) \int_{-\infty}^{+\infty} \mathrm{d}\omega \mathrm{e}^{-i\omega t} \exp\left(-\frac{1}{2}\big\langle \Delta\phi^2(t) \big\rangle\right)\end{aligned} \tag{B.24}$$

with

$$\Delta\phi(t) = \phi(t) - \phi(0)\,. \tag{B.25}$$

However $\Delta\phi^2(t)$ is connected to the Fourier-transformed phase by

$$\Delta\phi^2(t) = \frac{1}{2\pi} \int_{-\infty}^{+\infty} \mathrm{d}\omega \int_{-\infty}^{+\infty} \mathrm{d}\omega' |\phi(\omega)|^2 \left(\mathrm{e}^{i\omega t} - 1\right) \left(\mathrm{e}^{-i\omega' t} - 1\right) \tag{B.26}$$

as shown in [43]. The solution of $\phi(\omega)$ can be extracted from (B.21),

$$\begin{aligned}\phi(\omega) &= \frac{\alpha}{2} r I_{\mathrm{st}} \frac{F_N(\omega) + i\omega^{-1}\Omega/Q F_I(\omega)}{\Delta_\omega} - i\omega^{-1} F_\phi(\omega)\,, \\ \Delta_\omega &= r I_{\mathrm{st}}\Omega/Q + i\omega(\Gamma + i\omega)\,,\end{aligned} \tag{B.27}$$

It can be derived from (B.2) that the Fourier-transformed stochastic forces have to satisfy the relation

$$\big\langle F_\mu(\omega) F_\nu(\omega') \big\rangle = 2\big\langle D_{A_\mu A_\nu} \big\rangle \delta(\omega - \omega')\,. \tag{B.28}$$

After inserting (B.27) into (B.26) one is confronted with contour integrations which have to be solved. There are three poles appearing in the $\Delta\phi^2(t)$ expression. One at $\omega = 0$ and the two zeroes of $|\Delta_\omega|$ which are localised in the complex plane at

$$\omega_\pm = i\Gamma/2 \pm \Omega_{\mathrm{rel}}\,, \quad \Omega_{\mathrm{rel}}^2 = \Omega_{\mathrm{rel},0}^2 + (\Gamma/2)^2 = (r I_{\mathrm{st}}\Omega/Q)^2 + (\Gamma/2)^2\,. \tag{B.29}$$

and give the relaxation oscillation sidebands. In the limit $\omega \to 0$ one finds that

$$\big\langle \Delta\phi^2(t) \big\rangle \to \frac{\big\langle r_{\mathrm{em}} \big\rangle}{2I}(1 + \alpha^2) t\,. \tag{B.30}$$

If one inserts this result into (B.24) and calculate the width of the $\omega = 0$ peak, the result will be a line-width of

$$\delta\omega = \frac{1}{2}(1 + \alpha^2)\delta\omega_0\,. \tag{B.31}$$

with $\delta\omega_0 = \langle r_{\mathrm{em}} \rangle / I$ being the *Schawlow-Townes* line-width. However, a full treatment of all the poles [43] result in the spectral intensity

$$\begin{aligned} \mathcal{S}(\omega) = I_{\mathrm{st}} \exp\left(-\frac{\alpha^2 \langle r_{\mathrm{em}} \rangle \cos(3\delta)}{4\Gamma I_{\mathrm{st}} \cos(\delta)} \right) \cdot \quad \int_{-\infty}^{+\infty} \mathrm{d}t \; \mathrm{e}^{-i\omega t} \\ \times \exp\left(-\frac{\langle r_{\mathrm{em}} \rangle}{4 I_{\mathrm{st}}} \left[(1+\alpha^2)|t| - \frac{\alpha^2 \exp(-\Gamma|t|/2) \cos(\Omega_{\mathrm{rel}}|t| - 3\delta)}{\Gamma \cos(\delta)} \right] \right) \end{aligned} \tag{B.32}$$

with

$$\delta = \ln\left(\frac{\Omega_{\mathrm{rel},0} + i\Gamma/2}{\Omega_{\mathrm{rel}}^2} \right) . \tag{B.33}$$

The spectrum is characterised by a centre peak with the sidebands of the relaxation frequency on both sides as shown in FIGURE B.1.

C Numerical Implementation of the Models

C.1 Discretisation Scheme for the Longitudinal Model

The implementation of a stable *finite-difference* (FD) solution algorithm for the coupled equations (2.3), (2.6) and (2.8) affords a suitable spacial and temporal centring of the fields. For the following we introduce i as the spacial grid index and n as the temporal grid index. These are connected to the real space and time coordinates by $z = i\Delta z$ and $t = n\Delta t$. Firstly, we apply the Yee-algorithm to Maxwell's equations (2.3) which utilises space and time grids displaced by half steps. In one dimension one can calculate the electromagnetic fields E and H at all interior points $i = 1 \dots L$ by

$$\begin{aligned} H|_{i+1/2}^{n} &= H|_{i+1/2}^{n-1} + c\frac{\Delta t}{\Delta z}\left(E|_{i+1}^{n-1/2} - E|_{i}^{n-1/2}\right) , \\ E|_{i}^{n+1/2} &= E|_{i}^{n-1/2} + \epsilon^{-1}c\frac{\Delta t}{\Delta z}\left(H|_{i+1/2}^{n} - H|_{i-1/2}^{n}\right) - \epsilon^{-1}\Delta t\,\left(J + \partial_t P\right)|_{i}^{n} . \end{aligned} \tag{C.1}$$

At the left and right boundary point $i = 0$ and $i = L + 1$ we choose to have open boundary conditions. According to [146] we set in first order approximation

$$\begin{aligned} E|_{0}^{n+1/2} &= E|_{1}^{n-1/2} + \frac{s-1}{s+1}\left(E|_{1}^{n+1/2} - E|_{0}^{n-1/2}\right) , \\ E|_{L+1}^{n+1/2} &= E|_{L}^{n-1/2} + \frac{s-1}{s+1}\left(E|_{L}^{n+1/2} - E|_{L+1}^{n-1/2}\right) . \end{aligned} \tag{C.2}$$

where we defined

$$s = \epsilon^{-1}c\frac{\Delta t}{\Delta z} . \tag{C.3}$$

A self-consistent treatment of the coupled differential equations for P, E and N can be achieved by centring P at time-steps $n - 1/2$. After the discretisation of (2.6) we get

$$\begin{aligned} \frac{1+\gamma\Delta t}{\Delta t^2}P|^{n+1/2} =& \frac{2-\omega_0^2\Delta t^2}{\Delta t^2}P|^{n-1/2} - \frac{1-\gamma\Delta t}{\Delta t^2}P|^{n-3/2} \\ & - 2\epsilon_0^{-1}\,\xi E|^{n-1/2}\left(N|^{n-1/2} - N_{tr}\right) \end{aligned} \tag{C.4}$$

which demands E and N to be available at $n - 1/2$. The equation (2.8) for N has to be time centred at n. This leads to

$$\frac{1+\gamma_{nr}\Delta t/2}{\Delta t}N|^{n+1/2} = \frac{1-\gamma_{nr}\Delta t/2}{\Delta t}N|^{n-1/2} + \Lambda + \epsilon_0^{-1}\frac{1}{\hbar\omega}(\partial_t P)|^{n}E|^{n} \tag{C.5}$$

with

$$E|^n = \frac{E|^{n+1/2} + E|^{n-1/2}}{2}\,, \quad (\partial_t P)|^n = \frac{P|^{n+1/2} - P|^{n-1/2}}{\Delta t}\,.$$

The sequence in which the equations are to be solved is determined by the time centring. In our case, we have choosen to firstly solve the equation (C.4), as both E and N enter this equation explicitly at the old time-step. After that we solve the discrete Maxwell's equation (C.1) and eventually (C.5), the equation for the carrier density N. This method minimises the local errors within the given scheme as far as possible.

Even though the time-centring may be self-consistent the choice is not necessarily unique. We also note, that the exactness is reduced in order as we had to apply time averages for the field quantities on the right hand sides of the equations.

C.2 Longitudinal Delayed Feedback Boundaries

In the section above, a discretisation scheme for the one-dimensional laser equations (2.3), (2.6) and (2.8) was presented. The usual boundary conditions are either *open boundaries* – implemented via (C.2) – or *reflecting boundaries* (or metallic boundaries), that is $E = 0$ at the boundary points. An extension of the open boundary conditions are *delayed feedback boundaries* (or external mirror boundaries), which can be considered in between the open and the reflecting boundaries. The picture is that the light leaves the structure at one of the (open) boundaries, propagates to a mirror some distance D away, is reflected at the mirror surface and then is fed back into the structure after the round-trip time $\tau = 2D/c$. The numerical implementation – which is both fast and of low memory consumption – works as follows: we assume that the left boundary (at $i = 0$) is implemented as open boundary described by (C.2). In order to extend it to an external mirror boundary condition we follow the idea of the well-known total-field/scattered-field approach, pick up the (outgoing) average electric field E at grid coordinate $1 + 1/2$ and the average H-field at grid coordinate $i = 2$ and put them into a delay line $E_{\text{ext}}(t)$ and $H_{\text{ext}}(t)$. At grid coordinate $i = 4$ and $i = 3 + 1/2$, however, we add the recorded E_{ext} and H_{ext} values to the grid values E and H, but multiplied with a damping factor of $\sqrt{1-\gamma_{\text{ext}}}$ and an associated round-trip delay of τ. Within the discretisation scheme, this reads

$$\begin{aligned}
E_{\text{ext}}|^{n+1/2} &= \sqrt{1-\gamma_{\text{ext}}}\frac{1}{2}\left(E|_1^{n+1/2} + E|_2^{n+1/2}\right)\\
H_{\text{ext}}|^{n} &= \sqrt{1-\gamma_{\text{ext}}}\frac{1}{2}\left(H|_{2-1/2}^{n} + H|_{2+1/2}^{n}\right)\\
E|_4^{n+1/2} &= E|_4^{n+1/2} + E_{\text{ext}}|^{n+1/2-N}\\
H|_{3+1/2}^{n} &= H|_{3+1/2}^{n} - H_{\text{ext}}|^{n-N}
\end{aligned} \tag{C.6}$$

with $\tau = N \cdot \Delta t$ being the round-trip (or delay) time. FIGURE C.1 illustrates the staggered E and H grids, the positions, where the outgoing fields are recorded, and

where the incoming (reflected) fields are injected again. Note, that we average the outgoing fields over two adjacent grid points to avoid the amplification of the cut-off frequency oscillations.

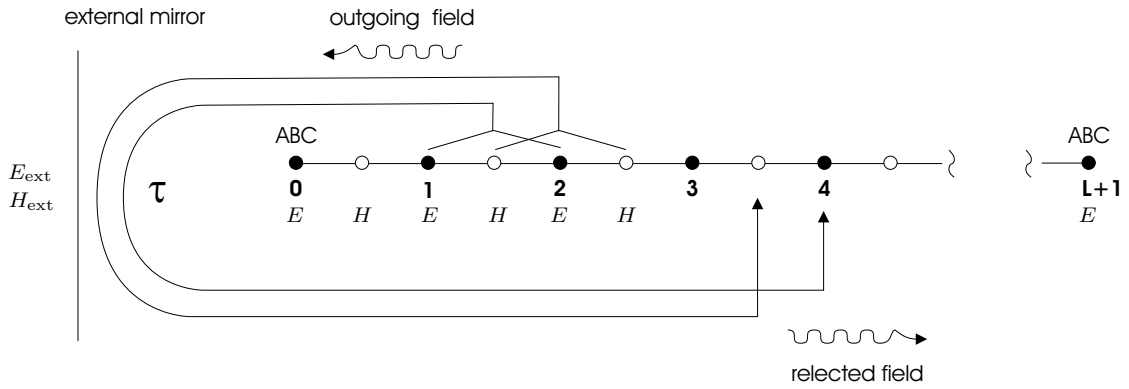

Figure C.1: Staggered E and H grids and the delayed feedback boundary condition. See text for explanation.

C.3 One-Dimensional Cavity Mode Solver

Algorithms like the one presented in the previous section are suitable for studying time dynamics of a laser system and might also be used to extract cavity modes. Naturally, there are more efficent ways to calculate cavity modes without performing an explicit time integration of the system. By applying ansatz

$$E = g(z)\exp(-i\Omega t) \tag{C.7}$$

to the one-dimensional Maxwell equations, we can extract an wave equation of the structure

$$\partial_z^2 g(z) + \epsilon(z) K_0 g(z) = 0\,, \quad K_0 = \frac{\Omega}{c} \tag{C.8}$$

While $\epsilon(z)$ reflects the dielectric structure of the system, K_0 has to be considered as a complex eigenvalue. $g(z)$ the corresponding eigenfunctions have to fulfill (C.8) together with the conditions

$$\frac{\partial_z g(\pm L/2)}{g(\pm L/2)} = iK_0 \tag{C.9}$$

which hold at the boundary points $z = -L/2$ and $z = +L/2$. This connects our system at the boundaries to air. We note, that (C.9) are boundary conditions of the homogeneous type $\alpha g' + \beta g = 0$.

As we aim to modes, in particular confined cavity modes, we apply an additional condition. If we are looking for symmetric modes we demand

$$g(0) = 1 \qquad \text{and} \qquad \partial_z g(0) = 0\,. \tag{C.10}$$

This can be fulfilled only if the solution is symmetric with respect to $z = 0$. In the same manner, the asymmetric modes can be characterised by

$$\partial_z g(0) = 1 \qquad \text{and} \qquad g(0) = 0\,. \tag{C.11}$$

The mode calculation algorithm works as follows: firstly an initial guess $\tilde{K}_0 = j2\pi/L$ is made for the eigenvalue. The first condition of either (C.10) or (C.11) is used as inhomogeneous boundary together with one of the homogeneous conditions, e.g. $\partial_z g(+L/2) = i\tilde{K}_0 g(+L/2)$. Then we can determine a solution $\tilde{g}(z)$ associated with $\tilde{K}_0$ by applying a boundary problem solver (e.g. the fast *Thomas-Algorithm*) to (C.8). After that we use the second conditions of (C.10) or (C.11) as a measure how close $\tilde{K}_0$ and $\tilde{g}(z)$ are to the system's eigenvalue and eigenfunction. We now either look for a minimum of $|\partial_z \tilde{g}(0)|$ (symmetric case) or for a minimum of $|\tilde{g}(0)|$ (asymmetric case) to approach the eigenfunction $g(z)$. The imaginary part of K_0 is directly related to the energy loss of the mode over time.

C.4 Discretisation of the Transversal Model

In principle, there are two finite-difference schemes for solving partial differential equations (PDEs) on a structured regular grid. The explicit method, which treats all of the variables appearing on the rhs explicitly,

$$X^{n+1} - X^n = \Delta t \cdot F[X^n] \tag{C.12}$$

or the implicit method, which assumes the rhs to be given at the new time-step

$$X^{n+1} - X^n = \Delta t \cdot F[X^{n+1}]\,. \tag{C.13}$$

The explicit scheme can be easily realised. An application to a two- or three-dimensional systems is straight-forward, however, it features a very limited stability. For that reason, there are rarely cases where a pure explicit scheme is practicable. Implicit schemes, on the other hand, are usually very stable, but one encounters the problem that for a calculation of the rhs of the equation the solution has to be already known. There are some simple cases where it is possible to resolve the equation with respect to the updated variables X^{n+1}. For two-dimensional problems, such as the wave-equation (5.1), which are extremely time-critical, one better uses an efficient hybrid method of mixed explicit and implicit nature. A prominent two-dimensional PDE solver which can be used for solving (5.1) and (5.2) is the *Hop-Scotch* method [147]. This unconditionallty stable method performs firstly an explicit half-step and applies afterwards an implicit looking

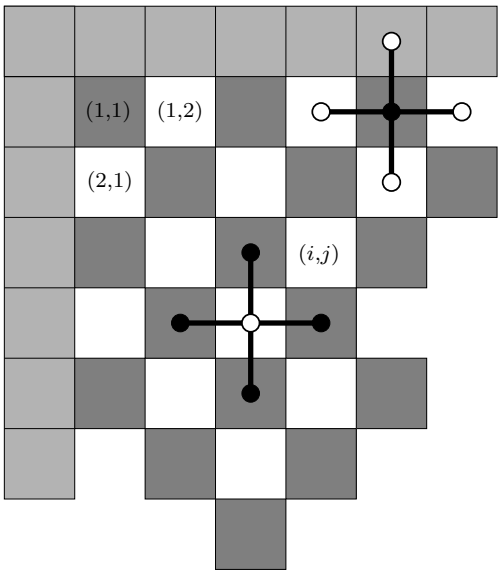

Figure C.2: *Hop-Scotch* PDE solver. Shown is the checker-board pattern of the two-dimensional grid and the five-point integration stencils. If one assumes that all of the white tiles are calculated explicitly, one can afterwards integrate the black tiles in an implicit time-step. Then we exchange black and white and perform an explicit step for the black tiles and an implicit one for the white tiles.

half-step but on different fields. In order to illustrate the algorithm we assume a first order discretisation and map the wave-equation to the matrix equation,

$$\begin{aligned} X_{ij}^{n+1} = X_{ij}^{n} + \Delta t \cdot \big(& C_{ij}^{(0,0)} X_{ij}^{\circ} \\ & + C_{ij}^{(1,0)} X_{i+1,j}^{\circ} + C_{ij}^{(-1,0)} X_{i-1,j}^{\circ} + C_{ij}^{(0,1)} X_{i,j+1}^{\circ} + C_{ij}^{(0,-1)} X_{i,j-1}^{\circ} + D_{ij} \big) \, . \end{aligned} \tag{C.14}$$

The computational pattern makes use of a 5-point stencil weighted by coefficients $C^{(0,0)}$, $C^{(1,0)}$, $C^{(-1,0)}$, $C^{(0,1)}$, $C^{(0,-1)}$. D_{ij} represents all kind of source and loss terms which are independent from X_{ij}. The $\circ$-symbol is a placeholder for either n or $n+1$ depending on, whether we treat the rhs in an explicit or an implicit way. The picture of a checker-board style black-white pattern (see FIGURE C.2) helps understanding the method: we assume that at some time-step n we want to calculate the white fields. For calculating the white fields we have to know the values of the adjacent black tiles. We avaoid to diagonalise huge matrices at each time-step, and calculate the white fields in an explicit time-step, that is

$$\begin{aligned} X_{ij}^{n+1} = X_{ij}^{n} + \Delta t \cdot \big(& C_{ij}^{(0,0)} X_{ij}^{n} \\ & + C_{ij}^{(1,0)} X_{i+1,j}^{n} + C_{ij}^{(-1,0)} X_{i-1,j}^{n} + C_{ij}^{(0,1)} X_{i,j+1}^{n} + C_{ij}^{(0,-1)} X_{i,j-1}^{n} + D_{ij} \big) \, . \end{aligned} \tag{C.15}$$

After that, all the white fields are updated to the new time. Therefore, it is possible to

evaluate the black fields in an implicit looking step

$$\begin{aligned}\left(1-\Delta t\cdot C_{ij}^{(0,0)}\right)X_{ij}^{n+1} = X_{ij}^{n} + \Delta t\cdot\big(\\ C_{ij}^{(1,0)}X_{i+1,j}^{n+1} + C_{ij}^{(-1,0)}X_{i-1,j}^{n+1} + C_{ij}^{(0,1)}X_{i,j+1}^{n+1} + C_{ij}^{(0,-1)}X_{i,j-1}^{n+1} + D_{ij}\big)\,.\end{aligned} \tag{C.16}$$

Having done that, one reverses back and white in the next time step, that is calculates the black fields first (explicitly) and then the white ones (implicitly). After two time-steps each grid point has been subject to an explicit and an implicit step. This significantly improves stability compared to pure explicit schemes. The biggest advantage, however, is that we did not have to deal with additional fields and that we calculated the complete two-dimensional grid within two (stride-two) sweeps. Although, there are methods more accurate and stable, we consider none of them being as efficient as the Hop-Scotch integration.

D State of Polarisation and Stokes Parameters

The state of polarised light can be completely described by four measurable parameters known as *Stokes Parameters* [137]. The first of them, S_0, gives the intensity of the light, whereas the remaining three describe the polarisation state. Assuming a plane wave with $k_z = \Omega/c$ we define the complex amplitudes $\hat{E}_x$ and $\hat{E}_y$ at $z = 0$ by setting

$$\begin{aligned} E_x(t) &= \hat{E}_{0,x}\, \mathrm{e}^{i\delta_x} \mathrm{e}^{i\Omega t} = \hat{E}_x \mathrm{e}^{i\Omega t} \,, \\ E_y(t) &= \hat{E}_{0,y}\, \mathrm{e}^{i\delta_y} \mathrm{e}^{i\Omega t} = \hat{E}_y \mathrm{e}^{i\Omega t} \,. \end{aligned} \tag{D.1}$$

$\hat{E}_{0,x}$, $\hat{E}_{0,y}$ represent the real valued amplitudes and δ_x, δ_y contain the phase information of the wave incident to a detector at $z = 0$. Thus, there are four degrees of freedom available, equivalent to the real and imaginary parts of $\hat{E}_x$ and $\hat{E}_y$. These free parameters can be transformed to the set of Stokes parameters,

$$S_0 = \hat{E}_{0,x}^2 + \hat{E}_{0,y}^2 = \hat{E}_x \hat{E}_x^* + \hat{E}_y \hat{E}_y^* \,, \tag{D.2}$$

$$S_1 = \hat{E}_{0,x}^2 - \hat{E}_{0,y}^2 = \hat{E}_x \hat{E}_x^* - \hat{E}_y \hat{E}_y^* \,, \tag{D.3}$$

$$S_2 = 2\hat{E}_{0,x}\hat{E}_{0,y}\cos\delta = \hat{E}_x \hat{E}_y^* + \hat{E}_y \hat{E}_x^* \,, \tag{D.4}$$

$$S_3 = 2\hat{E}_{0,x}\hat{E}_{0,y}\sin\delta = i(\hat{E}_x \hat{E}_y^* - \hat{E}_y \hat{E}_x^*) \,, \tag{D.5}$$

thereby introducing $\delta = \delta_y - \delta_x$. The Stokes parameters are real, measurable quantities which have to obey the inequality $0 \leq \hat{S}_i = S_i/S_0 \leq 1$ (i=1,2,3). $\hat{S}_1 = +1$ accounts for horizontal (0°) and $\hat{S}_1 = -1$ for vertical (90°) linear polarised. $\hat{S}_2$ describes the intensity concentrated in the diagonally (±45°) linear polarised states (+1) and (-1). $\hat{S}_3$ comprises the intensity concentrated in the right circular polarised state (+1) and in the left circular polarised state (-1). Using Schwarz's inequality one can show that

$$0 \leq \underbrace{\sqrt{\hat{S}_1^2 + \hat{S}_2^2 + \hat{S}_3^2}}_{P_{\mathrm{pol}}} \leq 1 \,. \tag{D.6}$$

P_{pol}, is the degree of polarisation. It takes a value of +1 for totally polarised light and of 0 for unpolarised, stochastic light. The state of polarisation can be mapped on the so-called *Poincaré-sphere* which is obtained by transforming the Stokes parameters to the set (S_0, ψ, χ). The orientation angle ψ, and the ellipticity angle χ are defined by

$$\begin{aligned} \tan 2\psi &= \hat{S}_2/\hat{S}_1 \,, \\ \sin 2\chi &= \hat{S}_3 \,. \end{aligned} \tag{D.7}$$

For a state of totally polarised light $P_{\mathrm{pol}} = 1$ one can show that

$$\begin{aligned} \hat{S}_1 &= \cos 2\chi \cos 2\psi \,, \\ \hat{S}_2 &= \cos 2\chi \sin 2\psi \,, \\ \hat{S}_3 &= \sin 2\chi \,. \end{aligned} \tag{D.8}$$

ψ gives the polarisation direction and χ the ellipticity. Each state of polarisation can be associated with a dot on the surface of a sphere with a radius of S_0. This is called the Poincaré-sphere representation (depicted in FIGURE D.1).

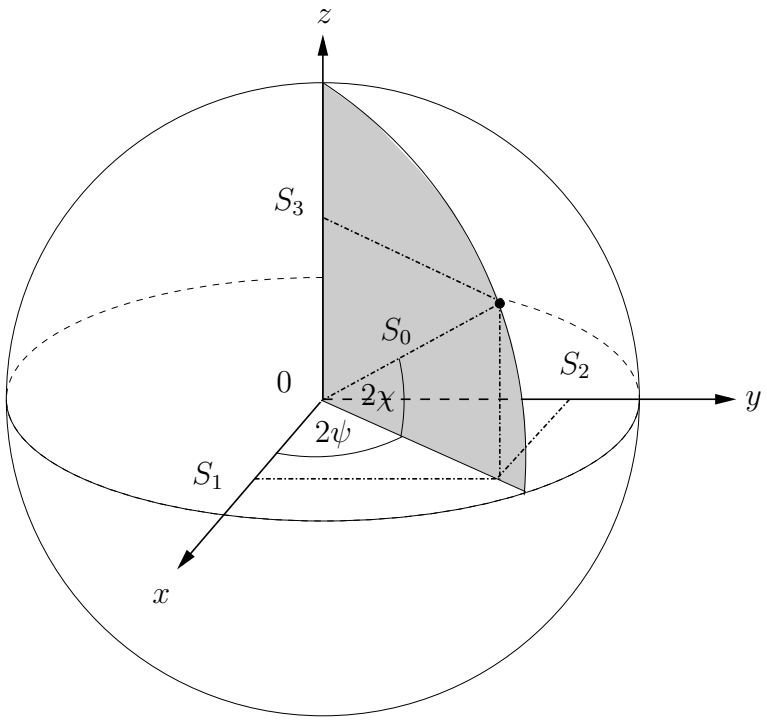

Figure D.1: Poincaré-sphere indicating the state of polarisation. For totally polarised light, the polarisation state is represented by a dot on the surface of the sphere. The radius of the sphere is equivalent to the intensity, while the two angles ψ and χ define the polarisation direction and the ellipticity. Partial unpolarised light could be represented by stochastic cloud on the sphere's surface. Totally unpolarised light would then be a stochastic cloud covering the whole surface of the sphere.

The electric field components can be either represented in a circular $(\mathbf{e}_+, \mathbf{e}_-)$ or a Cartesian $(\mathbf{e}_x, \mathbf{e}_y)$ coordinate base. Applying the base transformation

$$\mathbf{e}_\pm = \frac{1}{\sqrt{2}} \left(\mathbf{e}_x \pm i \mathbf{e}_y \right) \,, \tag{D.9}$$

we obtain the component transformation rules

$$E^\pm = \frac{1}{\sqrt{2}} \left(E_x \mp i E_y \right) \tag{D.10}$$

and

$$\begin{aligned} E_x &= \frac{1}{\sqrt{2}} \left(E^+ + E^- \right) \ , \\ E_y &= \frac{i}{\sqrt{2}} \left(E^+ - E^- \right) \ . \end{aligned} \tag{D.11}$$

Inserting this transformation rules into (D.5) one obtains expressions for the respective stokes parameters in dependence on the circular field components.

E Al-GaAs material parameters

Here we give a brief summary of optical and electronic material parameters which have been used for the simulations. These parameters are typical for Al-GaAs/GaAs VCSEL structures. GaAs, and AlAs are of zinc-blende structure and are very well lattice-matched. $Ga_{1-x}Al_xAs$ has a lattice constant around $5.65 - 5.66$ Å depending on the concentration x. Band parameters for other III-V compound semiconductors can be found in [3]. [100] is a review article summarising many physical parameters for GaAlAs material. Until not stated explicitly we give parameters for the Γ-point, room temperature ($T = 300\,\mathrm{K}$), and a vacuum wavelength of 815 nm. If no specific source is given the parameters are estimated from various sources, like websites, papers, and other publications.

Table E.1: List of important GaAs/AlAs material parameters.

GaAs / AlAs Material Parameters			
Physical Entity	*GaAs*	*AlAs*	*Ref*
Electronic			
bandgap: $\mathcal{E}_{\mathrm{g}\ (T=300K)}$ [eV]	1.420	2.168	[3, 100]
bandgap: $\mathcal{E}_{\mathrm{g}\ (T=0K)}$ [eV]	1.517	3.099	[3]
split-off: Δ_{so} [meV]	0.341	0.28	[3]
effective electron mass: m^*_{e} [m_0]	0.065	0.15	[3]
effective light-hole mass: m^*_{lh} [m_0]	0.087	0.150	[100]
effective heavy-hole mass: m^*_{hh} [m_0]	0.62	0.76	[100]
effectivesplit-off hole mass: m^*_{so} [m_0]	0.15	0.24	[100]
electron mobility: μ_{e} [$\mathrm{cm}^2/(\mathrm{Vs})$]	8500	–	
hole mobility: μ_{h} [$\mathrm{cm}^2/(\mathrm{Vs})$]	$1.4 \cdot 10^{-3}$	–	
electro-optic tensor-component: r_{41} [nm/V]	$1.4 \cdot 10^{-3}$	–	
non-radiative recombination-time: τ_{nr} [ns]	$5 - 10$	–	
Auger coefficient: τ_{aug} [cm^6/s]	$10 \cdot 10^{-30}$	–	
eff. polarisation dephasing-time: τ^{h} [ps]	$0.05 - 0.10$	–	
electron diffusion-constant: D^{e}_f [cm^2/s]	994	–	
hole diffusion-constant: D^{e}_f [cm^2/s]	41	–	
ambipolar diffusion-constant: D_f [cm^2/s]	79	–	
dipole matrix-element (cv): M_{cv} [$\mathrm{e} \cdot \mathrm{nm}$]	0.3	–	
intrinsic carrier density: n_i/p_i [$10^6\mathrm{cm}^{-1}$]	1.84	–	
Optical			
static dielectric constant: ϵ	13.18	10.06	[100]

continued on next page ...

... continued from previous page			
Physical Entity	*GaAs*	*AlAs*	*Ref*
dielectric constant for $\Omega \to \infty$: ϵ_∞	10.89	8.16	[100]
Lattice			
LO-phonon energy: $\hbar\omega_{\mathrm{LO}}$ [meV]	36.25	50.09	[100]
TO-phonon energy: $\hbar\omega_{\mathrm{TO}}$ [meV]	33.29	44.88	[100]
Varshni parameter: α[meV/K]	0.5405	0.7	[3]
Varshni parameter: β[K]	204	530	[3]
spec. heat per volume: $c_{\mathrm{q,V}}$ [eV/nm^{3}K]	$1.12 \cdot 10^2$	$1.08 \cdot 10^2$	[100]
Fröhlich coupling const.: α_{F}	0.068	0.126	[100]

In addition to this there are a couple of interpolation formulas which allow the calculation of material properties of the $\mathrm{Ga}_{1-x}\mathrm{Al}_x\mathrm{As}$ compound in dependence of x [3, 100], e.g.:

- lattice constant [ ]: $5.6533 + 0.0078 \cdot x$
- Fröhlich-coupling constant α_{F}: $0.068 + 0.058 \cdot x$
- optical phonon energy [meV]: $36.25 + 1.83 \cdot x + 17.12 \cdot x^2 - 5.11 \cdot x^3$
- hole mobility [cm^2/(Vs)]: $370 - 970 \cdot x + 740 \cdot x^2$
- electron mobility [cm^2/(Vs)]: $8. \cdot 10^3 - 2.2 \cdot 10^4 \cdot x + 1. \cdot 10^4 \cdot x^2$
- infrared refractive index: $3.3 - 0.53 \cdot x + 0.09 \cdot x^2$
- energy gap at Γ [eV]: $1.424 + 1.155 \cdot x + 0.37 \cdot x^2$
- static dielectric constant: $13.18 - 3.12 \cdot x$
- high-freq. dielectric constant: $10.89 - 2.73 \cdot x$

Bibliography

[1] J. Niamtu. Clinical Applications of the 532-nm Diode Laser for the Treatment of Facial Telangiectasia and Pigmented Lesions: Literature Review, History, and Discussion of Clinical Experience. *Am. J. of Cosm. Surg.*, 18(2), 2001.

[2] R. N. Hall, G. E. Fenner, J. D. Kingsley, T. G. Soltys, and R. O. Carlson. Coherent light emission from GaAs junctions. *Phys. Rev. Lett.*, 9:336, 1962.

[3] I. Vurgaftman, J. R. Meyer, and L. R. Ram-Mohan. Band parameters for III-V compound semiconductors and their alloys. *Appl. Phys. Rev.*, 89(11):5815, 2001.

[4] W. Z. Shen, S. C. Shen, W. G. Tang, Y. Zhao, and A. Z. Li. Optical investigation of quaternary GaInAsSb/AlGaAsSb strained multiple quantum wells. *Appl. Phys. Lett.*, 67(23):3432, December 1995.

[5] S. Nakamura, T. Mukai, and M. Senoh. High-brightness InGaN/AlGaN double heterostructure blue-green-light-emitting diodes. *J. Appl. Phys.*, 76:8189–8191, 1994.

[6] L. Ajili and et al. Continuous-wave operation of far-infrared quantum-cascade lasers. *Electron. Lett.*, 38(25), December 2002.

[7] R. Jäger, M. Grabherr, C. Jung, R. Michalzik, G. Reiner, B. Weigl, and K. J. Ebeling. 57% wallplug efficiency oxide-confined 850nm wavelength GaAs VCSELs. *Electron. Lett.*, 33(4):330–331, February 1997.

[8] H. Haken. *Licht und Materie I+II.* BI Wissenschaftsverlag, 1979.

[9] T. Rössler, R. A. Indik, G. K. Harkness, and J. V. Moloney. Modeling the interplay of thermal effects and transverse mode behaviour in native-oxide confined vertical-cavity surface emitting lasers. *Phys. Rev. A.*, 58(4), October 1998.

[10] T. V. Sarkisyan and et al. Nonlinear gain and carrier temperature dynamics in semiconductor laser media. *J. Opt. Soc. Am. B*, 15(3):1107, March 1998.

[11] G. Khitrova, H. M. Gibbs, F. Jahnke, M. Kira, and S. W. Koch. Nonlinear optics of normal-mode-coupling semiconductor microcavities. *Rev. Mod. Phys.*, 71(5):1591, October 1999.

[12] G. P. Bava, L. Fratta, and P. Debernardi. Quantum noise in vertical-cavity surface-emitting lasers with polarization competition. *J. Opt. Soc. Am. B*, 16(11):2147–2157, November 1999.

[13] J. Kaiser, C. Degen, and W. Elsäßer. Amplitude-squeezed emission from a transverse single-mode vertical-cavity surface-emitting laser with weak anti-correlated polarization modes. *Optics Lett.*, 26(21):1720–1722, November 2001.

[14] S. M. Goodnick and P. Lugli. Effect of electron-electron scattering on nonequilibrium transport in quantum-well systems. *Phys. Rev. B*, 37:2578, 1988.

[15] M. Grupen and K. Hess. Simulation of Carrier Transport and Nonlinearities in Quantum-Well Laser Diodes. *IEEE J. Quan. Electron.*, 34(1):120, January 1998.

[16] Y. Nishikawa, A. Tackeuchi, S. Nakamura, S. Muto, and N. Yokoyama. All-optical picosecond switching of a quantum well etalon using spin-polarization relaxation. *Appl. Phys. Lett.*, 66(7):839, February 1995.

[17] H. Soda, K. Iga, T. Kitahara, and T. Suematsu. GaInAsP/InP surface emitting injection lasers. *Jpn. J. Appl. Phys.*, 18(12):2329–2330, October 1979.

[18] K. Iga, F. Koyama, and S. Kinoshita. Surface Emitting Semiconductor Lasers. *IEEE J. Quan. Electron.*, 24(9):1845–1855, September 1988.

[19] M. C. Amman, M. Ortsiefer, and R. Shau. Vertical-cavity surface-emitting laser diodes for telecommunication wavelength. In *Proc. ITCOM*, volume 4871, pages 123–127, 2002.

[20] M. R. Hofmann and et al. Emission Dynamics and Optical Gain of 1.3-μm (GaIn)(NAs)/GaAs lasers. *IEEE J. Quan. Electron.*, 38(2):213–221, February 2002.

[21] A. Markus and et al. Comparison of radiative properties of InAs quantum dots and GaInNAs quantum wells emitting around 1.3μm. *Appl. Phys. Lett.*, 80(6):911–913, February 2002.

[22] Y. Ohiso, H. Okamoto, R. Iga, K. Kishi, and C. Amano. Single Transverse Mode Operation of 1.55-μm Buried Heterostructure Vertical-Cavity Surface-Emitting Lasers. *IEEE Phot. Tech. Lett.*, 14(6):738–740, June 2002.

[23] M. Kondow and et al. GaInNAs: A novel material for long-wavelength- range laser diodes with excellent high-temperature performance. *Jpn. J. Appl. Phys.*, 35:1273–1278, 1996.

[24] H. B. Serreze and Y. C. Chen. Low-threshold, strained-layer, GaInP/AlGaInP GRINSCH visible diode lasers. *IEEE Phot. Tech. Lett.*, 3(5):397–399, 1991.

[25] P. Debernardi, L. Fratta, and G. P. Bava. Spectral Linewidth in Oxide-Confined Vertical-Cavity Surface-Emitting Lasers. *IEEE J. Quan. Electron.*, 37(8):1084–1094, August 2001.

[26] D. Burak and R. Binder. Cold-Cavity Vectorial Eigenmodes of VCSEL's. *IEEE J. Quan. Electron.*, 33(7):1205–1215, July 1997.

[27] D. Burak and R. Binder. Electromagnetic characterization of vertical-cavity surface-emitting lasers based on a vectorial eigenmode calculation. *Appl. Phys. Lett.*, 72(8):891–893, February 1998.

[28] G. P. Bava, P. Debernardi, and L. Fratta. Three-dimensional model for vectorial fields in vertical-cavity surface-emitting lasers. *Phys. Rev. A*, 63(023816), January 2001.

[29] P. Bienstman and et al. Comparison of Optical VCSEL Models on the Simulation of Oxide-Confined Devices. *IEEE J. Quan. Electron.*, 37(12):1618–1631, December 2001.

[30] M. P. Exter, A. Al-Remawi, and J. P. Woerdman. Polarization Fluctuations Demonstrate Nonlinear Anisotropy of a Vertical-Cavity Semiconductor Laser. *Phy. Rev. Lett.*, 80(22):4875–4878, June 1998.

[31] M. S. Skolnick, T. A. Fisher, and D. M. Whittaker. Strong coupling phenomena in quantum microcavity structures. *Semicond. Sci. Tech.*, 13:645–669, 1998.

[32] G. Messin and et al. Parametric Polariton Amplification in Semiconductor Microcavities. *Phys. Rev. Lett.*, 87(12), 17 September 2001.

[33] R. Butté and et al. Transition from strong to weak coupling and the onset of lasing in semiconductor microcavities. *Phys. Rev. B*, 65(205310), 2002.

[34] H. F. Hofmann and O. Hess. Quantum Maxwell-Bloch equations for spatially inhomogeneous semiconductor lasers. *Phys. Rev. A*, 59(3):1, 1999.

[35] O. Hess and T. Kuhn. Maxwell-Bloch equations for spatially inhomogeneous semiconductor Lasers: I. Theoretical formulation. *Phys. Rev. A*, 54(4):3347, 1996.

[36] A. Taflove and S. C. Hagness. *Computational Electrodynamics: The Finite-Difference Time-Domain Method*. Artech House, 2 edition, 2000.

[37] A. S. Nagra and R. A. York. FDTD Analysis of Wave Propagation in Nonlineaer Absorbing Gain Media. *IEE Trans. Ant. Prop.*, 46(3):334, March 1998.

[38] R. Luebbers and et al. A Frequency-Dependent Finite-Difference Time-Domain Formulation for Dispersive Materials. *IEEE Trans. Electromag. Comp.*, 32(3):222, 1990.

[39] S. A. Basinger and D. J. Brady. Finite-difference time-domain modeling of dispersive nonlinear Fabry-Perot cavities. *J. Opt. Soc. Am. B*, 11(8):1504, 1994.

[40] R. W. Ziolkowski, J. M. Arnold, and D. M. Gogny. Ultrafast pulse interactions with two-level atoms. *Phys. Rev. A*, 52(4), October 1995.

[41] A. Klaedtke, J. Hamm, and O. Hess. *Computational Material Science - From Basic Principles to Material Properties*, chapter Simulation of Active and Nonlinear Photonic Nano-Materials in the Finite-Difference Time-Domain (FDTD) Framework. Lecture Notes in Physics. Springer-Verlag, 2004.

[42] A. Yariv. *Quantum Electronics*. John Wiley & Sons Inc., 1988.

[43] W. W. Chow, S. W. Koch, and M. Sargent III. *Semiconductor-Laser Physics*. Springer-Verlag, 1994.

[44] R. Loudon. *The Quantum Theory of Light*. Oxford Science Pub., 3 edition, 2000.

[45] P. Meystre and M. Sargent III. *Elements of Quantum Optics*. Springer Verlag, 1998.

[46] H. Haken. *Quantenfeldtheorie des Festkörpers*. B. G. Teubner, 2 edition, 1993.

[47] H. Haug and S. W. Koch. *Quantum Theory of the Optical and Electronic Properties of Semiconductors*. World-Scientific, 1993.

[48] C. M. Bowden and G. P. Agrawal. Maxwell-Bloch formulation for semiconductors: Effects of coherent COulomb exchange. *Phys. Rev. A*, 51(5), May 1995.

[49] E. Gehrig. *Raumzeitliche Dynamik von Hochleistungshalbleiterlasern unter kohärenter Strahlungsinjektion*. PhD thesis, Universität Kaiserslautern, 1999.

[50] C. Z. Ning and P. M. Goorjian. Microscopic modeling and simulation of transverse-mode dynamics of vertical-cavity surface-emitting lasers. *J. Opt. Soc. Am. B*, 16(11):2072–2082, November 1999.

[51] A. Valle and L Pesquera. Analytical calculation of transverse-mode characteristics in vertical-cavity surface-emitting lasers. *J. Opt. Soc. Am. B*, 19(7):1549–1557, July 2002.

[52] G. Björk, Y. Yamamoto, and H. Heitmann. *Confined Electrons and Photons*, chapter Spontaneous emission control in semiconductor microcavities, pages 467–501. Plenum Press, New York, 1995.

[53] M. Kira, F. Jahnke, W. Hoyer, and S. W. Koch. Quantum Theory of Spontaneous Emission and Coherent Effects in Semiconductor Microstructures. *Prog. Quan. Electron.*, 23:189, 1999.

[54] C. W. Gardiner. *Quantum Noise*. Springer-Verlag, 1991.

[55] C. H. Henry and R. F. Kazarinov. Quantum noise in photonics. *Rev. Mod. Phys.*, 68(3):801, July 1996.

[56] H. F. Hofmann. *Quantum Noise and Spontaneous Emission in Semiconductor Laser Devices*. PhD thesis, Universität Stuttgart, March 1999.

[57] P. Debernardi, G. P. Bava, and L. Fratta. Linewidth evaluation of gain-guided VCSELs. *Procs. of SPIE*, 3627, 1999.

[58] Y. Yamamoto. *Mesoscopic Quantum Optics*. Wiley, September 1999.

[59] E. Binder. *Mikroskopische Modellierung des Zerfalls von Interband- und Intraband-Kohärenz in optisch angeregten Halbleitern*. PhD thesis, Universität Stuttgart, 1996.

[60] T. Kuhn. *Ladungsträgerdynamik in Halbleitersystemen fern vom Gleichgewicht: Elektronisches Rauschen und kohärente Prozesse; Habilitationsschrift*. Universität Stuttgart, 1994.

[61] V. S. Filinov, W. Hoyer, M. Bonitz, M. Kira, V. E. Fortov, and S. W. Koch. Spontaneous emission of semiconductors in the Wigner approach. *J. Opt. B: Quantum Semiclass. Opt.*, 5:299–305, 9 June 2003.

[62] Y. Yamamoto. *Coherence, Amplification, and Quantum Effects in Semiconductor Lasers*. Wiley Interscience, 1991.

[63] G. Björk, S. Machida, Y. Yamamoto, and K. Igeta. Modification of spontaneous emission rate in planar dielectric microcavity structures. *Phys. Rev. A*, 44(1):669, July 1991.

[64] T. Baba, T. Hamano, F. Koyama, and K. Iga. Spontaneous Emission Factor of a Microcavity DBR Surface Emitting Laser (II) - Effects of Electron Quantum Confinement. *IEEE J. Quan. Electron.*, 28(5):1310–1319, May 1992.

[65] D. Kleppner. Inhibited Spontaneous Emission. *Phys. Rev. Letters*, 47(4):233, July 1981.

[66] Y. Yamamoto and S. Machida. Microcavity semiconductor laser with enhanced spontaneous emission. *Phys. Rev. A*, 44(1):657, July 1991.

[67] K. Streubel, N. Linder, R. Wirth, and A Jaeger. High Brightness AlGaInP Light-Emitting Diodes. *IEEE J. Sel. Top. Quan. Electron.*, 8(2), April 2002.

[68] D. Preißer. *Theorie der quantenoptischen und nichtlinear-dynamischen Eigenschaften von Halbleiterlasern*. PhD thesis, Universität Stuttgart, 2001.

[69] W. Krauth and S. Großmann. Linewidths of lasers with broken polarization symmetry. *Phys. Rev. A*, 35(10):4192–4199, May 1987.

[70] A. P. Ongstad, G. C. Dente, and M. L. Tilton. Carrier heating and the power independent linewidth in semiconductor lasers. *J. Appl. Phys.*, 82(1):84, July 1997.

[71] S. Balle. Simple analytical approximations for the gain and refractive index spectra in quantum-well lasers. *Phys. Rev. A*, 57(2), 1998.

[72] J. Hader, J. V. Moloney, and S. W. Koch. Microscopic Theory of Gain, Absorption, and Refractive Index in Semiconductor Laser Materials - Influence of COnduction-Band Nonparabolicity and Coulomb-Induced Intersubband Coupling. *IEEE J. of. Quan. Electron.*, 35(12), December 1999.

[73] C. Z. Ning, R. A. Indik, and J. V. Moloney. Effective Bloch Equations for Semiconductor Lasers and Amplifiers. *IEEE J. Quan. Electron.*, 33(9):1543–1550, September 1997.

[74] B. Klein, L. F. Register, M. Grupen, and K. Hess. Numerical simulation of vertical cavity surface emitting lasers. *Opt. Express*, 2(4), 16 February 1998.

[75] P. Debernardi and G. P. Bava. Effects of Anisotropies on Vectorial Modes of Vertical-Cavity Surface-Emitting Lasers. *phys. stat. sol.*, 188(3):967–977, July 2001.

[76] P. Debernardi, G. P. Bava, F. Monti di Sopra, and M. B. Willemsen. Features of Vectorial Modes in Phase-Coupled VCSEL Arrays: Experiments and Theory. *IEEE J. Quan. Electron.*, 39(1):109–119, January 2003.

[77] J. Mulet, C. R. Mirasso, S. Balle, and M. San Miguel. Transverse and Polarization Mode Selection in VCSELs. *Procs. of SPIE*, 4283:139–149, January 2001.

[78] P. Seurin and et al. Modal competition in implant apertured index-guided vertical-cavity surface-emitting lasers. *Appl. Phys. Lett.*, 77(23):3686–3688, April 2000.

[79] S. F. Yu. An Improved Time-Domain Traveling-Wave Model for Vertical-Cavity Surface-Emitting Lasers. *IEEE J. Quan. Electron.*, 34(10):1938–1948, October 1998.

[80] M. Lax, W. H. Louisell, and W. B. McKnight. From Maxwell to paraxial wave optics. *Phys. Rev. A*, 11(4):1365, 1975.

[81] O. Hess. *Raum-zeitliche Dynamik gekoppelter Halbleiterlaser und deren Kontrolle; Habilitationsschrift*. Universität Stuttgart, 1997.

[82] J. van Hemmen, W. M. Kistler, and E. G. F. Thomas. Calculation of Volterra Kernels for Solutions of Nonlinear Differential Equations. *Siam J. Appl. Math.*, 61(1):1–21, 2000.

[83] D. Censor and T. Melamed. Volterra Differential Constitutive Operators and Locality Considerations in Electromagnetic Theory. *Prog. In Electromagn. Res. (PIER)*, 36:121–137, 2002.

[84] P. Goorjian and C. Z. Ning. Transverse mode dynamics of VCSELs through space-time domain simulation. *Opt. Express*, 5(3):55–62, 2 August 1999.

[85] T. Makino. Transfer-Matrix Theory of the Modulation and Noise of Multielement Semiconductor Lasers. *IEEE J. Quan. Electron.*, 29(11):2762–2770, November 1993.

[86] M. Born and E. Wolf. *Principles of Optics*. Cambridge University Press, 7 edition, 1999.

[87] M. P. Exter, A. K. Jansen van Doorn, and J. P. Woerdman. Electro-optic effect and birefringence in semiconductor vertical-cavity lasers. *Appl. Phys. Lett.*, 56(1):845–853, July 1997.

[88] J. Kaiser, C. Degen, and W. Elsäßer. Polarization-switching influence on the intensity noise of vertical-cavity surface-emitting lasers. *J. Opt. Soc. Am. B*, 19(4):672, April 2002.

[89] C. Degen, B. Krauskopf, G. Jennemann, I. Fischer, and W. Elsäßer. Polarization selective symmetry breaking in the near-fields of vertical cavity surface emitting lasers. *J. Opt. B: Quantum Semiclass. Opt.*, 2:517–525, 2000.

[90] A. Yariv and P. Yeh. *Optical Waves in Crystals: Propagation and Control of Laser Radiation*. Wiley Europe, 1984.

[91] Optical Society of America. *Handbook of Optics I+II*. Mc Graw Hill, 1995.

[92] B. Nagler and et al. Polarization-mode hopping in single-mode vertical-cavity surface-emitting lasers: Theory and experiment. *Phys. Rev. A*, 68:013813–1, July 2003.

[93] L. M. Augustin and et al. Controlled Polarization Switching in VCSELs by Means of Asymmetric Current Injection. *IEEE Phot. Tech. Lett.*, 16(3), March 2004.

[94] A. E. Siegman. *Lasers*. University Science Books, 3 edition, 1986.

[95] S. V. Vonsovsky and M. I. Katsnelson. *Quantum Solid-State Physics*. Springer-Verlag, 1989.

[96] O. Hess. *Spatio-Temporal Dynamics of Semiconductor Lasers; Doktorarbeit*. WuT, 1993.

[97] M. Bonitz. *Quantum Kinetic Theory*. B. G. Teubner, 1998.

[98] W. Batty, U. Ekenberg, A. Ghit, and E. P. O'Reilly. Valence subband structure and optical gain of GaAs-AlGaAs (111) quantum wells. *Semicond. Sci. Technol.*, 4(11):904–909, November 1989.

[99] M. San Miguel, Q. Feng, and J. V. Moloney. Light-polarization dynamics in surface-emitting semiconductor lasers. *Phys. Rev. A*, 52(2):1728–1739, August 1995.

[100] S. Adachi. GaAs, AlAs, and $Al_xGa_{1-x}As$: Material parameters for use in research and device applications. *J. Appl. Phys.*, 58(3), 1985.

[101] E. P. O'Reilly. Valence band engineering in strained-layer structures. *Semicond. Sci. Technol.*, 4(3):121–137, March 1989.

[102] E. Wigner. On the Quantum Correction For Thermodynamic Equilibrium. *Phys. Rev.*, 40:749, 1932.

[103] W. E. Brittin and W. R. Chappell. The Wigner Distribution Function and Second Quantization in Phase Space. *Rev. Mod. Phys.*, 34(4):620, 1962.

[104] M. Lindberg and S. W. Koch. Effective Bloch equations for semiconductors. *Phys. Rev. B*, 38:3342–3350, 1988.

[105] C. Z. Ning, J. V. Moloney, A. Egan, W.W. Chow, R. Binder, A. Girndt, and S. W. Koch. Incorporating many-body effects into modeling semiconductor lasers and amplifiers. In *Proc. of SPIE*, 1997.

[106] D. K. Sadana and C. M. Lampert, editors. *Advanced Semiconductor Processing and Characterization of Electrical and Optical Materials, Proceedings of SPIE*, volume 463, 1984.

[107] C. Z. Ning, R. A. Indik, J. V. Moloney, and S. W. Koch. Effects of plasma and lattice heating in VCSELs. *Procs. of SPIE*, 2399:617, 1995.

[108] H. M. Cohen and J. C. Phillips. Dielectric Screening and Self-Consistent Crystal Fields. *Phys. Rev.*, 124:1818–1824, 1961.

[109] R. Zimmermann. Final state interactions in the gain and absorption spectra of electron-hole liquids. *Phys. Status Solidi B*, 86(K63), 1978.

[110] R. Zimmermann. *Many Particle Theory of Highly Excited Semiconductors*. Teubner, Leipzig, 1988.

[111] M. Bonitz, D. Kremp, D. C. Scott, R. Binder, W. D. Kraeft, and H. S.| Köhler. Numerical analysis of non-Markovian effects in charge-carrier scattering: one-time versus two-time kinetic equations. *J. Phys. Condens. Matter*, 8:6057–6071, 1996.

[112] F. Prati, L. Fratta, and M. Travagnin. Band model for light-polarization selection in unstrained quantum-well vertical-cavity surface-emitting lasers. *Phys. Rev. A*, 62(033819), August 2000.

[113] D. Burak, J. V. Moloney, and R. Binder. Microscopic theory of polarization properties of optically anisotropic vertical cavity surface-emitting lasers. *Phys. Rev. A*, 61(053809), April 2000.

[114] J. Hamm, K. Boehringer, and O. Hess. Spatially resolved polarization and temperature dynamics in quantum-well vertical-cavity surface emitters: a mesoscopic approach. *Proc. of SPIE*, 4646:176–189, June 2002.

[115] E. Gehrig and O. Hess. Nonequilibrium spatiotemporal dynamics of the Wigner distributions in broad-area semiconductor lasers. *Phys. Rev. A*, 57(3):2150, 1998.

[116] E. Gehrig and O. Hess. Pulse trapping and nonequilibrium spatiotemporal wave mixing in broad-area semiconductor lasers. *JOSA B*, 15(12):2861–2867, December 1998.

[117] H. Haug and S. W. Koch. Semiconductor laser theory with many-body effects. *Phys. Rev. A*, 39:1887–1898, 1989.

[118] J. W. Scott, R. S. Geels, S. W. Corzine, and L. A. Coldren. Modeling Temperature Effects and Spatial Hole Burning to Optimize Vertical-Cavity Surface-Emitting Laser Performance. *IEEE J. Quan. Electron.*, 29(5):1295–1307, May 1993.

[119] J. S. Gustavsson, J. A. Vukusic, J. Bengtsson, and A. Larsson. A Comprehensive Model for the Modal Dynamics of Vertical-Cavity Surface-Emitting Lasers. *IEEE J. Quan. Electron.*, 38(2):203–212, February 2002.

[120] I. Fischer, O. Hess, W. Elsäßer, and E. Göbel. Complex Spatio-Temporal Dynamics in the Near-Field of a Broad-Area Semiconductor Laser. *Europhys. Lett.*, 35(8):579–584, 1996.

[121] C. Simmendinger, D. Preißer, and O. Hess. Stabilisation of chaotic spatiotemporal filamentation in large broad area lasers by spatially structured optical feedback. *Opt. Express*, 5(3):48–52, 2 August 1999.

[122] A. Barchanski, T. Gensty, C. Degen, I. Fischer, and W. Elsäßer. Picosecond Emission Dynamics of Vertical-Cavity Surface-Emitting Lasers: Spatial, Spectral, and Polarization-Resolved Characterization. *IEEE J. Quan. Electron.*, 39(7), 2003.

[123] A. Tackeuchi, Y. Nishikawa, and O. Wada. Room-temperature electron spin dynamics in GaAs/AlGaAs quantum wells. *Appl. Phys. Lett.*, 68(6):797, February 1996.

[124] T. V. Sarkisyan, A. T. Rosenberger, A. N. Oraevsky, and D. K. Bandy. Gain and carrier temperature response for semiconductor laser media to short optical pulses. *J. Opt. Soc. Am. B*, 17(5):840, May 2000.

[125] S. P. Hegarty, G. Huyet, J. G. McInerney, K. D. Choquette, K. M. Geib, and H. Q. Hou. Size dependence of transverse mode structure in oxide-confined vertical-cavity laser diodes. *Appl. Phys. Lett.*, 73(5):596–598, August 1998.

[126] C. Degen, I. Fischer, and W. Elsäßer. Transverse modes in oxide confined VCSELs: Influence of pump profile, spatial hole burning, and thermal effects. *Opt. Express*, 5(3):38, 1999.

[127] C. Z. Ning and J. V. Moloney. Thermal effects on the threshold of vertical-cavity surface-emitting lasers: first- and second-order phase transitions. *Opt. Lett.*, 20(10):1151, May 1995.

[128] C. Z. Ning, R. A. Indik, and J. V. Moloney. Self-consistent approach to thermal effects in vertical-cavity surface-emitting lasers. *J. Opt. Soc. Am. B*, 12(10):1993, October 1995.

[129] S. F. Yu. *Analysis and Design of Vertical Cavity Surface Emitting Lasers*. John Wiley & Sons, September 2003.

[130] D. Burak, S. A. Kemme, R. K. Kostuk, and R. Binder. Spectral identification of transverse lasing modes of multimode index-guided vertical-cavity surface-emitting lasers. *Appl. Phys. Lett.*, 73(24):3501–3503, December 1998.

[131] L. Fratta, P. Debernardi, and G. P. Bava. Spatially inhomogeneously polarized transverse modes in vertical-cavity surface-emitting lasers. *Phys. Rev. A*, 64(031803), August 2001.

[132] J. Mulet and S. Balle. Transverse mode dynamics in vertical-cavity surface-emitting lasers: Spatiotemporal versus modal expansion descriptions. *Phys. Rev. A*, 66(053802), 2002.

[133] S. F. Pereira, M. B. Willemsen, M. P. van Exter, and J. P. Woerdman. Pinning of daisy modes in optically pumped vertical-cavity surface-emitting lasers. *Appl Phys. Lett.*, 73(16):2239–2241, October 1998.

[134] K. D. Choquette, D. A. Richie, and R. E. Leibenguth. Temperature dependence of gain-guided vertical-cavity surface emitting laser polarization. *Appl. Phys. Lett.*, 64(16):2062, 18 April 1994.

[135] B. Ryvkin and et al. Effect of photon-energy-dependent loss and gain mechanisms on polarization switching in vertical-cavity surface-emitting lasers. *J. Opt. Soc. Am. B.*, 16(11):2106–2113, November 1999.

[136] T. Erneux, J. Danckaert, K. Panajotov, and I. Veretennicoff. Two-variable reduction of the San Miguel-Feng-Moloney model. *Phys. Rev. A*, 59(6):4660–4667, July 1998.

[137] E. Collett. *Polarized Light*. Marcel Dekker, Inc., 1993.

[138] H. F. Hofmann and O. Hess. Polarization fluctuations in vertical-cavity surface-emitting lasers: a key to the mechanism behind polarization stability. *J. Opt. B: Quantum Semiclass. Opt.*, 10:87–96, 1998.

[139] M. Travagnin, M. P. Exter, and J. P. Woerdman. Influence of carrier dynamics on the polarization stability and noise-induced polarization hopping in surface-emitting semiconductor lasers. *Phys. Rev. A*, 56(2):1497–1507, August 1997.

[140] A. Valle, L. Pesquera, and K. S. Shore. Polarization behaviour of birefringent multi-transverse mode vertical cavity surface emitting lasers. *IEEE Photon. Tech. Lett.*, 9:557–559, 1997.

[141] M. Brunner, K. Gulden, R. Hövel, M. Moser, and M. Ilegems. Thermal lensing effects in small oxide confined vertical-cavity surface-emitting lasers. *Appl. Phys. Lett.*, 76(1):7–9, January 2000.

[142] E. Gehrig and O. Hess. Microscopic theory of spatiotemporal multiwave mixing in broad-area semiconductor laser amplifiers. *Phys. Rev. A*, 60:5035–5045, 1999.

[143] A. Barchanski. Pikosekunden Emissionsdynamik von Oberflächenemittierenden Halbleiterlasern mit Vertikalresonatoren. Diplomarbeit, Universität Darmstadt, December 2002.

[144] M. Kuznetsov, F. Hakimi, R. Sprague, and A. Mooradian. Design and Characteristics of High-Power (>0.5-W CW) Diode-Pumped Vertical-External-Cavity Surface-Emitting Semiconductor Lasers with Circular TEM$_{00}$ Beams. *IEEE J. Sel. Top. Quan. Electron.*, 5(3):561–573, May 1999.

[145] A. Gahl, S. Balle, and M. San Miguel. Polarization Dynamics of Optically Pumped VCSEL's. *IEEE J. Quan. Electron.*, 35(3):342–350, March 1999.

[146] G. Mur. Absorbing Boundary Conditions for the Finite-Difference Approximation of the Time-Domain Electromagnetic-Field Equations. *IEEE Trans. Elec. Comp.*, 23(4):377, 1981.

[147] M. J. Moran, H. N. Shapiro, P. Schmidt, O. Ezekoye, J. Howell, and D. Baker. *Fundamentals of Engineering Thermodynamics*. Wiley, 4 edition, 2002.